

**Transient Ground Deformation in Tectonically Active Regions  
and Implications for the Mechanical Behavior of the Crust and  
Upper Mantle**

by

Trevor T. Hines

A dissertation submitted in partial fulfillment  
of the requirement for the degree of  
Doctor of Philosophy  
(Earth and Environmental Sciences)  
in the University of Michigan  
2017

Doctoral Committee:

Associate Professor Eric Hetland, Chair  
Associate Professor Jeremy Bassis  
Professor Jeroen Ritsema  
Professor John Boyd  
Associate Professor Nathan Niemi

Trevor T. Hines  
hinest@umich.edu  
ORCID iD: 9999-9999-9999-9999

## **ACKNOWLEDGEMENTS**

Blerg blargle blorg blerp

## PREFACE

Blerg blargle blorg blerp

## TABLE OF CONTENTS

<b>ACKNOWLEDGEMENTS</b>	<b>iii</b>
<b>PREFACE</b>	<b>iv</b>
<b>LIST OF FIGURES</b>	<b>xvi</b>
<b>LIST OF TABLES</b>	<b>xvii</b>
<b>LIST OF APPENDICES</b>	<b>xviii</b>
<b>ABSTRACT</b>	<b>xix</b>
<b>CHAPTER 1: Bias in estimates of lithosphere viscosity from interseismic deformation</b>	<b>1</b>
1.1 Abstract . . . . .	1
1.2 Introduction . . . . .	1
1.3 Interseismic models . . . . .	3
1.3.1 Depth-dependence of $\tau$ . . . . .	3
1.4 Determination of apparent strength . . . . .	4
1.5 Biases in apparent strength . . . . .	7
1.6 Lower crustal shear zones . . . . .	8
1.7 Discussion . . . . .	8
1.8 Conclusions . . . . .	10
1.9 Acknowledgments . . . . .	11
1.10 Supporting information . . . . .	11
<b>CHAPTER 2: Rapid and simultaneous estimation of fault slip and heterogeneous lithospheric viscosity from postseismic deformation</b>	<b>16</b>
2.1 Summary . . . . .	16

2.2	Introduction . . . . .	16
2.3	Approximation for postseismic deformation . . . . .	17
2.3.1	Two-dimensional earthquake models . . . . .	18
2.3.2	Three-dimensional earthquake models . . . . .	23
2.4	Inversion method . . . . .	24
2.5	Synthetic test . . . . .	26
2.5.1	Green's functions . . . . .	27
2.5.2	Synthetic model with Maxwell viscoelasticity . . . . .	28
2.5.3	Synthetic model with Burgers viscoelasticity . . . . .	34
2.6	Discussion . . . . .	35
2.7	Conclusion . . . . .	39
	Appendix 2A: Inverse Laplace transform through series expansion . . . . .	39
	Appendix 2B: Postseismic approximation for a two-dimensional earthquake model with a depth dependent viscosity . . . . .	40
<b>CHAPTER 3: Rheologic constraints on the upper mantle from five years of postseismic deformation following the El Mayor-Cucapah earthquake</b>		<b>42</b>
3.1	Abstract . . . . .	42
3.2	Introduction . . . . .	42
3.3	Data processing . . . . .	44
3.4	Postseismic modeling . . . . .	52
3.4.1	Elastic postseismic inversion . . . . .	53
3.4.2	Early postseismic inversion . . . . .	56
3.4.3	Full postseismic inversion . . . . .	62
3.5	Discussion . . . . .	66
3.6	Conclusion . . . . .	69
3.7	Acknowledgements . . . . .	69
3.8	Supporting information . . . . .	69
<b>CHAPTER 4: Unbiased characterization of noise in geodetic data</b>		<b>74</b>
4.1	Abstract . . . . .	74
4.2	Introduction . . . . .	74
4.3	Maximum likelihood methods . . . . .	76
4.4	Synthetic demonstration . . . . .	78
4.5	Discussion and conclusion . . . . .	80
4.6	Acknowledgements . . . . .	81

Appendix 4A: REML algorithm . . . . .	81
<b>CHAPTER 5: Revealing transient strain in geodetic data with Gaussian process regression</b>	<b>82</b>
5.1 Summary . . . . .	82
5.2 Introduction . . . . .	82
5.3 Estimating transient strain rates . . . . .	85
5.4 Outlier detection . . . . .	88
5.5 Application to Cascadia slow slip events . . . . .	89
5.5.1 Noise model . . . . .	90
5.5.2 Prior model . . . . .	92
5.5.3 Transient strain rates . . . . .	98
5.6 Discussion . . . . .	99
5.7 Conclusion . . . . .	104
5.8 Acknowledgements . . . . .	104
<b>CHAPTER 6: Validating Plate Boundary Observatory borehole strainmeter data with GNSS derived strain</b>	<b>105</b>
6.1 Introduction . . . . .	105
6.2 BSM Data . . . . .	105
6.3 GNSS derived strain . . . . .	108
6.4 Results . . . . .	110
6.5 Conclusion . . . . .	112
<b>REFERENCES</b>	<b>122</b>

## LIST OF FIGURES

<p>1.1 Schematic of the earthquake cycle model: springs indicate elasticity and dash-pots indicate Newtonian viscosity. Example depth-dependent <math>\tau</math> profiles are shown in the upper mantle, for the case when <math>\tau_{UM}^{\min} = 10^{-2}</math>, <math>\tau_{UM}^{\max} = 10^2</math>, and <math>\bar{\tau}_{UM}</math> indicated by vertical dotted lines. . . . .</p> <p>1.2 A) Velocities for a depth-dependent model, <math>v_{DD}</math> (black solid lines) and the best fitting velocities predicted by a layered model, <math>v_L</math> (colored solid lines). Black dashed line is the velocities predicted by an elastic earthquake model with the same <math>D</math> and <math>v_T</math>. B) <math>\tau</math> profiles corresponding to <math>v_{DD}</math> in (A) and <math>\hat{\tau}_j</math> associated with the best fitting <math>v_L</math> in (A). C) <math>\bar{\tau}_j</math> for the <math>\tau</math> profile in (B) with <math>\hat{\tau}_j</math> for each of the cases in (B). Solid lines indicate misfit contours in the grid-search estimation of <math>v_L</math> in (A); contours shown are RMSE = 0.02 (dark lines) and 0.04 (faded lines), and color indicates the time. . . . .</p> <p>1.3 <math>\bar{\tau}_j</math> for all depth-dependent <math>\tau</math> models considered (gray dots), along with the estimation Bias(<math>\hat{\tau}_j</math>) (vectors) early (A), midway (B), and late (C) in the interseismic period. Each vector points to the mean <math>\hat{\tau}_j</math> estimated from depth-dependent models with the same <math>\bar{\tau}_j</math>, and the gray ovals indicate one standard deviation of <math>\hat{\tau}_j</math>. The vector colors reflect the magnitude of the bias and help to distinguish overlapping vectors. . . . .</p> <p>1.4 A) Interseismic velocities, <math>v_{SZ}</math>, in a model with both a lower crustal shear zone and depth-dependent <math>\tau</math> in the surrounding lithosphere (black lines) along with the best fit <math>v_L</math> (colored lines). Shown as light blue lines are the velocities in a layered model with the dark blue viscosity profile shown in (b), which are the apparent viscosities estimated from <math>v_{SZ}</math> at <math>t/T = 0.01</math>. B) <math>\tau</math> profile outside of the shear zone corresponding to <math>v_{SZ}</math> (black line; <math>\tau = 10^{-2}</math> within the shear zone), <math>\bar{\tau}</math> outside the shear zone, and <math>\hat{\tau}_j</math> associated with the best fitting <math>v_L</math> in (A) (colored lines, color corresponds to time in cycle). Inset in (B) shows <math>\bar{\tau}_j</math> and <math>\hat{\tau}_j</math> (dot color corresponds to line colors in (A) and (B)). . . . .</p>	<p>4</p> <p>5</p> <p>6</p> <p>9</p>
--------------------------------------------------------------------------------------------------------------------------------------------------------------------------------------------------------------------------------------------------------------------------------------------------------------------------------------------------------------------------------------------------------------------------------------------------------------------------------------------------------------------------------------------------------------------------------------------------------------------------------------------------------------------------------------------------------------------------------------------------------------------------------------------------------------------------------------------------------------------------------------------------------------------------------------------------------------------------------------------------------------------------------------------------------------------------------------------------------------------------------------------------------------------------------------------------------------------------------------------------------------------------------------------------------------------------------------------------------------------------------------------------------------------------------------------------------------------------------------------------------------------------------------------------------------------------------------------------------------------------------------------------------------------------------------------------------------------------------------------------------------------------------------------------------------------------------------------------------------------------------------------------------------------------------------------------------------------------------------------------------------------------------------------------------------------------------------------------------------------------------------------------------------------------------------------------------------------------------------------------------------------------------------------------------------------------------------------------------------------------------------------------------------------------------------------------------------------------------------------------------------------------------------------------------------------------------------------------------------------------------------------------------------------------------------------------------------------------------------------------------------------------------------------------------------------	-------------------------------------

- 1.5 Surface velocities at  $t/T = 0.01$  in models with uniform  $\tau$  in the lower crust or uppermost mantle layers ( $\tau = \tau_M/T = (\eta T)/\mu$ , where  $T$  is the earthquake repeat time,  $\tau_M$  is the Maxwell relaxation time,  $\eta$  is the Newtonian viscosity, and  $\mu$  is the elastic shear modulus). Velocities in models with constant tau in the upper mantle ( $\tau_{UM}$ ), and variable tau in the lower crust ( $\tau_{LC}$ ) are shown in (A). Models with constant  $\tau_{LC}$  and variable  $\tau_{UM}$  are shown in (B). For sufficiently high  $\tau_{UM}$  or  $\tau_{LC}$  the surface velocities converge, indicating that the surface deformation is insensitive to layer viscosities when  $\log_{10}(\tau)$  is above about 1, as the layer is effectively elastic over earthquake repeat time scales. . . . . 12
- 1.6  $\bar{\tau}_j$  (gray dots) for all depth dependent  $\tau$  models considered, along with the estimation of  $\text{Bias}(\hat{\tau}u_j)$ , represented as vectors, early (A), midway (B), and late (C) in the interseismic period. Each vector points to the mean value of  $\hat{\tau}_j$  estimated from depth dependent models with the same  $\bar{\tau}_j$ . Colored dots indicate  $\hat{\tau}_j$  of each of the best fit layered models (dot color corresponds to the RMSE of how well  $v_L$  fits  $v_{DD}$ ). . . . . 13
- 1.7  $\bar{\tau}_j$  (gray dots) for all depth dependent  $\tau$  models with a homogeneous lower crust (A,B,C) or homogeneous upper mantle (D,E,F), along with the estimation of  $\text{Bias}(\hat{\tau}_j)$ , represented as vectors, early (A), midway (B), and late (C) in the interseismic period. Each vector points to the mean value of  $\hat{\tau}u_j$  estimated from depth dependent models with the same  $\bar{\tau}u_j$ , and the gray ovals indicate one standard deviation of  $\hat{\tau}u_j$  estimated from models with the same  $\bar{\tau}u_j$ . . . . . 14
- 1.8  $\bar{\tau}_j$  (gray dots) for all depth dependent  $\tau$  models in which  $\tau$  in the lower crust and upper mantle decreases with depth more than log-linearly (i.e., with  $\tau$  at any depth lower than would be predicted by a log-linear decrease, for instance the left-most  $\tau$  profiles shown in Figure 1.1), along with the estimation of  $\text{Bias}(\hat{\tau}_j)$ , represented as vectors, early (A), midway (B), and late (C) in the interseismic period. Each vector points to the mean value of  $\hat{\tau}_j$  estimated from depth dependent models with the same  $\bar{\tau}_j$ , and the gray ovals indicate one standard deviation of  $\hat{\tau}_j$  estimated from models with the same  $\bar{\tau}_j$ . The estimated biases in these models are similar to the biases estimated from all depth-dependent tau models considered in this paper (Figure 1.3), indicating that consideration of tau profiles that decay less than log-linearly do not drive our conclusions that the lower crust (uppermost mantle) appear stronger (weaker) than the average  $\tau$  during much of the interseismic period. . . . . 15

2.1	Surface displacements predicted by eq. (2.10) truncated after ten terms (green) and the approximation given by eq. (2.11) (dotted black). Times are normalized by the lowest relaxation time in the lithosphere, $\tau_2$ , and distances are normalized by the fault locking depth, $D$ . Displacements are shown as a function of distance from the fault at times $t/\tau_2 = 0.0, 0.5, 1.0$ and $1.5$ . The inset figure shows displacement time series at locations $x/D = 1, 2, 4$ and $8$ . . . . .	21
2.2	L-curves used to select the penalty parameters. Panel (a) shows the trade-off between slip smoothness and data misfit while varying $\lambda_s$ and keeping $\lambda_v$ fixed at zero. Panel (b) shows the trade off between smoothness of inferred viscosity and misfit while varying $\lambda_v$ and keeping $\lambda_s$ fixed at the value chosen from Panel (a). Stars indicate our chosen penalty parameters. . . . .	26
2.3	Slip distribution imposed in both synthetic models (left), slip recovered for the synthetic model with Maxwell viscoelasticity (middle), and uncertainty in the recovered slip magnitude (right). Colors indicate magnitude of slip and arrows indicate direction of slip (arrows pointing right indicate left-lateral and up is thrust). The panels showing afterslip display cumulative slip over the specified time interval. The slip uncertainties are the standard deviation of inferred slip magnitude during the specified period, which were derived from 100 iterations of bootstrapping. . . . .	29
2.4	Synthetic and recovered lithospheric viscosities (left) and associated fluidities (right). Semi-transparent lines are recovered models found through bootstrapping and indicate the degree of uncertainty on the inferred viscosity structure. . . . .	30
2.5	Synthetic surface displacements (black) and best fitting surface displacements using eq. (2.20) (green). Vertical displacements are used in the inversion but are not shown here. Panel (a) shows coseismic displacements and the remaining panels show the cumulative displacements over the indicated time intervals. Ellipses indicate 1 standard deviation uncertainty in the synthetic data. Red dot indicates the position of the time series shown in Figure 2.6 and Figure 2.9. The surface projection of the discretized synthetic fault is depicted in red. . . . .	31
2.6	Displacement time series for the position shown in Figure 2.5 (black), best fitting surface displacements using the approximation from eq. (2.20) (green) and surface displacements computed with PyLith using the inferred slip distribution and viscosity structure (red). Coseismic displacements at $t = 0$ are not shown. . . . .	32

2.7	Approximation error at $t = 10$ years and $t = 20$ years. Circles with 1 mm radius are centered at each station to compare the accuracy of $\vec{u}(\vec{x}, t)$ to the noise in the synthetic data. . . . .	33
2.8	Synthetic and recovered lithospheric viscosities (left) and fluidities (right) for the synthetic model with a Burgers rheology. Dotted and dashed lines show the Maxwell and Kelvin viscosity in the synthetic model, respectively. The solid black line indicates the effective viscosity from eq. (2.25). The red, green, and blue lines show the inferred viscosities and fluidities when inverting a 0.5, 2.0, and 5.0 year long time series, respectively. The light red lines are the bootstrapped fluidities and viscosities inferred using the 0.5 year time series. . . . .	36
2.9	Afterslip moment over time for the synthetic model (black) and the inferred afterslip moment when inverting 0.5, 2.0, and 5.0 years of displacements (red, green, and blue). . . . .	36
2.10	Synthetic and predicted displacement time series with length 0.5, 2.0, and 5.0 years. The time series shown is for the observation point indicated in Fig 5.. . . . .	37
3.1	Map of the region considered in this study. The large focal mechanism is the GCMT solution for the El Mayor-Cucapah earthquake, and the three small focal mechanisms are for the Ocotillo earthquake and the two main shocks during the Brawley swarm. The black dots indicate the locations of GPS stations used in this study. The fault geometry used in this study is shown in magenta where dashed lines indicate buried edges of the fault segments. The green and red boxes demarcate the extent of the near-field and far-field maps (Figures 3.4 and 3.5). Stations inside the blue sector, which highlights the area within $10^\circ$ of the El Mayor-Cucapah P-axis, are used in Figures 3.7 and 3.10. . . . .	45
3.2	Left panels show GPS time series from UNAVCO (black) and the predicted displacement (blue) from eq. (3.2) for a near-field station. Red lines indicate the times of the El Mayor-Cucapah and Ocotillo earthquake. The right panels show estimated coseismic and postseismic displacements, $u_{\text{post}}$ , which are extracted from the predicted displacements. The 68% confidence interval is shown in light blue. . . . .	48
3.3	same as Figure 3.2 but for a far-field station. . . . .	49

3.4 Near-field coseismic and cumulative postseismic displacements over the indicated time periods (black) and predicted displacements for our preferred model from Section 3.4.3 (green). The black error ellipses show the 68% confidence interval for the observed horizontal displacements. Observed vertical displacements are shown as an interpolated field and predicted vertical displacements are shown within the green circles. Note that the interpolant is not well constrained in Mexico where there is no data available. . . . .	50
3.5 Same as Figure 3.4 but for far-field stations. . . . .	51
3.6 Coseismic slip and cumulative afterslip over the indicated time intervals when assuming the crust and mantle are elastic. Color indicates the magnitude of slip and arrows indicate the motion of the hanging wall. . . . .	54
3.7 Scaled radial component of postseismic displacements. Downward motion indicates that the station is moving toward the El Mayor-Cucapah epicenter. Displacement time series are scaled so that the minimum and maximum observed values lie on the grid lines. The observed postseismic displacements, $u_{\text{post}}$ are shown in black with gray indicating the 68% confidence interval. The displacements predicted by the best fitting elastic model are shown in red. The blue and green lines are the predicted postseismic displacements for the models discussed in Section 3.4.3. The blue lines show the predicted displacements for the model with a Maxwell viscoelastic lower crust and upper mantle. The green line shows the predicted displacements for our preferred model, which has a Maxwell viscoelastic lower crust and a Zener viscoelastic upper mantle. The effective viscosities are the same for both models and are shown in Figure 3.12. . . . .	55
3.8 Schematic illustration of the rheologic models considered in this paper as well as their effective viscosities. . . . .	56
3.9 Displacements resulting from fault slip at lower crustal depths (a), and initial velocities resulting from subsequent relaxation of a viscoelastic lower crust (b). The fault segment dips 75° to the north-east and its surface projection is outlined in magenta. The highlighted area on the fault extends from 15 to 30 km depth and indicates where 1 meter of right-lateral slip was imposed. The elastic properties of the crust and mantle are the same as in Table 1, and $\eta_{\text{eff}}$ is $10^{18}$ Pa s in the lower crust. Vertical displacements are interpolated between station locations. . . . .	58
3.10 Observed postseismic displacements (black) and best fitting predictions of eq. (3.14) to 5.0 (blue), 3.0 (green), and 0.8 (yellow) years of the postseismic data. 60	

3.11 Coseismic slip and afterslip inferred by fitting eq. (3.14) to the first 0.8 years of postseismic displacements. . . . .	62
3.12 Effective viscosities and associated fluidities inferred by fitting eq. (3.14) to the first 0.8 years of postseismic displacements. 95% confidence intervals, estimated from bootstrapping, are indicated by shaded regions. . . . .	63
3.13 Mean chi-squared value as a function of the transient shear modulus relative to the elastic shear modulus in a Zener rheology upper mantle. Large dot indicates our preferred ratio. . . . .	64
3.14 Inferred coseismic slip and afterslip for our preferred model, which has a Maxwell rheology in the lower crust and a Zener rheology in the upper mantle. The transient viscosity, $\eta_K$ , in the mantle and steady-state viscosity, $\eta_M$ , in the crust are set equal to the effective viscosities from Figure 3.12. We use $\frac{\mu_K}{\mu} = 0.375$ in the upper mantle. . . . .	66
3.15 Trade-off curves used to determine the damping parameters $\lambda_s$ and $\lambda_\eta$ in eq. (15) of the main text. The left panel shows the trade-off curve for the fault slip penalty parameter, $\lambda_s$ . We pick $\lambda_s$ while keeping the penalty parameter for fluidity, $\lambda_\eta$ , fixed at zero. The right panel shows the trade off curve for selecting $\lambda_\eta$ , where we fix $\lambda_s$ at the chosen value from the left panel. Chosen values are indicated with the larger marker. When picking $\lambda_s$ , we try to find a good balance between the mean chi-squared value, $\bar{\chi}^2$ , and the size of the slip parameters, $\ s\ $ . Our choice of $\lambda_\eta$ is a balance between $\bar{\chi}^2$ and the size of the Laplacian of fluidity, $\ \nabla \eta_{\text{eff}}^{-1}\ $ . . . . .	70
3.16 Checkerboard test used to assess the resolving power of the inversion in Section 3.4.2 of the main text. We create synthetic data at all of the GPS stations considered in this study by evaluating eq. (14) with the synthetic coseismic slip distribution and fluidity distributions. Our synthetic fluidity model has a jump from 0.0 to $10^{-18}$ Pa <sup>-1</sup> s <sup>-1</sup> at 60 km depth. Our synthetic slip model does not include afterslip, although we estimate afterslip along with coseismic slip and fluidity in this test. We estimate these values in the same way as described in the main text and we also use the same penalty parameters. We do not add any noise to our synthetic data so that the recovered model just indicates how much the regularization influences the solution. Note that our ability to recover slip decreases towards the southern end of the fault, farthest from the available data. Also note that the smoothing constraint on fluidity largely obscures the jump in the synthetic model. . . . .	71

3.17 Elastic (black) and viscoelastic (green) components of the near-field predicted displacements for the preferred Zener model from Section 3.4.3. The elastic component is the deformation resulting from fault slip and the viscoelastic component is the deformation resulting from viscoelastic relaxation of stresses induced by the fault slip. The elastic and viscoelastic components are calculated from the first and second terms in eq. (11), respectively. The vertical elastic component is shown as an interpolated field and the vertical viscoelastic component is shown within the green circles. . . . .	72
3.18 Same as figure 3.17 but for far-field stations. . . . .	73
4.1 Random walk amplitudes, $\sigma_{rw}$ , estimated by the MLE and REML methods from synthetic data. The length of the synthetic time series used to estimate $\sigma_{rw}$ is varied from 0.1 yr to 2.5 yr. The black line indicates the true random walk amplitude ( $\sigma_{rw} = 1.3$ ), the light blue region shows the 10-90 percentile of estimates, the dark blue region shows the 25-75 percentile of estimates, the solid blue line indicates the median, and the dashed blue line indicates the mean. . . . .	79
5.1 Positions of continuous GNSS stations used to estimate transient strain rates. The colored regions indicate the distribution of seismic tremor as determined by <i>Wech</i> (2010). The red dots show the positions of GNSS stations mentioned in this paper. The blue dot indicates the location of the transient strain rates shown in Figure 5.7 and the signal-to-noise ratio shown in Figure 5.8. The blue dashed circle demarcates the spatial extent of the tremors shown in Figure 5.8. . . . .	91
5.2 Distribution of estimated FOGM hyperparameters (eq. 5.20). Hyperparameters are estimated with the REML method for 38 stations in Cascadia that are east of 121°W. “IQR” is the interquartile range. . . . .	93
5.3 Two FOGM noise samples for each component. The FOGM hyperparameters have been set to the median values from Figure 5.2. . . . .	94
5.4 Detrended easting component of displacements at station SC03, which is located on Mount Olympus in Washington. The orange markers indicate outliers that were automatically detected using the algorithm from Section 5.4. The error bars show one standard deviation uncertainties. Note that outliers tend be observed in the winter, suggesting that they were caused by snow or ice. . . . .	96

5.5	Observed easting component of displacements at station P436 and predicted displacements when using different covariance functions for $T$ . The one standard deviation uncertainties are shown for the observations and the predicted displacements when using the SE covariance function. For clarity, uncertainties are not shown for the IBM and Wendland covariance functions, but they are nearly equivalent to the uncertainties for the SE covariance function. . . . .	98
5.6	Estimated transient strain rates during the Winter 2015-2016 SSE. Strain glyphs show the normal strain rate along each azimuth, where orange indicates compression and blue indicates extension. The shaded regions indicate one standard deviation uncertainties in the normal strain rates. . . . .	100
5.7	Three components of the transient horizontal strain rate tensor estimated at the position shown in Figure 5.1. The shaded regions indicate one standard deviation uncertainty. . . . .	101
5.8	(top) Signal-to-noise ratio (eq. 5.15) at the position shown in Figure 5.1. (bottom) Frequency of tremors in the region shown in Figure 5.1. . . . .	102
6.1	Location of BSM and GNSS stations used in this study. . . . .	106
6.2	differential (left) and engineering shear (right) strains during the summer 2010 SSE observed at BSMs (solid) and derived from GNSS data (dashed). The horizontal dotted lines are spaced by 0.1 micro-strain. The shaded region around the GNSS derived strains show the one standard deviation confidence interval. The dotted line for station B018 shows the BSM data using the optimal instrument orientation. The shown BSM data has been detrended by estimating and removing a second-order polynomial from each timeseries. . .	109
6.3	GNSS derived differential and engineering shear strains for station B018. The shaded blue regions indicate the one standard deviation confidence interval. The shaded gray regions indicate times of strain drops, which are the result of SSEs. . . . .	111
6.4	Gauge readings at station B018. The gray shaded regions indicate times of strain drops from Figure 6.3. . . . .	112
6.5	GNSS derived strain drops at station B018 during the 11 events identified in Figure 6.3 (blue dots), BSM strain drops using the recorded orientation for B018 (orange dots), and BSM strain drops using the optimal orientation for B018 (green dots). . . . .	113
6.6	Misfit as a function of instrument orientation for station B018. . . . .	114
6.7	Same as Figure 6.2, but for the spring 2009 SSE. . . . .	115

6.8	Same as Figure 6.2, but for the summer 2011 SSE.	116
6.9	Same as Figure 6.2, but for the summer 2012 SSE.	117
6.10	Same as Figure 6.2, but for the fall 2013 SSE.	118
6.11	Same as Figure 6.2, but for the fall 2014 SSE.	119
6.12	Same as Figure 6.2, but for the winter 2015-2016 SSE.	120
6.13	Same as Figure 6.2, but for the winter 2017 SSE.	121

## LIST OF TABLES

3.1 Assumed and estimated material properties. $\lambda$ and $\mu$ are assumed known <i>a priori</i> and are based on the values used for the coseismic model by <i>Wei et al.</i> (2011b). The values for $\eta_{\text{eff}}$ are estimated in Section 3.4.2, and $\frac{\mu_k}{\mu}$ are the optimal shear moduli ratios found in Section 3.4.3 for a Zener rheology upper mantle. . . . .	52
5.1 Optimal hyperparameters for the prior on transient displacements determined with the REML method. The temporal covariance function is indicated by the “ $T$ ” column. The SE, IBM, and Wendland covariance functions are defined in eqs. (5.24), (5.25), and (5.27), respectively. The spatial covariance function, $X$ , is the squared exponential (eq. 5.23) in all cases. The hyperparameters are estimated for each of the seven SSEs considered in this study, and the tabulated values indicate the median and interquartile ranges of estimates. The “diff log(REML)” column compares the log REML likelihood to the log REML likelihood when using the SE covariance function for $T$ . Negative values indicate that observations are more consistent with the SE covariance function. . . . .	97

## **LIST OF APPENDICES**

Appendix 2A: Inverse Laplace transform through series expansion . . . . .	39
Appendix 2B: Postseismic approximation for a two-dimensional earthquake model with a depth dependent viscosity . . . . .	40
Appendix 4A: REML algorithm . . . . .	81

## **ABSTRACT**

# CHAPTER 1

## Bias in estimates of lithosphere viscosity from interseismic deformation\*

### 1.1 Abstract

The estimation of uniform viscosities representing the lower crust and uppermost mantle from post- or interseismic deformation (i.e., apparent viscosities) is inherently biased with respect to a depth-dependence of the viscosities within each layer. Estimates are biased toward a more viscous lower crust or a less viscous lithospheric mantle, depending on the relative geometric mean viscosities of the two layers. When there is a low viscosity shear zone beneath the fault, apparent viscosities are close to that of the shear zone immediately after the earthquake, although the apparent viscosities increase significantly during the later interseismic period. Inferences made from interseismic deformation that the lower crust is more viscous than the upper mantle may be entirely consistent with depth-dependent viscosity profiles that have a significant increase in viscosity from the lowermost crust to the uppermost mantle.

### 1.2 Introduction

Numerous studies in tectonically active regions have sought estimates of the viscosities of the ductile lithosphere, including the lower crust and uppermost mantle (e.g., *Hetland*, 2003; *Pollitz*, 2003, 2005; *Johnson et al.*, 2007; *Hearn et al.*, 2009). Here we consider estimates of the ductile lithosphere made by fitting predictions of surface deformation from mechanical models to geodetic measurements of interseismic deformation, including both post- and interseismic deformation. Most studies of interseismic deformation concluded that the lower crust has a higher viscosity than the uppermost mantle (*Bürgmann and Dresen*, 2008; *Thatcher*

---

\*This chapter has been published as: Hines, T. T., and Hetland, E. A. (2013). Bias in estimates of lithosphere viscosity from interseismic deformation. *Geophysical Research Letters*, 40, 4260–4265, doi:10.1002/grl.50839.

*and Pollitz*, 2008). The majority of mechanical models used in these studies approximated the ductile lithosphere using two homogeneous viscoelastic layers representing the lower crust and uppermost mantle (e.g., *Hetland*, 2003; *Pollitz*, 2003; *Hearn et al.*, 2009). These simplistic layered models are commonly used because they are computationally cheap and because geodetic data are only capable of resolving a limited number of independent rheologic parameters (e.g., *Riva and Govers*, 2009; *Pollitz and Thatcher*, 2010). However, the simplifications made in the layered models may result in inferred viscosities that are not directly applicable to the real viscosity structure of the ductile lithosphere (*Riva and Govers*, 2009).

Temperature increases with depth and viscosity has a strong temperature dependence (e.g., *Kohlstedt et al.*, 1995). The viscosity of the ductile lithosphere also has a stress-dependence (e.g., *Kohlstedt et al.*, 1995), although the ductile lithosphere is often approximated as Maxwell viscoelastic in these models (e.g., *Hetland*, 2003; *Johnson et al.*, 2007; *Riva and Govers*, 2009; *Yamasaki and Houseman*, 2012b). This may be a reasonable approximation if stresses resulting from coseismic deformation are small compared to background stresses. The Newtonian viscosity inferred in postseismic deformation studies may not be constant over time and could be interpreted as an effective viscosity of a power-law creep (e.g., *Freed et al.*, 2006a). Indeed, to describe geodetic observations, models of postseismic deformation in the months to years following an earthquake often require apparent viscosities up to several orders of magnitude smaller than those required in models of deformation later in the interseismic period (e.g., *Pollitz*, 2005; *Johnson et al.*, 2007; *Meade et al.*, 2013). It is important to note that estimates of viscosities from the first few months following an earthquake may not be directly applicable to the steady viscosities of the lithosphere, as the immediate transient postseismic deformation is often considered to be due to postseismic fault creep, poroelastic rebound, or a transient rheology (e.g., *Pollitz*, 2003; *Freed et al.*, 2006a; *Hearn et al.*, 2009). We save the investigation of models with non-linear, power-law creep and/or stress driven fault creep to a subsequent study, and here we only consider stress-linear viscoelasticity, allowing for a robust depth-dependence of viscosities.

We address the question of how inferences of single viscosities representing the entire lower crust and uppermost mantle are related to depth-dependent viscosities throughout the ductile lithosphere. We consider inferred viscosities made from rheologically idealized models of interseismic deformation to be apparent viscosities, and explore the biases incurred through using simplified models. For brevity, we use the term “strength” to refer to viscosity, or equivalently Maxwell relaxation time,  $\tau_M$  ( $\tau_M = \eta/\mu$ , where  $\eta$  is viscosity and  $\mu$  is shear modulus), and thus we use “strong” or “weak” to refer to high or low viscosities, respectively. We show that estimates of the lithosphere’s strength, based on simplified layered models, are almost always biased towards a stronger lower crust or a weaker upper mantle.

## 1.3 Interseismic models

We create synthetic surface deformation using 2D earthquake cycle models composed of an infinite length, vertical strike-slip fault in an elastic layer of thickness  $D$  representing the upper crust, overlying a Maxwell viscoelastic substrate representing the ductile lithosphere (Figure 1.1). We impose uniform slip on the fault with repeat time  $T$ , until the surface deformation reaches a cycle invariant state (i.e., the model is spun-up). The lower viscoelastic substrate is composed of a layer of thickness  $D$ , representing the lower crust, and a layer of thickness  $8D$ , representing the lithospheric mantle. We choose the thickness of the latter to be large enough such that the specific thickness does not affect the surface deformation. Below  $10D$ , in the asthenosphere, we assume a homogeneous viscosity of  $10^{19}$  Pa·sec to the base of the model domain. Models of infinite length, vertical strike-slip faults are anti-symmetric, and we only model one side of the fault. We use the finite element program GeoFEST (*Lyzenga et al.*, 2000) and take the model domain to be  $120D$  wide by  $100D$  deep. We impose an anti-symmetry boundary condition on the model edge containing the fault, a far-field velocity,  $v_T$ , on the opposite boundary, chosen so that there is no net strain accumulation in each earthquake cycle, and the top and bottom of the model are stress free (the bottom of the model domain is sufficiently deep that the bottom stress free boundary condition does not affect the surface deformation). We consider only Maxwell viscoelasticity, but include depth-dependent viscosities within the lower crust and uppermost mantle. We assume that the shear modulus is uniform throughout the model and that viscosities vary smoothly, except possibly at  $z = 2D$  (i.e., the Moho) and at  $z = 10D$  (i.e., base of the lithosphere). We non-dimensionalize the spatial dimensions by the fault locking depth,  $D$ , and time by  $T$ , and thus the non-dimensional Maxwell relaxation time is  $\tau = \tau_M/T$ .

### 1.3.1 Depth-dependence of $\tau$

Motivated by the fact that effective viscosity decreases exponentially with increasing temperature (e.g., *Kohlstedt et al.*, 1995), we take  $\tau$  to decrease exponentially with depth. For generality, we do not assume any particular geotherm or composition of the ductile lithosphere, and instead specify that  $\tau$  decreases in each layer as

$$\tau(z) = \alpha + \beta e^{-\gamma z}, \quad (1.1)$$

where  $z$  is depth within the layer, and  $\alpha$ ,  $\beta$ , and  $\gamma$  are parameters that vary for each layer. The parameters in equation (1.1) depend on the maximum,  $\tau_j^{\max}$ , minimum,  $\tau_j^{\min}$ , and geometric mean,  $\bar{\tau}_j$ , relaxation times within layer  $j$ , where  $j$  is “LC” or “UM” for the lower

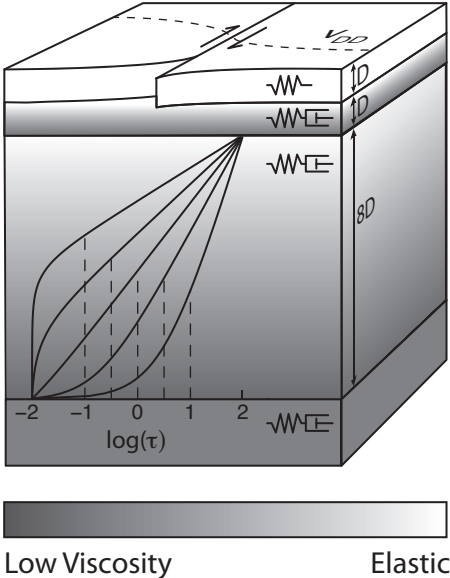


Figure 1.1: Schematic of the earthquake cycle model: springs indicate elasticity and dashpots indicate Newtonian viscosity. Example depth-dependent  $\tau$  profiles are shown in the upper mantle, for the case when  $\tau_{UM}^{\min} = 10^{-2}$ ,  $\tau_{UM}^{\max} = 10^2$ , and  $\bar{\tau}_{UM}$  indicated by vertical dotted lines.

crust or mantle lithosphere, respectively. We consider a wide range of viscosity profiles such that  $10^{-1} \leq \tau_j^{\max} \leq 10^2$ ,  $10^{-2} \leq \tau_j^{\min} \leq 10^1$ , and  $10^{-1} \leq \bar{\tau}_j \leq 10^1$ , in increments of  $10^{0.5}$ . With these ranges, we consider 5,625 depth-dependent lithosphere viscosity structures. The relaxation times are non-dimensionalized by  $T$ , so for a 100 year recurrence time, the shortest and longest Maxwell relaxation times we consider are 1 year and  $10^4$  years, respectively (corresponding to viscosities of about  $10^{18}$  Pa·s and  $10^{22}$  Pa·s for  $\mu \approx 30$  GPa). Note that we consider profiles both in which the largest decrease of  $\tau$  is predominantly in the top or bottom of the layer (Figure 1.1), and we remark on the impact of this on our results below.

## 1.4 Determination of apparent strength

We define the apparent relaxation times (or equivalently the apparent viscosities) of the lower crust,  $\hat{\tau}_{LC}$ , and mantle lithosphere,  $\hat{\tau}_{UM}$ , as the relaxation times inferred from surface interseismic deformation using a model composed of constant viscosities in the two layers (i.e., a layered model). In general,  $\hat{\tau}_{LC}$  and  $\hat{\tau}_{UM}$  have a temporal (*Riva and Govers*, 2009) and spatial (*Yamasaki and Houseman*, 2012a) dependence. Both of which can be thought of as variables of interseismic surface deformation given a particular mechanical representation of the ductile lithosphere, but here we only consider the time dependence of inferred viscosities. We denote the interseismic surface velocities in the models with depth-dependent  $\tau$  as  $v_{DD}$ , and the velocities in a layered model as  $v_L$ . We use a grid search to determine the  $\hat{\tau}_j$  in a

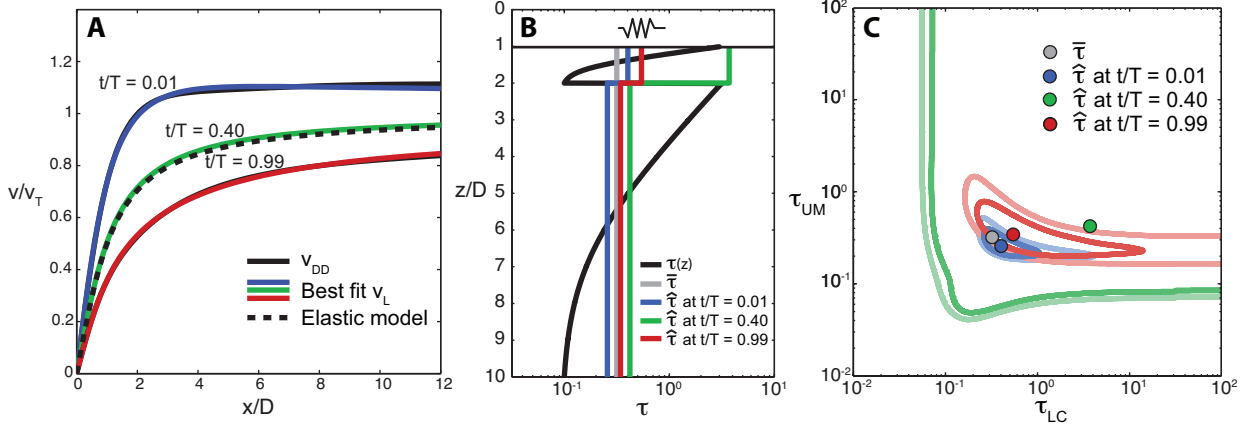


Figure 1.2: A) Velocities for a depth-dependent model,  $v_{DD}$  (black solid lines) and the best fitting velocities predicted by a layered model,  $v_L$  (colored solid lines). Black dashed line is the velocities predicted by an elastic earthquake model with the same  $D$  and  $v_T$ . B)  $\tau$  profiles corresponding to  $v_{DD}$  in (A) and  $\hat{\tau}_j$  associated with the best fitting  $v_L$  in (A). C)  $\bar{\tau}_j$  for the  $\tau$  profile in (B) with  $\hat{\tau}_j$  for each of the cases in (B). Solid lines indicate misfit contours in the grid-search estimation of  $v_L$  in (A); contours shown are RMSE = 0.02 (dark lines) and 0.04 (faded lines), and color indicates the time.

layered model that produced surface velocities that closest match the surface velocities in each of the depth-dependent models at 100 evenly spaced times throughout the interseismic period. In the grid search, we search over  $10^{-2} \leq \hat{\tau}_j \leq 10^2$ , minimizing the root mean square error (RMSE) between  $v_{DD}$  and  $v_L$  at  $0.5D$  increments of distance from the fault from  $0.5D$  to  $12D$ . We note that the upper limit of  $\hat{\tau}_j$  searched over is a bit excessive because, for practical purposes,  $v_L$  is insensitive to changes in relaxation time for  $\tau \gtrsim 10^1$ , as the layer is effectively elastic over interseismic periods (*Savage and Prescott, 1978*) (Figure 1.5). Finally, we assume that the fault slip-rate and thickness of the lower crust and upper mantle are known.

About halfway through the interseismic period, surface deformation for almost all models we consider, both layered and depth-dependent, is indistinguishable from the deformation predicted by an elastic model with slip rate  $v_T$  and locking depth  $D$  (*Savage and Burford, 1973*) (Figure 1.2A). Because all models simultaneously predict surface interseismic velocities similar to the elastic model,  $\hat{\tau}_j$  cannot be definitively resolved for a period during the middle of the earthquake cycle (Figure 1.3C). The exact times within the earthquake cycle in which the elastic model describes  $v_{DD}$  as well as a layered model, depends on the specific  $\tau$  profiles, but it is during the time period about  $.4T - .5T$  for most of the models.

In general, the misfit between  $v_{DD}$  and  $v_L$  is largest early in the earthquake cycle for models with low  $\bar{\tau}_{LC}$  and/or  $\bar{\tau}_{UM}$  (Figure 1.6). The heightened misfit reflects the fact that there is more postseismic creep in the mid-crust and/or beneath the Moho in the layered models, resulting in differences in the wavelength of surface deformation compared to the

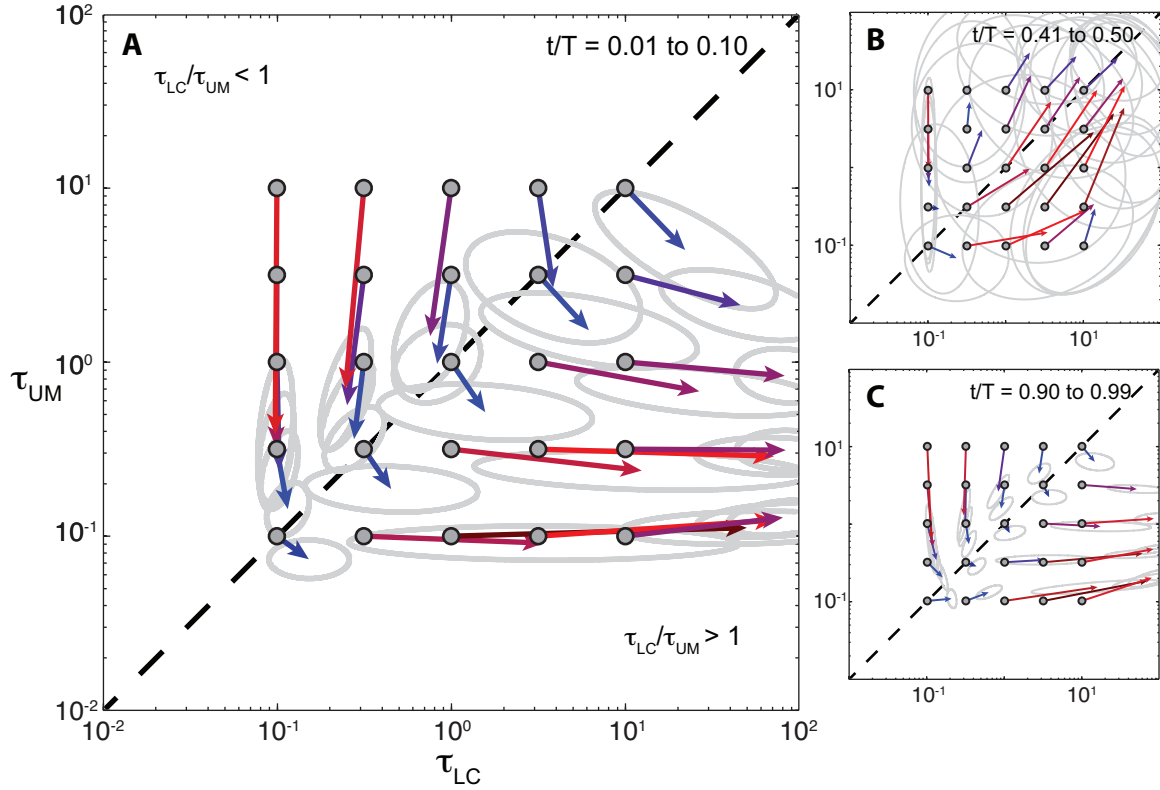


Figure 1.3:  $\bar{\tau}_j$  for all depth-dependent  $\tau$  models considered (gray dots), along with the estimation Bias( $\hat{\tau}_j$ ) (vectors) early (A), midway (B), and late (C) in the interseismic period. Each vector points to the mean  $\hat{\tau}_j$  estimated from depth-dependent models with the same  $\bar{\tau}_j$ , and the gray ovals indicate one standard deviation of  $\hat{\tau}_j$ . The vector colors reflect the magnitude of the bias and help to distinguish overlapping vectors.

depth-dependent models in which  $\tau$  is larger in the mid-crust and/or beneath the Moho. Misfit decreases to a minimum halfway into the earthquake cycle when deformation appears elastic. The misfit increases again late in the earthquake cycle, although  $v_L$  is a significantly better match to  $v_{DD}$  compared to immediately after the earthquake.

We illustrate the determination of  $\hat{\tau}_j$  using a model with a depth-dependent  $\tau$  profile such that  $\bar{\tau}_{LC} = \bar{\tau}_{UM} = 10^{-0.5}$ ,  $\tau_{LC}^{\max} = \tau_{UM}^{\max} = 10^{0.5}$ , and  $\tau_{LC}^{\min} = \tau_{UM}^{\min} = 10^{-1}$  (Figure 1.2). For this particular case, the misfit surfaces in the grid search shows clear minima and  $\hat{\tau}_j$  is a fair approximation for  $\bar{\tau}_j$  early and late in the interseismic period, although the lower crust relaxation time is slightly overestimated (Figure 1.2C). About halfway into the cycle, the layered model that best fits  $v_{DD}$  dramatically overestimates the lower crust relaxation time (Figure 1.2B); however, there is a large range of  $\hat{\tau}_j$  that would sufficiently match  $v_{DD}$  (Figure 1.2C), since during this period the surface velocities for all models are very close to the velocities for the elastic model with identical fault slip rate and locking depth (Figure 1.2A). In this particular depth-dependent model, the velocities throughout the interseismic period are quite similar to those from elastic models, albeit with different slip rates and

locking depths.

## 1.5 Biases in apparent strength

One might assume that the apparent  $\tau$  estimated using a simple layered model,  $\hat{\tau}_j$ , reflects the geometric mean  $\tau$  in those layers,  $\bar{\tau}_j$ . In general,  $\hat{\tau}_j$  estimated from  $v_{DD}$  at any time in one of the depth-dependent models may be significantly different than  $\bar{\tau}_j$ . We consider the difference between the two values to be an error in the estimation of  $\bar{\tau}_j$  and approximate the bias in the estimation throughout the interseismic period as

$$\text{Bias}(\hat{\tau}_j; \bar{\tau}_j) = E[\hat{\tau}_j] - \bar{\tau}_j, \quad (1.2)$$

where  $E[\hat{\tau}_j]$  is the geometric mean of  $\hat{\tau}_j$  estimated from the collection of the depth-dependent models that all have the same  $\bar{\tau}_j$ .

$\text{Bias}(\hat{\tau}_j; \bar{\tau}_j)$  represents the bias in the estimated relaxation times for the lower crust and uppermost mantle with respect to the geometric mean relaxation time of the two layers. In the wide range of models we considered, the bias depends on the contrast between the geometric mean relaxation times in the lower crust and upper mantle,  $\bar{\tau}_{LC}/\bar{\tau}_{UM}$ . Early and late in the earthquake cycle there is a distinct bias towards an apparently weak upper mantle when  $\bar{\tau}_{LC}/\bar{\tau}_{UM} < 1$  and a bias exaggerating the strength of the lower crust by up to a few orders of magnitude when  $\bar{\tau}_{LC}/\bar{\tau}_{UM} > 1$  (Figure 1.3A,C). About halfway through the interseismic period, the biases we calculate are not well constrained, but are generally towards a stronger lower crust and uppermost mantle (Figure 1.3B). These biases hold when we only consider  $\tau$  profiles in which  $\tau$  decays with depth faster than log-linearly (Figure 1.8), which indicates the biases are not sensitive to the specific decay of viscosity with depth provided that there is still some depth-dependence within both layers.

When we consider models in which the lower crust is homogeneous, and include a depth-dependent  $\tau$  only in the uppermost mantle, there is no clear bias when  $\bar{\tau}_{LC}/\bar{\tau}_{UM} < 1$ . However, when  $\bar{\tau}_{LC}/\bar{\tau}_{UM} > 1$ , there is a bias to a stronger lower crust and only a slight bias in the upper mantle strength (Figure 1.7A,C). Conversely, when the uppermost mantle has a uniform relaxation time and  $\tau$  is depth-dependent only in the lower crust, there is no bias when  $\bar{\tau}_{LC}/\bar{\tau}_{UM} > 1$ , but when  $\bar{\tau}_{LC}/\bar{\tau}_{UM} < 1$  there is a bias towards a weaker upper mantle, while the lower crust relaxation time is accurately represented (Figure 1.7D,F). This may be counterintuitive, as one might think that if the lower crust or mantle was truly homogenous with respect to its relaxation time, then a simplified layered model should accurately capture that uniform relaxation time. In the case of both the lower crust and uppermost mantle being

homogeneous, this would be true. However, if only one layer has a homogeneous relaxation time which is longer than the mean relaxation time in the depth-dependent layer, then strength estimates for that layer are biased. This leads us to conclude that the biases are created by the depth-dependence of  $\tau$  in the weaker of the two ductile lithospheric layers.

## 1.6 Lower crustal shear zones

It is likely that highly sheared rocks directly beneath a fault are considerably weaker than the surrounding lower crust (e.g., *Montési and Hirth*, 2003), and lower crustal shear zones are well documented (e.g., *Vauchez and Tommasi*, 2003). In all of the models that we present above, the largest  $\tau$  in the lower crust is immediately beneath the fault. These long relaxation times may suppress the relaxation of coseismic stresses in the lowermost crust, where the relaxation times are shorter, and thus may significantly influence our above conclusion that estimates of lower crustal strength are biased to stronger values than its geometric mean strength. To investigate the potential effect of a lower crustal shear zone on the biases in  $\hat{\tau}_j$ , we include a  $D$  wide vertical shear zone extending through the lower crust beneath the fault. We assume that the shear zone is Maxwell viscoelastic with a constant relaxation time of  $\tau_{SZ} = 10^{-2}$ , which is at least an order of magnitude faster than the surrounding lower crust.

With a weak shear-zone, immediately following an earthquake the velocities are quite large, and as a result both the lower crust and uppermost mantle appear uniformly weaker than their geometric mean strength, with  $\hat{\tau}_{LC}$  close to  $\tau_{SZ}$  (Figure 1.4). These heightened postseismic velocities decay rapidly, although how  $\hat{\tau}_{LC}$  or  $\hat{\tau}_{UM}$  increases over time depends on  $\bar{\tau}_{LC}/\bar{\tau}_{UM}$ . If  $\bar{\tau}_{LC}/\bar{\tau}_{UM} > 1$  then  $\hat{\tau}_{LC}$  increases by orders of magnitude, exceeding  $\bar{\tau}_{LC}$  (Figure 1.4B). Otherwise,  $\hat{\tau}_{UM}$  rapidly increases early in the cycle. For all models,  $\hat{\tau}_j$  evolves towards a more reasonable approximation of  $\bar{\tau}_j$  late in the cycle (Figure 1.4B). Additionally, the velocities are relatively steady throughout the later interseismic period compared to a model without a shear zone but with similar heightened postseismic velocities (Figure 1.4A).

## 1.7 Discussion

In the wide range of cases we consider, the biases in  $\hat{\tau}_j$  inferred throughout the interseismic period almost always are such that  $\hat{\tau}_{LC}/\hat{\tau}_{UM}$  is larger than  $\bar{\tau}_{LC}/\bar{\tau}_{UM}$ , except for midway through the interseismic period when all velocities are close to the elastic limit (Figure 1.3B). Additionally,  $\hat{\tau}_{LC}$  is often larger than  $\tau_{LC}^{\max}$  and  $\hat{\tau}_{UM}$  is often lower than  $\tau_{UM}^{\min}$ . In models where  $\bar{\tau}_{LC} \neq \bar{\tau}_{UM}$ , inferences of  $\hat{\tau}_{LC}/\hat{\tau}_{UM} > 1$  ( $< 1$ ) correspond to models in which  $\bar{\tau}_{LC}/\bar{\tau}_{UM} > 1$  ( $< 1$ ). In other words, a lower crust that appears stronger than the mantle

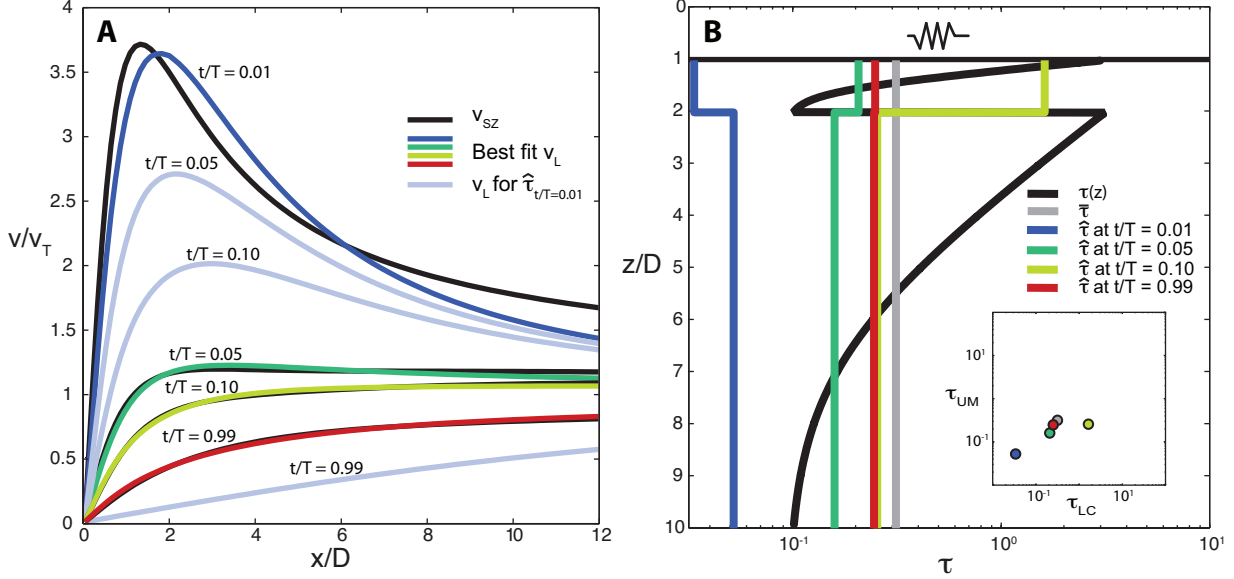


Figure 1.4: A) Interseismic velocities,  $v_{SZ}$ , in a model with both a lower crustal shear zone and depth-dependent  $\tau$  in the surrounding lithosphere (black lines) along with the best fit  $v_L$  (colored lines). Shown as light blue lines are the velocities in a layered model with the dark blue viscosity profile shown in (b), which are the apparent viscosities estimated from  $v_{SZ}$  at  $t/T = 0.01$ . B)  $\tau$  profile outside of the shear zone corresponding to  $v_{SZ}$  (black line;  $\tau = 10^{-2}$  within the shear zone),  $\bar{\tau}$  outside the shear zone, and  $\hat{\tau}_j$  associated with the best fitting  $v_L$  in (A) (colored lines, color corresponds to time in cycle). Inset in (B) shows  $\bar{\tau}_j$  and  $\hat{\tau}_j$  (dot color corresponds to line colors in (A) and (B)).

when approximated by uniform strength layers corresponds to models in which the geometric mean strength of the lower crust is also stronger than that in the mantle, and vice versa. We note that several of the  $\tau$  profiles with  $\bar{\tau}_{LC} > \bar{\tau}_{UM}$  are characterized by significant portions of the lowermost crust having much lower viscosities than the uppermost mantle.

The biases we present in this paper can be viewed as relating  $\hat{\tau}_j$  to  $\bar{\tau}_j$ . However, the specific relationship between  $\hat{\tau}_j$  and  $\bar{\tau}_j$  depends not only on the details of how  $\tau$  varies in the ductile lithosphere, but also on the time in the interseismic period. In the latter regard, it is also important to note that we have assumed periodic offsets on an infinite length fault, whereas real earthquakes are non-periodic and finite. It is also important to note that we grouped all  $\tau$  profiles according to the  $\bar{\tau}_j$  in each layer irrespective of  $\tau_j^{\max}$  and  $\tau_j^{\min}$ , and only considered how profiles with the same  $\bar{\tau}_j$  relate to  $\hat{\tau}_j$ . For these reasons, these biases cannot be used to back-out specific depth-dependent  $\tau$  profiles, or even unique  $\bar{\tau}_j$ , consistent with  $\hat{\tau}_j$  estimated from geodetic data using a simplified model of the lithosphere. The coherency of the bias estimates suggest that it may be possible to develop probabilistic relationships between  $\hat{\tau}_j$  and  $\bar{\tau}_j$ , assuming that the general time within the earthquake cycle the geodetic data are sampling is known. For example, if  $\hat{\tau}_{LC} \approx 10^1$  and  $\hat{\tau}_{UM} \approx 10^{-1}$  were inferred from geodetic data late in a seismic cycle, then those estimates would be equivalent to depth-

dependent  $\tau$  profiles with  $\bar{\tau}_{LC}$  around  $10^{-0.5}$  to  $10^1$  and  $\bar{\tau}_{UM}$  on order of  $10^{-1}$  (Figure 1.3C). Further exploration of the relationships between specific  $\tau$  profiles and  $\hat{\tau}_j$  would be required in order to establish whether inferences of apparent strength could be used to constrain the range of permissible  $\tau$  profiles that are consistent with surface deformation at any one time. It may also be possible to constrain depth-dependent  $\tau$  profiles by considering how inferred viscosities vary as a function of distance from the fault (*Yamasaki and Houseman, 2012a*).

In the depth-dependent  $\tau$  models we consider, the postseismic velocities are either only slightly above the elastic velocities or are large but decay over a relatively long portion of the interseismic period. Both of these cases are in contrast with many observations of heightened postseismic velocities decaying over on order of a decade following earthquakes (e.g., *Ergintav et al., 2009*). Models including transient rheologies or power-law creep have been proposed to explain transient postseismic velocities (e.g., *Pollitz, 2003; Freed et al., 2006a; Ryder et al., 2007*). Adding a weak shear zone to a model with depth-dependent  $\tau$  and only Maxwell viscoelasticity can also result in heightened postseismic velocities that rapidly decay over the postseismic period, while the surface velocities throughout the majority of the latter interseismic period are only slightly depressed compared to those in an elastic model with identical slip-rate and locking depth (Figure 1.4A).

## 1.8 Conclusions

Assuming a uniform viscosity for the lower crust and uppermost mantle results in biased estimates of viscosity for those two layers if the viscosity is highly depth-dependent. Estimates of viscosity tend to be biased either towards a weaker upper mantle or a stronger lower crust, depending on the relative viscosity of the two layers. When there is a low viscosity lower crustal shear zone present, immediately after the earthquake the lower crust and uppermost mantle both appear weak, with apparent viscosities close to that of the shear zone, and then the apparent strength of the lower crust or upper mantle increases dramatically over the early interseismic period. Using simplified models, inferences made from interseismic deformation that the lower crust is orders of magnitude more viscous than the upper mantle may be entirely consistent with depth-dependent viscosity profiles that have smaller contrasts between the geometric mean viscosities of lower crust and upper mantle and may be associated with a significant increase in viscosity across the Moho.

## 1.9 Acknowledgments

This research was funded by NSF grant EAR 1045372. We thank editor E. Calais, G. Houseman, and an anonymous reviewer.

## 1.10 Supporting information

The following figures provide additional information supporting our conclusions regarding the biases in apparent viscosities estimated for the lower crust and upper mantle. The sensitivity of surface deformation to viscosities in the lower crust or upper mantle is shown in Figure 1.5. Figure 1.6 is the same as Figure 1.3, except Figure 1.7 also shows all of the  $\hat{\tau}$  for the lower crust and uppermost mantle estimated from  $v_{DD}$  for all models, as well as indicates the misfit of the associated  $v_L$  to  $v_{DD}$ . Figure 1.7 shows the bias for end-member scenarios when only the lower crust or upper mantle has a depth dependent tau. Figure 1.8 shows the bias when tau in the lower crust and upper mantle has a high decay rate (i.e., a decay rate larger than a log-linear decrease in  $\tau$ ).

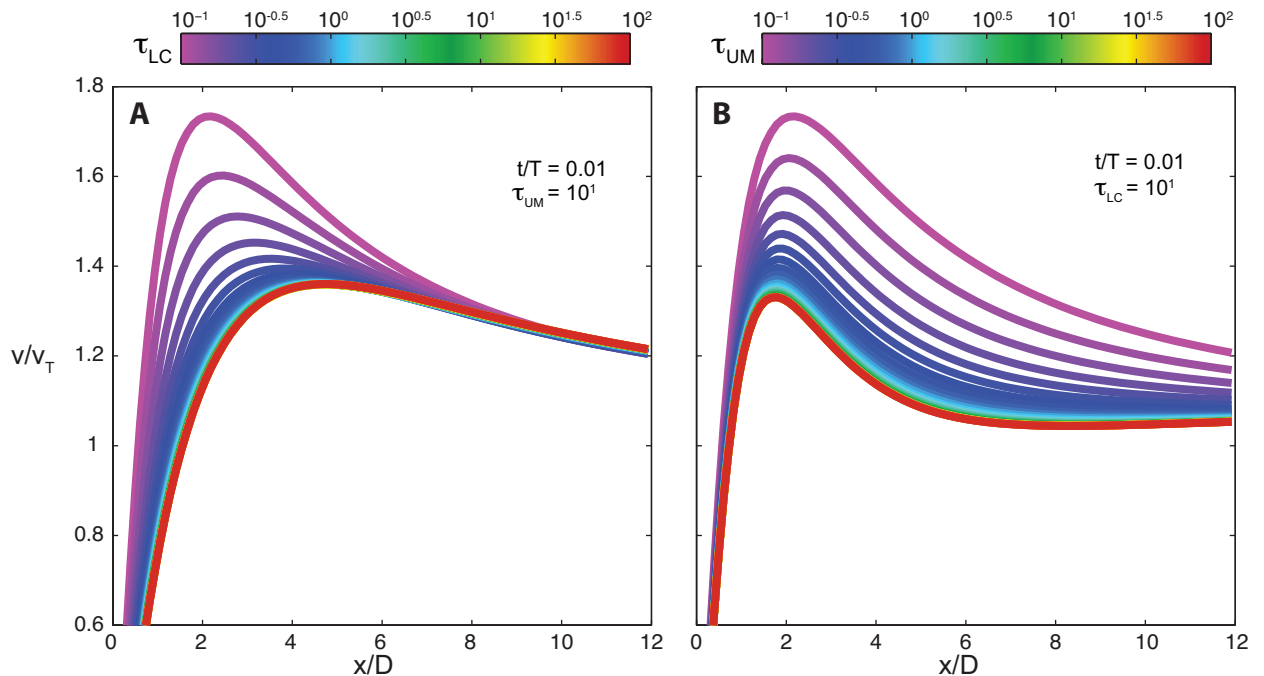


Figure 1.5: Surface velocities at  $t/T = 0.01$  in models with uniform  $\tau$  in the lower crust or uppermost mantle layers ( $\tau = \tau_M/T = (\eta T)/\mu$ , where  $T$  is the earthquake repeat time,  $\tau_M$  is the Maxwell relaxation time,  $\eta$  is the Newtonian viscosity, and  $\mu$  is the elastic shear modulus). Velocities in models with constant  $\tau$  in the upper mantle ( $\tau_{UM}$ ), and variable  $\tau$  in the lower crust ( $\tau_{LC}$ ) are shown in (A). Models with constant  $\tau_{LC}$  and variable  $\tau_{UM}$  are shown in (B). For sufficiently high  $\tau_{UM}$  or  $\tau_{LC}$  the surface velocities converge, indicating that the surface deformation is insensitive to layer viscosities when  $\log_{10}(\tau)$  is above about 1, as the layer is effectively elastic over earthquake repeat time scales.

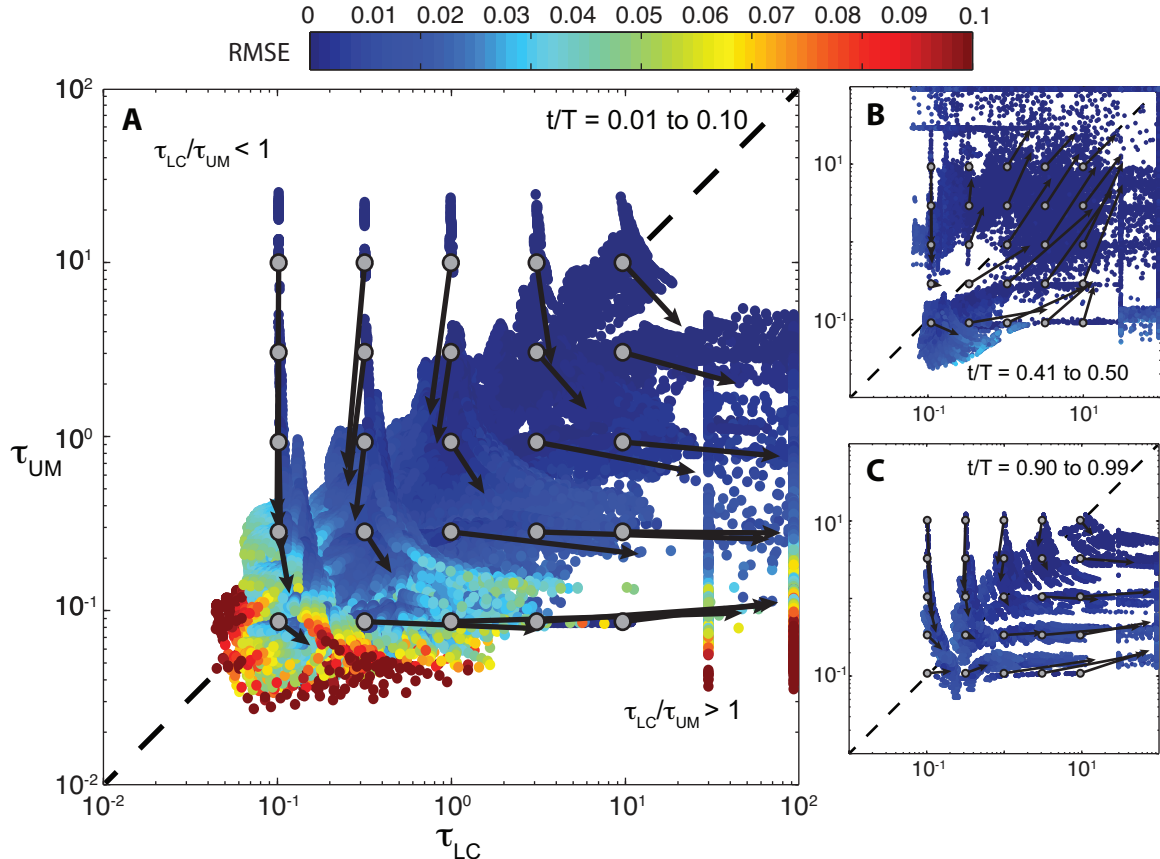


Figure 1.6:  $\bar{\tau}_j$  (gray dots) for all depth dependent  $\tau$  models considered, along with the estimation of  $\text{Bias}(\hat{\tau}_j)$ , represented as vectors, early (A), midway (B), and late (C) in the interseismic period. Each vector points to the mean value of  $\hat{\tau}_j$  estimated from depth dependent models with the same  $\bar{\tau}_j$ . Colored dots indicate  $\hat{\tau}_j$  of each of the best fit layered models (dot color corresponds to the RMSE of how  $v_L$  fits  $v_{DD}$ ).

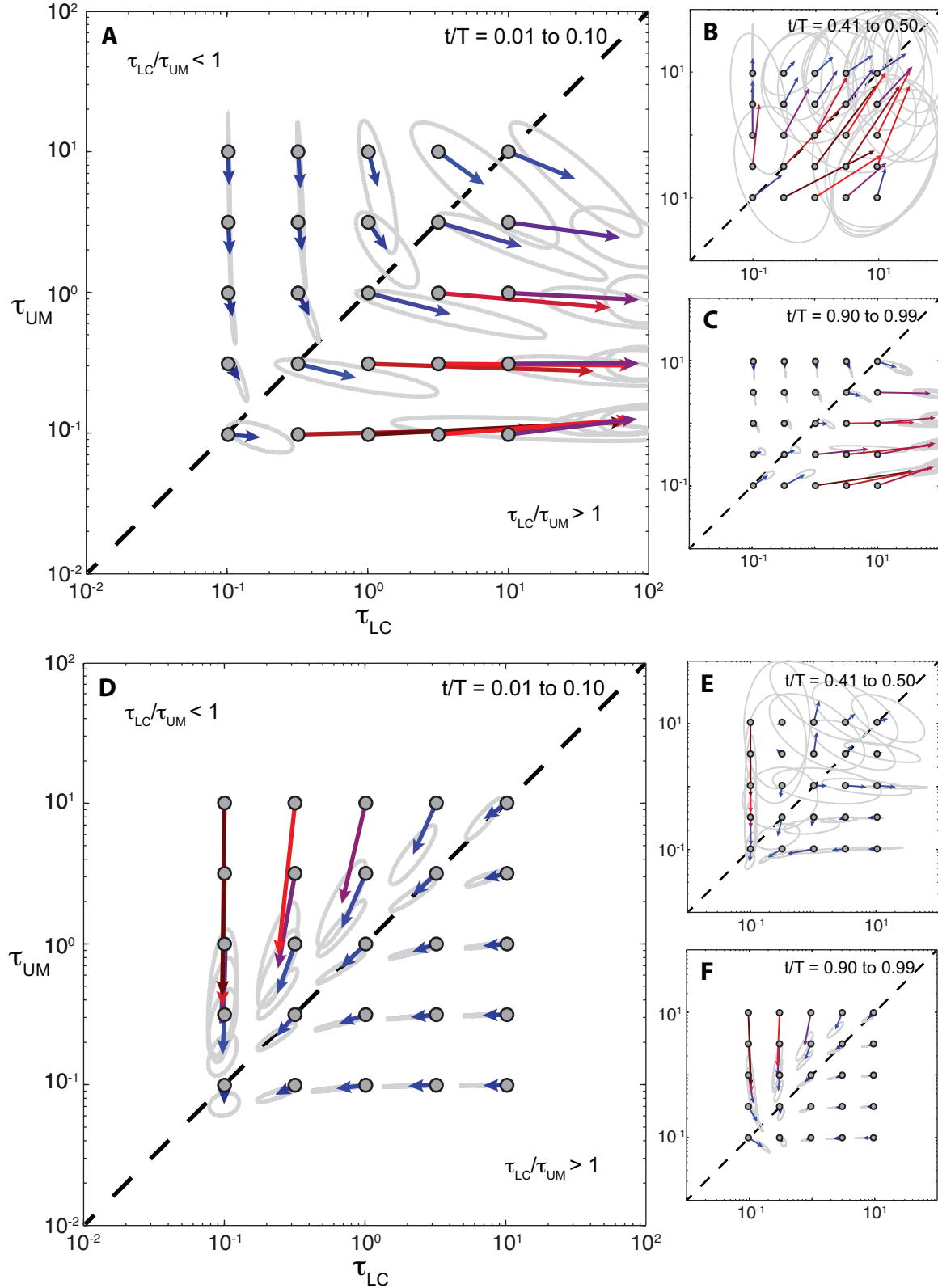


Figure 1.7:  $\bar{\tau}_j$  (gray dots) for all depth dependent  $\tau$  models with a homogeneous lower crust (A,B,C) or homogeneous upper mantle (D,E,F), along with the estimation of  $Bias(\hat{\tau}_j)$ , represented as vectors, early (A), midway (B), and late (C) in the interseismic period. Each vector points to the mean value of  $\hat{\tau}_{ij}$  estimated from depth dependent models with the same  $\bar{\tau}_{ij}$ , and the gray ovals indicate one standard deviation of  $\hat{\tau}_{ij}$  estimated from models with the same  $\bar{\tau}_{ij}$ .

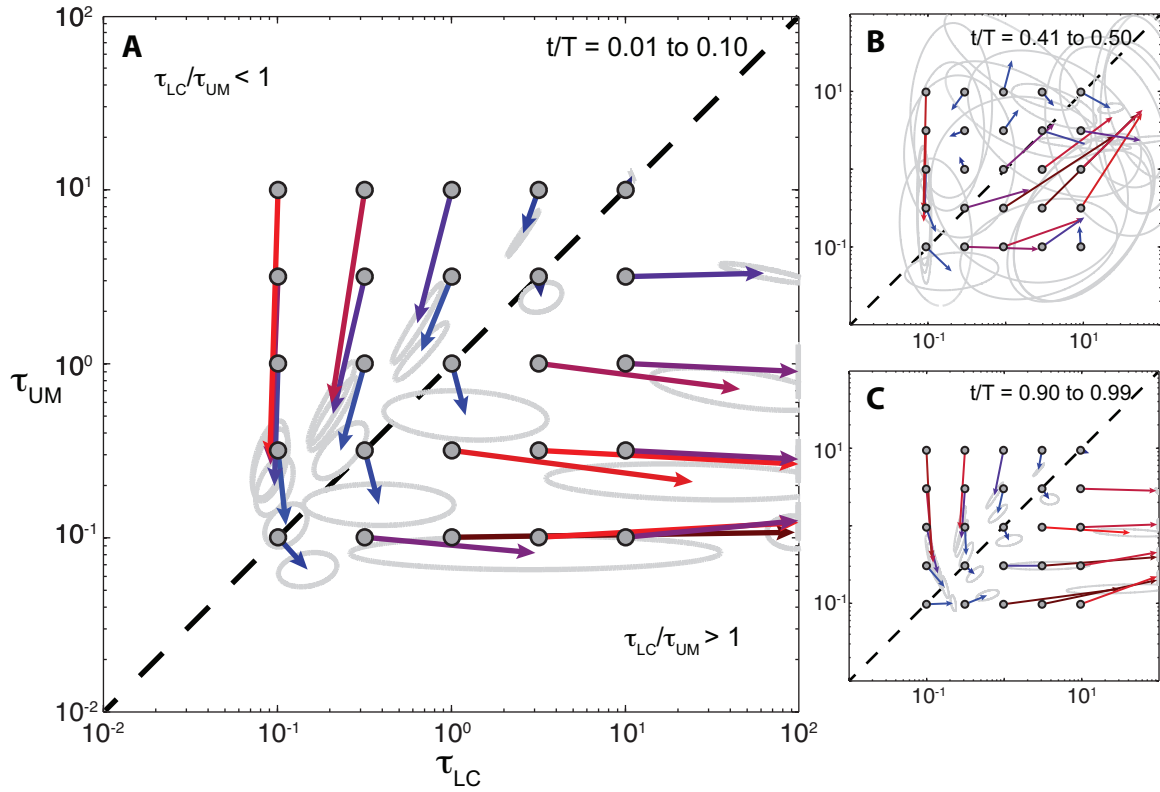


Figure 1.8:  $\bar{\tau}_j$  (gray dots) for all depth dependent  $\tau$  models in which  $\tau$  in the lower crust and upper mantle decreases with depth more than log-linearly (i.e., with  $\tau$  at any depth lower than would be predicted by a log-linear decrease, for instance the left-most  $\tau$  profiles shown in Figure 1.1), along with the estimation of Bias( $\hat{\tau}_j$ ), represented as vectors, early (A), midway (B), and late (C) in the interseismic period. Each vector points to the mean value of  $\hat{\tau}_j$  estimated from depth dependent models with the same  $\bar{\tau}_j$ , and the gray ovals indicate one standard deviation of  $\hat{\tau}_j$  estimated from models with the same  $\bar{\tau}_j$ . The estimated biases in these models are similar to the biases estimated from all depth-dependent tau models considered in this paper (Figure 1.3), indicating that consideration of tau profiles that decay less than log-linearly do not drive our conclusions that the lower crust (uppermost mantle) appear stronger (weaker) than the average  $\tau$  during much of the interseismic period.

## CHAPTER 2

# Rapid and simultaneous estimation of fault slip and heterogeneous lithospheric viscosity from postseismic deformation\*

### 2.1 Summary

Postseismic deformation is commonly attributed to viscoelastic relaxation and/or afterslip, although discerning between the two driving mechanisms can be difficult. A major complication in modeling postseismic deformation is that forward models can be computationally expensive, making it difficult to adequately search model space to find the optimal fault slip distribution and lithospheric viscosity structure that can explain observable postseismic deformation. We propose an inverse method which uses coseismic and early postseismic deformation to rapidly and simultaneously estimate a fault slip history and an arbitrarily discretized viscosity structure of the lithosphere. Our method is based on an approximation which is applicable to the early postseismic period and expresses surface deformation resulting from viscoelastic relaxation as a linearized function with respect to lithospheric fluidity. We demonstrate this approximation using two-dimensional earthquake models. We validate the approximation and our inverse method using two three-dimensional synthetic tests. The success of our synthetic tests suggests that our method is capable of distinguishing the mechanisms driving early postseismic deformation and recovering an effective viscosity structure of the lithosphere.

### 2.2 Introduction

Geodetic observations of surface deformation in the months to years following an earthquake are often attributed to afterslip (e.g., *Marone et al.*, 1991), viscoelastic relaxation in the lithosphere (e.g., *Nur and Mavko*, 1974), and/or poroelastic relaxation (e.g., *Peltzer et al.*,

---

\*This chapter has been published as: Hines, T. T., and Hetland, E. A. (2015). Rapid and simultaneous estimation of fault slip and heterogeneous lithospheric viscosity from post-seismic deformation. *Geophysical Journal International*, 204, 569582, doi:10.1093/gji/ggv477.

1998). If postseismic deformation can be entirely described by afterslip, then one could easily constrain the spatial distribution of slip on prescribed fault geometries with a linear least squares inversion (e.g., *Harris and Segall*, 1987; *Bürgmann et al.*, 2002; *Freed*, 2007), which could then provide insight into the frictional properties of faults (e.g., *Hsu et al.*, 2006; *Barbot et al.*, 2009). However, postseismic deformation following large ( $M_w \geq 7$ ) earthquakes is often attributed to viscoelastic relaxation in the lithosphere (e.g., *Hetland*, 2003; *Pollitz*, 2003, 2005) or a combination of both afterslip and viscoelastic relaxation (e.g., *Freed et al.*, 2006b; *Hearn et al.*, 2009; *Johnson et al.*, 2009; *Rollins et al.*, 2015). In such cases, postseismic deformation can be used to also constrain the viscous properties of the lithosphere, although this is a more difficult task than constraining just a slip distribution. Not only do the competing deformation mechanism need to be discerned, finding the viscosity distribution of the lithosphere from postseismic deformation is a computationally expensive nonlinear inverse problem. Typically, the estimation of viscosities is approached with a forward modeling, grid search or Monte Carlo method. These forward modeling techniques require the number of unknown parameters being estimated to be small, meaning that significant and potentially inappropriate modeling assumptions must be made. Namely, studies seeking to estimate the viscosity structure of the lithosphere often assume for computational tractability that the lithosphere is composed of two or three homogeneously viscoelastic layers, which may not be appropriate for describing a more realistic depth dependent viscosity structure (*Riva and Govers*, 2009; *Hines and Hetland*, 2013).

In this paper we propose a relatively fast method to invert coseismic and postseismic deformation to simultaneously estimate a time-dependent distribution of fault slip and an arbitrarily discretized viscosity structure of the lithosphere. Our method is based on an approximation which linearizes the rate of early postseismic deformation with respect to the viscosity of the lithosphere. We demonstrate the effectiveness and limitations of our method through two synthetic tests.

### 2.3 Approximation for postseismic deformation

We assume that the lithosphere can be approximated as a Maxwell viscoelastic material on the timescales of postseismic deformation, where shear stress,  $\sigma$ , and strain,  $\varepsilon$ , are related by

$$\frac{\partial \varepsilon}{\partial t} = \frac{\sigma}{2\eta} + \frac{1}{2\mu} \frac{\partial \sigma}{\partial t}. \quad (2.1)$$

We use  $\eta$  and  $\mu$  to represent viscosity and shear modulus, respectively. This constitutive relationship implies that a sudden strain from an earthquake will instantaneously stress

the lithosphere elastically (assuming the lithosphere is undergoing quasi-static deformation). Viscoelastic creep will initiate immediately after the earthquake, where the initial viscous strain rate in each parcel of the lithosphere will be proportional to the fluidity ( $1/\eta$ ) in that parcel, and independent of the fluidity elsewhere because the initial stresses are only controlled by the elastic properties of the lithosphere. Stresses from the earthquake will dissipate over time through viscoelastic relaxation. During the period in which stress changes from viscoelastic relaxation are small compared to the initial elastic stresses, each parcel will continue to creep at a rate that is approximately proportional to its fluidity. In this early postseismic period, the surface deformation from creep in each parcel will have an amplitude that is also proportional to the fluidity in that parcel and independent of the fluidity elsewhere. As we will show, the early surface expression of creep in the entire lithosphere is therefore a sum of the surface deformation from each parcel and is linear with respect to lithospheric fluidity. We demonstrate this property of early postseismic surface deformation in this section using simple infinite length, strike-slip earthquake models, where the lithosphere is approximated as a layered half-space. In Section 2.5 we consider two finite fault models with an arbitrarily discretized lithospheric viscosity structure, the first with only Maxwell viscoelasticity and the second with Burgers viscoelasticity.

### 2.3.1 Two-dimensional earthquake models

The easiest way to demonstrate how postseismic deformation can be linearized with respect to lithospheric viscosity is with a two-dimensional earthquake model consisting of a long, vertical, surface rupturing, strike-slip fault that is embedded in a viscoelastic horizontal layer overlying a viscoelastic half-space. We make use of the Correspondence Principle of Viscoelasticity (e.g., *Flügge*, 1975), which states that the Laplace transform of deformation in a viscoelastic body has the same form as the Laplace transform of deformation in a elastic body with the same geometry and subjected to the same boundary conditions. The solution for displacements following an earthquake in a viscoelastic lithosphere can then be readily found provided that the corresponding elastic solution is known (e.g., *Nur and Mavko*, 1974; *Savage and Prescott*, 1978; *Hetland and Hager*, 2005). One only needs to replace the shear modulus in the Laplace transform of the elastic solution with the effective viscoelastic shear modulus and then compute the inverse Laplace transform.

## Two layered model

From the solution of *Rybicki* (1971), surface displacements,  $u_e(x, t)$ , resulting from slip on a fault in an elastic surface layer overlying a semi-infinite elastic substrate are

$$u_e(x, t) = b(t) \left( \frac{1}{2} W(0) + \sum_{n=1}^{\infty} \Gamma^n W(n) \right), \quad (2.2)$$

where

$$W(n) = \frac{1}{\pi} \left( \tan^{-1} \left( \frac{2nH + D}{x} \right) - \tan^{-1} \left( \frac{2nH - D}{x} \right) \right) \quad (2.3)$$

and

$$\Gamma = \frac{\mu_1 - \mu_2}{\mu_1 + \mu_2}. \quad (2.4)$$

In the above equation,  $b(t)$  describes cumulative slip on the fault through time and can describe coseismic slip and/or afterslip.  $D$  is the locking depth of the fault,  $H$  is the thickness of the upper layer, and  $\mu_1$  and  $\mu_2$  are the shear moduli in the upper layer and lower substrate, respectively. The Laplace transform of eq. (2.2) is

$$\hat{u}_e(x, s) = \hat{b}(s) \left( \frac{1}{2} W(0) + \sum_{n=1}^{\infty} \Gamma^n W(n) \right). \quad (2.5)$$

We replace  $\mu_1$  and  $\mu_2$  in eq. (2.5) with the equivalent shear moduli for Maxwell materials in the Laplace domain,  $\hat{\mu}_1$  and  $\hat{\mu}_2$ , to get the Laplace transform of surface displacements in the two-layered, viscoelastic half-space,

$$\hat{u}_v(x, s) = \hat{b}(s) \left( \frac{1}{2} W(0) + \sum_{n=1}^{\infty} \hat{\Gamma}^n W(n) \right), \quad (2.6)$$

where

$$\hat{\Gamma} = \frac{\hat{\mu}_1 - \hat{\mu}_2}{\hat{\mu}_1 + \hat{\mu}_2} \quad (2.7)$$

and

$$\hat{\mu}_i = \frac{s}{\frac{s}{\mu_i} + \frac{1}{\eta_i}}. \quad (2.8)$$

To find the surface displacements in the time domain one must find the inverse Laplace transform of eq. (2.6), which is typically done using the method of residues. However, we are interested in characterizing the behavior of only the early postseismic deformation and it serves us better to instead perform the inverse Laplace transform with an extension of the initial value theorem (Appendix A). We assume for simplicity that the shear modulus for the

viscoelastic lithosphere is homogeneous (i.e.  $\mu_1 = \mu_2$ ) and demonstrate in a supplementary IPython notebook that our conclusions still hold when  $\mu_1 \neq \mu_2$ . The surface displacements in the time domain are

$$u_v(x, t) = b(t) \frac{1}{2} W(0) + b(t) * \mathcal{L}^{-1} \left[ \sum_{n=1}^{\infty} \hat{\Gamma}^n W(n) \right], \quad (2.9)$$

where we use  $*$  to denote a convolution with respect to time. Evaluating the above inverse Laplace transform using the method described in Appendix A, we find

$$\begin{aligned} u_v(x, t) = & b(t) \frac{1}{2} W(0) + \\ & b(t) * \left( \frac{\mu}{2\eta_2} W(1) - \frac{\mu}{2\eta_1} W(1) \right) + \\ & b(t) * \left( \left( \frac{\mu^2 t}{4\eta_2^2} - \frac{\mu^2 t}{4\eta_1 \eta_2} \right) (W(1) - W(2)) + \left( \frac{\mu^2 t}{4\eta_1 \eta_2} - \frac{\mu^2 t}{4\eta_1^2} \right) (W(1) + W(2)) \right) + \\ & \dots \end{aligned} \quad (2.10)$$

The first term in eq. (2.10) is the elastic response to slip on the fault. The remaining terms describe the surface displacement due to viscoelastic relaxation. We refer to the first of these remaining terms as the initial viscoelastic response, which describes surface deformation resulting from viscoelastic creep during the period in which the stresses from fault slip are unaltered by viscoelastic relaxation. The initial viscoelastic response is linear with respect to the fluidity in each of the two layers.

If the time since the rupture is sufficiently small compared to the relaxation times of each layer,  $\tau_i = \eta_i/\mu$ , (i.e. the third and following terms in eq. (2.10) are small) and the timescale of slip described by  $b(t)$  is also short compared to the relaxation times in the half-space, then we can truncate the series and approximate early surface deformation using only the elastic response and the initial viscoelastic response,

$$u_v(x, t) \approx b(t) \frac{1}{2} W(0) + \int_0^t b(\theta) \left( \frac{\mu}{2\eta_2} W(1) - \frac{\mu}{2\eta_1} W(1) \right) d\theta. \quad (2.11)$$

An approximation similar to eq. (2.11) was demonstrated by *Segall* (2010) for an elastic layer over a Maxwell viscoelastic substrate.

Figure 2.1 shows the series solution from eq. (2.10) truncated after sufficiently many terms along with the approximation given by eq. (2.11). In this comparison, we use  $H = 15$  km,  $D = 10$  km and a shear modulus of 32 GPa throughout the lithosphere. The upper layer is given a viscosity of  $10^{20}$  Pa s ( $\tau \approx 100$  years) and the substrate is given a viscosity of  $10^{19}$

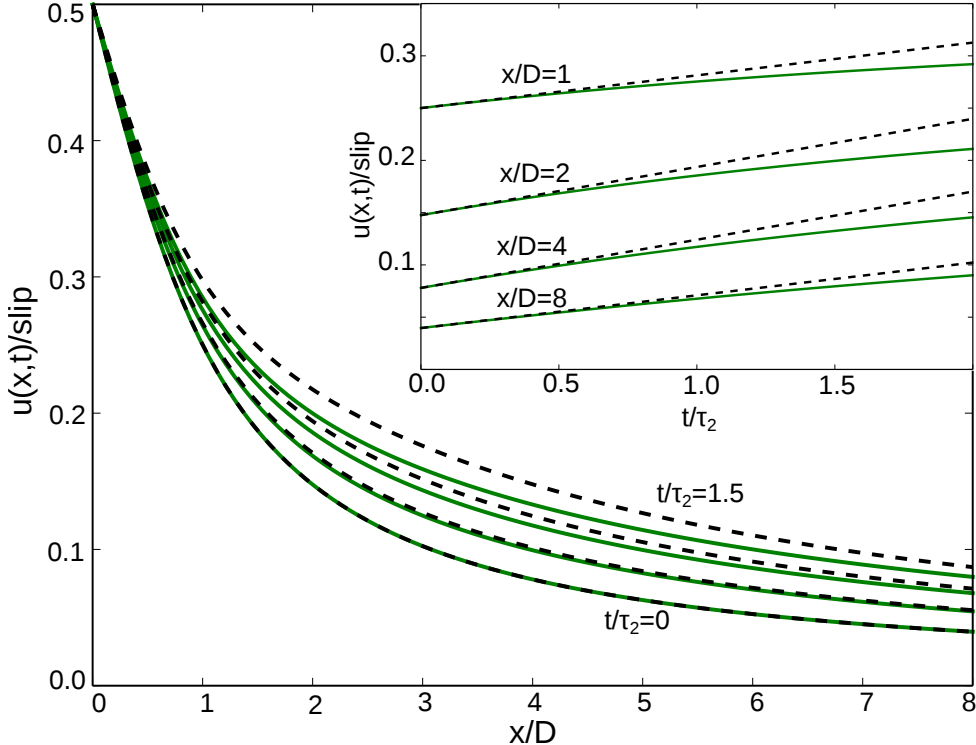


Figure 2.1: Surface displacements predicted by eq. (2.10) truncated after ten terms (green) and the approximation given by eq. (2.11) (dotted black). Times are normalized by the lowest relaxation time in the lithosphere,  $\tau_2$ , and distances are normalized by the fault locking depth,  $D$ . Displacements are shown as a function of distance from the fault at times  $t/\tau_2 = 0.0, 0.5, 1.0$  and  $1.5$ . The inset figure shows displacement time series at locations  $x/D = 1, 2, 4$  and  $8$ .

Pa s ( $\tau \approx 10$  years). We let  $b(t)$  describe a unit of instantaneous slip at  $t = 0$ . In the series solution, the rate of surface deformation decreases over time as stresses in the half-space decay through viscoelastic relaxation. Because  $b(t)$  is a constant after  $t = 0$ , the initial viscoelastic response in eq. (2.11) describes a constant rate of surface deformation and so eq. (2.11) is a good approximation for as long as the rate of deformation predicted by eq. (2.10) is also approximately constant. We find the that the approximation is indistinguishable from the series solution for at least as long as half the lowest of the two relaxation times, regardless of our choice of model parameters. The approximation breaks down faster than what is show in Figure 2.1 when the upper layer is more fluid than the substrate or when we decrease the depth of the material interface (i.e. when the more fluid material is closer to the fault). We also note that the approximation has more longevity for locations further away from the fault, where it starts to break down at about the minimum relaxation time in the lithosphere.

### Three layered and continuous depth dependent models

We follow the same procedure as above to find the surface deformation resulting from slip on a strike-slip fault in a three layered viscoelastic half-space. Starting from the layered elastic solution from *Chinnery and Jovanovich* (1972), we evaluate the solution for the viscoelastic problem in our supplementary IPython notebook. We find the initial viscoelastic response to a unit of slip to be

$$\frac{\partial}{\partial t} u(x, t)|_{t=0} = \frac{\mu}{2\eta_3} W(1, 1) + \frac{\mu}{2\eta_2} (W(0, 1) - W(1, 1)) - \frac{\mu}{2\eta_1} W(0, 1), \quad (2.12)$$

where

$$W(n, m) = \frac{1}{\pi} \left( \tan^{-1} \left( \frac{2nH_2 + 2mH_1 + D}{x} \right) - \tan^{-1} \left( \frac{2nH_2 + 2mH_1 - D}{x} \right) \right), \quad (2.13)$$

$\eta_1$ ,  $\eta_2$ , and  $\eta_3$  are the viscosities of the top, middle, and bottom layers, respectively, and  $H_1$  and  $H_2$  are the thicknesses of the top and middle layers, respectively. We see that eq. (2.12) is once again linear with respect to the fluidity in each of the three layers. We can approximate early postseismic deformation resulting from slip described by  $b(t)$  as

$$u(x, t) \approx b(t) \frac{1}{2} W(0, 0) + \int_0^t b(\theta) \left( \frac{\mu}{2\eta_3} W(1, 1) + \frac{\mu}{2\eta_2} (W(0, 1) - W(1, 1)) - \frac{\mu}{2\eta_1} W(0, 1) \right) d\theta. \quad (2.14)$$

We can see that eq. (2.14) reduces to eq. (2.11) when  $\eta_3 = \eta_2$ .

At this point we posit that a similar approximation can be made for an arbitrarily layered lithosphere. In Appendix B we use eq. (2.12) to find an initial viscoelastic response kernel. We then integrate that kernel over the depth of the lithosphere to find the initial viscoelastic response for an arbitrary depth dependent viscosity structure. If the lithosphere is elastic above the fault depth,  $D$ , and described by  $\eta(z)$  below  $D$  then early postseismic deformation can be approximated as

$$u(x, t) \approx \frac{b(t)}{\pi} \tan^{-1} \left( \frac{D}{x} \right) + \int_0^t \int_D^\infty \frac{\mu b(\theta)}{2\pi\eta(z)} \left( \frac{2x}{x^2 + (D + 2z)^2} - \frac{2x}{x^2 + (2z - D)^2} \right) dz d\theta. \quad (2.15)$$

Although the above equation is capable of describing surface deformation for an arbitrary depth dependent viscosity structure, it falls short of being useful as the forward solution in an inverse problem aimed at estimating lithospheric viscosity. This shortcoming is because the above equation makes the nonphysical assumption that the fault is infinitely long, in addition to the restriction of only being applicable to a vertical strike-slip fault. The assumption of

infinite length would introduce first order errors, which would likely wash out the second order effect of viscosity. However, eq. (2.15) is useful for making estimates of the depth sensitivity of postseismic deformation.

### 2.3.2 Three-dimensional earthquake models

Motivated by our above results, we make the assertion that the initial viscoelastic response to an instantaneous unit dislocation in a three-dimensional Maxwell viscoelastic medium, which has been arbitrarily discretized into  $N$  regions, will have the form

$$\frac{\partial}{\partial t} \vec{u}(\vec{x}, t)|_{t=0} = \sum_j^N \frac{1}{\eta_j} G_j(\vec{x}). \quad (2.16)$$

We denote  $\vec{u}$  and  $\vec{x}$  as vectors to emphasize that eq. (2.16) is generalized to three-dimensional problems. We use  $G_j(\vec{x})$  to represent the initial rate of surface deformation at position  $\vec{x}$  resulting from viscoelastic creep in region  $j$  with unit fluidity, where fluidity is zero (i.e. elastic) in all other regions. In this sense,  $G_j(\vec{x})$  can be thought of as a Green's function for the initial viscoelastic response, and thus we refer to  $G_j(\vec{x})$  as the initial viscoelastic Green's functions. We verify eq. (2.16) numerically in Section 2.5.2 and save a theoretical justification for a later paper.

Using eq. (2.16), we can approximate early surface deformation in a form that is consistent with eqs. (2.11) and (2.14):

$$\vec{u}(\vec{x}, t) \approx b(t)F(\vec{x}) + \sum_j^N \int_0^t \frac{b(\theta)}{\eta_j} G_j(\vec{x}) d\theta, \quad (2.17)$$

where  $F(\vec{x})$  is the elastic Green's function, which describes the elastic deformation resulting from a dislocation. We further generalize the approximation of surface deformation in eq. (2.17) to allow for an arbitrary spatial distribution of slip by using linear superposition. If the elastic deformation in a viscoelastic lithosphere can be described in terms of  $M$  elastic dislocation sources, then early surface deformation resulting from both elastic dislocations and viscous creep can be approximated as

$$\vec{u}(\vec{x}, t) \approx \sum_i^M b_i(t)F_i(\vec{x}) + \sum_i^M \sum_j^N \int_0^t \frac{b_i(\theta)}{\eta_j} G_{ij}(\vec{x}) d\theta. \quad (2.18)$$

The initial viscoelastic Green's function is dependent upon both the region it represents as well as the dislocation source inducing the viscoelastic creep in that region, hence the two in-

dices on  $G_{ij}(\vec{x})$ . It is worth restating that the approximation given above does not account for the viscoelastic coupling between the regions, since in eq. (2.18) each region's contribution to surface deformation is independent of the viscosity elsewhere. This approximation is therefore appropriate for as long as the regions do not significantly transfer stresses between each other through viscoelastic deformation. Alternatively, since our initial viscoelastic Green's functions do not have time dependence, one could view eq. (2.18) as being appropriate up until surface velocities resulting from viscoelastic creep have decayed appreciably.

## 2.4 Inversion method

The approximation of postseismic deformation given by eq. (2.18) can be cast as an inverse problem aimed at finding the distribution of slip on a fault and an arbitrarily complicated lithosphere viscosity structure from postseismic deformation. We assume that the slip history in any one direction on each fault patch,  $b_i(t)$ , can be expressed as  $P$  linear terms such that

$$b_i(t) = \sum_k^P \alpha_{ik} A_k(t), \quad (2.19)$$

where  $A_k(t)$  can be any parameterized slip function. For this paper  $A_k(t)$  consists of either unit step functions describing coseismic slip on a fault patch, or ramp functions, which increase from 0 to 1 over some time interval, that are intended to represent afterslip. The coefficient  $\alpha_{ik}$  then represents either the amount of coseismic slip or the cumulative slip over a time interval. The approximation given by eq. (2.18) now becomes

$$\vec{u}(\vec{x}, t) \approx \sum_i^M \sum_k^P \alpha_{ik} F_i(\vec{x}) A_k(t) + \sum_i^M \sum_j^N \sum_k^P \int_0^t \frac{\alpha_{ik}}{\eta_j} G_{ij}(\vec{x}) A_k(\theta) d\theta. \quad (2.20)$$

If we assume a fault geometry and the elastic properties of the lithosphere,  $F_i(\vec{x})$  can be computed with finite element software or with an analytic solution, for instance using *Okada* (1992) or *Meade* (2007). Likewise,  $G_{ij}(\vec{x})$  can be computed using finite element software. If the assumed geometry of the viscoelastic regions is sufficiently simple,  $G_{ij}(\vec{x})$  may also be computed with semi-analytic techniques (e.g., *Pollitz*, 1997; *Fukahata and Matsu'ura*, 2006; *Barbot and Fialko*, 2010).

We estimate the unknown slip parameters,  $\alpha_{ik}$ , and unknown viscosities in each region of the lithosphere,  $\eta_j$ , from observations of surface deformation in a least squares sense. Let  $\mathbf{u}_{\text{obs}}$  be a vector of observed coseismic and postseismic surface displacements at various locations and points in time. Let  $\mathbf{m}$  be a vector of all the unknown parameters  $\alpha_{ik}$  and  $\eta_j$ ,

and let  $\mathbf{u}(\mathbf{m})$  be a vector of postseismic surface displacements predicted by eq. (2.20). We seek to solve

$$\min \|\mathbf{f}(\mathbf{m})\|_2^2 \quad (2.21)$$

subject to the constraint that

$$\mathbf{m} \geq 0, \quad (2.22)$$

where

$$\mathbf{f}(\mathbf{m}) = \begin{bmatrix} \mathbf{W}(\mathbf{u}(\mathbf{m}) - \mathbf{u}_{\text{obs}}) \\ \lambda_s \mathbf{L}_s \mathbf{m} \\ \lambda_v \mathbf{L}_v \mathbf{m} \end{bmatrix}. \quad (2.23)$$

In the above equation,  $\mathbf{W}$  is a diagonal matrix containing the reciprocal of the data uncertainties (i.e.  $\mathbf{W}^T \mathbf{W} = \mathbf{C}_d^{-1}$  where  $\mathbf{C}_d$  is the data covariance matrix), and  $\mathbf{L}_s$  and  $\mathbf{L}_v$  are regularization matrices.

We impose a non-negativity constraint on  $\mathbf{m}$  which ensures that inferred slip is in one predominant direction and that viscosities are positive. Specifically, the rake of the inferred slip on each fault patch is constrained to be within a  $90^\circ$  window defined by the rakes of chosen orthogonal basis slip directions. For instance, the basis slip directions could be chosen such that only slip rakes within  $45^\circ$  of pure strike-slip, normal, or thrust are permissible.

Because this inverse problem inevitably has non-unique solutions for  $\mathbf{m}$ , we put additional constraints on the inferred slip and inferred viscosity with the matrices  $\mathbf{L}_s$  and  $\mathbf{L}_v$ , respectively. In our following synthetic test, we constrain the solution by minimizing the Laplacian of the spatial distribution of fault slip and lithospheric viscosity by letting  $\mathbf{L}_s$  and  $\mathbf{L}_v$  be umbrella operators (Desbrun *et al.*, 1999). The parameters  $\lambda_v$  and  $\lambda_s$  in eq. (23) control how much we enforce the smoothness constraint. In our synthetic test, we choose these parameters using L-curves, which describe the trade off between the model smoothness and data misfit. We first set  $\lambda_v = 0$  and then use an L-curve to pick  $\lambda_s$ . We then fix  $\lambda_s$  at our chosen value and use another L-curve to pick  $\lambda_v$ . We explored using cross-validation to choose our model parameters, but we found that the optimal pair of penalty parameters picked through cross-validation tended to significantly degrade our fit to near-field sites.

We find  $\mathbf{m}$  that satisfies the above conditions using the Gauss-Newton method (e.g., Aster *et al.*, 2011). The best fit model parameters are found by making an initial guess for the solution and then iteratively solving

$$\mathbf{J}(\mathbf{m}^k) \mathbf{m}^{k+1} = -\mathbf{f}(\mathbf{m}^k) + \mathbf{J}(\mathbf{m}^k) \mathbf{m}^k \quad (2.24)$$

for  $\mathbf{m}^{k+1}$ , where  $\mathbf{J}(\mathbf{m}^k)$  is the Jacobian of  $\mathbf{f}(\mathbf{m})$  with respect to  $\mathbf{m}$  evaluated at  $\mathbf{m}^k$ . We

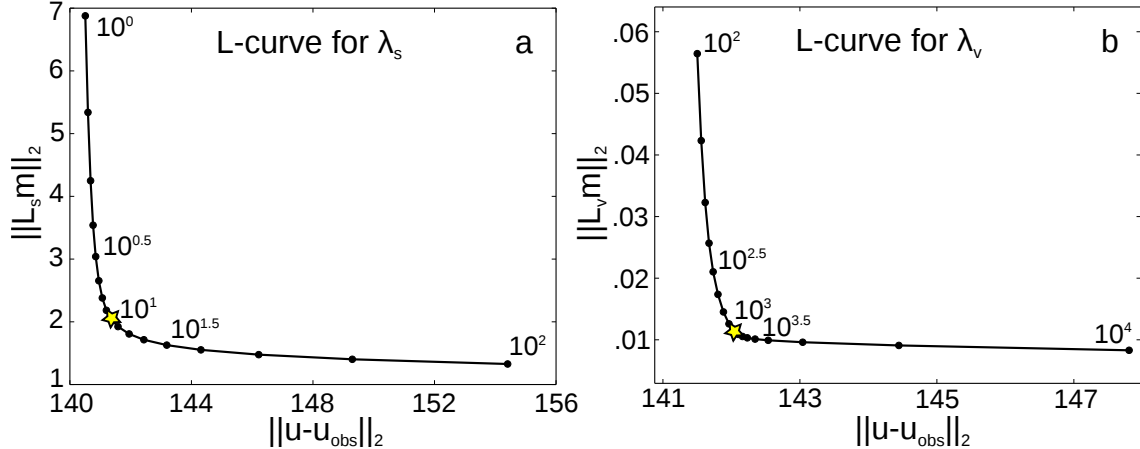


Figure 2.2: L-curves used to select the penalty parameters. Panel (a) shows the trade-off between slip smoothness and data misfit while varying  $\lambda_s$  and keeping  $\lambda_v$  fixed at zero. Panel (b) shows the trade off between smoothness of inferred viscosity and misfit while varying  $\lambda_v$  and keeping  $\lambda_s$  fixed at the value chosen from Panel (a). Stars indicate our chosen penalty parameters.

impose the non-negativity constraint on  $\mathbf{m}$  by solving eq. (2.24) with a non-negative least squares algorithm (*Lawson and Hanson, 1995*). In a nonlinear least squares algorithm, computing the Jacobian can often be the largest computational burden when an analytic solution for the Jacobian is not available. By linearizing the viscoelastic response in early postseismic deformation with respect to  $1/\eta_j$ , we have made our forward problem, eq. (2.20), sufficiently simple that evaluating its Jacobian for a given  $\mathbf{m}$  only requires a few computationally inexpensive matrix operations. Consequently, our nonlinear least squares algorithm converges to a solution for  $\mathbf{m}$  in a matter of seconds on a desktop computer. The main computational burden is in computing  $F_i(x)$  and  $G_{ij}(x)$  which only needs to be done once for a given fault and lithosphere geometry.

## 2.5 Synthetic test

We demonstrate with two synthetic tests that our inverse method is capable of recovering fault slip and an effective lithospheric viscosity from postseismic deformation. We use the finite element software, PyLith (*Aagaard et al., 2013*), to compute the surface deformation resulting from a specified amount of slip on a fault in a lithosphere with either Maxwell or Burgers viscoelasticity. We invert this synthetic surface deformation using the method described above to recover the imposed model parameters. The synthetic tests also serve to demonstrate that eqs. (2.16) and (2.18) are indeed valid for three dimensional earthquake models.

Our synthetic models consist of a 50 km long by 20 km wide strike-slip fault, striking to

the north and dipping  $60^\circ$  to the east (Figure 2.5). At  $t = 0$  we impose  $6.5 \times 10^{19}$  N m of surface rupturing, right-lateral coseismic slip with a distribution shown in Figure 2.3. After the coseismic slip, we impose 2 years of afterslip just below the coseismic rupture zone. The spatial distribution of afterslip on the fault remains constant throughout the 2 years but the rate of afterslip decreases by a factor of 2 every 0.5 years. The cumulative moment of afterslip over the first year is about  $1.6 \times 10^{19}$  N m, while the cumulative moment of afterslip over the second year is  $4.0 \times 10^{18}$  N m. We do not impose any fault slip beyond  $t = 2$  years.

We compute surface displacements at 50 randomly chosen observation points within a 400 km square centered about the fault (Figure 2.5), which is intended to roughly correspond with the density of GPS station at a well instrumented plate boundary. Displacements are computed at 0.05 year intervals up until  $t = 10$  years. We add temporally correlated noise to the computed displacements through time, consistent with what one would expect from GPS observations. The standard deviation of northing and easting displacements is 1 mm, and the standard deviation of the vertical displacements is 2.5 mm. We add temporal covariance with an exponential noise model that has a characteristic timescale of 0.25 years, which is intended to simulate seasonal processes that are typically present in GPS time series.

### 2.5.1 Green's functions

We invert the synthetic surface displacements for fault slip on a 4 km by 4 km discretization of the planar fault. We estimate a constant viscosity in 10 km thick horizontal layers from the surface down to 70 km depth and for a lower substrate. We compute the elastic Green's functions,  $F_i(\vec{x})$ , and initial viscoelastic Green's functions,  $G_{ij}(\vec{x})$ , numerically using PyLith. The elastic Green's functions are the initial surface displacements resulting from 1 m of imposed slip on fault patch  $i$ . For each fault patch, we use basis slip directions with rake  $45^\circ$  up-dip and  $45^\circ$  down-dip of pure right-lateral slip. These slip basis directions restrict all inferred slip to have rakes within  $45^\circ$  of right-lateral. We find the initial viscoelastic Green's functions,  $G_{ij}(\vec{x})$ , by computing the initial rate of surface deformation due to 1 m of slip on fault patch  $i$  in a model that is elastic everywhere except in region  $j$ , which is assigned a unit fluidity. In the interests of numerical stability we used  $10^{-18}$  Pa $^{-1}$  s $^{-1}$  as our unit of fluidity. We emphasize that the amount we perturb the fluidity in region  $j$  will have no influence on our computation of  $G_{ij}(x)$  because the initial rate of deformation computed with Pylith will be proportional to  $G_{ij}(x)$  times our fluidity perturbation.

We define the basis slip functions,  $A_k(t)$ , as a Heaviside function centered at  $t = 0$  and twenty ramp functions which describe 1 m of cumulative slip over the time intervals  $t = (0, 0.5), (0.5, 1.0), \dots, (9.5, 10.0)$  years. We note that the synthetic model does not have any fault slip from  $t = 2$  to 10 years and the postseismic deformation over that interval

is resulting purely from viscoelastic creep.

### 2.5.2 Synthetic model with Maxwell viscoelasticity

The lithosphere in our first synthetic model is Maxwell viscoelastic with homogeneous Lamé parameters  $\lambda = 32$  GPa and  $\mu = 32$  GPa. The viscosity in the lithosphere decays from  $10^{21}$  Pa s ( $\tau \approx 1,000$  years) at the surface to  $10^{19}$  Pa s ( $\tau \approx 10$  years) at 75 km depth (Figure 2.4). For the timescales of this synthetic test, the uppermost lithosphere is effectively elastic.

We use the penalty parameters chosen in Figure 2.2 and our recovered model of slip on the fault is shown in Figure 2.3. We use 100 iterations of bootstrapping to assess how sensitive our recovered model is to the imposed data noise. The standard deviation of coseismic slip and cumulative afterslip over the indicated interval is shown in the right column of Figure 2.3. The spatial distribution and direction of inferred coseismic slip are a good match to the synthetic coseismic slip. The distribution of afterslip was decently recovered but not as well as the coseismic slip was recovered. Inferred afterslip over the first year is smoother than the true slip due to the regularization, although there is a high concentration of slip on the northern portion of the fault which is consistent with the synthetic model. We attribute the better resolved northern portion of the fault to a proximal surface observation point. There are a few artifacts in the distribution of inferred afterslip from  $t = 1$  to 2 years which are not present in the synthetic model, such as slip on the deepest portion of the fault. Our inability to recover the details of the imposed afterslip as well as the coseismic slip could be because the data noise is obscuring some of the postseismic signal (Figure 2.5b and 2.5c compared to Figure 2.5a) and causing higher variability in inferred slip models. Nevertheless, the inferred moment of both coseismic slip and afterslip, which is proportional to slip integrated over the fault plane, is within 10% of the moment in the synthetic model. Although the spatial distribution of inferred slip may be more difficult to recover, the slip moment seems to be consistently recovered.

The inferred slip over the last time interval,  $t = 2$  to 10 years, is also consistent with the synthetic model. The moment of slip over this interval is  $8.1 \times 10^{17}$  N m, which is two orders of magnitude smaller than the moment for the coseismic slip in the synthetic model and is accounting for, at most, a few mm's of surface displacement from  $t = 2$  to 10 years, which is on order of the data uncertainty. We can further dismiss inferred afterslip during this period as being negligibly small because the magnitude of inferred slip is on order of the the uncertainty inferred from bootstrapping (Figure 2.3). The majority of surface deformation during this time interval (Figure 2.5d) is therefore being properly attributed to viscoelastic relaxation in the inversion results.

The inferred viscosities in each of the eight layers are shown in Figure 2.4a. The recov-

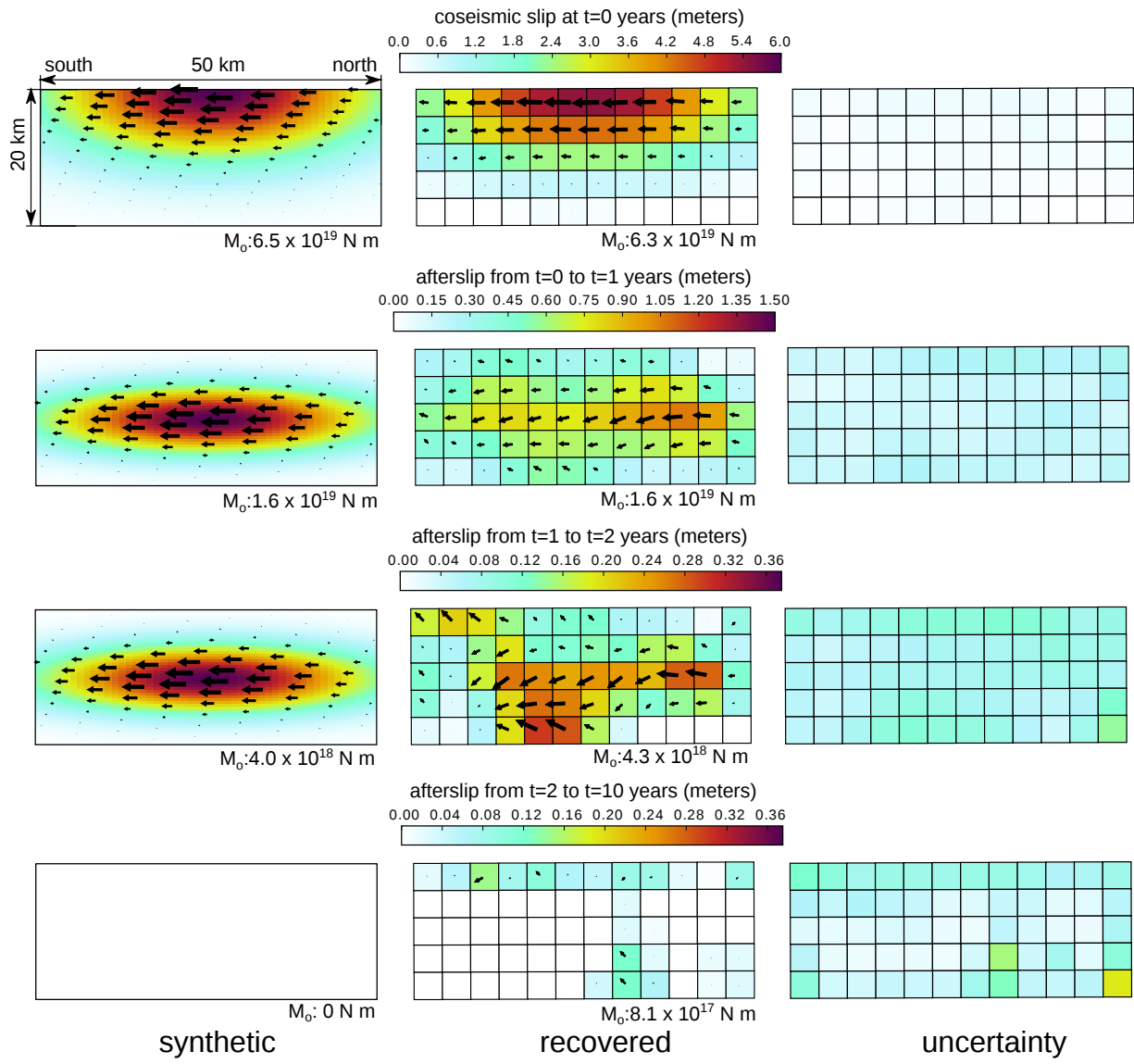


Figure 2.3: Slip distribution imposed in both synthetic models (left), slip recovered for the synthetic model with Maxwell viscoelasticity (middle), and uncertainty in the recovered slip magnitude (right). Colors indicate magnitude of slip and arrows indicate direction of slip (arrows pointing right indicate left-lateral and up is thrust). The panels showing afterslip display cumulative slip over the specified time interval. The slip uncertainties are the standard deviation of inferred slip magnitude during the specified period, which were derived from 100 iterations of bootstrapping.

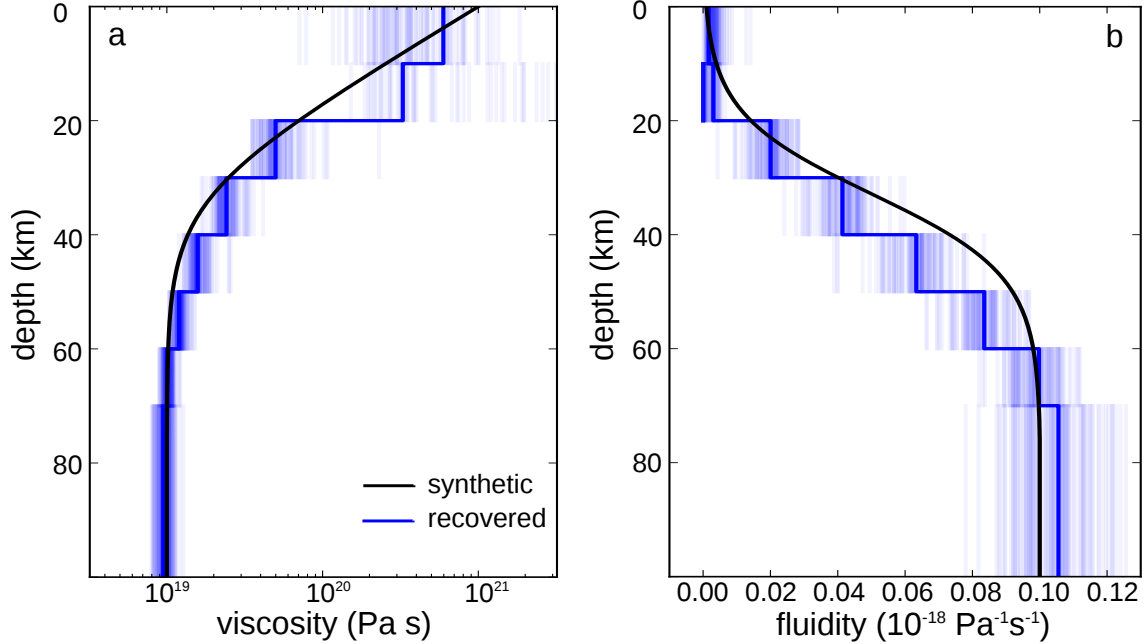


Figure 2.4: Synthetic and recovered lithospheric viscosities (left) and associated fluidities (right). Semi-transparent lines are recovered models found through bootstrapping and indicate the degree of uncertainty on the inferred viscosity structure.

ered viscosities correspond well with the synthetic model. The uncertainties of the recovered viscosities are inferred using bootstrapping and we find that the strongest layers near the surface, despite being close to the earthquake source, have the highest uncertainties. However, viscosities greater than  $10^{20}$  Pa s are effectively elastic on the timescales of this synthetic test and so a wide range of high viscosities for the upper layers would just as adequately be able to describe the synthetic surface displacements. When looking at inferred values of fluidity (Figure 2.4b), we see that the uncertainties are lowest at the surface and increase with depth, as is perhaps more intuitive.

Viscoelastic relaxation immediately below the fault and afterslip on the fault would have similar surface manifestations, and thus it is reasonable to explore the trade-off between these processes. We use the collection of models obtained through bootstrapping and compute the correlation coefficient between the estimates of cumulative afterslip moment over 10 years and the inferred fluidity for select layers. Not surprisingly, the correlation coefficient is -0.16, and -0.25 in the layer from 10 to 20 km depth and 20 to 30 km depth, respectively, which means that higher estimates of fluidities in those layers tend to be compensated by lower estimates of slip on the fault. Interestingly, there is a positive correlation of 0.38 between cumulative afterslip moment and the fluidity in the uppermost layer containing the fault. The positive correlation is because deformation resulting from viscoelastic relaxation in the uppermost layer containing the fault tends to be in the opposite direction as deformation

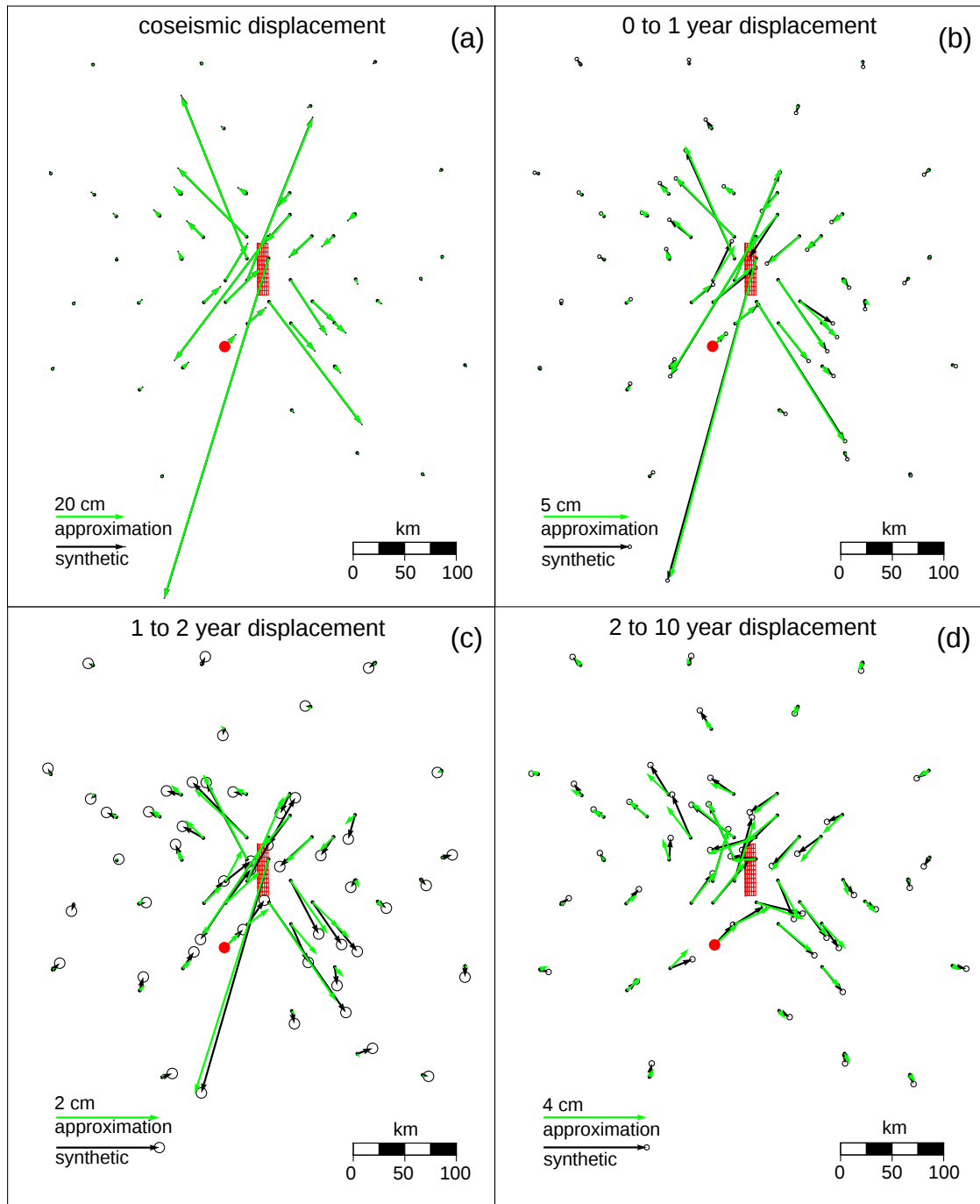


Figure 2.5: Synthetic surface displacements (black) and best fitting surface displacements using eq. (2.20) (green). Vertical displacements are used in the inversion but are not shown here. Panel (a) shows coseismic displacements and the remaining panels show the cumulative displacements over the indicated time intervals. Ellipses indicate 1 standard deviation uncertainty in the synthetic data. Red dot indicates the position of the time series shown in Figure 2.6 and Figure 2.9. The surface projection of the discretized synthetic fault is depicted in red.

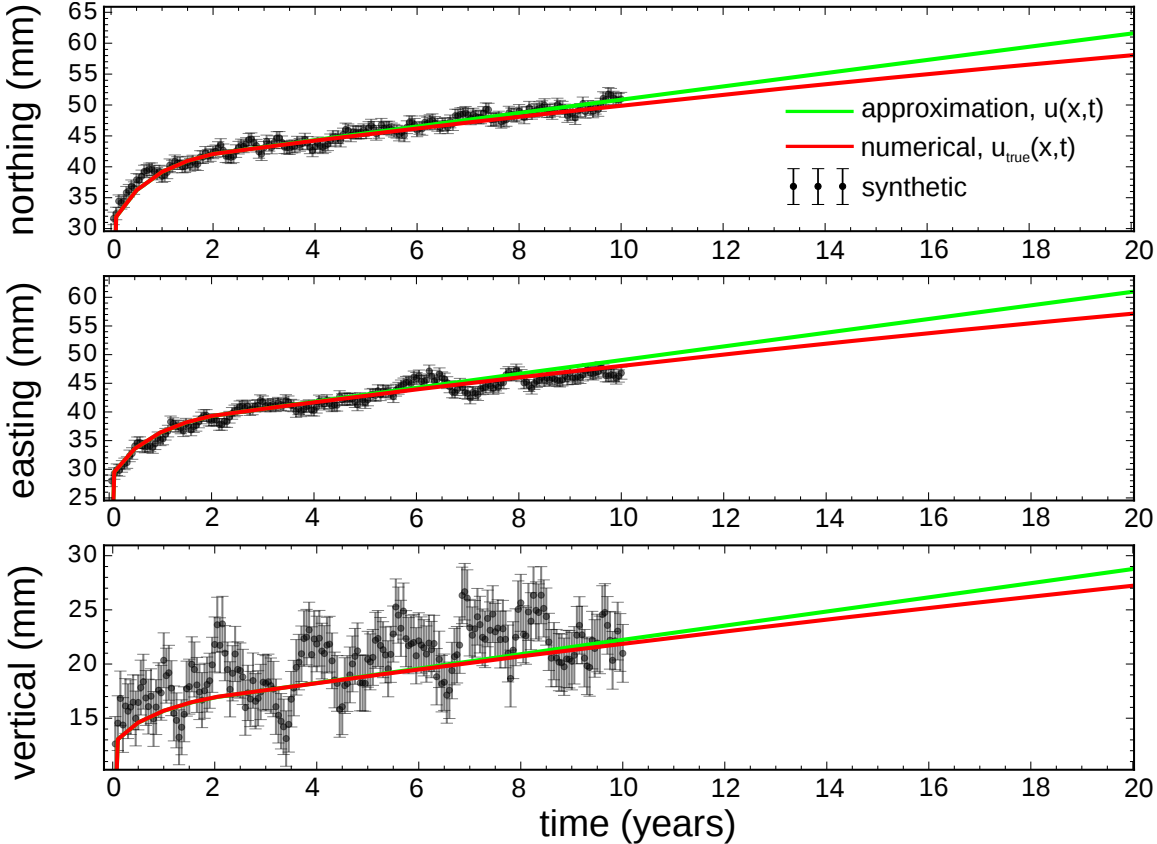


Figure 2.6: Displacement time series for the position shown in Figure 2.5 (black), best fitting surface displacements using the approximation from eq. (2.20) (green) and surface displacements computed with PyLith using the inferred slip distribution and viscosity structure (red). Coseismic displacements at  $t = 0$  are not shown.

resulting from fault slip. This means that a high fluidity in the uppermost layer will tend to produce deformation that is balanced out by higher amounts of slip. It is conceivable that such a correlation could lead to unrealistic inferences of viscosity in the near surface and it may be necessary to assume that viscous regions containing a fault are elastic. There is no significant correlation between afterslip and fluidity in layers below 30 km depth.

## Validation

The fact that our recovered fault slip and lithospheric viscosity are in good agreement with the synthetic model suggests that the approximation given by eq. (2.20) is accurate over the 10 years of synthetic data. We further assess the accuracy of eq. (2.20) by running a forward model with PyLith where the imposed fault slip and lithospheric viscosity are those estimated from the synthetic data. We then compare the displacements from the numerically computed forward model with the displacements predicted by eq. (2.20). We refer to the numerically computed displacements as  $\vec{u}_{\text{true}}(\vec{x}, t)$  and the displacements predicted by the

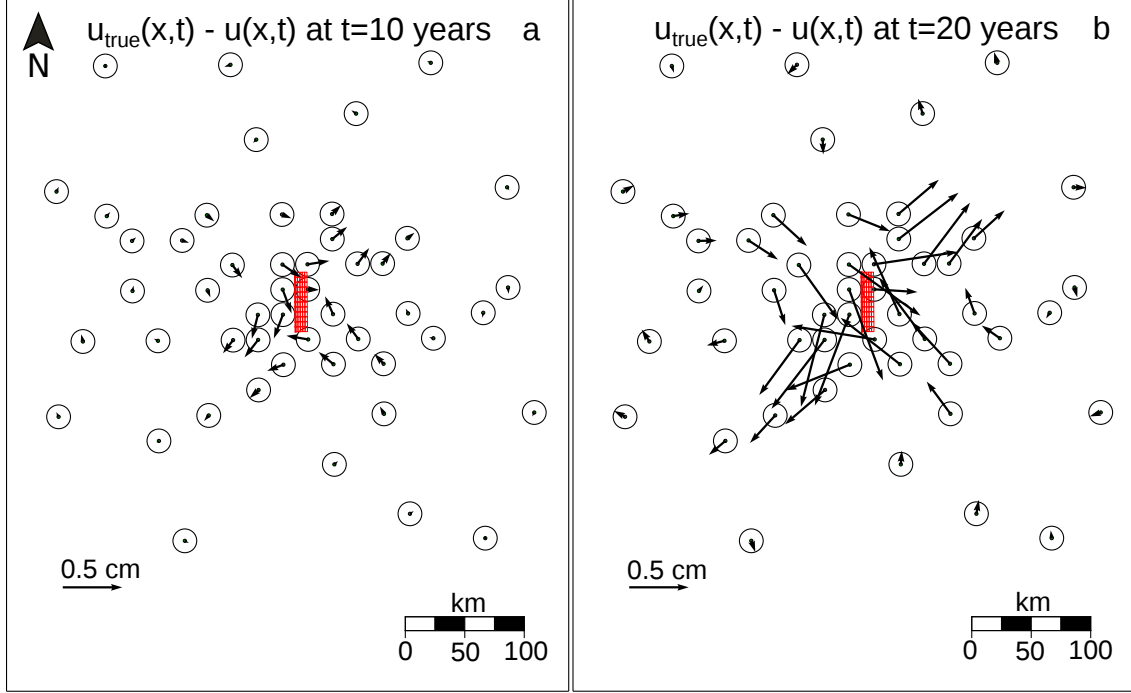


Figure 2.7: Approximation error at  $t = 10$  years and  $t = 20$  years. Circles with 1 mm radius are centered at each station to compare the accuracy of  $\vec{u}(\vec{x}, t)$  to the noise in the synthetic data.

approximation as  $\vec{u}(\vec{x}, t)$  (Figure 2.6). We refer to the difference between  $\vec{u}_{\text{true}}(\vec{x}, t)$  and  $\vec{u}(\vec{x}, t)$  as the approximation error (Figure 2.7). At  $t = 10$  years the approximation error is on order of a few mm's for each location, which is the magnitude of the data uncertainty. Additionally, the approximation error is small compared to the cm's of deformation resulting from viscoelastic relaxation, indicating that eq. (2.20) is indeed a fair approximation up to  $t = 10$  years. At  $t = 20$  years the approximation error is about one cm in magnitude for near field sites, indicating that the approximation has broken down in the near field by this time, while the error is still on order of a few mm's for the far field sites. The faster divergence for the near field sites is consistent with the comparison we made between the approximate and true displacements for a two-dimensional, two layered earthquake model in Section 2.3.1 (Figure 2.1).

The accuracy of eq. (2.20) is also demonstrated in Figure 2.6, which shows  $\vec{u}(\vec{x}, t)$  and  $\vec{u}_{\text{true}}(\vec{x}, t)$  at a sample site near the fault. The numerical solution asymptotically approaches the rate of deformation predicted by eq. (2.20) as time goes to zero, demonstrating that eq. (2.16) accurately describes the initial viscoelastic response. Additionally, the magnitude of the difference between  $\vec{u}(\vec{x}, t)$  and  $\vec{u}_{\text{true}}(\vec{x}, t)$  is smaller than the uncertainty of our synthetic data throughout the time series, indicating that eq. (2.20) is appropriate for this synthetic test. For this site and other near field sites, the approximation starts to break down at about

$t = 10$  years. The lowest relaxation time in our synthetic lithosphere is also about 10 years and so the duration over which eq. (2.20) is accurate is longer than what we found in our analysis for a two-dimensional, two layered earthquake model in Section 2.3.1.

### 2.5.3 Synthetic model with Burgers viscoelasticity

In the above synthetic example, we conveniently picked the length of our displacement time series to correspond with the shortest relaxation time in the lithosphere. If the length of the time series is significantly shorter than the relaxation time of the lithosphere, then eq. (2.20) would be an appropriate approximation and fault slip would be accurately recovered, although there would not be a significant amount of deformation resulting from viscoelastic relaxation and so inferences of viscosity would have high uncertainty. When the length of the time series is significantly longer than the shortest relaxation time of the lithosphere then the approximation would not be accurate and we would see a notable misfit in our best fitting prediction of the data. Here we use another synthetic test to demonstrate an iterative approach to finding the optimal time series duration. We also use this synthetic test to demonstrate how fluidities inferred using our inverse method can be used to constrain the viscous properties of a non-Maxwell viscoelastic lithosphere.

We consider a synthetic model with the same fault geometry and prescribed slip as the synthetic model described in Section 2.5.2, but the lithosphere now has a Burgers rheology. A Burgers rheology can be modeled schematically as a Maxwell spring-dashpot system connected in series with a Kelvin spring-dashpot system. There are five rheologic parameters needed to describe a Burgers rheology, the first Lamé parameter,  $\lambda$ , shear moduli of the Maxwell and Kelvin elements,  $\mu_m$  and  $\mu_k$ , and the viscosities of the Maxwell and Kelvin elements,  $\eta_m$  and  $\eta_k$ . In this synthetic test, we set  $\mu_m = \lambda = 32$  GPa and  $\eta_m$  equal to the viscosity structure from the synthetic model in Section 2.5.2. We also set  $\mu_k = \mu_m$  and  $\eta_k = 0.1\eta_m$  so the lowest kelvin relaxation time ( $\eta_k/\mu_k$ ) in our synthetic model is 1 year (Figure 2.8).

We use the same  $F_i(\vec{x})$ ,  $G_{ij}(\vec{x})$ , and  $A_k(t)$ , described in Section 2.5.1 and estimate an effective Maxwell viscosity by using 0.5, 2.0 and 5.0 years of synthetic data. Our inverse method allows us to estimate a single value of viscosity for each discretized region of the lithosphere and so we are unable to recover both  $\eta_k$  and  $\eta_m$ . Instead, our method allows us to estimate an effective viscosity for a Burgers viscoelastic lithosphere during the early postseismic period. We demonstrate in our supplementary IPython notebook that when assuming  $\mu_m$  is equal to the shear modulus used to construct  $F_i(\vec{x})$  and  $G_{ij}(\vec{x})$  then the

effective fluidity inferred using our method,  $1/\eta$ , is equivalent to

$$\frac{1}{\eta} = \left( \frac{1}{\eta_k} + \frac{1}{\eta_m} \right). \quad (2.25)$$

The recovered viscosities for each time series duration are shown in Figure 2.8 and we show the moment of inferred afterslip as a function of time in Figure 2.9. The synthetic and predicted displacement time series at the observation point indicated in Figure 2.5 are shown in Figure 2.10. We are able to accurately predict the synthetic displacements (red line in Figure 2.10) and recover the fluidities expected following eq. (2.25) when using a 0.5 year time series. The relatively few number of observations constraining the fluidity inferences leads to large uncertainties as indicated by the distribution of bootstrapped models. When we use 2 years of displacements, exceeding the minimum Kelvin relaxation time in the synthetic model, the best fitting predicted displacements are still a good fit to the synthetic data (green line), but it is difficult to discern whether some of the systematic misfit is due to the inability of eq. (2.20) to describe the transient displacement or because of the temporal correlation of our added noise. The inferences of fluidity when using 2 years of displacement are consistently off by a factor of 0.5. The underestimation of fluidity is then compensated by a slight overestimation of cumulative fault slip (Figure 2.9). Although the estimated fluidities are incorrect, the relative strength of the different layers is well recovered. When using 5 years of synthetic deformation, the depth dependence of fluidity no longer resembles the true depth dependence and the inferred moment of afterslip is appreciably higher than what was imposed in the synthetic model. Even though additional afterslip is describing some of the transient viscoelastic deformation, there is still a systematic misfit in the best fitting prediction to the 5 year time series (Figure 2.10) indicating that eq. (2.20) is not valid for that duration of time. The length of the time series used for our inverse method should be just long enough so that the best fitting predictions to the data do not have any systematic misfit. It is difficult to distinguish by the fit to the data whether the model recovered using a 0.5 year time series or a 2 year time series is a better estimate of the true model, although one can easily run a forward calculation for each of the recovered models to see how well they predict the later deformation.

## 2.6 Discussion

A fundamental assumption in our method for estimating slip and viscosity from postseismic deformation is that the timescale of relaxation in the weakest part of the lithosphere is at least as long as the timescales over which postseismic deformation is observed. This assumption

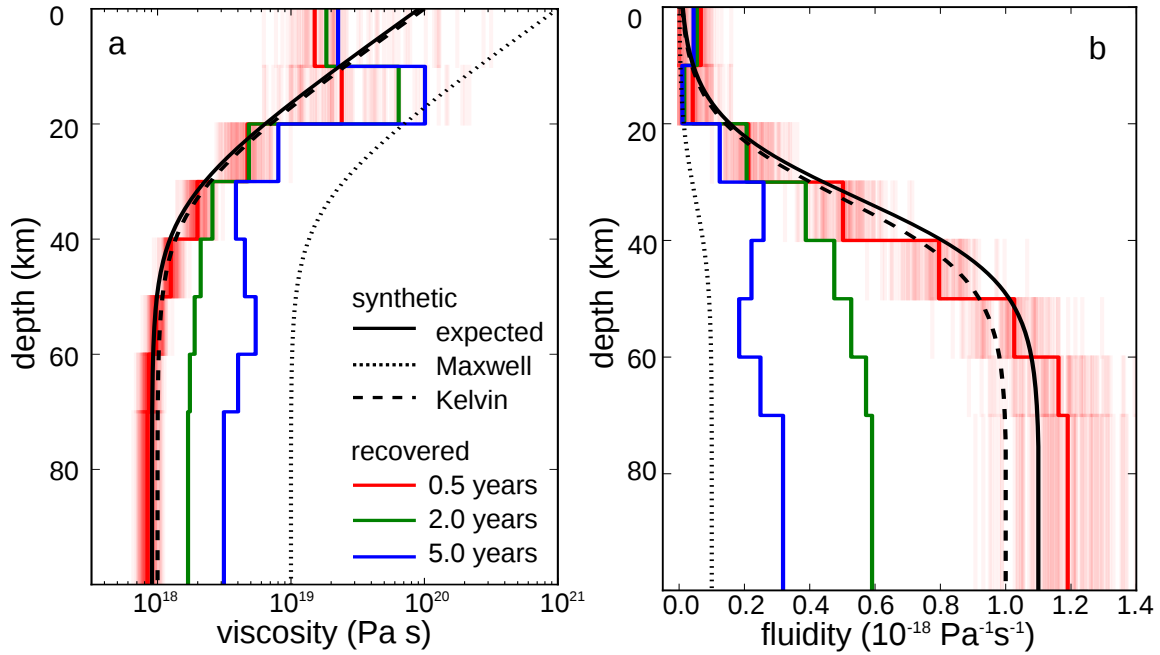


Figure 2.8: Synthetic and recovered lithospheric viscosities (left) and fluidities (right) for the synthetic model with a Burgers rheology. Dotted and dashed lines show the Maxwell and Kelvin viscosity in the synthetic model, respectively. The solid black line indicates the effective viscosity from eq. (2.25). The red, green, and blue lines show the inferred viscosities and fluidities when inverting a 0.5, 2.0, and 5.0 year long time series. The light red lines are the bootstrapped fluidities and viscosities inferred using the 0.5 year time series.

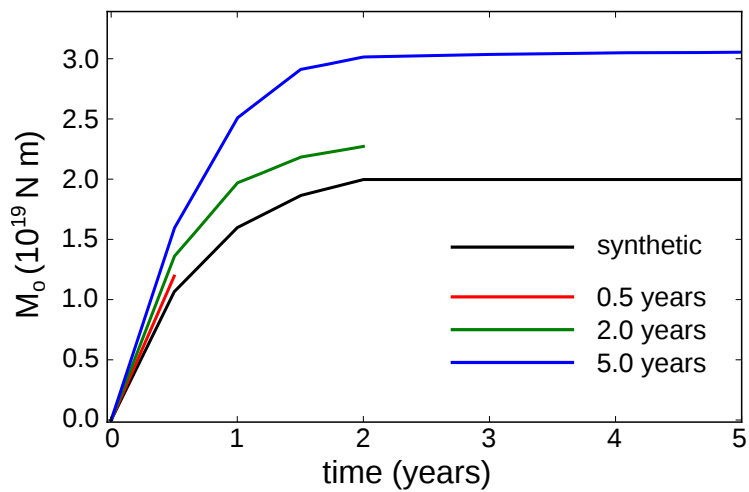


Figure 2.9: Afterslip moment over time for the synthetic model (black) and the inferred afterslip moment when inverting 0.5, 2.0, and 5.0 years of displacements (red, green, and blue).

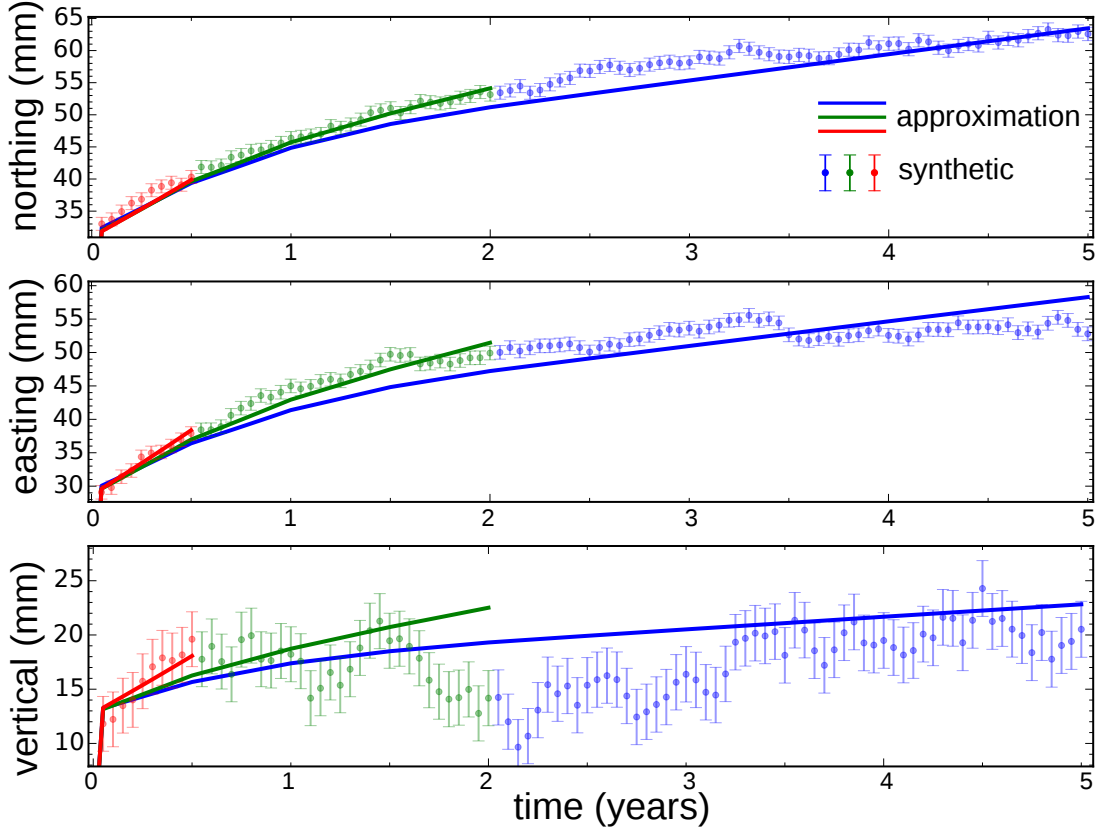


Figure 2.10: Synthetic and predicted displacement time series with length 0.5, 2.0, and 5.0 years. The time series shown is for the observation point indicated in Fig 5.

allows us to approximate the surface expression of viscous creep as a linear system with respect to lithospheric fluidity, which greatly facilitates and expedites the inverse problem. Since the relaxation times in a given region are generally not well known *a priori*, one must use an iterative approach as described in Section 2.5.3 to determine the appropriate length of the time series used in the inversion.

We can look at previous studies to gauge the duration over which our approximation would be accurate. Surface deformation following large ( $\geq M_w = 7$ ) earthquakes often is characterized by transient and rapid postseismic deformation in the first year after an earthquake followed by steady deformation in later years (e.g., *Savage and Svartc*, 1997; *Savage et al.*, 2005a; *Ergintav et al.*, 2009). Several studies have attributed rapid early transient deformation following an earthquake to afterslip, while describing the later steady deformation with viscous relaxation in a Maxwell viscoelastic lower crust or upper mantle (e.g., *Perfettini et al.*, 2005; *Johnson et al.*, 2009; *Hearn et al.*, 2009; *Freed et al.*, 2006b; *Rollins et al.*, 2015). These studies have found that lithospheric relaxation times no shorter than years or decades are needed to describe postseismic deformation. Indeed, *Perfettini*

*et al.* (2005) describes the trend in two years of postseismic deformation following the 2001  $M_w = 8.4$  Peru earthquake by assuming that the lithospheric viscosity was sufficiently high that the rate of deformation from viscoelastic creep could be considered constant, which is the assumption that we make in formulating eq. (2.18). If transient postseismic deformation can be attributed to fault slip followed by steady viscoelastic creep, then eq. (2.18) should be able to describe displacements on the timescale of years or decades after an earthquake.

Several studies have used rheologies containing a transient phase of deformation to explain the early postseismic deformation. For example, Pollitz (2003, 2005) invoked a Burgers rheology upper mantle to explain surface displacements following the 2002  $M_w = 7.9$  Denali earthquake and the 1999  $M_w = 7.1$  Hector Mine earthquake. In both cases the best fitting transient relaxation time was on the order of a month and the best fitting steady-state relaxation time was on the order of years. Postseismic deformation following the Denali earthquake was also successfully modeled by Freed *et al.* (2006a) with a power-law rheology in the upper mantle, consistent with laboratory studies (e.g., Kirby and Kronenberg, 1987). The power-law rheology was able to reproduce the observed transient surface deformation because the high stresses in the earthquake decreased the effective viscosity of the upper mantle to  $\sim 10^{17}$  Pa s resulting in fast surface deformation. As stresses from the earthquake relaxed, the effective viscosity increased and the predicted surface deformation became steadier. Based on the success of Pollitz (2003, 2005) and Freed *et al.* (2006a), one may dismiss our method as being unrealistic because we assume that the lithosphere is Maxwell viscoelastic. However, our method does not necessarily preclude the possibility of a Burgers rheology, as demonstrated in Section 2.5.3, or a stress-nonlinear viscosity. As long as stresses in the lithosphere remain roughly equal to the the stresses transferred elastically through fault slip, then a viscosity structure inferred using our method could be interpreted as the effective viscosity in a transient viscoelastic or power-law rheology. One could also use eq. (2.25) to constrain the rheologic properties for a Burgers rheology. If the commonly observed early transient postseismic deformation truly is the result of viscous relaxation in the lithosphere rather than afterslip, then the results from Pollitz (2003, 2005) and Freed *et al.* (2006a) suggest that the time interval over which eq. (2.18) is appropriate is on order of a month after an earthquake. In such case, our method can be used to get an initial estimate of lithospheric viscosity, while unused portion of the displacement time series could be incorporated in a gradient based nonlinear inverse method where the forward problem is computed numerically rather than with eq. (2.18).

Postseismic transient deformation could also be the result of creep in a weak ductile shear zone which is embedded in a stronger viscoelastic lithosphere (e.g., Hetland and Zhang, 2014). Sufficiently localized creep in a shear zone can be modeled as slip on a down-dip extension

of the ruptured fault (e.g., *Hearn et al.*, 2002; *Kenner and Segall*, 2003; *Johnson and Segall*, 2004) because the two processes are kinematically indistinguishable. Likewise, *Freed et al.* (2006a) noted that deep fault slip could serve as a proxy for distributed viscous relaxation in a weak lower crust when only considering horizontal displacements. The applicability of our method should therefore be unaffected by localized viscous deformation with the understanding that inferences of fault slip could be absorbing that deformation.

## 2.7 Conclusion

We present a method to invert coseismic and postseismic deformation to simultaneously estimate a time dependent distribution of fault slip and an arbitrarily discretized viscosity structure of the lithosphere. We take advantage of an approximation for early postseismic deformation resulting from fault slip and viscoelastic relaxation. This approximation is computationally efficient which allows us to rapidly search a high dimensional model space and make higher resolution estimates of effective lithospheric viscosity than what can feasibly be done with the commonly used grid search methods. Our method is applicable for as long as this approximation is appropriate, that is, for as long as stresses resulting from coseismic slip and afterslip have not significantly decayed due to viscoelastic relaxation. Based on inferences of lithospheric viscosity from other studies, we estimate that our method could be used for postseismic deformation ranging from months to years after an earthquake. Despite our methods application to a limited portion of the postseismic period, we demonstrate that our method is capable of robustly recovering the mechanisms driving postseismic deformation.

## Appendix 2A: Inverse Laplace transform through series expansion

Let  $f(t)$  be analytic at  $t = 0$  and let there be a real valued  $M$ , and  $C$  such that

$$|f^{(n)}(t)| < Ce^{Mt} \quad \forall t \geq 0 \text{ and } \forall n \in \{0, 1, 2, \dots\}, \quad (2.26)$$

where  $f^{(n)}(t)$  denotes the  $n^{\text{th}}$  derivative of  $f(t)$ . We define the Laplace transform of  $f(t)$  as

$$\mathcal{L}[f(t)] := \hat{f}(s) := \int_0^\infty f(t)e^{-st}dt \quad (2.27)$$

and we restrict our attention to  $s \in \mathbb{R}$ . The constraints on  $f^{(n)}(t)$  from eq. (2.26) ensure that

$$\lim_{s \rightarrow \infty} \mathcal{L}[f^{(n)}(t)] = 0. \quad (2.28)$$

It can be shown using integration by parts that

$$\mathcal{L}[f^{(n)}(t)] = s^n \hat{f}(s) - \sum_{m=1}^n s^{m-1} f^{(n-m)}(0) \quad \forall s > M. \quad (2.29)$$

Substituting eq. (2.29) into eq. (2.28) and then rearranging the terms gives us a recursive formula for  $f^{(n)}(0)$  in terms of  $\hat{f}(s)$ :

$$f^{(n)}(0) = \lim_{s \rightarrow \infty} s^{n+1} \hat{f}(s) - \sum_{m=1}^n s^m f^{(n-m)}(0), \quad (2.30)$$

where the base case,  $n = 0$ , is the initial value theorem:

$$f(0) = \lim_{s \rightarrow \infty} s \hat{f}(s). \quad (2.31)$$

Since we request  $f(t)$  to be analytic at  $t = 0$ , we can construct a Taylor series expansion of  $f(t)$  such that

$$f(t) = \sum_{n=0}^{\infty} \frac{f^{(n)}(0)}{n!} t^n \quad (2.32)$$

for all values of  $t$  within some neighborhood of  $t = 0$ . We find the inverse Laplace transform of  $\hat{f}(s)$  by combining eq. (2.32) with eqs. (2.30) and (2.31) so that  $f(t)$  is expressed in terms of  $\hat{f}(s)$ .

## Appendix 2B: Postseismic approximation for a two-dimensional earthquake model with a depth dependent viscosity

We seek to find an approximation for early postseismic deformation in a two-dimensional, strike-slip earthquake model with an arbitrary depth-dependent viscosity below the fault locking depth,  $D$ . We first find the initial rate of surface deformation following a unit of slip in a lithosphere that is elastic except for a viscoelastic layer which is at depth  $z$  and with thickness  $\Delta z$ . This is found by making the substitutions  $H_1 \rightarrow z$ ,  $H_2 \rightarrow \Delta z$ ,  $\eta_1 \rightarrow \infty$ ,  $\eta_3 \rightarrow \infty$ , and  $\eta_2 \rightarrow \eta$  in eq. (2.12), which gives us

$$\frac{\partial}{\partial t} u_1(x, t)|_{t=0} = \frac{1}{\eta} (W(z + \Delta z) - W(z)), \quad (2.33)$$

where

$$W(z) = \frac{\mu}{2\pi} \left( \tan^{-1} \left( \frac{2z - D}{x} \right) - \tan^{-1} \left( \frac{2z + D}{x} \right) \right). \quad (2.34)$$

From eq. (2.16) we know that the initial rate of surface deformation for a lithosphere composed of  $N$  discrete layers, each with viscosity  $\eta_i$ , at depth  $z_i$ , and having thickness  $\Delta z$ , is then

$$\frac{\partial}{\partial t} u_N(x, t)|_{t=0} = \sum_i^N \frac{1}{\eta_i} (W(z_i + \Delta z) - W(z_i)). \quad (2.35)$$

The initial rate of surface deformation for a viscosity structure given by  $\eta(z)$  is found by taking the limit as  $\Delta z \rightarrow 0$  and  $N \rightarrow \infty$ :

$$\frac{\partial}{\partial t} u(x, t)|_{t=0} = \int_D^\infty \frac{1}{\eta(z)} \frac{\partial}{\partial z} W(z) dz \quad (2.36)$$

$$= \int_D^\infty \frac{\mu}{2\pi\eta(z)} \left( \frac{2x}{x^2 + (D + 2z)^2} - \frac{2x}{x^2 + (2z - D)^2} \right) dz. \quad (2.37)$$

Finally, we add the elastic component of deformation and integrate eq. (2.36) with the fault slip history to obtain an approximation for early postseismic deformation:

$$u(x, t) \approx \frac{b(t)}{\pi} \tan^{-1}\left(\frac{D}{x}\right) + \int_o^t \int_D^\infty \frac{\mu b(\theta)}{2\pi\eta(z)} \left( \frac{2x}{x^2 + (D + 2z)^2} - \frac{2x}{x^2 + (2z - D)^2} \right) dz d\theta. \quad (2.38)$$

## CHAPTER 3

# Rheologic constraints on the upper mantle from five years of postseismic deformation following the El Mayor-Cucapah earthquake\*

### 3.1 Abstract

We analyze five years of Southern California GPS data following the  $M_w=7.2$  El Mayor-Cucapah earthquake. We observed transient postseismic deformation which persists for three years at epicentral distances greater than  $\sim 200$  km. In the near-field, rapid postseismic transience decays to a sustained rate which exceeds its preseismic trend. We attempt to determine the mechanisms driving this deformation, where we consider afterslip at seismogenic depths and viscoelastic relaxation in the lower crust and upper mantle as candidate mechanisms. We find that early, rapid, near-field deformation can be explained with afterslip on the fault that ruptured coseismically. The later, sustained, near-field deformation can be explained with viscoelastic relaxation in the lower crust with a steady-state viscosity of  $\sim 10^{19}$  Pa s and possibly continued afterslip. The later postseismic deformation in the far-field is best explained with a transient viscosity of  $\sim 10^{18}$  Pa s in the upper mantle. We argue that a transient rheology in the mantle is preferable over a Maxwell rheology because it better predicts the decay in postseismic deformation, and also because it does not conflict with the generally higher, steady-state viscosities inferred from studies of geophysical processes occurring over longer time scales.

### 3.2 Introduction

Ground deformation in the years following a large ( $M_w \gtrsim 7$ ) earthquake can be used to gain insight into the mechanical behavior of the crust and upper mantle. The interpretations of

---

\*This chapter has been published as: Hines, T. T., and Hetland, E. A. (2016). Rheologic constraints on the upper mantle from five years of postseismic deformation following the El Mayor-Cucapah earthquake. *Journal of Geophysical Research: Solid Earth*, 121, doi:10.1002/2016JB013114.

postseismic deformation are not always conclusive because multiple postseismic deformation mechanisms, such as afterslip or viscoelastic relaxation in the lower crust and upper mantle, can have qualitatively similar surface expressions (e.g., *Savage*, 1990). This non-uniqueness complication can potentially be remedied if the postseismic deformation occurs in an area that is sufficiently well instrumented with GPS stations (*Hearn*, 2003). Owing to the dense geodetic network deployed throughout the 2000s as part of the Plate Boundary Observatory, the postseismic deformation following the April 4, 2010, Mw=7.2 El Mayor-Cucapah earthquake in Baja California was observed at more GPS stations than any other earthquake in California to date (see *Hauksson et al.* (2011) and *Fletcher et al.* (2014) for a detailed description of this earthquake and its seismotectonic context). With such a large collection of data, we attempt to discern the mechanisms driving the postseismic deformation. Previous studies which have modeled postseismic deformation following the El Mayor-Cucapah earthquake include *Pollitz et al.* (2012), *Gonzalez-Ortega et al.* (2014), *Spinler et al.* (2015), and *Rollins et al.* (2015). Of these studies, *Gonzalez-Ortega et al.* (2014) and *Rollins et al.* (2015) have attempted to describe the postseismic deformation with afterslip in an elastic half-space. *Gonzalez-Ortega et al.* (2014) described five months of postseismic deformation, observed by InSAR and GPS stations within  $\sim$ 50 km of the rupture, with afterslip and contraction on the coseismically ruptured fault. *Gonzalez-Ortega et al.* (2014) noted that their preferred model underestimated the GPS displacements for stations  $\gtrsim$  25 km from the rupture and suggested that it could be the result of unmodeled viscoelastic relaxation. Using only continuous GPS stations, which are mostly north of the rupture zone, *Rollins et al.* (2015) found that three years of postseismic deformation can be adequately explained by afterslip, albeit with an implausibly large amount of slip inferred on the least constrained, southern-most fault segment. Here, we suggest the afterslip inferred by *Rollins et al.* (2015) may have been acting as a proxy for distributed relaxation in the upper mantle.

*Pollitz et al.* (2012), *Rollins et al.* (2015) and *Spinler et al.* (2015) explored viscoelastic relaxation in the lower crust and upper mantle as a potential postseismic deformation mechanism. The rheology of the crust and mantle is largely unknown and so modeling postseismic deformation with viscoelastic relaxation requires one to assume a rheologic model and then find the best fitting rheologic parameters. The inference of these rheologic parameters is a computationally expensive non-linear inverse problem which is typically approached with a forward modeling grid search method. Consequently, a simplified structure for the Earth must be assumed in order to minimize the number of rheologic parameters that need to be estimated. For example, it is commonly assumed that the lower crust and upper mantle are homogeneous, Maxwell viscoelastic layers, which may be too simplistic for postseismic studies (*Riva and Govers*, 2009; *Hines and Hetland*, 2013). To further reduce the dimensions

of the model space, it is also necessary to make simplifying assumptions about the behavior of afterslip. For example, one can assume a frictional model for afterslip and parametrize afterslip in terms of the unknown rheologic properties of the fault (e.g., *Johnson et al.*, 2009; *Johnson and Segall*, 2004). One can also assume that afterslip does not persist for more than a few months and then model the later postseismic deformation assuming it to be the result of only viscoelastic relaxation (e.g., *Pollitz et al.*, 2012; *Spinler et al.*, 2015). However, afterslip in similar tectonic settings has been observed to persist for decades following earthquakes (*Cakir et al.*, 2012; *Cetin et al.*, 2014). Indeed, the preferred viscoelastic model from *Pollitz et al.* (2012) significantly underestimates deformation in the Imperial Valley, which could be indicative of unmodeled continued afterslip. Neglecting to allow for sustained afterslip as a postseismic mechanism could then lead to biased inferences of viscosities.

In this study, we perform a kinematic inversion for fault slip, allowing it to persist throughout the postseismic period, while simultaneously estimating the viscosity of the lower crust and upper mantle. We create an initial model of the fault slip and effective viscosity necessary to describe early postseismic deformation using the method described in *Hines and Hetland* (2015). This method uses a first-order approximation of surface deformation resulting from viscoelastic relaxation which is only applicable to the early postseismic period. In this case, our initial model describes the first 0.8 years of postseismic deformation following the El Mayor-Cucapah earthquake. We then use the inferred effective viscosity structure from the initial model to create a suite of postseismic models which we test against the five years of postseismic data available to date. Of the suite of models tested, we find that postseismic deformation following the El Mayor-Cucapah earthquake can be explained with a combination of afterslip on a fault segment running through the Sierra Cucapah and viscoelastic relaxation in a Zener rheology upper mantle with a transient viscosity on the order of  $10^{18}$  Pa s.

### 3.3 Data processing

We use continuous GPS position time series provided by University Navstar Consortium (UNAVCO) for stations within a 400 km radius about the El Mayor-Cucapah epicenter. We collectively describe the coseismic and postseismic displacements resulting from the El Mayor-Cucapah earthquake as  $u_{\text{post}}(t)$ . We consider the GPS position time series,  $u_{\text{obs}}(t)$ , to be the combination of  $u_{\text{post}}(t)$ , secular tectonic deformation, annual and semi-annual oscillations, and coseismic offsets from significant earthquakes over the time span of this study. The June 14, 2010, Mw=5.8 Ocotillo earthquake and the Brawley swarm, which included an Mw=5.5 and an Mw=5.4 event on August 26, 2012 (Figure 3.1), are the only

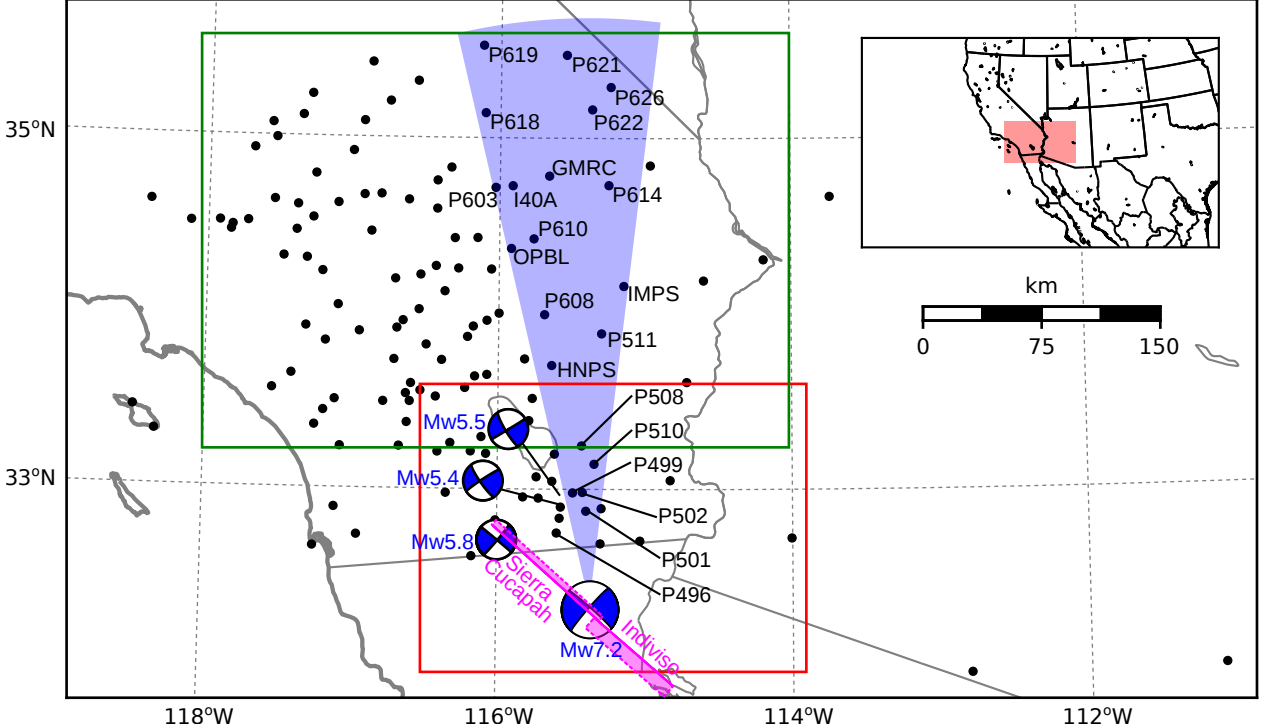


Figure 3.1: Map of the region considered in this study. The large focal mechanism is the GCMT solution for the El Mayor-Cucapah earthquake, and the three small focal mechanisms are for the Ocotillo earthquake and the two main shocks during the Brawley swarm. The black dots indicate the locations of GPS stations used in this study. The fault geometry used in this study is shown in magenta where dashed lines indicate buried edges of the fault segments. The green and red boxes demarcate the extent of the near-field and far-field maps (Figures 3.4 and 3.5). Stations inside the blue sector, which highlights the area within  $10^\circ$  of the El Mayor-Cucapah P-axis, are used in Figures 3.7 and 3.10.

earthquakes that produced noticeable displacements in any of the time series. We treat the displacements resulting from the Brawley swarm as a single event because the daily solutions provided by UNAVCO cannot resolve the separate events. Although the Ocotillo earthquake had its own series of aftershocks (Hauksson *et al.*, 2011), neither the Ocotillo earthquake nor the Brawley swarm produced detectable postseismic deformation. We model displacements resulting from these events with only a Heaviside function,  $H(t)$ , describing the coseismic offsets. We then model  $u_{\text{obs}}(t)$  as

$$u_{\text{obs}}(t) = u_{\text{pred}}(t) + \epsilon, \quad (3.1)$$

where

$$\begin{aligned} u_{\text{pred}}(t) = & u_{\text{post}}(t)H(t - t_{\text{emc}}) + c_0 + c_1 t + \\ & c_2 \sin(2\pi t) + c_3 \cos(2\pi t) + c_4 \sin(4\pi t) + c_5 \cos(4\pi t) + \\ & c_6 H(t - t_{\text{oc}}) + c_7 H(t - t_{\text{bs}}). \end{aligned} \quad (3.2)$$

In the above equations,  $t_{\text{emc}}$ ,  $t_{\text{oc}}$  and  $t_{\text{bs}}$  are the times of the El Mayor-Cucapah earthquake, Ocotillo earthquake, and the Brawley swarm, respectively,  $c_0$  through  $c_7$  are unknown coefficients, and  $\epsilon$  is the observation noise. We are using years as our unit of time which makes  $c_2$  through  $c_5$  the coefficients for annual and semi-annual oscillations. We only estimate jumps associated with the Ocotillo earthquake and Brawley swarm for stations within 40 km of their epicenters.

Stations which recorded displacements that clearly cannot be described by the aforementioned processes are not included in our analysis. This includes stations in the Los Angeles basin, where anthropogenic deformation can be larger than the postseismic signal that we are trying to estimate (*Bawden et al.*, 2001; *Argus et al.*, 2005). In order to ensure an accurate estimation of the secular deformation, we only use stations that were installed at least six months prior to El Mayor-Cucapah earthquake even though several GPS stations were installed after the earthquake to get better coverage of the postseismic deformation field (*Spinler et al.*, 2015). It would be possible to subtract secular velocities derived from elastic block models (e.g., *Meade and Hager*, 2005) from velocities recorded at the newly installed stations to get an estimate of postseismic velocities at those stations. However, estimating velocities from an already noisy displacement time series can introduce significant uncertainties depending on exactly how the estimation is done. We therefore use coseismic and postseismic displacements, rather than velocities, in our inverse method described in Section 3.4. This choice prevents us from using the newly installed stations for our analysis.

The October 16, 1999, Mw=7.1 Hector Mine earthquake, which occurred  $\sim$ 270 km north of the El Mayor-Cucapah epicenter, produced transient postseismic deformation which we do not wish to model, either mechanically or through empirical line fitting. We thus restrict our analysis to deformation observed six years after the Hector Mine earthquake, which is when postseismic velocities at sites near the Hector Mine epicenter are approximately constant (*Savage and Svarc*, 2009). When appraising our model fit in Section 3.4, we see some systematic residuals in the vicinity of the Hector Mine epicenter, which may be the result of errors in the assumption that the trend in Hector Mine postseismic deformation is linear after six years.

Studies of postseismic deformation typically assume a parametric form for  $u_{\text{post}}(t)$ , such as one with a logarithmic or exponential time dependence (e.g., *Savage et al.*, 2005b). However, by assuming a logarithmic or exponential form of  $u_{\text{post}}(t)$  we run the risk of over fitting the GPS time series and inferring a non-existent postseismic signal. We therefore do not assume any parametric form for  $u_{\text{post}}(t)$  and rather treat it as integrated Brownian motion, so that

$$\dot{u}_{\text{post}}(t) = \sigma^2 \int_0^t w(s) ds, \quad (3.3)$$

where  $w(t)$  is white noise and the variance of  $\dot{u}_{\text{post}}(t)$  increases linearly with time by a factor of  $\sigma^2$ . We use a Kalman filtering approach to estimate  $u_{\text{post}}(t)$  and the unknown parameters in eq. (3.2). In the context of Kalman filtering, our time varying state vector is

$$\mathbf{X}(t) = [u_{\text{post}}(t), \dot{u}_{\text{post}}(t), c_0, \dots, c_7] \quad (3.4)$$

and eq. (3.2) is the observation function which maps the state vector to the GPS observations. We initiate the Kalman filter by assuming a prior estimate of  $\mathbf{X}(t)$  at the first time epoch, denoted  $\mathbf{X}_{1|0}$ , which has a sufficiently large covariance, denoted  $\Sigma_{1|0}$ , to effectively make our prior uninformed. For each time epoch,  $t_i$ , Bayesian linear regression is used to incorporate GPS derived estimates of displacement with our prior estimate of the state,  $\mathbf{X}_{i|i-1}$ , to form a posterior estimate of the state,  $\mathbf{X}_{i|i}$ , which has covariance  $\Sigma_{i|i}$ . We then use the posterior estimate of the state at time  $t_i$  to form a prior estimate of the state at time  $t_{i+1}$  through the transition function

$$\mathbf{X}_{i+1|i} = \mathbf{F}_{i+1} \mathbf{X}_{i|i} + \delta_{i+1}, \quad (3.5)$$

where

$$\mathbf{F}_{i+1} = \begin{bmatrix} 1 & (t_{i+1} - t_i) & \mathbf{0} \\ 0 & 1 & \mathbf{0} \\ \mathbf{0} & \mathbf{0} & \mathbf{I} \end{bmatrix} \quad (3.6)$$

and  $\delta_{i+1}$  is the process noise, which has zero mean and covariance described by

$$\mathbf{Q}_{i+1} = \sigma^2 \begin{bmatrix} \frac{(t_{i+1}-t_i)^3}{3} & \frac{(t_{i+1}-t_i)^2}{2} & \mathbf{0} \\ \frac{(t_{i+1}-t_i)^2}{2} & (t_{i+1} - t_i) & \mathbf{0} \\ \mathbf{0} & \mathbf{0} & \mathbf{0} \end{bmatrix}. \quad (3.7)$$

The covariance of the new prior state,  $\mathbf{X}_{i+1|i}$ , is then described by

$$\Sigma_{i+1|i} = \mathbf{F}_{i+1} \Sigma_{i|i} \mathbf{F}_{i+1}^T + \mathbf{Q}_{i+1}. \quad (3.8)$$

This process is repeated for each of the  $N$  time epochs. We then use Rauch-Tung-Striebel smoothing (*Rauch et al.*, 1965) to find  $\mathbf{X}_{i|N}$ , which is an estimate of the state at time  $t_i$  that incorporates GPS observation for all  $N$  time epochs. Our final estimates of  $u_{\text{post}}(t)$  are used in subsequent analysis, while the remaining components of the state vector are considered nuisance parameters. In the interests of computational tractability, we down sample our smoothed time series from daily solutions down to weekly solutions.

The smoothness of  $u_{\text{post}}(t)$  is controlled by the chosen value of  $\sigma$ , which describes how

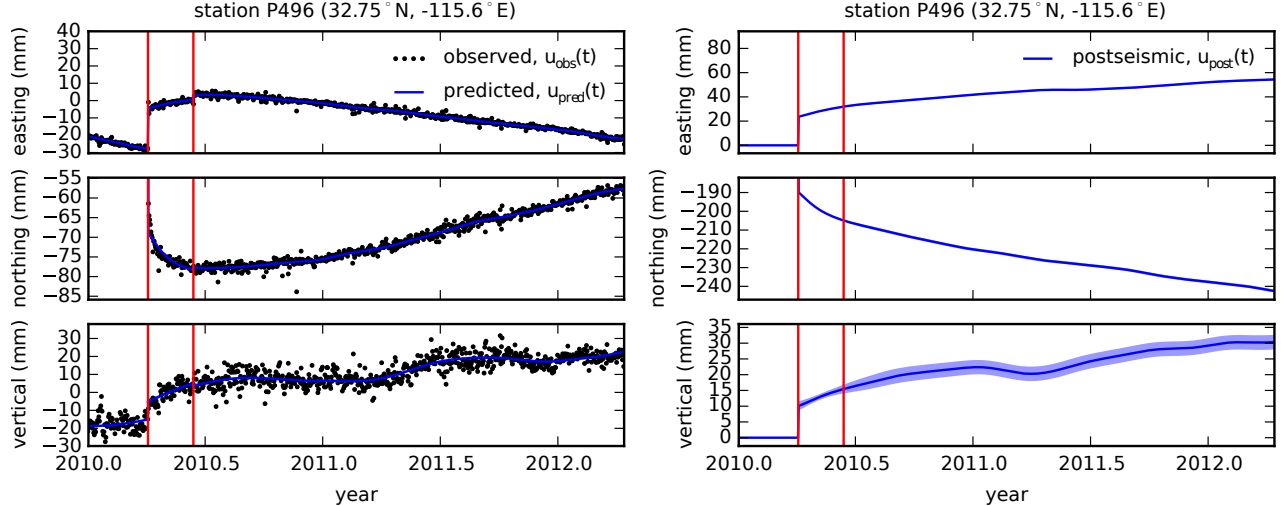


Figure 3.2: Left panels show GPS time series from UNAVCO (black) and the predicted displacement (blue) from eq. (3.2) for a near-field station. Red lines indicate the times of the El Mayor-Cucapah and Ocotillo earthquake. The right panels show estimated coseismic and postseismic displacements,  $u_{\text{post}}$ , which are extracted from the predicted displacements. The 68% confidence interval is shown in light blue.

rapidly we expect postseismic displacements to vary over time. Setting  $\sigma$  equal to zero will effectively result in modeling  $u_{\text{post}}(t)$  as a straight line which is insufficient to describe the expected transient behavior in postseismic deformation. The other end member, where  $\sigma$  is infinitely large, will result in  $u_{\text{pred}}(t)$  overfitting the data. While one can use a maximum likelihood based approach for picking  $\sigma$  (e.g., Segall and Mathews, 1997), we instead take a subjective approach and choose a value for  $\sigma$  that is just large enough to faithfully describe the observed deformation at the most near-field station in our study, P496, which exhibits the most rapid changes in velocity. This ensures that  $\sigma$  will be sufficiently large so that our estimate of  $u_{\text{post}}(t)$  does not smooth out potentially valuable postseismic signal at the remaining stations. We find that using  $\sigma = 50 \text{ mm/yr}^{1.5}$  adequately describe all but the first week of postseismic deformation at station P496, which slightly increases our estimate of coseismic displacements (Figure 3.2). We include an example of estimating  $u_{\text{post}}(t)$  for a far-field station, P619, which is about 359 km north of the El Mayor-Cucapah epicenter (Figure 3.3). At station P619, along with all the other stations in the Mojave region, there is a south-trending postseismic transience that persists for the first three years after the El Mayor-Cucapah earthquake. Postseismic deformation that extends to these epicentral distances has also been observed after the Hector Mine earthquake (Freed et al., 2007).

It is important to note that the shown uncertainties in  $u_{\text{post}}(t)$  do not account for the non-negligible epistemic uncertainty in eq. (3.2). For example, we assume a constant rate of secular deformation, which appears to be an appropriate approximation for all but perhaps the stations closest to the Hector Mine epicenter, as noted above. Also, our model for

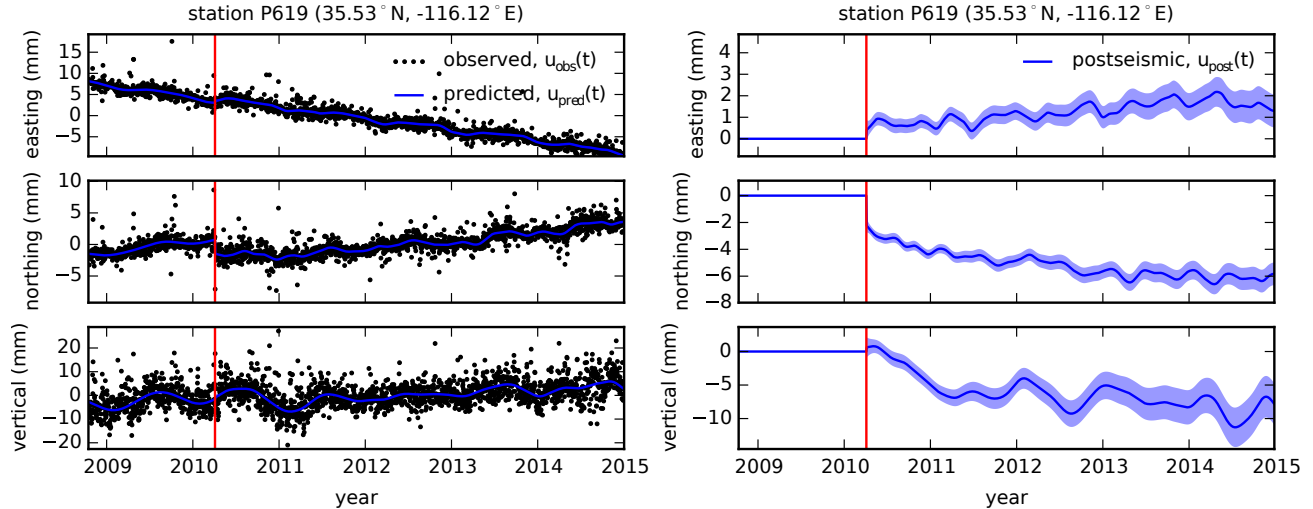


Figure 3.3: same as Figure 3.2 but for a far-field station.

seasonal deformation in eq. (3.2) assumes a constant amplitude over time, which means that any yearly variability in the climatic conditions could introduce systematic residuals (*Davis et al.*, 2012). Indeed, it would be more appropriate to consider the seasonal amplitudes  $c_2 - c_5$  in eq. (3.2) as stochastic variables (*Murray and Segall*, 2005). By using constant seasonal amplitudes, our estimate of  $u_{\text{post}}(t)$  seems to describe some of the unmodeled annual and semi-annual oscillations (e.g. Figure 3.3).

We show in Figures 3.4 and 3.5 the near and far-field coseismic displacements and the postseismic displacements accumulated over the time intervals 0-1 years, 1-3 years, and 3-5 years. Stations at epicentral distances beyond  $\sim 200$  km have an elevated rate of deformation for the first three years following the earthquake. This far-field deformation is trending southward at a rate of a few millimeters per year along the direction of the El Mayor-Cucapah P-axis. A similar eastward trend can be seen in the few far-field stations in Arizona, located along the T-axis. After three years, the trend in far-field postseismic deformation is barely perceptible. Most far-field stations display an initial subsidence for the first year after the El Mayor-Cucapah earthquake followed by continued uplift. This trend in vertical deformation can be observed in all three of the quadrants where postseismic data is available, which means that the vertical deformation does not exhibit an anti-symmetric quadrant pattern, as would be expected for postseismic processes. Although we use vertical deformation in our analysis in Section 3.4, we do not put an emphasis on trying to describe the vertical deformation because it likely does not have postseismic origins.

The near-field postseismic deformation is notably sustained when compared to the far-field deformation. Namely, the station in this study which is closest to the El Mayor-Cucapah epicenter, P496, has a steady postseismic trend of  $\sim 1.5$  cm/yr to the south after about one

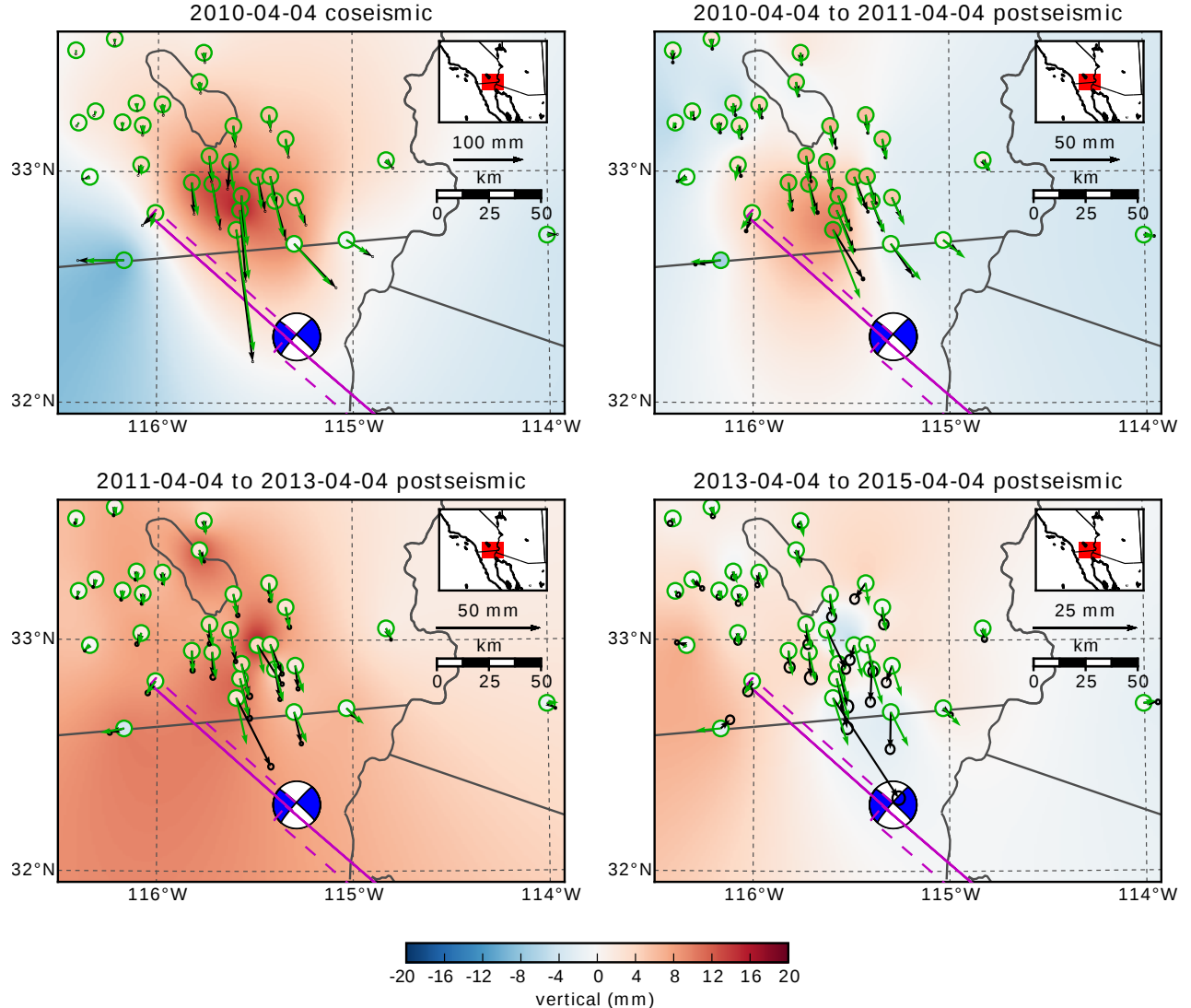


Figure 3.4: Near-field coseismic and cumulative postseismic displacements over the indicated time periods (black) and predicted displacements for our preferred model from Section 3.4.3 (green). The black error ellipses show the 68% confidence interval for the observed horizontal displacements. Observed vertical displacements are shown as an interpolated field and predicted vertical displacements are shown within the green circles. Note that the interpolant is not well constrained in Mexico where there is no data available.

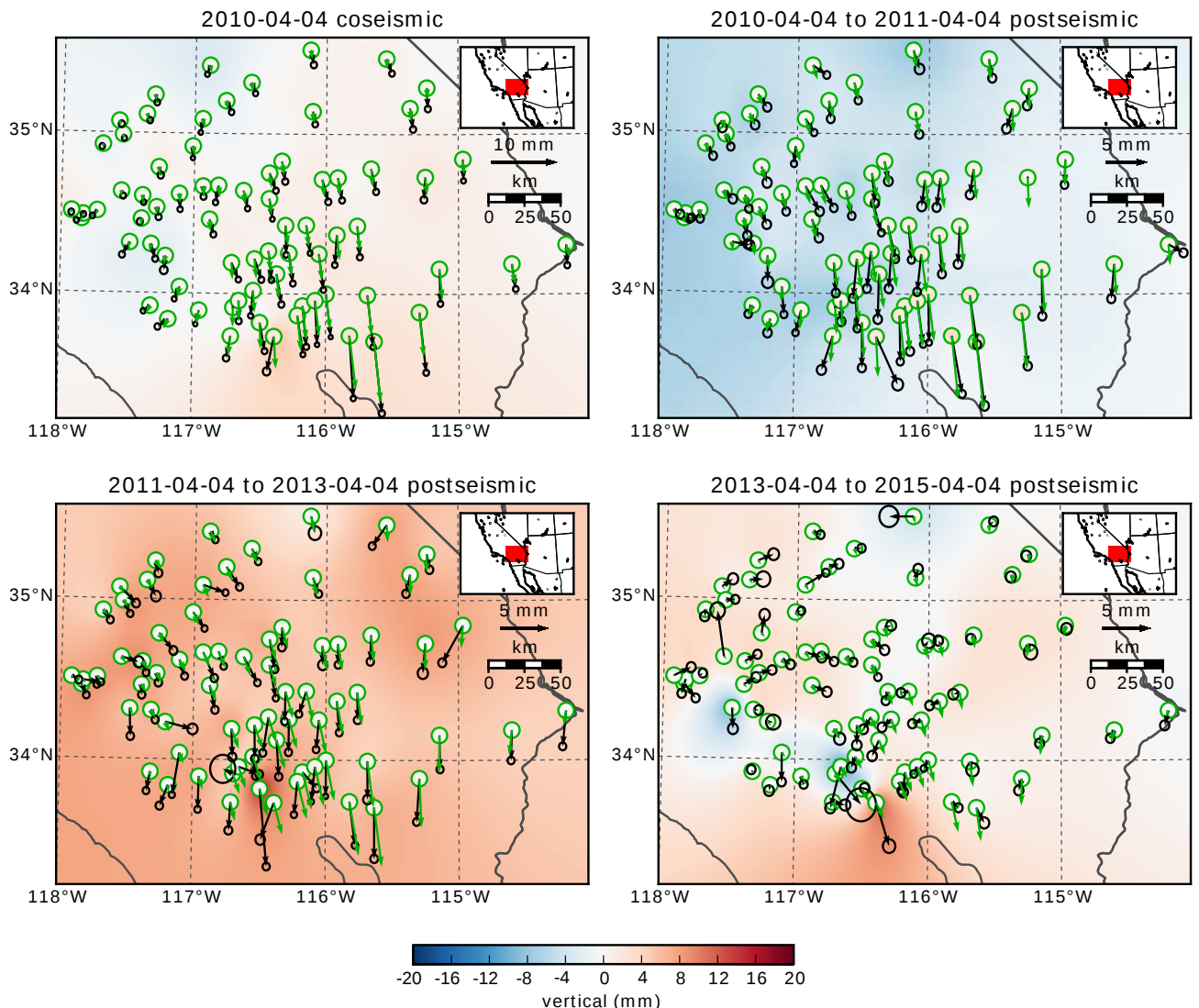


Figure 3.5: Same as Figure 3.4 but for far-field stations.

depth (km)	$\lambda$ (GPa)	$\mu$ (GPa)	$\eta_{\text{eff}}$ ( $10^{18}$ Pa s)	$\mu_k/\mu$
0-5	24.0	24.0	-	-
5-15	35.0	35.0	-	-
15-30	42.0	42.0	44.3	0.0
30-60	61.0	61.0	5.91	0.375
60-90	61.0	61.0	1.99	0.375
90-120	61.0	61.0	1.31	0.375
120-150	61.0	61.0	1.10	0.375
150- $\infty$	61.0	61.0	1.07	0.375

Table 3.1: Assumed and estimated material properties.  $\lambda$  and  $\mu$  are assumed known *a priori* and are based on the values used for the coseismic model by *Wei et al.* (2011b). The values for  $\eta_{\text{eff}}$  are estimated in Section 3.4.2, and  $\frac{\mu_k}{\mu}$  are the optimal shear moduli ratios found in Section 3.4.3 for a Zener rheology upper mantle.

year. Vertical postseismic deformation in the near-field does display a quadrant pattern which is consistent with the coseismic vertical deformation, suggesting that it is resulting from postseismic processes. However, the vertical postseismic signal is only apparent for the first year after the earthquake (Figure 3.4). As with the far-field deformation, there is a general trend of uplift in the near-field after about one year.

### 3.4 Postseismic modeling

We seek to find the mechanisms driving five years of postseismic deformation following the El Mayor-Cucapah earthquake and we consider afterslip and viscoelastic relaxation as candidate mechanisms. Poroelastic rebound has also been used to model postseismic deformation (e.g., *Jónsson et al.*, 2003); however, *Gonzalez-Ortega et al.* (2014) found that poroelastic rebound is unlikely to be a significant contributor to postseismic deformation following the El Mayor-Cucapah earthquake. Furthermore, we consider stations which are sufficiently far away from the rupture that poroelastic rebound should be insignificant.

We estimate coseismic and time-dependent postseismic fault slip, both of which are assumed to occur on a fault geometry modified from *Wei et al.* (2011b). Field studies (*Fletcher et al.*, 2014) and LIDAR observations (*Oskin et al.*, 2012) have revealed a significantly more complicated fault geometry than what was inferred by *Wei et al.* (2011b), especially within the Sierra Cucapah. However, we find that a relatively simple coseismic fault geometry based on (*Wei et al.*, 2011b) is adequate because most of the stations used in this study are sufficiently far from the El Mayor-Cucapah rupture that they are insensitive to the details in the fault geometry found by *Fletcher et al.* (2014) and *Oskin et al.* (2012). The fault geometry used in this study (Figure 3.1) consists of the two main fault segments inferred by *Wei et al.* (2011b), where the northern segment runs through the Sierra Cucapah up to

the US-Mexico border and the southern segment is the Indiviso fault which extends down to the Gulf of California. Both segments extend from the surface to 15 km depth. We extend the northern segment by 40 km to the northwest, which is motivated by the clustering of aftershocks on the northern tip of the coseismic rupture zone (*Hauksson et al.*, 2011; *Kroll et al.*, 2013). This extended fault segment was also found to be necessary by *Rollins et al.* (2015) and *Pollitz et al.* (2012) in order to describe the postseismic deformation.

### 3.4.1 Elastic postseismic inversion

We consider a variety of rheologic models for the lower crust and upper mantle. The simplest rheologic model is to consider them to be effectively elastic and isotropic. In such case, the rheologic parameters consist of the reasonably well known Lamé parameters,  $\lambda$  and  $\mu$ , and we use the same values used by *Wei et al.* (2011b) throughout this paper (Table 1). The only unknown is the distribution of fault slip, which can be estimated from postseismic deformation through linear least squares. *Rollins et al.* (2015) used a subset of the GPS stations considered in this study and found that three years of postseismic deformation following the El Mayor-Cucapah earthquake can be explained with afterslip on the coseismic fault plane without requiring any viscoelastic relaxation. We also perform an elastic slip inversion, but we use GPS stations within a larger radius about the El Mayor-Cucapah epicenter (400 km instead of  $\sim 200$  km). Our forward problem describing predicted postseismic deformation,  $u_{\text{pred}}$ , in terms of time dependent fault slip,  $s$ , is

$$u_{\text{pred}}(x, t) = \int_F s(\xi, t) g(x, \xi) d\xi, \quad (3.9)$$

where  $F$  denotes the fault and  $g(x, \xi)$  is the elastic Green's function describing displacement at surface position  $x$  resulting from slip at  $\xi$  on the fault. We estimate coseismic slip and the rate of afterslip over the postseismic time intervals 0.0-0.125, 0.125-0.25, 0.25-0.5, 0.5-1.0, 1.0-2.0, 2.0-3.0, 3.0-4.0, and 4.0-5.0 years. Each fault segment is discretized into roughly 4 km by 4 km patches and we impose that the direction of slip and slip rate are within  $45^\circ$  of right-lateral. We also add zeroth-order Tikhonov regularization so that our solution for  $s$  satisfies

$$\min_s \left( \left\| \frac{u_{\text{pred}}(s) - u_{\text{post}}}{\sigma_{\text{post}}} \right\|_2^2 + \lambda_s \|s\|_2^2 \right), \quad (3.10)$$

where  $\sigma_{\text{post}}$  is the uncertainty on postseismic displacements and  $\lambda_s$  is a penalty parameter which is chosen with a trade-off curve. We use Pylith (*Aagaard et al.*, 2013) to compute the Green's functions for this inversion as well as for the remaining inversions in this paper.

Our coseismic slip and afterslip solutions are shown in Figure 3.6. Similar to *Rollins et al.*

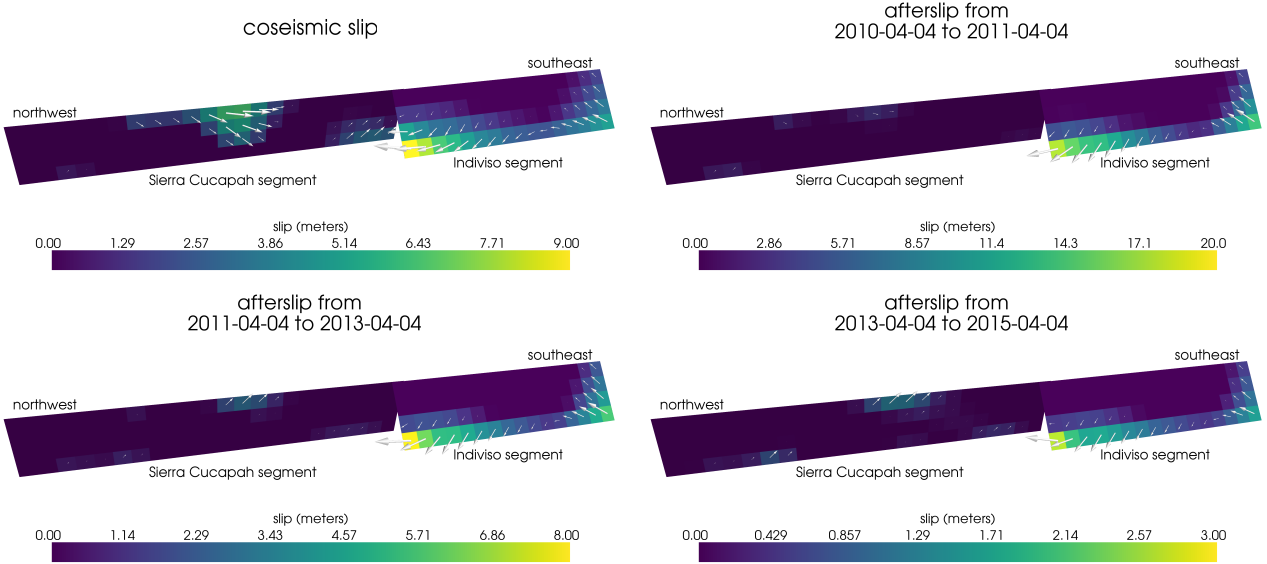


Figure 3.6: Coseismic slip and cumulative afterslip over the indicated time intervals when assuming the crust and mantle are elastic. Color indicates the magnitude of slip and arrows indicate the motion of the hanging wall.

(2015), we find that a large amount of afterslip on the Indiviso fault segment is required to explain the observations. The potency of our inferred coseismic slip is  $3.2 \times 10^9 \text{ m}^3$ , equivalent to a  $\text{Mw}=7.28$  earthquake when assuming a shear modulus of 32 GPa. The potency of our inferred cumulative five years of afterslip is  $6.1 \times 10^9 \text{ m}^3$ , equivalent to a  $\text{Mw}=7.46$  earthquake, which is unrealistically large if we consider afterslip to be driven by coseismically induced stresses. Figure 3.7 shows the time series for the observed and predicted postseismic displacements at stations along the El Mayor-Cucapah P-axis. We show the radial component of displacements with respect to the El Mayor-Cucapah epicenter and we also rescale the displacements so that the difference between the minimum and maximum observed displacements are the same for each station. Our elastic slip model accurately describes near-field postseismic deformation and systematically underestimates postseismic deformation at epicentral distances  $\gtrsim 150 \text{ km}$ . When the fault segments used in the inversion are extended down to 30 km depth, rather than 15 km, the systematic far-field residuals are smaller but remain apparent. Because an elastic model requires an unrealistic amount of afterslip and is unable to predict far-field deformation, we move on to consider viscoelastic models in the next section.

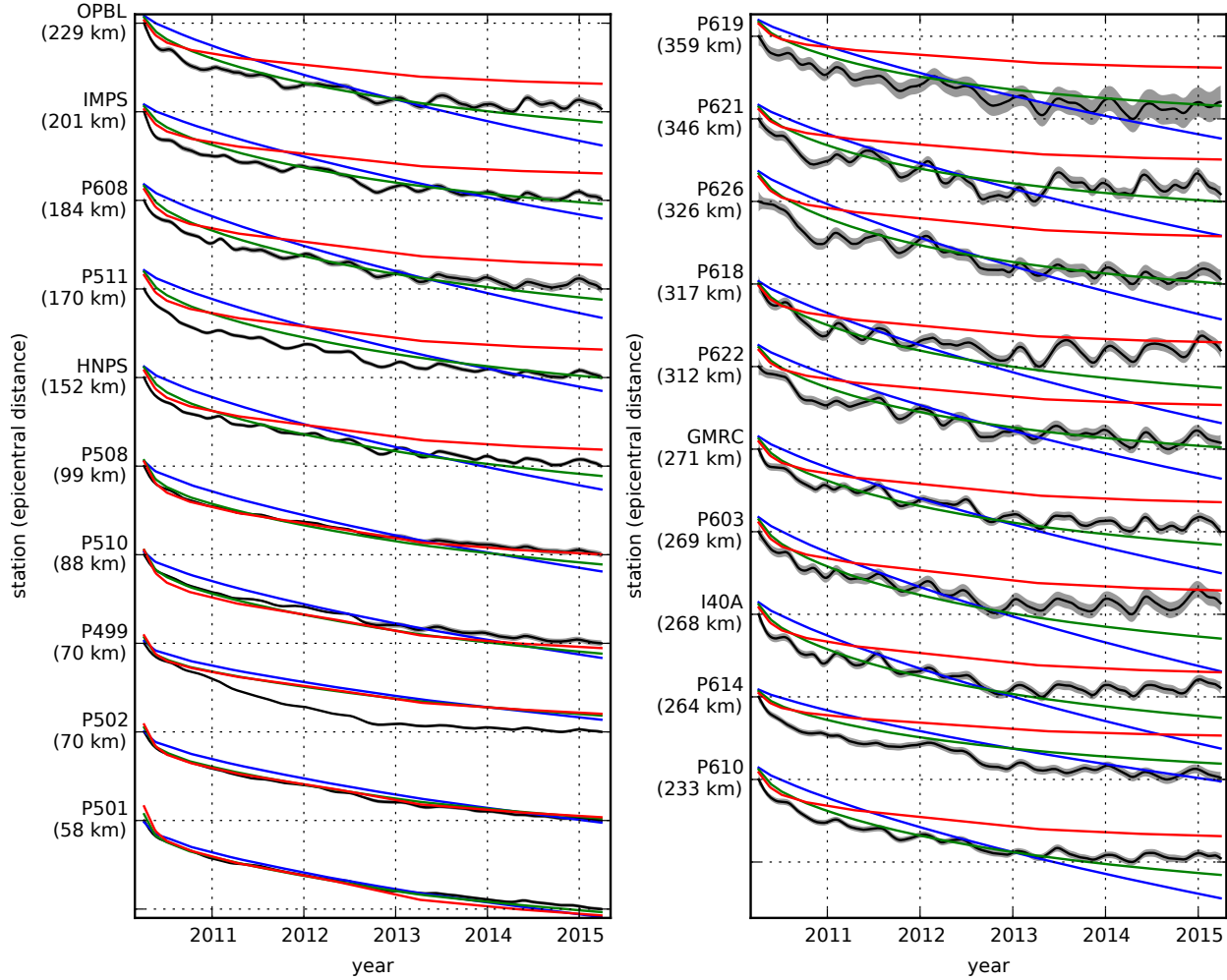


Figure 3.7: Scaled radial component of postseismic displacements. Downward motion indicates that the station is moving toward the El Mayor-Cucapah epicenter. Displacement time series are scaled so that the minimum and maximum observed values lie on the grid lines. The observed postseismic displacements,  $u_{\text{post}}$  are shown in black with gray indicating the 68% confidence interval. The displacements predicted by the best fitting elastic model are shown in red. The blue and green lines are the predicted postseismic displacements for the models discussed in Section 3.4.3. The blue lines show the predicted displacements for the model with a Maxwell viscoelastic lower crust and upper mantle. The green line shows the predicted displacements for our preferred model, which has a Maxwell viscoelastic lower crust and a Zener viscoelastic upper mantle. The effective viscosities are the same for both models and are shown in Figure 3.12.

Maxwell	$\mu \quad \eta_M$
$\eta_{\text{eff}} = \eta_M$	
Zener	$\mu \quad \mu_K$
$\eta_{\text{eff}} = \eta_K$	
Burgers	$\mu \quad \mu_K \quad \eta_M$
$\eta_{\text{eff}} = (1/\eta_M + 1/\eta_K)^{-1}$	
General Kelvin	$\mu \quad \mu_{K_1} \quad \mu_{K_N} \quad \eta_M$
$\eta_{\text{eff}} = (1/\eta_M + 1/\eta_{K_1} + \dots + 1/\eta_{K_N})^{-1}$	

Figure 3.8: Schematic illustration of the rheologic models considered in this paper as well as their effective viscosities.

### 3.4.2 Early postseismic inversion

For any linear viscoelastic rheology of the crust and mantle, postseismic displacements resulting from time dependent fault slip can be described as

$$u_{\text{pred}}(x, t) = \int_F s(\xi, t) g(x, \xi) d\xi + \int_0^t \int_F s(\xi, \tau) f(t - \tau, x, \xi) d\xi d\tau, \quad (3.11)$$

where  $f(t, x, \xi)$  describes the time-dependent velocity at  $x$  resulting from viscoelastic relaxation of stresses induced by slip at  $\xi$ .  $f$  is a function of  $\lambda$ ,  $\mu$ , and any additional rheologic parameters controlling the viscoelastic response, which are generally not well known. Schematic representations of the viscoelastic rheologic models considered in this study are shown in Figure 3.8. We discuss these rheologic models and their use in geophysical studies in Section 3.5.

In order to greatly simplify the inverse problem, we use the method described in *Hines and Hetland* (2015) to constrain an initial effective viscosity structure from the early postseismic deformation. Our method uses the fact that coseismic stresses throughout the crust and upper mantle depend on the instantaneous elastic parameters and are independent of the viscoelastic parameters which we wish to estimate. Immediately following an earthquake, each parcel will have a strain rate that is proportional to the coseismic stress and inversely proportional to the parcel's effective viscosity,  $\eta_{\text{eff}}$ . Using one-dimensional rheologic models, we define the effective viscosity as

$$\eta_{\text{eff}} = \left. \frac{\sigma}{\dot{\varepsilon}} \right|_{t=0}, \quad (3.12)$$

where  $\sigma$  is an applied stress at  $t = 0$  and  $\dot{\varepsilon}$  is the resulting strain rate. Figure 3.8 shows how

$\eta_{\text{eff}}$  relates to the parameters for various linear viscoelastic rheologies. We can deduce that the initial rate of surface deformation resulting from viscoelastic relaxation is a summation of the surface deformation resulting from relaxation in each parcel, scaled by the reciprocal of the parcel's effective viscosity. That is to say

$$f(0, x, \xi) = \int_L \frac{h(x, \xi, \zeta)}{\eta_{\text{eff}}(\zeta)} d\zeta, \quad (3.13)$$

where  $L$  denotes the crust and mantle and  $h(x, \xi, \zeta)$  describes the initial rate of deformation resulting from viscoelastic relaxation at  $\zeta$  induced by slip at  $\xi$ . We can combine eq. (3.13) with eq. (3.11) to get a first-order approximation for early postseismic deformation,

$$u_{\text{pred}}(x, t) \approx \int_F s(\xi, t) g(x, \xi) d\xi + \int_0^t \int_F \int_L \frac{s(\tau, \xi)}{\eta_{\text{eff}}(\zeta)} h(x, \xi, \zeta) d\zeta d\xi d\tau, \quad (3.14)$$

which is valid for as long as the rate of deformation resulting from viscoelastic relaxation is approximately constant. Although eq. (3.14) may only be valid for a short portion of the postseismic period, its utility becomes apparent when noting that  $g$  and  $h$  are only functions of the fault geometry and instantaneous elastic properties,  $\lambda$  and  $\mu$ , and thus  $g$  and  $h$  can be computed numerically as a preprocessing step. The forward problem in eq. (3.14) can then be rapidly evaluated for any realization of  $s$  and  $\eta_{\text{eff}}$ . This is in contrast to evaluating the full forward problem, eq. (3.11), numerically for each realization of  $s$  and the unknown rheologic properties.

Details on how eq. (3.14) is used to estimate  $s$  and  $\eta_{\text{eff}}$  from postseismic deformation can be found in *Hines and Hetland* (2015). A non-linear Kalman filter based inverse method can also be used to estimate  $s$  and  $\eta_{\text{eff}}$  in a manner similar to *Segall and Mathews* (1997) or *McGuire and Segall* (2003), in which we would not have to explicitly impose a time dependent parametrization of  $s$ . We have thoroughly explored Kalman filter based approaches, but we ultimately prefer the method described in *Hines and Hetland* (2015) because of its relative simplicity. Moreover, we believe the piecewise continuous representation of slip with respect to time is sufficiently general for the resolving power of these GPS data.

We estimate coseismic slip and afterslip with the same spatial and temporal discretization as in Section 3.4.1. Simultaneously, we estimate  $\eta_{\text{eff}}$  within six vertically stratified layers which have depths ranging from 15-30 km, 30-60 km, 60-90 km, 90-120 km, 120-150 km, and from 150 km to the bottom of our numerical model domain at 800 km. We again restrict fault slip to occur between 0 and 15 km depth, which is done in order to help eliminate inevitable non-uniqueness in the inversion. It is well understood that fault slip at sufficiently great depths can produce surface deformation that is indistinguishable from viscoelastic

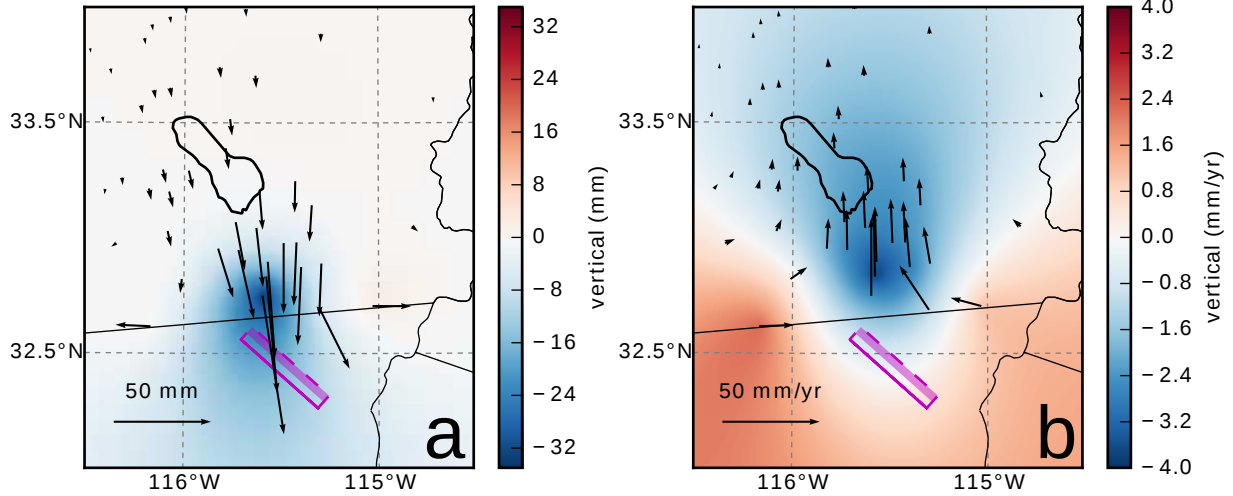


Figure 3.9: Displacements resulting from fault slip at lower crustal depths (a), and initial velocities resulting from subsequent relaxation of a viscoelastic lower crust (b). The fault segment dips  $75^\circ$  to the north-east and its surface projection is outlined in magenta. The highlighted area on the fault extends from 15 to 30 km depth and indicates where 1 meter of right-lateral slip was imposed. The elastic properties of the crust and mantle are the same as in Table 1, and  $\eta_{\text{eff}}$  is  $10^{18}$  Pa s in the lower crust. Vertical displacements are interpolated between station locations.

relaxation, at least in two-dimensional earthquake models (Savage, 1990). Additionally, we note that when simultaneously estimating both afterslip and viscosity in the lower crust, the inverse problem becomes particularly ill-posed. This ill-posedness is illustrated in Figure 3.9, which shows the displacements resulting from a meter of slip on a fault extending from 15 to 30 km depth and the initial velocity resulting from subsequent viscoelastic relaxation in the lower crust, which is given a viscosity of  $10^{18}$  Pa s. In this demonstration, the viscoelastic relaxation is entirely driven by the fault slip in the lower crust. The horizontal displacements from fault slip are in the opposite direction as the displacements resulting from viscoelastic relaxation. This means that surface displacements resulting from afterslip at lower crustal depths can be cancelled out, at least partially, by a low viscosity lower crust. We eliminate this null space by allowing only one mechanism in the lower crust, which we choose to be viscoelastic relaxation. This is not to say that we do not believe deep afterslip is a possibility; rather, we restrict slip to seismogenic depths as a modeling necessity. Although, it has been noted that the pattern of vertical postseismic deformation following the El Mayor-Cucpah earthquake indicates that a significant amount of afterslip must be shallow (Rollins *et al.*, 2015).

We must determine at which point the early postseismic approximation breaks down, which we will denote as  $t_{\text{bd}}$ . As noted, eq. (3.14) is valid for as long as the rate of deformation resulting from viscoelastic relaxation is approximately constant. We can almost certainly assume that deformation at the most far-field stations, which are  $\sim 400$  km away from the El

Mayor-Cucapah epicenter, is the result of viscoelastic relaxation. The approximation should then be valid for as long as a linear trend adequately approximates the far-field deformation. Using this logic, it would appear that  $t_{bd}$  is about one year after the El Mayor-Cucapah earthquake. Another way to determine  $t_{bd}$  is to find the best fitting prediction of eq. (3.14) to observed deformation using increasing durations of the postseismic time series.  $t_{bd}$  should be the point when eq. (3.14) is no longer capable of describing the observed deformation without incurring systematic misfits. When using eq. (3.14) to fit the entire five years of postseismic displacements, we see that the near-field displacements (e.g., station P501) are accurately predicted. When looking at displacements in the far-field (e.g., station P621), we see that eq. (3.14) overestimates the rate of deformation in the later postseismic period and underestimates the rate of deformation in the early period (Figure 3.10). Due to the low signal-to-noise ratios for far-field stations, it is difficult to determine at what point eq. (3.14) is no longer able to predict the observed displacements; however, we settle on  $t_{bd} = 0.8$  years after the earthquake, while acknowledging that the choice is subjective. As noted in *Hines and Hetland* (2015), overestimating  $t_{bd}$  will result in a bias towards overestimating  $\eta_{eff}$ , while picking a  $t_{bd}$  which is too low will not necessarily result in a biased estimate of  $\eta_{eff}$ , although the uncertainties would be larger. We can then consider inferences of  $\eta_{eff}$  to be an upper bound on the viscosity needed to describe the far-field rate of deformation during the first 0.8 years of postseismic deformation.

We estimate coseismic slip, afterslip, and effective viscosities by solving

$$\min_{s, \eta_{eff}} \left( \left\| \frac{u_{pred}(s, \eta_{eff}) - u_{post}}{\sigma_{post}} \right\|_2^2 + \lambda_s \|s\|_2^2 + \lambda_\eta \|\nabla \eta_{eff}^{-1}\|_2^2 \right), \quad (3.15)$$

where  $u_{post}$  consists of the first 0.8 years of postseismic deformation and  $u_{pred}$  are the predicted displacements from eq. (3.14). Due to inherent non-uniqueness, we have added zeroth-order Tikhonov regularization to estimates of  $s$  and second-order Tikhonov regularization to estimates of effective fluidity  $\eta_{eff}^{-1}$ . The degree to which we impose the regularization on slip and fluidity is controlled by the penalty parameters  $\lambda_s$  and  $\lambda_\eta$ , which are chosen with trade-off curves (Figure 3.15). Our goal is to get a prior constraint on  $\eta_{eff}$  to minimize the amount of searching we have to do when describing the postseismic deformation over the full five years, which we do in Section 3.4.3. Estimates of  $s$  made here will not be used in Section 3.4.3, and so the motivation behind adding regularization to  $s$  is to ensure that the slip driving viscoelastic relaxation in eq. (3.14) is sensible.

Our initial estimate for coseismic slip and cumulative afterslip over the first 0.8 years after the El Mayor-Cucapah earthquake are shown in Figure 3.11. Similar to our elastic slip model from Section 3.4.1, a significant amount of right-lateral and normal coseismic

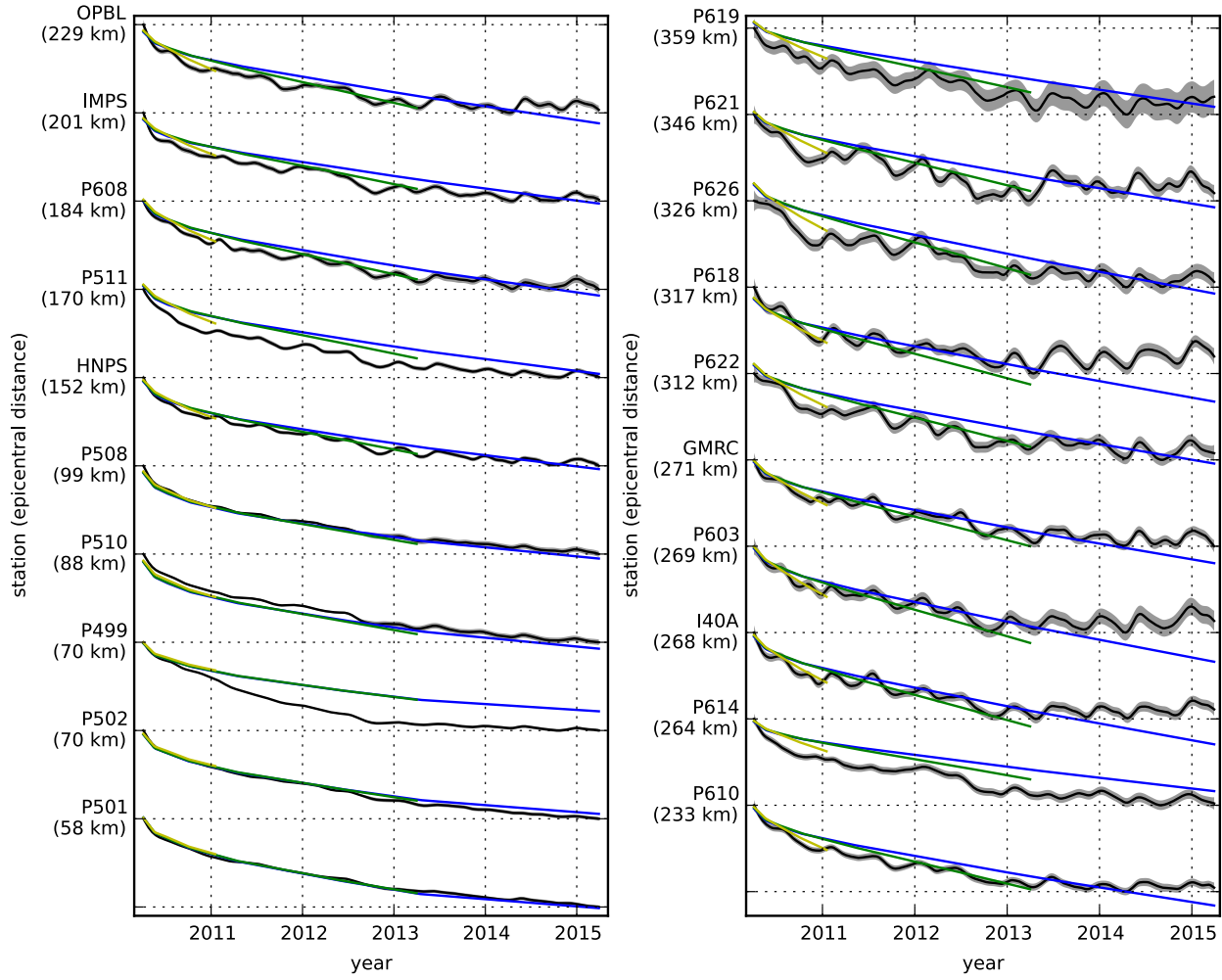


Figure 3.10: Observed postseismic displacements (black) and best fitting predictions of eq. (3.14) to 5.0 (blue), 3.0 (green), and 0.8 (yellow) years of the postseismic data.

slip is inferred to be on the Sierra Cucapah segment. Our coseismic slip solution on the Sierra Cucapah segment is consistent with field studies (*Fletcher et al.*, 2014) and the model from *Wei et al.* (2011b). Our inferred slip on the Indiviso fault segment differs from *Wei et al.* (2011b) because the GPS data used in this study is not capable of resolving the spatial distribution of fault slip on that segment (Figure 3.16). The potency of inferred coseismic slip is  $3.3 \times 10^9 \text{ m}^3$ , which is also about the same as that inferred from Section 3.4.1. The present inference of afterslip on the Indiviso fault is significantly less than what was found in the Section 3.4.1 where we did not account for viscoelasticity. When fault slip is simultaneously estimated with viscosity, the potency of inferred afterslip over the first 0.8 years after the earthquake is  $0.85 \times 10^9 \text{ m}^3$ , compared to  $3.5 \times 10^9 \text{ m}^3$  when we assume the crust and upper mantle are elastic. The significant amount of afterslip inferred on the Indiviso fault in Section 3.4.1 seems to be compensating for unmodeled viscoelastic relaxation. The fact that there is still an appreciable amount of afterslip inferred on the Indiviso fault raises the question of whether it is compensating for viscoelastic relaxation that is more localized than what we allow for since we only estimate depth dependent variations in viscosity.

Our estimated effective viscosities, and corresponding fluidities, are shown in Figure 3.12. Although fluidity is rarely used in geophysical literature, eq. (3.13) is linear with respect to fluidity and so the fluidity indicates the amplitude of the viscoelastic signal coming from each layer. We use bootstrapping to find the 95% confidence intervals for our estimated effective viscosities which are shown as shaded regions in Figure 3.12. It is important to remember that the presented effective viscosities were estimated with a smoothing regularization constraint and so the uncertainties are almost certainly underestimated (*Aster et al.*, 2011). Indeed, many viscosity profiles which are outside of the shown confidence intervals can just as adequately described the first 0.8 years of postseismic deformation. Our solution in Figure 3.12 should be interpreted as the smoothest effective viscosity profile which is capable of describing the data. This means that any sharp viscosity transitions will be tapered out in the inversion, which we demonstrate with a synthetic test in Figure 3.16. Nonetheless, a robust feature that we see with a variety of choices for  $\lambda_s$ ,  $\lambda_\eta$ , and  $t_{\text{bd}}$  is that the largest jump in fluidity is at 60 km depth, which is consistent with the range of lithosphere–asthenosphere boundary depths inferred by *Lekic et al.* (2011). This transitional depth is also consistent with the the viscosity structure required to explain far-field postseismic deformation following the Hector Mine earthquake (*Freed et al.*, 2007). We find that the viscosity below 60 km depth needs to be  $\sim 1 \times 10^{18} \text{ Pa s}$  to describe the early rate of postseismic deformation at far-field stations while the lower crust and uppermost mantle need to be relatively stronger. The viscosity of the lower crust has the largest uncertainties because there is no evidence of relaxation in that layer, meaning that it is effectively elastic over the first 0.8 years after the

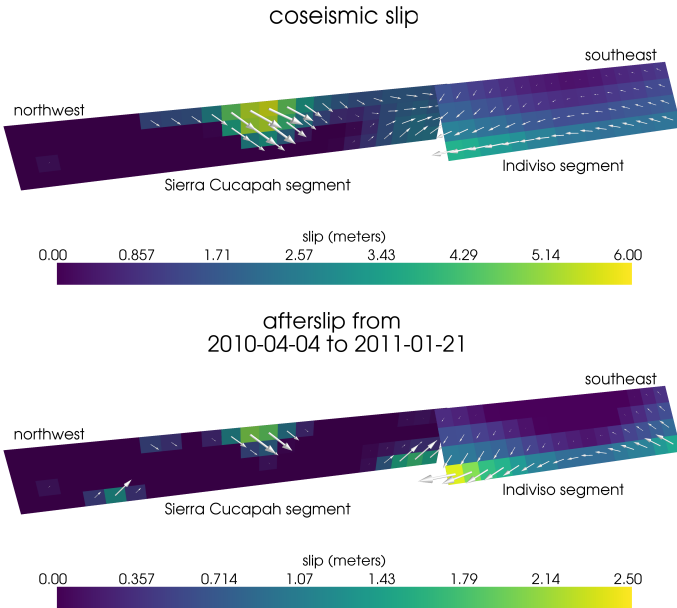


Figure 3.11: Coseismic slip and afterslip inferred by fitting eq. (3.14) to the first 0.8 years of postseismic displacements.

earthquake.

### 3.4.3 Full postseismic inversion

In the previous section, we used the inverse method from *Hines and Hetland* (2015) to constrain the effective viscosity structure required to explain the first 0.8 years of postseismic deformation. In this section, we use these effective viscosities as a prior constraint when searching for models which are capable of describing the available five years of postseismic data, where our forward problem is now eq. (3.11) rather than the approximation given by eq. (3.14). We perform a series of fault slip inversions assuming a variety of rheologies for the lower crust and upper mantle which are consistent with our findings from Section 3.4.2. We appraise each model using the mean chi-squared value,

$$\bar{\chi}^2 = \frac{1}{N} \left\| \frac{u_{\text{pred}} - u_{\text{post}}}{\sigma_{\text{post}}} \right\|_2^2, \quad (3.16)$$

where  $N$  is the number of observations.

We first assume that the crust and mantle can be described with a Maxwell rheology, and we set the steady-state viscosity,  $\eta_M$ , equal to our inference of  $\eta_{\text{eff}}$ . We compute  $f$  and  $g$  from eq. (3.11) using Pylith, and we use the same spatial and temporal discretization of  $s$  as in Sections 3.4.1 and 3.4.2. We estimate  $s$  using linear least squares and find a misfit of

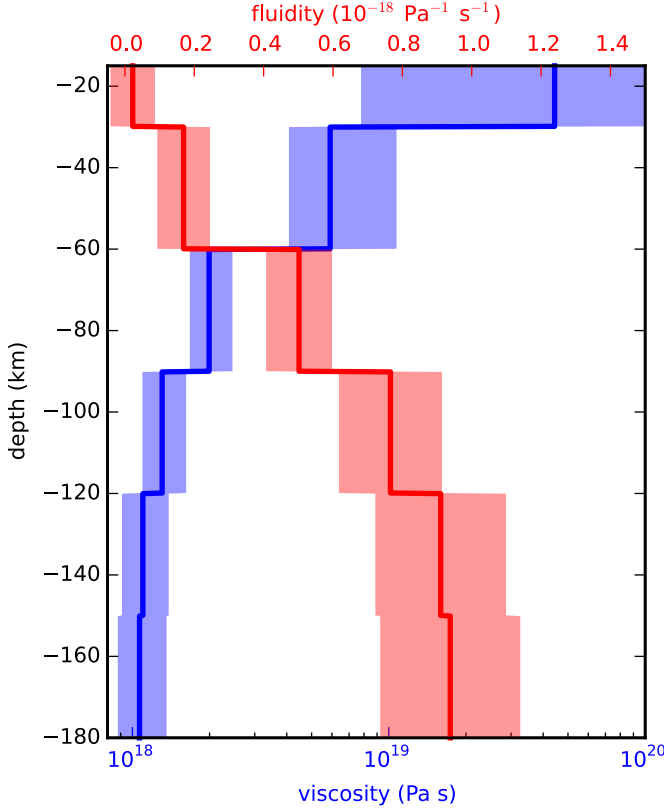


Figure 3.12: Effective viscosities and associated fluidities inferred by fitting eq. (3.14) to the first 0.8 years of postseismic displacements. 95% confidence intervals, estimated from bootstrapping, are indicated by shaded regions.

$\bar{\chi}^2 = 37.4$ . For comparison,  $\bar{\chi}^2 = 35.3$  for the elastic model from Section 3.4.1. The Maxwell viscoelastic model has a larger misfit because it tends to overestimate the rate of deformation after about three years (Figure 3.7). Since our initial estimates of  $\eta_{\text{eff}}$  may be biased towards overestimating viscosities, we have also performed the slip inversion where we use uniformly lower viscosities in the crust and mantle; however, decreasing the viscosity only increases the misfit. Although, the viscosities used here are consistent with the successful Maxwell viscoelastic models found by *Rollins et al.* (2015) and *Spinler et al.* (2015), which had mantle viscosities on the order of  $10^{18}$  Pa s and relatively higher lower crustal viscosities, we find that such a model is incapable of describing the entire postseismic time series. *Pollitz et al.* (2001) similarly recognized this deficiency in a Maxwell rheology, which then motivated their exploration of a Burgers rheology upper mantle (*Pollitz*, 2003).

Instead of exploring a Burgers rheology mantle, which introduces two new parameters that need to be estimated, the transient viscosity,  $\eta_K$ , and transient shear modulus,  $\mu_K$ , we first consider a Zener rheology for the mantle, which only introduces one unknown model parameter,  $\mu_K$ . We assume that the lower crust still has a Maxwell rheology. The steady-state viscosity in the crust and the transient viscosity in the mantle are set equal to the

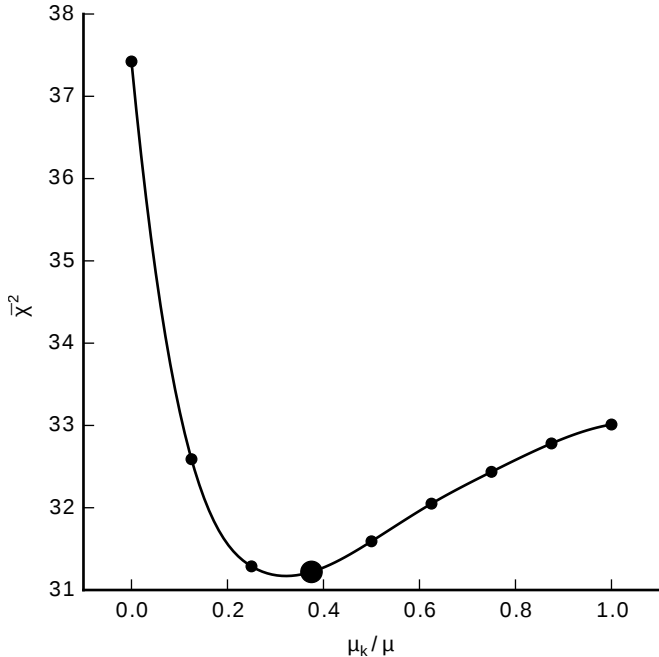


Figure 3.13: Mean chi-squared value as a function of the transient shear modulus relative to the elastic shear modulus in a Zener rheology upper mantle. Large dot indicates our preferred ratio.

inferred effective viscosities. We then estimate the ratio of shear moduli,  $\frac{\mu_K}{\mu}$ . We compute nine different sets of Green's functions,  $f$  and  $g$ , where we assume values of  $\frac{\mu_K}{\mu}$  ranging from 0 to 1. The former being a degenerate case where the Zener model reduces to the above Maxwell model. We estimate coseismic slip and afterslip for each realization of  $\frac{\mu_K}{\mu}$ . We find that a shear moduli ratio of 0.375 yields the best prediction to the observed postseismic displacements with a misfit of  $\bar{\chi}^2 = 31.2$  (Figure 3.13). The improvement in the Zener model over the Maxwell model can be seen in the fit to the far-field data (Figure 3.7) where the Zener model does a significantly better job at explaining the transient rate of deformation throughout the five years considered in this study. The rheologic parameters for our preferred Zener model are summarized in Table 1.

Because we are able to adequately describe the available five years of postseismic deformation with a Zener model, we do not find it necessary to explore the parameter space for a more complicated Burgers rheology. However, since the Zener model is a Burgers model with an infinite steady-state viscosity, we can conclude that any Burgers rheology that has a transient viscosity consistent with that found in Section 3.4.2 and a steady-state viscosity  $\gtrsim 10^{20}$  Pa s, which is effectively infinite on the time scale of five years, would also be able to satisfactorily describe the observable postseismic deformation.

The regularized inference of coseismic slip and afterslip for our preferred Zener model is shown in Figure 3.14. The inferred coseismic potency is  $3.0 \times 10^9$  m<sup>3</sup>, equivalent to a

Mw=7.26 earthquake, where most of the slip is shallow and on the Sierra Cucapah fault segment. The potency of five years of afterslip is  $1.1 \times 10^9$  m<sup>3</sup>. Most of the afterslip in our preferred model occurs within the first year after the earthquake and coincides with the location of our inferred coseismic slip. Inferred afterslip within the first year is accounting for the most rapid near-field transient deformation (Figure 3.17). After one year, afterslip is inferred to be deeper down on the Sierra Cucapah segment. The sustained near-field postseismic deformation is being explained by this continued afterslip as well as viscoelastic relaxation in the lower crust. We emphasize, that the GPS station closest to where we infer afterslip, P496, is still about 30 km away, which is too far for us to conclusively discern deep afterslip from viscoelastic relaxation in the lower crust. The deep afterslip inferred after one year could potentially be compensating for an overestimated lower crustal viscosity. To test this, we have modified our preferred model by decreasing the lower crustal viscosity from  $5.91 \times 10^{19}$  Pa s to  $1 \times 10^{19}$  Pa s, which is still consistent with our viscosity inference from Section 3.4.2, and we inverted for fault slip. We find that a model with a weaker lower crust adequately describes the postseismic displacements without any afterslip after one year, while still requiring about the same amount of afterslip over the first year. We do believe that the early afterslip on the Sierra Cucapah segment is a robust feature in our preferred model, while we are not confident in our inference of later deep afterslip.

The postseismic displacements predicted by our preferred Zener model are shown in Figures 3.4, 3.5 and 3.7. The largest misfit occur within the Imperial Valley where there does not appear to be any systematic trend in the residuals. This suggests that the large errors are due to localized processes such as fault slip in the Imperial Valley triggered by the El Mayor-Cucapah earthquake (*Wei et al.*, 2011a, 2015). We do not see any pattern in the residuals that would suggest a laterally heterogeneous viscosity structure, which has been explored by *Pollitz et al.* (2012) and *Rollins et al.* (2015). We do notice regional scale seasonal oscillations in the lateral and vertical components of the residuals with an amplitude of 1-2 millimeters. This is the result of our method for data processing which is not able to completely remove the seasonal signal in the GPS data, which was discussed in Section 3.3. Additionally, we see systematic misfit in the later postseismic period west of the Landers and Hector Mine earthquakes, which may be the result of unmodeled postseismic deformation following those earthquakes. Lastly, there are clear discrepancies between the observed and predicted vertical displacements following the first year after the El Mayor-Cucapah earthquake. We observe a broad uplift throughout Southern California which is inconsistent with any postseismic model.

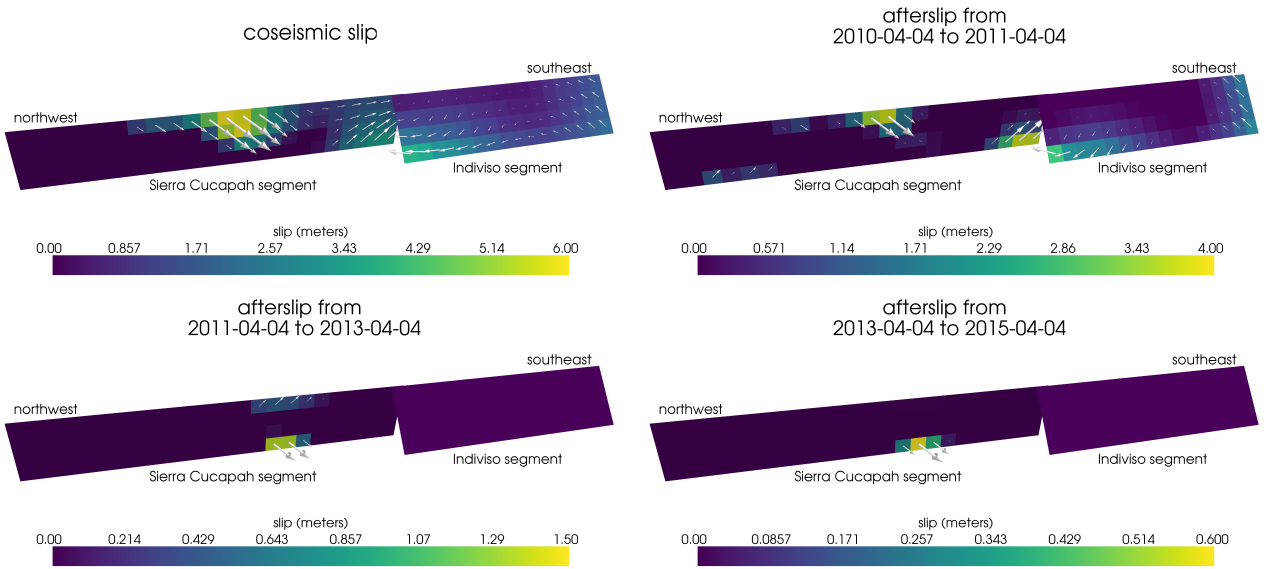


Figure 3.14: Inferred coseismic slip and afterslip for our preferred model, which has a Maxwell rheology in the lower crust and a Zener rheology in the upper mantle. The transient viscosity,  $\eta_K$ , in the mantle and steady-state viscosity,  $\eta_M$ , in the crust are set equal to the effective viscosities from Figure 3.12. We use  $\frac{\mu_K}{\mu} = 0.375$  in the upper mantle.

### 3.5 Discussion

It has long been recognized that deep afterslip and viscoelastic relaxation following an upper crustal earthquake can result in similar horizontal ground deformation at the surface (e.g., *Savage*, 1990; *Pollitz et al.*, 2001; *Hearn*, 2003; *Feigl and Thatcher*, 2006). The similarity of the horizontal postseismic deformation results in a non-uniqueness in inferences of afterslip or viscoelastic relaxation. The spatial pattern of vertical postseismic deformation has been proposed to be a discriminant between deep afterslip and viscoelastic relaxation (e.g., *Pollitz et al.*, 2001; *Hearn*, 2003). It is, however, important to note that patterns of vertical deformation are very sensitive to the depth-dependence of viscosity below the upper crust (*Yang and Toksöz*, 1981; *Hetland and Zhang*, 2014). The similarity between deformation resulting from deep afterslip and viscoelastic relaxation of coseismic stresses is different from the ill-posedness described in Section 3.4.2. In our method, any inferred afterslip will also mechanically drive additional viscoelastic relaxation. The horizontal deformation resulting from deep afterslip will generally be in the opposite direction as horizontal deformation resulting from viscoelastic relaxation of subsequent stresses in the lower crust (Figure 3.9). As a result, there is a trade-off between inferences of deep afterslip and lower crustal viscosity. In our synthetic tests in *Hines and Hetland* (2015), we have found that inverting surface deformation for afterslip and viscosity within the same depth interval tends to result in overestimated afterslip and an underestimated viscosity.

Most postseismic studies assume Maxwell viscoelasticity in the lower crust and upper mantle (e.g., *Nur and Mavko*, 1974; *Pollitz et al.*, 2000; *Hetland*, 2003; *Freed et al.*, 2006b; *Johnson et al.*, 2009; *Hearn et al.*, 2009), which is the simplest viscoelastic rheologic model. In Southern California, postseismic studies following the Landers (*Pollitz et al.*, 2000), Hector Mine (*Pollitz et al.*, 2001), and El Mayor-Cucapah earthquake (*Spinler et al.*, 2015; *Rollins et al.*, 2015), have assumed Maxwell viscoelasticity in the lower crust and upper mantle and have inferred upper mantle viscosities on the order of  $10^{17}$  to  $10^{18}$  Pa s and lower crust viscosities  $\gtrsim 10^{19}$  Pa s. These postseismic studies are consistent with *Kaufmann and Amelung* (2000) and *Cavalié et al.* (2007), who found that an upper mantle viscosity of  $10^{18}$  Pa s and a crustal viscosity  $\gtrsim 10^{20}$  Pa s are necessary to describe subsidence resulting from changes in loading from Lake Mead. This isostatic adjustment is a process with similar spatial and temporal scales as postseismic deformation, and thus the inferred viscosities of these two types of studies would likely agree. While these studies found viscosities that are consistent with our effective viscosities from Section 3.4.2, they are inconsistent with viscosity estimates made from geophysical processes that occur over longer time scales. For example, *Lundgren et al.* (2009) found that lower crust and upper mantle viscosities on the order of  $10^{21}$  and  $10^{19}$  Pa s, respectively, are needed to describe interseismic deformation along the Southern San Andreas fault zone in the Salton Sea region. An even higher mantle viscosity, on the order of  $10^{20}$  Pa s, is required to describe isostatic adjustment resulting from the draining of Lake Bonneville, which occurs on the time scales of  $10^4$  years (*Crittenden*, 1967; *Bills and May*, 1987).

An additional deficiency with the Maxwell rheology is that it predicts a steady decay in the rate of postseismic deformation over time, which fails to describe the commonly observed rapid, early transience followed by a relatively steady rate of postseismic deformation. One could explain the early transient postseismic deformation with fault creep and the later phase with relaxation in a Maxwell viscoelastic lower crust and upper mantle (e.g. *Hearn et al.*, 2009; *Johnson et al.*, 2009). However, postseismic deformation at distances greater than  $\sim 200$  km from the El Mayor-Cucapah epicenter can only be attributed to viscoelastic relaxation (e.g., *Freed et al.*, 2007) and we have demonstrated that the far-field deformation cannot be explained with a Maxwell rheology (Figure 3.7).

We found that a Zener rheology in the upper mantle with a transient viscosity of  $\sim 10^{18}$  Pa s does a noticeably better job at predicting far-field postseismic deformation. A generalization of the Zener viscoelastic model, schematically represented as several Kelvin elements connected in series, is commonly used to describe seismic attenuation (*Liu et al.*, 1976). The highest viscosity needed to describe seismic attenuation is on the order of  $10^{16}$  Pa s (*Yuen and Peltier*, 1982) which has a characteristic relaxation time on the order of days. Even though

our inferred transient viscosity is orders of magnitude larger than that required for seismic attenuation models, the two models are not incompatible. Rather, the delayed elasticity in seismic attenuation models occurs on such short time scales that it can be considered part of the instantaneous elastic phase of deformation associated with the preferred Zener model in this study.

Of course, a Zener rheology provides an incomplete description of the asthenosphere because it does not have the fluid-like behavior required to explain isostatic rebound or convection in the mantle (*O'Connell*, 1971). *Yuen and Peltier* (1982) proposed a Burgers rheology with a low transient viscosity ( $\eta_K \approx 10^{16}$  Pa s) and high steady-state viscosity ( $\eta_M \approx 10^{21}$  Pa s) to describe both seismic attenuation and long term geologic processes. The justification of a Burger's rheology mantle is further supported by laboratory experiments on olivine (*Chopra*, 1997). *Pollitz* (2003) sought to describe postseismic deformation following Hector Mine with a Burgers rheology mantle and they found a best fitting transient viscosity of  $1.6 \times 10^{17}$  Pa s and steady-state viscosity of  $4.6 \times 10^{18}$  Pa s. While the Burgers rheology was introduced as a means of bridging the gap between relaxation observed in long and short term geophysical processes, the inferred steady state viscosity from *Pollitz* (2003) is still inconsistent with the Maxwell viscosities inferred from studies on the earthquake cycle and Lake Bonneville. The transient viscosity inferred by *Pollitz* (2003) is constrained by the earliest phase of postseismic deformation following the Hector Mine earthquake. While *Pollitz* (2003) ruled out deep afterslip as an alternative mechanism based on inconsistent vertical deformation, it is still possible to successfully describe all components of early postseismic deformation following the Hector Mine earthquake with afterslip at seismogenic depths (*Jacobs et al.*, 2002). It is then possible that the preferred rheologic model from *Pollitz* (2003) was biased towards inferring a particularly low transient viscosity by neglecting to account for afterslip. This is in contrast to the present study, where we have inferred a viscosity structure simultaneously with afterslip. We also argue that a transient rheology is necessary to explain postseismic deformation; however, our preferred transient viscosity of  $\sim 10^{18}$  Pa s in the upper mantle is an order of magnitude larger than the transient viscosity found by *Pollitz* (2003). The transient viscosity inferred here is consistent with the results of *Pollitz* (2015), who reanalyzed postseismic data following the Landers and Hector Mine earthquake allowing the first few months of transient deformation to be described by afterslip. Since a Zener model is able to describe the available postseismic deformation following the El Mayor-Cucapah earthquake, any Burgers rheology with a steady-state viscosity that is  $\gtrsim 10^{20}$  Pa s, effectively infinite over five years, would also be able to describe the postseismic deformation. Such a Burgers model might then be consistent with the steady-state viscosities necessary for lake loading, interseismic deformation, and mantle dynamics.

### **3.6 Conclusion**

We have extracted a smoothed estimate of postseismic deformation following the El Mayor-Cucapah earthquake from GPS displacement time series. Our estimated postseismic deformation reveals far-field (epicentral distances  $\gtrsim 200$  km) transient deformation which is undetectable after about three years. Near-field deformation exhibits transience that decays to a sustained, elevated rate after about one or two years. We found that near-field transient deformation can be explained with shallow afterslip. The sustained rate of near-field deformation can be explained with viscoelastic relaxation in the lower crust and possibly continued afterslip. Far-field transient deformation can be more definitively ascribed to viscoelastic relaxation at depths greater than  $\sim 60$  km. Beneath that depth, a transient viscosity of  $\sim 1 \times 10^{18}$  Pa s is required to describe the rate of far-field deformation throughout the five years considered in this study. By describing the available postseismic deformation with a transient rheology in the mantle, our preferred model does not conflict with the generally higher steady-state viscosities inferred from geophysical processes occurring over longer time scales.

### **3.7 Acknowledgements**

We thank Andy Freed for an illuminating discussion on the data used in this study. We thank Fred Pollitz and an anonymous reviewer for comments that improved this manuscript. We also thank the editor, Martha Savage. This material is based on EarthScope Plate Boundary Observatory data services provided by UNAVCO through the GAGE Facility with support from the National Science Foundation (NSF) and National Aeronautics and Space Administration (NASA) under NSF Cooperative Agreement No. EAR-1261833. The data used in this study can be found at [www.unavco.org](http://www.unavco.org). This material is based upon work supported by the National Science Foundation under Grant Numbers EAR 1045372 and EAR 1245263.

### **3.8 Supporting information**

Figures 3.15 and 3.16 provide additional information about the inversion in Section 3.4 of the main text. Figures 3.17 and 3.18 show the predicted displacements, which have been decomposed into elastic and viscoelastic components, for the preferred model from Section 3.4.3.

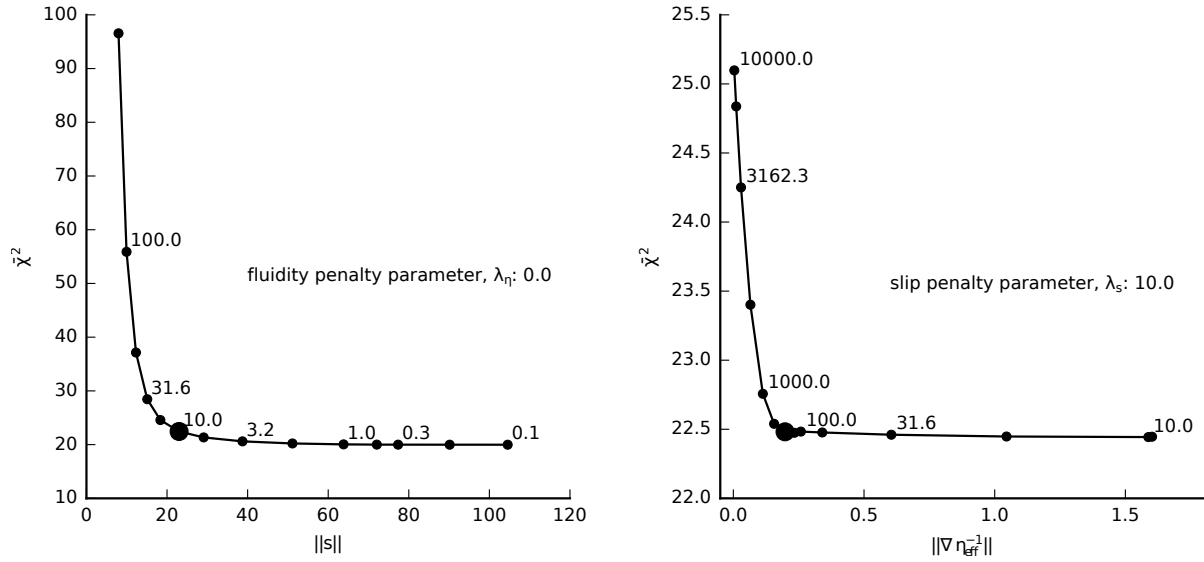


Figure 3.15: Trade-off curves used to determine the damping parameters  $\lambda_s$  and  $\lambda_\eta$  in eq. (15) of the main text. The left panel shows the trade-off curve for the fault slip penalty parameter,  $\lambda_s$ . We pick  $\lambda_s$  while keeping the penalty parameter for fluidity,  $\lambda_\eta$ , fixed at zero. The right panel shows the trade-off curve for selecting  $\lambda_\eta$ , where we fix  $\lambda_s$  at the chosen value from the left panel. Chosen values are indicated with the larger marker. When picking  $\lambda_s$ , we try to find a good balance between the mean chi-squared value,  $\bar{\chi}^2$ , and the size of the slip parameters,  $\|s\|$ . Our choice of  $\lambda_\eta$  is a balance between  $\bar{\chi}^2$  and the size of the Laplacian of fluidity,  $\|\nabla \eta_{\text{eff}}^{-1}\|$ .

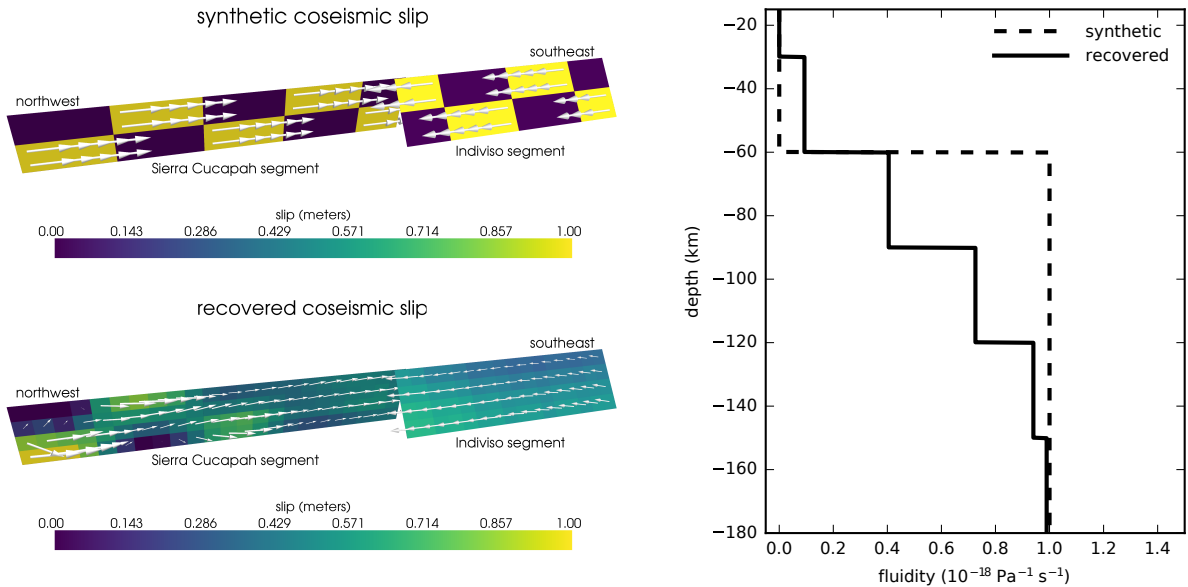


Figure 3.16: Checkerboard test used to assess the resolving power of the inversion in Section 3.4.2 of the main text. We create synthetic data at all of the GPS stations considered in this study by evaluating eq. (14) with the synthetic coseismic slip distribution and fluidity distributions. Our synthetic fluidity model has a jump from 0.0 to  $10^{-18} \text{ Pa}^{-1} \text{ s}^{-1}$  at 60 km depth. Our synthetic slip model does not include afterslip, although we estimate afterslip along with coseismic slip and fluidity in this test. We estimate these values in the same way as described in the main text and we also use the same penalty parameters. We do not add any noise to our synthetic data so that the recovered model just indicates how much the regularization influences the solution. Note that our ability to recover slip decreases towards the southern end of the fault, farthest from the available data. Also note that the smoothing constraint on fluidity largely obscures the jump in the synthetic model.

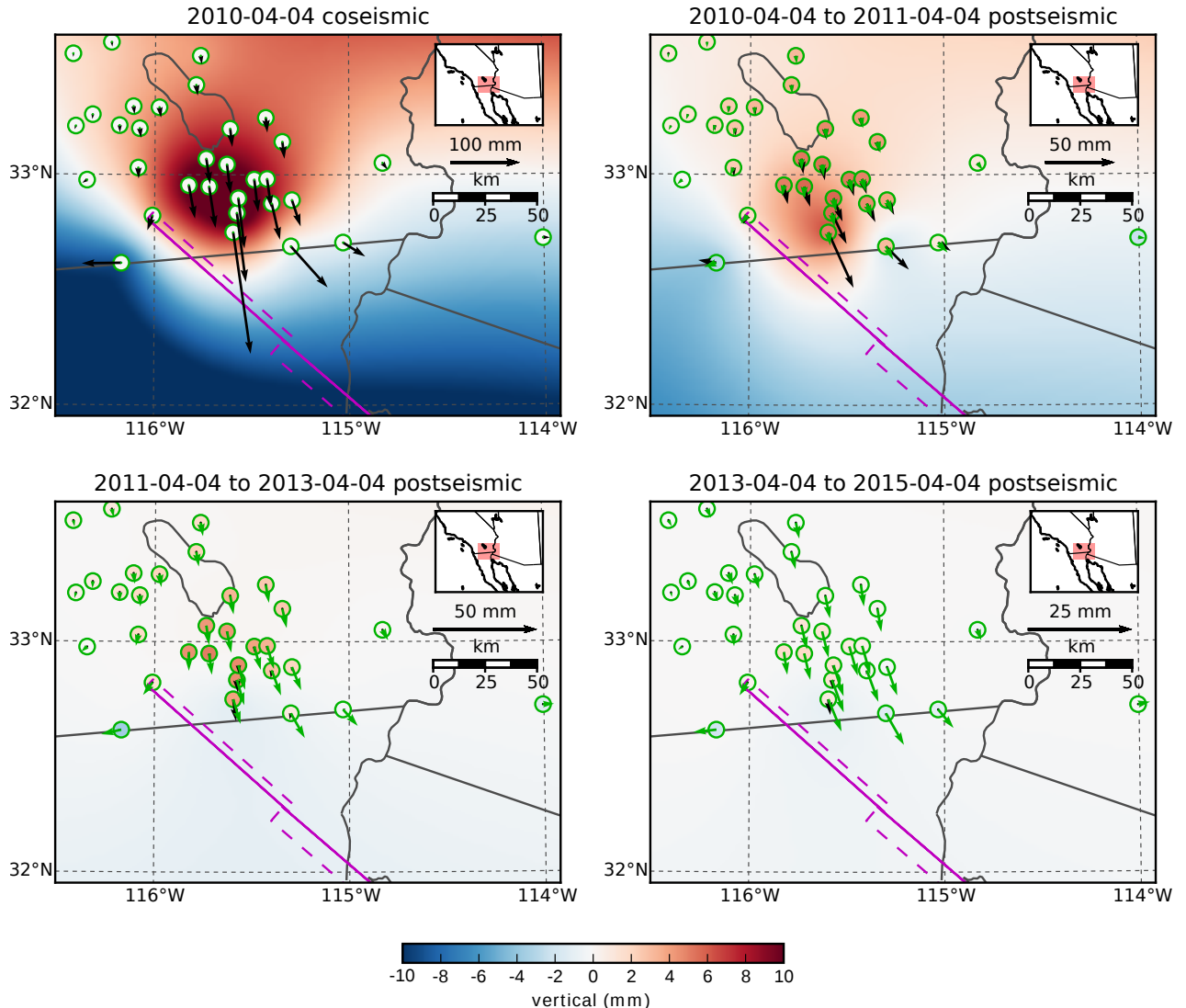


Figure 3.17: Elastic (black) and viscoelastic (green) components of the near-field predicted displacements for the preferred Zener model from Section 3.4.3. The elastic component is the deformation resulting from fault slip and the viscoelastic component is the deformation resulting from viscoelastic relaxation of stresses induced by the fault slip. The elastic and viscoelastic components are calculated from the first and second terms in eq. (11), respectively. The vertical elastic component is shown as an interpolated field and the vertical viscoelastic component is shown within the green circles.

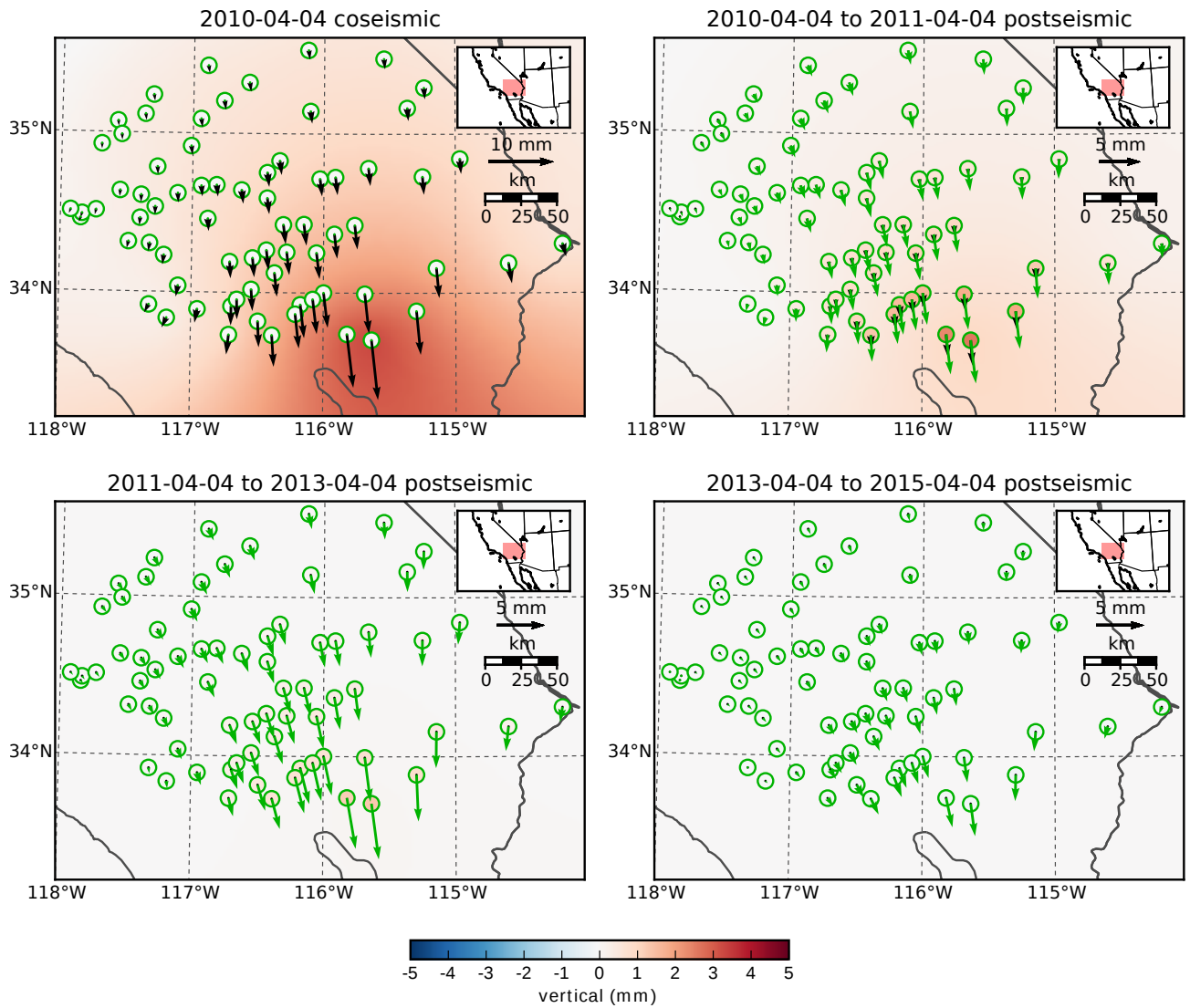


Figure 3.18: Same as figure 3.17 but for far-field stations.

## CHAPTER 4

### Unbiased characterization of noise in geodetic data<sup>†</sup>

#### 4.1 Abstract

Geodetic time series contain temporally correlated noise that must be quantified before the data can be used to make geophysical inferences. If the noise is not accurately quantified then there is a risk of underestimating the uncertainties on inferred geophysical parameters. The maximum likelihood estimation (MLE) method is commonly used to characterize noise in geodetic time series; however, this method is known to be biased. Specifically, the MLE method has a tendency to underestimate the amplitude of random walk noise. This bias is most pronounced when estimating the noise in shorter time series. We discuss an unbiased alternative to the MLE method, which is known as the restricted maximum likelihood (REML) method. We use synthetic tests to demonstrate that the REML method does not suffer from the bias inherent in the MLE method. Considering that the computational costs of the REML and MLE methods are nearly equivalent, there is no reason to prefer the MLE method over the REML method for quantifying noise in geodetic data.

#### 4.2 Introduction

Before geodetic data can be used to make geophysical inferences, it is necessary to have an accurate noise model. Here we consider noise to be any observed deformation that is not representative of tectonic processes. The noise in geodetic time series is temporally correlated and its power spectrum is often described by the power law relationship (*Agnew, 1992*)

$$P(f) = P_o f^{-k}, \quad (4.1)$$

where  $f$  is frequency,  $k$  is the spectral index and  $P_o$  is the noise amplitude. For data recorded by strain and tilt meters (*Wyatt, 1982, 1989*) and electronic distance measuring

---

<sup>†</sup>This chapter is under review at Journal of Geodesy.

(EDM) instruments (*Langbein and Johnson*, 1997), the temporally correlated noise can be modeled as a random walk ( $k = 2$ ). In those studies, the random walk noise was attributed to unstable geodetic monuments. Global Navigation Satellite System (GNSS) data, which is prone to additional non-physical sources of error, often has temporally correlated noise that is best modeled as flicker noise ( $k = 1$ ) (e.g., *Zhang et al.*, 1997; *Mao et al.*, 1999; *Williams et al.*, 2004). However, the most appropriate model can vary between stations. Generally, the noise in GNSS data is best described as white noise plus some combination of random walk and flicker noise (*Langbein*, 2008).

If temporally correlated noise is mismodeled or ignored then the uncertainties in geophysical parameters inferred from geodetic data may be underestimated (e.g., *Zhang et al.*, 1997; *Langbein*, 2012). Since no single noise model is universally appropriate, it may be preferable to determine a noise model for each station before attempting to study any underlying signal. *Langbein and Johnson* (1997) introduced a maximum likelihood estimation (MLE) method to determine the hyperparameters (e.g.,  $P_o$  and  $k$ ) that best characterize the noise in geodetic time series. Furthermore, the MLE method can be used to discern which type of stochastic process (e.g., power law or Gauss-Markov) is most appropriate (*Langbein*, 2004). There are other methods for determining noise models, such as the least squares variance component estimation method (*Amiri-Simkooei et al.*, 2007) and the network noise estimator (*Dmitrieva et al.*, 2015). However, the MLE method from *Langbein and Johnson* (1997) is the most widely used (e.g., *Langbein*, 2004, 2008; *Zhang et al.*, 1997; *Mao et al.*, 1999; *Williams et al.*, 2004; *Hill et al.*, 2009; *King and Williams*, 2009; *Murray and Svarc*, 2017).

One deficiency with the MLE method, which was recognized by *Langbein and Johnson* (1997), is that it can be biased towards underestimating the amplitude of random walk noise. The MLE method is biased because it assumes that residual geodetic time series, with geophysical signals estimated and removed, are representative samples of noise. This is not always a fair assumption because estimating and removing geophysical signals will inevitably also remove low frequency components of noise. *Langbein* (2012) further explored the bias in the MLE method and how it propagates into the uncertainties for estimated tectonic rates of deformation. They demonstrated with synthetic data, consisting of white noise and random walk noise, that the bias is stronger for shorter time series. *Langbein* (2012) emphasized the role of the crossover frequency,  $f_c$ , which is the frequency where the power of the white noise is equal to the power of the random walk noise. They suggested that a time series should be several times longer than  $f_c^{-1}$  in order to accurately quantify its random walk noise.

In this paper we discuss an alternative to the MLE method, which is known as the

restricted maximum likelihood (REML) method (e.g., *Cressie*, 1993). We use synthetic tests to demonstrate that the REML method produces unbiased estimates of random walk noise. With the REML method, we can accurately quantify the random walk noise in time series that are as short as  $f_c^{-1}$ . Furthermore, the REML and MLE methods have practically equivalent computational costs. For these reasons, we argue that there is no reason to prefer using the MLE method over the unbiased REML method.

### 4.3 Maximum likelihood methods

In this section we briefly describe the MLE method and explain why it is biased. We then provide a description of the REML method. Let  $\mathbf{d}_*$  denote a column vector of  $n$  observations. We treat  $\mathbf{d}_*$  as a realization of the random vector

$$\mathbf{d} = \mathbf{G}\mathbf{m} + \epsilon, \quad (4.2)$$

where  $\epsilon$  is the data noise vector,  $\mathbf{G}$  is an  $n \times m$  matrix with linearly independent columns that are used to describe geophysical signal in  $\mathbf{d}$  (e.g., secular rates, coseismic offsets, postseismic transience), and  $\mathbf{m}$  is a column vector of  $m$  model parameters which have uninformative priors (i.e.  $\mathbf{m} \sim \mathcal{N}(\mathbf{0}, \lambda\mathbf{I})$  in the limit as  $\lambda \rightarrow \infty$ ). We assume that the data noise can be described as  $\epsilon \sim \mathcal{N}(\mathbf{0}, \Sigma(\theta))$ , where  $\theta$  are the hyperparameters which we want to estimate appropriate values for. If we had chosen an informed prior for  $\mathbf{m}$ , we would select  $\theta$  such that the probability of drawing  $\mathbf{d}_*$  from  $\mathbf{d}$ ,  $p_{\mathbf{d}}(\mathbf{d}_*|\theta)$ , is maximized. However, the uninformed prior on  $\mathbf{m}$  makes  $\mathbf{d}$  improper and  $p_{\mathbf{d}}$  is infinitesimally small for all choices of  $\theta$ . Consequently, it is not possible to numerically maximize  $p_{\mathbf{d}}$  and we must seek an alternative likelihood function to maximize.

The MLE method chooses  $\theta$  such that the probability of sampling the least squares residual vector,

$$\mathbf{r}_* = \left( \mathbf{I} - \mathbf{G} \left( \mathbf{G}^T \Sigma(\theta)^{-1} \mathbf{G} \right)^{-1} \mathbf{G}^T \Sigma(\theta)^{-1} \right) \mathbf{d}_*, \quad (4.3)$$

from  $\epsilon$  is maximized. To put it explicitly, The MLE method maximizes the probability density function

$$p_\epsilon(\mathbf{r}_*|\theta) = \left( \frac{1}{(2\pi)^n |\Sigma(\theta)|} \right)^{\frac{1}{2}} e^{-\frac{1}{2} \mathbf{d}_*^T \mathbf{K}(\theta) \mathbf{d}_*} \quad (4.4)$$

with respect to  $\theta$ , where

$$\mathbf{K}(\theta) = \Sigma(\theta)^{-1} - \Sigma(\theta)^{-1} \mathbf{G} \left( \mathbf{G}^T \Sigma(\theta)^{-1} \mathbf{G} \right)^{-1} \mathbf{G}^T \Sigma(\theta)^{-1}. \quad (4.5)$$

Implementations of the MLE method typically maximize the logarithm of eq. (4.4) with the downhill simplex method (*Press et al.*, 2007). It is important to recognize that the MLE method assumes that  $\mathbf{r}_*$  is a representative sample of  $\epsilon$ . This assumption is only valid when  $n$  is sufficiently large. To elaborate, we note that  $\mathbf{r}_*$  is a sample of the random variable

$$\mathbf{r} = \left( \mathbf{I} - \mathbf{G} \left( \mathbf{G}^T \Sigma(\theta)^{-1} \mathbf{G} \right)^{-1} \mathbf{G}^T \Sigma(\theta)^{-1} \right) \mathbf{d}, \quad (4.6)$$

which is distributed as

$$\mathbf{r} \sim \mathcal{N} \left( \mathbf{0}, \Sigma(\theta) - \mathbf{G} \left( \mathbf{G}^T \Sigma(\theta)^{-1} \mathbf{G} \right)^{-1} \mathbf{G}^T \right). \quad (4.7)$$

The term being subtracted in eq. (4.7) is the covariance of the least squares prediction vector, which will typically get smaller as  $n$  increases. The distribution of  $\mathbf{r}$  will then tend towards that of  $\epsilon$  as  $n$  increases. Hence, we can only assume that  $\mathbf{r}_*$  is a representative sample of  $\epsilon$  when  $n$  is sufficiently large. We can also observe from eq. (4.7) that the variance of  $\mathbf{r}$  will always be less than the variance of  $\epsilon$ . This is the reason why the MLE method is biased towards underestimating the noise in short time series.

Having demonstrated that the MLE method is biased, we move on to discuss the REML method for selecting  $\theta$ . The REML method was introduced by *Patterson and Thompson* (1971), and is now established in the Kriging literature as an unbiased method for estimating covariance functions (e.g., *Cressie*, 1993). The REML method can be understood by first considering an  $(n-m) \times n$  matrix  $\mathbf{R}$  which satisfies  $\mathbf{R}\mathbf{G} = \mathbf{0}$ . We then consider the random variable  $\mathbf{x} = \mathbf{R}\mathbf{d}$ , which is distributed as  $\mathbf{x} \sim \mathcal{N}(\mathbf{0}, \mathbf{R}\Sigma(\theta)\mathbf{R}^T)$ . As opposed to  $\mathbf{d}$ ,  $\mathbf{x}$  is a proper random variable since it is independent of the prior on  $\mathbf{m}$ . The REML method chooses  $\theta$  such that the probability of drawing  $\mathbf{x}_* = \mathbf{R}\mathbf{d}_*$  from  $\mathbf{x}$ ,  $p_{\mathbf{x}}(\mathbf{x}_*|\theta)$ , is maximized. As shown by *Harville* (1974), the  $\theta$  which maximizes  $p_{\mathbf{x}}(\mathbf{x}_*|\theta)$  also maximizes  $p_{\mathbf{d}}(\mathbf{d}_*|\theta)$  because the two likelihood functions are proportional. The REML method thus circumvents the numerical difficulty that  $p_{\mathbf{d}}$  is infinitesimally small and identifies the  $\theta$  which we initially sought to find. The particular choice for  $\mathbf{R}$  does not matter because it will only change the likelihood function which we are maximizing by a scale factor. Following *Harville* (1974), we then let  $\mathbf{R}$  have the properties  $\mathbf{R}^T \mathbf{R} = \mathbf{I} - \mathbf{G}(\mathbf{G}^T \mathbf{G})^{-1} \mathbf{G}^T$  and  $\mathbf{R} \mathbf{R}^T = \mathbf{I}$ . The probability density function for  $\mathbf{x}$  can then be written as

$$p_{\mathbf{x}}(\mathbf{x}_*|\theta) = \left( \frac{|\mathbf{G}^T \mathbf{G}|}{(2\pi)^{n-m} |\Sigma(\theta)| |\mathbf{G}^T \Sigma(\theta)^{-1} \mathbf{G}|} \right)^{\frac{1}{2}} e^{-\frac{1}{2} \mathbf{d}_*^T \mathbf{K}(\theta) \mathbf{d}_*}. \quad (4.8)$$

Note the similarity between eq. (4.8) and eq. (4.4). If programmed efficiently (see Appendix

4A) and if  $m \ll n$ , the computational cost of the REML method is practically equivalent to that of the MLE method. What remains to be determined is whether the REML method remedies the bias in the MLE method. We demonstrate that this is indeed the case with a numerical test.

#### 4.4 Synthetic demonstration

We compare the REML and MLE methods by using them to estimate hyperparameters from synthetic data. This demonstration is modeled after the demonstration from *Langbein* (2012) which highlights bias in the MLE method. Our synthetic noise is a combination of white and random walk noise, which has a power spectrum described by

$$P(f) = \frac{\sigma_{rw}^2}{2\pi^2 f^2} + 2\sigma_w^2 \Delta t, \quad (4.9)$$

where  $\sigma_{rw}$  and  $\sigma_w$  are hyperparameters for the random walk and white noise components, respectively.  $\Delta t$  is the sampling period, which is set at one day. The crossover frequency for the synthetic noise is then

$$f_c = \frac{1}{2\pi\sqrt{\Delta t}} \frac{\sigma_{rw}}{\sigma_w}. \quad (4.10)$$

In order to use the MLE or REML method, we must express the power law relationship in the frequency domain as a covariance matrix in the time domain. A general procedure for doing so can be found in *Langbein* (2004). The components of the covariance matrix corresponding to eq. (4.9) can be concisely written as

$$\Sigma_{ij} = \sigma_{rw}^2 \min(i\Delta t, j\Delta t) + \sigma_w^2 \delta_{ij}, \quad (4.11)$$

where  $\delta_{ij}$  is the Kronecker delta function. Similar to *Langbein* (2012), we set  $\sigma_{rw} = 1.3$  mm/yr<sup>0.5</sup> and  $\sigma_w = 1.1$  mm. We generate 5,000 synthetic noise time series, which each have a length of 2.5 yr.

We consider  $\sigma_w$  to be known, and we want to estimate  $\sigma_{rw}$  from the synthetic data. Although our synthetic data just consists of noise, we assume that the unknown underlying geophysical signal (i.e. **Gm**) consists of an offset plus a linear trend. We estimate  $\sigma_{rw}$  with the MLE and REML methods using varying lengths of the synthetic time series. The time series lengths range from 0.1 yr to 2.5 yr at 0.1 yr increments. The distribution of estimated  $\sigma_{rw}$  is shown in Figure 4.1.

The distribution of  $\sigma_{rw}$  estimated by the MLE method indicates that there is a bias towards underestimating  $\sigma_{rw}$  when the length of the time series is comparable to  $f_c^{-1}$ , which

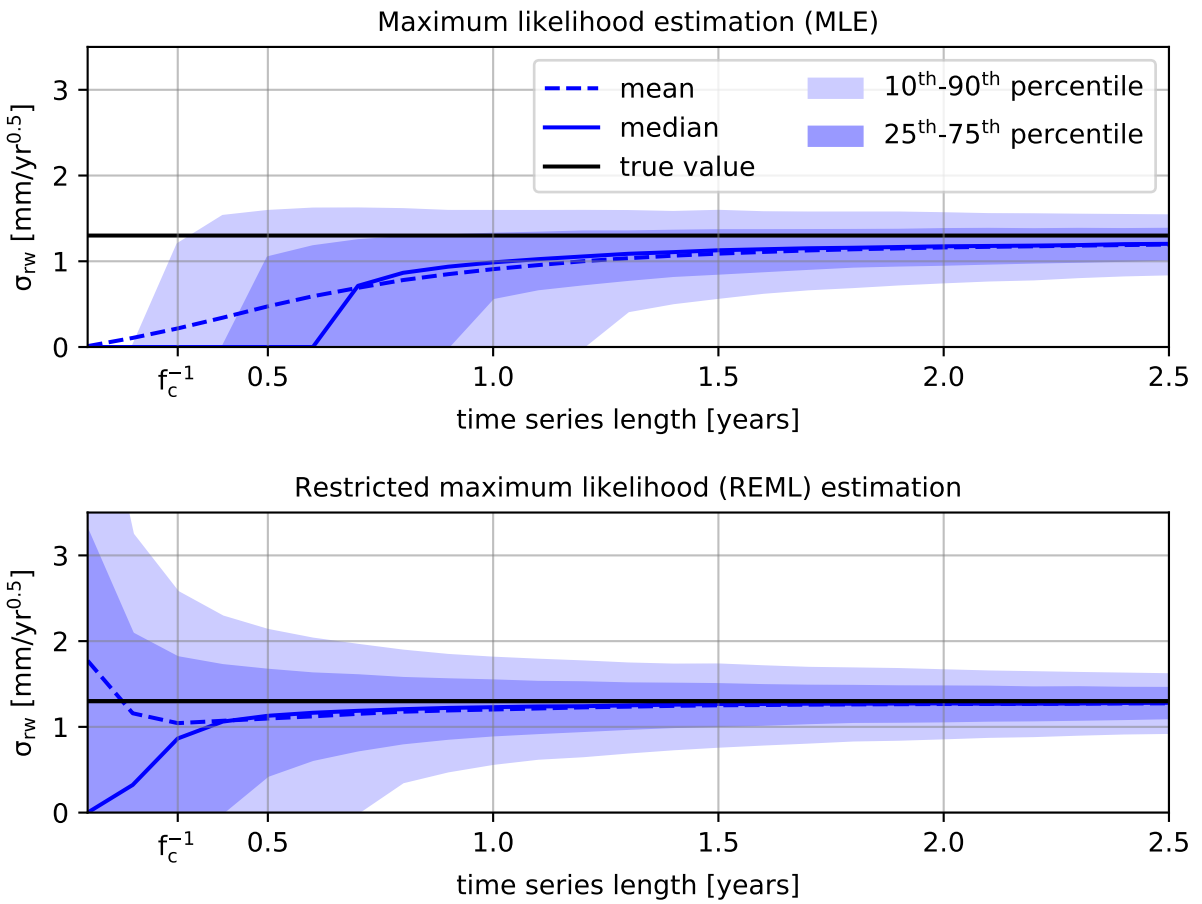


Figure 4.1: Random walk amplitudes,  $\sigma_{rw}$ , estimated by the MLE and REML methods from synthetic data. The length of the synthetic time series used to estimate  $\sigma_{rw}$  is varied from 0.1 yr to 2.5 yr. The black line indicates the true random walk amplitude ( $\sigma_{rw} = 1.3$ ), the light blue region shows the 10-90 percentile of estimates, the dark blue region shows the 25-75 percentile of estimates, the solid blue line indicates the median, and the dashed blue line indicates the mean.

is 0.3 yr in this demonstration. The bias is appreciable when the time series is shorter than  $\sim 1$  yr, and estimates of  $\sigma_{rw}$  cluster around 0.0 when the time series is shorter than  $f_c^{-1}$ . The distribution tightens up around the true value and remains relatively constant for time series with length greater than  $\sim 1$  yr. This is consistent with *Langbein and Johnson* (1997) who said that the time series should be at least 5 times greater than  $f_c^{-1}$  to get a good estimate of the random walk component. Even when the full length of the time series is used, the mean and median of the distribution tend to be slightly less than the true value.

In contrast, the REML method does significantly better at estimating  $\sigma_{rw}$ . For every time series length considered, the true value for  $\sigma_{rw}$  is within the 25-75 percentile of estimated  $\sigma_{rw}$ . For time series longer than  $f_c^{-1}$ , the mean and median of estimated  $\sigma_{rw}$  closely resembles the true value, indicating that the REML method is indeed unbiased. When the length of the time series is less than  $f_c^{-1}$ , the mean and median deviate from the true value and the variance of estimated  $\sigma_{rw}$  sharply increases. For such short time series, the random walk component cannot be resolved because it is being masked by the white noise.

## 4.5 Discussion and conclusion

The MLE method is the most commonly used method for quantifying noise in geodetic time series, despite the fact that it is known to be biased. The bias in the MLE method can result in underestimated uncertainties in geophysical parameters derived from geodetic time series (*Langbein*, 2012). The intention of this paper is to bring the REML method to light in the geodetic community as an unbiased alternative. Since the MLE method is well established, it may not be reasonable to suggest that researchers abandon it in favor of the REML method. However, the REML method is nearly identical to the MLE method in terms of its computational cost and in terms of its implementation. Indeed, the only difference between the log likelihood functions being maximized by the REML and MLE methods is that the REML method includes two additional, easily computed, terms (See Appendix 4A). We can therefore view the REML method as merely an unbiased correction to the MLE method.

In this paper, we have used synthetic tests to demonstrate that the REML method does not suffer from the bias inherent in the MLE method from *Langbein and Johnson* (1997). We show that the REML method is able to characterize random walk noise in geodetic time series that are as short as  $f_c^{-1}$ . In contrast, the MLE method can only accurately quantify random walk noise for time series that are several times longer than  $f_c^{-1}$ . We believe that the REML method should always be preferred over the MLE method for quantifying noise in geodetic time series.

## 4.6 Acknowledgements

This material is based upon work supported by the National Science Foundation under grant EAR 1245263.

## Appendix 4A: REML algorithm

Algorithm 1 demonstrates how to efficiently compute the log of the REML likelihood function. For comparison, we include Algorithm 2, which evaluates the log of the MLE likelihood function. If we assume that  $m \ll n$ , then the main computational burden in both algorithms is computing the Cholesky decomposition of  $\Sigma$ . Since we are just interested in finding the  $\Sigma$  that maximizes these functions, we can omit the terms in the log likelihood functions that are independent of  $\Sigma$ . In that case, the only difference between the two algorithms is that Algorithm 1 includes a summation along the diagonals of  $\mathbf{C}$  in the log likelihood function.

---

**Algorithm 1** Function that takes  $\mathbf{d}$ ,  $\Sigma$ , and  $\mathbf{G}$  as input and returns the logarithm of eq. (4.8). We use the notation  $\mathbf{X}\backslash\mathbf{Z}$  to denote solving the system of equations  $\mathbf{XY} = \mathbf{Z}$  for  $\mathbf{Y}$ .

---

```

function reml_log_likelihood( $\mathbf{d}, \Sigma, \mathbf{G}$ )
     $\mathbf{A} \leftarrow \text{cholesky}(\Sigma)$ 
     $\mathbf{B} \leftarrow \mathbf{A} \backslash \mathbf{G}$ 
     $\mathbf{C} \leftarrow \text{cholesky}(\mathbf{B}^T \mathbf{B})$ 
     $\mathbf{D} \leftarrow \text{cholesky}(\mathbf{G}^T \mathbf{G})$ 
     $\mathbf{a} \leftarrow \mathbf{A} \backslash \mathbf{d}$ 
     $\mathbf{b} \leftarrow \mathbf{C} \backslash (\mathbf{B}^T \mathbf{a})$ 
    return  $\sum_i^m \log(D_{ii}) - \sum_i^n \log(A_{ii}) - \sum_i^m \log(C_{ii}) - \frac{1}{2}\mathbf{a}^T \mathbf{a} + \frac{1}{2}\mathbf{b}^T \mathbf{b} - \frac{n-m}{2} \log(2\pi)$ 
end function
```

---



---

**Algorithm 2** Function that takes  $\mathbf{d}$ ,  $\Sigma$ , and  $\mathbf{G}$  as input and returns the logarithm of eq. (4.4).

---

```

function mle_log_likelihood( $\mathbf{d}, \Sigma, \mathbf{G}$ )
     $\mathbf{A} \leftarrow \text{cholesky}(\Sigma)$ 
     $\mathbf{B} \leftarrow \mathbf{A} \backslash \mathbf{G}$ 
     $\mathbf{C} \leftarrow \text{cholesky}(\mathbf{B}^T \mathbf{B})$ 
     $\mathbf{a} \leftarrow \mathbf{A} \backslash \mathbf{d}$ 
     $\mathbf{b} \leftarrow \mathbf{C} \backslash (\mathbf{B}^T \mathbf{a})$ 
    return  $-\sum_i^n \log(A_{ii}) - \frac{1}{2}\mathbf{a}^T \mathbf{a} + \frac{1}{2}\mathbf{b}^T \mathbf{b} - \frac{n}{2} \log(2\pi)$ 
end function
```

---

## CHAPTER 5

# Revealing transient strain in geodetic data with Gaussian process regression<sup>†</sup>

### 5.1 Summary

Transient strain rates derived from GNSS data can be used to detect and understand geo-physical phenomena such as slow slip events and postseismic deformation. Here we propose using Gaussian process regression (GPR) as a tool for estimating transient strain rates from GNSS data. GPR is a non-parametric, Bayesian method for interpolating scattered data. Transient strain rates estimated with GPR have meaningful uncertainties, allowing geophysical signal to be easily discerned from noise. In our approach, we assume a stochastic prior model for transient displacements. The prior describes how much one expects transient displacements to covary spatially and temporally. A posterior estimate of transient strain rates is obtained by differentiating the posterior displacements. One limitation with GPR is that it is not robust against outliers, so we introduce a pre-processing method for detecting and removing outliers in GNSS data. As a demonstration, we use GPR to detect transient strain resulting from slow slip events in Cascadia. Maximum likelihood methods are used to constrain a prior model for transient displacements in this region. The temporal covariance of our prior model is described by a compact Wendland covariance function, which significantly reduces the computational burden that can be associated with GPR. Our results reveal the spatial and temporal evolution of strain from slow slip events. We verify that the transient strain estimated with GPR is in fact geophysical signal by comparing it to the seismic tremor that is associated with Cascadia slow slip events.

### 5.2 Introduction

Crustal strain rates are fundamentally important quantities for assessing seismic hazard. Knowing where and how quickly strain is accumulating gives insight into where we can

---

<sup>†</sup>This chapter is under review at Geophysical Journal International.

expect stored elastic energy to be released seismically. Consequently, secular crustal strain rates estimated from GNSS data have been used to constrain seismic hazard models such as UCERF3 (*Field et al.*, 2014). Transient crustal strain, which is caused by geophysical phenomena such as slow slip events (SSEs) or postseismic deformation, is also relevant for assessing seismic hazard. While transient strain itself is not damaging, there is a risk that it can trigger major earthquakes (*Roeloffs*, 2006; *Freed and Lin*, 2001). Dense networks of continuous GNSS stations, such as the Plate Boundary Observatory (PBO), make it possible to identify transient strain with high fidelity. Developing and improving upon methods for deriving secular and transient strain from GNSS data is an active area of research.

Most methods for estimating strain rates from GNSS data assume some parametric form of the deformation signal. The simplest method for estimating secular strain rates assumes that GNSS derived velocities can be described with a first-order polynomial (i.e., having constant deformation gradients) over some subnetwork of the GNSS stations (e.g., *Feigl et al.*, 1990; *Murray and Lisowski*, 2000). The components of the strain rate tensor for each subnetwork are then determined through a least squares fit to the observations. The assumption that deformation gradients are spatially uniform is not appropriate when subnetworks span too large of an area. To help overcome this deficiency, *Shen et al.* (1996, 2015) used an inverse distance weighting scheme, in which the estimated strain rate at some point is primarily controlled by observations at nearby stations. However, the methods described in *Shen et al.* (1996, 2015) are still formulated by assuming that the deformation gradients are uniform over the entire network. The errors in this assumption manifest as implausibly low formal uncertainties for the estimated strain rates. Other methods for estimating secular strain rates have parameterized GNSS derived velocities with bi-cubic splines (*Beavan and Haines*, 2001), spherical wavelets (*Tape et al.*, 2009), and elastostatic Green's functions (*Sandwell and Wessel*, 2016). The type of basis functions and the number of degrees of freedom for a parameterization can be subjective. If there are too few degrees of freedom in the parameterization, then estimated strain rates will be biased and the uncertainties will be underestimated. On the other hand, if there are too many degrees of freedom, then there will not be any coherent features in the estimated strain rates. The methods described by *Beavan and Haines* (2001) and *Tape et al.* (2009) also require the user to specify penalty parameters that control a similar trade-off between bias and variance in the solution. One could parameterize deformation with a physically motivated model of interseismic deformation (e.g., *Meade and Hager*, 2005; *McCaffrey et al.*, 2007). In such models the lithospheric rheology and fault geometries are assumed to be known. Any errors in the assumed physical model could result in biased strain estimates and underestimated formal uncertainties.

The aforementioned studies are concerned with estimating secular strain rates. In recent

years the Southern California Earthquake Center (SCEC) community has shown interest in developing methods for detecting transient strain. SCEC supported a transient detection exercise (*Lohman and Murray*, 2013), where several research groups tested their methods for detecting transient geophysical signal with a synthetic GNSS dataset. Among the methods tested were the Network Strain Filter (NSF) (*Ohtani et al.*, 2010) and the Network Inversion Filter (NIF) (*Segall and Mathews*, 1997). The NSF uses a wavelet parameterization to describe the spatial component of geophysical signal. The NIF, which is intended for imaging slow fault slip from geodetic data, uses the elastic dislocation Green's functions from *Okada* (1992). For the NSF and NIF, the time dependence of the geophysical signal is modeled as integrated Brownian motion. The method described in *Holt and Shcherbenko* (2013) was also tested in the SCEC transient detection exercise, which calculates strain rates using a bi-cubic spatial parameterization of displacements between time epochs. *Holt and Shcherbenko* (2013) defined a detection threshold based on the strain rate magnitude, and below we demonstrate that this is indeed an effective criterion for identifying geophysical signal. For the same reasons described above, the transient deformation and corresponding uncertainties estimated by these methods can be biased by the chosen spatial parameterization. It is then difficult to distinguish signal from noise with these methods, which limits their utility for transient detection.

Here we propose using Gaussian process regression (GPR) (*Rasmussen and Williams*, 2006) to estimate transient strain from GNSS data. GPR is a Bayesian, non-parametric method for inferring a continuous signal from scattered data. Since GNSS stations are irregularly spaced and observation times may differ between stations, GPR is an ideal tool for synthesizing GNSS data into a spatially and temporally continuous representation of surface deformation. GPR is closely related to kriging (*Cressie*, 1993) and least squares collocation (*Moritz*, 1978). The latter has been used by *Kato et al.* (1998) and *El-Fiky and Kato* (1998) to estimate secular strain rates from GNSS data. GPR is Bayesian in that we describe our prior understanding of the geophysical signal with a Gaussian process. A Gaussian process is a normally distributed stochastic process that is fully defined in terms of a mean function and a positive definite covariance function. For example, Brownian motion,  $B(t)$ , is a well known Gaussian process in  $\mathbb{R}^1$  which has zero mean and covariance function  $\text{cov}(B(t), B(t')) = \min(t, t')$ , where  $t, t' \geq 0$ . If no prior information is available for the geophysical signal, then maximum likelihood methods can be used to objectively choose a prior Gaussian process that is most consistent with the observations. We incorporate GNSS observations with the prior to form a posterior estimate of transient strain. The posterior transient strain is also a Gaussian process, and we can use its distribution to confidently discern geophysical signal from noise. We use GPR to infer strain resulting from SSEs in

Cascadia, demonstrating that GPR is an effective tool for detecting transient geophysical processes.

### 5.3 Estimating transient strain rates

We seek a spatially and temporally dependent estimate of transient crustal strain rates. We consider transient strain rates to be any deviation from secular strain rates, and our attention is limited to horizontal strain rates in this study. We denote transient crustal strain rates as  $\dot{\varepsilon}(p)$ , where  $p$  represents the ordered pair  $(\vec{x}, t)$ ,  $\vec{x}$  are spatial coordinates in  $\mathbb{R}^2$ , and  $t$  is time. We determine  $\dot{\varepsilon}(p)$  by spatially and temporally differentiating estimates of transient displacements,  $\vec{u}(p)$ . We make a prior assumption that each component of  $\vec{u}$  is a Gaussian process,

$$u_i(p) \sim \mathcal{N}(0, C_{u_i}), \quad (5.1)$$

where  $C_{u_i}(p, p')$  is a covariance function indicating how we expect  $u_i(p)$  to covary with  $u_i(p')$ . For simplicity, we treat each component of displacements independently and ignore any potential covariance between them. Hence, we drop the component subscripts with the understanding that the same analysis is being repeated to estimate the easting and northing components of  $\vec{u}$ . We assume that  $C_u$  can be separated into spatial and temporal functions as

$$C_u((\vec{x}, t), (\vec{x}', t')) = X(\vec{x}, \vec{x}')T(t, t'). \quad (5.2)$$

As long as the functions  $X$  and  $T$  are positive definite,  $C_u$  is guaranteed to also be positive definite and thus a valid covariance function (*Rasmussen and Williams*, 2006, sec. 4.2.4). The appropriate choice for  $X$  and  $T$  may vary depending on the geophysical signal we are trying to describe, and we discuss this matter in Section 5.5.2.

We constrain  $u$  with GNSS data, which records  $u$  as well as other physical and non-physical processes that we are not interested in. We describe GNSS observations at position  $\vec{x}_i$  and time  $t_j$  as a realization of the random variable

$$\begin{aligned} d_{ij} = & u(\vec{x}_i, t_j) + \eta(\vec{x}_i, t_j) + w_{ij} + a_i^{(1)} + a_i^{(2)}t_j + \\ & a_i^{(3)} \sin(2\pi t_j) + a_i^{(4)} \cos(2\pi t_j) + a_i^{(5)} \sin(4\pi t_j) + a_i^{(6)} \cos(4\pi t_j), \end{aligned} \quad (5.3)$$

where  $a_i^{(1)}$  is an offset that is unique for each GNSS monument,  $a_i^{(2)}$  is the secular velocity at  $\vec{x}_i$ , and the sinusoids describe seasonal deformation (using units of years for  $t_j$ ). We use  $w_{ij}$  to denote normally distributed, uncorrelated noise. Correlated noise which does not have a parametric representation is denoted by  $\eta$ . For example,  $\eta$  can consist of temporally

correlated noise describing benchmark wobble (e.g., *Wyatt*, 1982, 1989), and/or spatially correlated noise describing common mode error (e.g., *Wdowinski et al.*, 1997). For now, we will only assume that  $\eta \sim \mathcal{N}(0, C_\eta)$ . We consider the six coefficients in eq. (5.3) to be uncorrelated random variables distributed as  $\mathcal{N}(0, \kappa^2)$  in the limit as  $\kappa \rightarrow \infty$  (i.e., the coefficients have diffuse priors). Of course, the secular velocities,  $a_i^{(2)}$ , are spatially correlated and we could invoke a tectonic model to form a prior on  $a_i^{(2)}$ . However, in our application to Cascadia, we will be using displacement time series which are long enough to sufficiently constrain  $a_i^{(2)}$  for each station, avoiding the need to incorporate a prior. Likewise, seasonal deformation is spatially correlated (*Dong et al.*, 2002; *Langbein*, 2008), and it may be worth exploring and exploiting such a correlation in a future study.

We now consider the column vector of  $n$  GNSS observations made at  $m$  stations,  $\mathbf{d}_*$ . Let  $\mathbf{P}$  be the set of  $(\vec{x}_i, t_j)$  pairs describing where and when each of the GNSS observations have been made. Let  $\mathbf{a}$  be the vector of coefficients from eq. (5.3) for each of the  $m$  GNSS stations. We use  $\mathbf{G}$  to represent the  $n \times 6m$  matrix of corresponding basis functions evaluated at each point in  $\mathbf{P}$ . We also denote the vector of uncorrelated noise for each observation as  $\mathbf{w}$ , whose standard deviations are given by the formal data uncertainty,  $\sigma$ . The observations can then be viewed as a realization of the random vector

$$\mathbf{d} = u(\mathbf{P}) + \eta(\mathbf{P}) + \mathbf{w} + \mathbf{G}\mathbf{a}, \quad (5.4)$$

which is distributed as  $\mathcal{N}(\mathbf{0}, \Sigma + \kappa^2 \mathbf{G}\mathbf{G}^T)$ , where

$$\Sigma = C_u(\mathbf{P}, \mathbf{P}) + C_\eta(\mathbf{P}, \mathbf{P}) + \text{diag}(\sigma^2). \quad (5.5)$$

It should be understood that notation such as  $u(\mathbf{P})$  and  $C_u(\mathbf{P}, \mathbf{P})$  represents the column vector  $[u(P_i)]_{P_i \in \mathbf{P}}$  and the matrix  $[C_u(P_i, P_j)]_{(P_i, P_j) \in \mathbf{P} \times \mathbf{P}}$ , respectively.

The prior for transient displacements is then conditioned with  $\mathbf{d}_*$  to form a posterior estimate of transient displacements,  $\hat{u} = u|\mathbf{d}_*$ . For now, we will assume that appropriate covariance functions and corresponding hyperparameters for  $C_u$  and  $C_\eta$  have already been chosen. In Section 5.5.1 and 5.5.2, we discuss how the covariance functions are chosen for our application to GNSS data from Cascadia. If  $\kappa$  is kept finite then, from *Rasmussen and Williams* (2006, sec. 2.2), we find that  $\hat{u}$  is distributed as  $\mathcal{N}(\mu_{\hat{u}}, C_{\hat{u}})$ , where

$$\mu_{\hat{u}}(p) = C_u(p, \mathbf{P}) (\Sigma + \kappa^2 \mathbf{G}\mathbf{G}^T)^{-1} \mathbf{d}_* \quad (5.6)$$

and

$$C_{\hat{u}}(p, p') = C_u(p, p') - C_u(p, \mathbf{P}) (\Sigma + \kappa^2 \mathbf{G}\mathbf{G}^T)^{-1} C_u(\mathbf{P}, p'). \quad (5.7)$$

However, we are interested in the limit as  $\kappa \rightarrow \infty$ , and the form for eq. (5.6) and eq. (5.7) is not suitable for evaluating this limit. We use a partitioned matrix inversion identity (*Press et al.*, 2007, sec. 2.7.4) to rewrite eq. (5.6) and eq. (5.7) as

$$\mu_{\hat{u}}(p) = \begin{bmatrix} C_u(p, \mathbf{P}) & \mathbf{0} \end{bmatrix} \begin{bmatrix} \Sigma & \mathbf{G} \\ \mathbf{G}^T & -\kappa^{-2}\mathbf{I} \end{bmatrix}^{-1} \begin{bmatrix} \mathbf{d}_* \\ \mathbf{0} \end{bmatrix} \quad (5.8)$$

and

$$C_{\hat{u}}(p, p') = C_u(p, p') - \begin{bmatrix} C_u(p, \mathbf{P}) & \mathbf{0} \end{bmatrix} \begin{bmatrix} \Sigma & \mathbf{G} \\ \mathbf{G}^T & -\kappa^{-2}\mathbf{I} \end{bmatrix}^{-1} \begin{bmatrix} C_u(\mathbf{P}, p') \\ \mathbf{0} \end{bmatrix}. \quad (5.9)$$

Taking the limit as  $\kappa \rightarrow \infty$ , we get the solution for the mean and covariance of  $\hat{u}$ ,

$$\mu_{\hat{u}}(p) = \begin{bmatrix} C_u(p, \mathbf{P}) & \mathbf{0} \end{bmatrix} \begin{bmatrix} \Sigma & \mathbf{G} \\ \mathbf{G}^T & \mathbf{0} \end{bmatrix}^{-1} \begin{bmatrix} \mathbf{d}_* \\ \mathbf{0} \end{bmatrix} \quad (5.10)$$

and

$$C_{\hat{u}}(p, p') = C_u(p, p') - \begin{bmatrix} C_u(p, \mathbf{P}) & \mathbf{0} \end{bmatrix} \begin{bmatrix} \Sigma & \mathbf{G} \\ \mathbf{G}^T & \mathbf{0} \end{bmatrix}^{-1} \begin{bmatrix} C_u(\mathbf{P}, p') \\ \mathbf{0} \end{bmatrix}. \quad (5.11)$$

We use eq. (5.10) and (5.11) to find the posterior easting and northing components of transient displacements. Using  $\hat{u}_i$  to denote the posterior transient displacements along direction  $i$  and  $x_i$  to represent the components of  $\vec{x}$ , we can write the components of  $\dot{\varepsilon}$  as

$$\dot{\varepsilon}_{ij}(p) = \frac{1}{2} \frac{\partial}{\partial t} \left( \frac{\partial \hat{u}_i(p)}{\partial x_j} + \frac{\partial \hat{u}_j(p)}{\partial x_i} \right). \quad (5.12)$$

The transient strain rate components are stochastic processes whose distributions can be interpreted as the distributions of samples of  $\hat{u}$  that have been differentiated by the operator from eq. (5.12). Since differentiation is a linear operation, the transient strain rate components are Gaussian processes. From *Papoulis* (1991, sec. 10.2), we find that the components of  $\dot{\varepsilon}$  have mean functions

$$\mu_{\dot{\varepsilon}_{ij}}(p) = \frac{1}{2} \frac{\partial}{\partial t} \left( \frac{\partial \mu_{\hat{u}_i}(p)}{\partial x_j} + \frac{\partial \mu_{\hat{u}_j}(p)}{\partial x_i} \right) \quad (5.13)$$

and covariance functions

$$C_{\dot{\varepsilon}_{ij}}(p, p') = \frac{1}{4} \frac{\partial^2}{\partial t \partial t'} \left( \frac{\partial^2 C_{\hat{u}_i}(p, p')}{\partial x_j \partial x'_j} + \frac{\partial^2 C_{\hat{u}_j}(p, p')}{\partial x_i \partial x'_i} \right). \quad (5.14)$$

Our motivation for estimating transient strain rates is, in part, to detect geophysical

phenomena. As we will see, geophysical signal can be easily identified by visually inspecting the solution for transient strain rates. However, if we want to detect geophysical phenomena automatically, then we need to define a detection criterion. We propose using a signal-to-noise ratio, SNR, based on  $\dot{\varepsilon}$  for our detection criterion. The Frobenius norm of  $\dot{\varepsilon}$ ,  $\|\dot{\varepsilon}\|_F$ , which is sometimes referred to as the second invariant of strain rate in the geodetic literature, is often used as a metric for the strain rate “magnitude”. Noting that  $\|\dot{\varepsilon}\|_F$  is a random variable, SNR can be taken as the ratio of the estimated mean and standard deviation of  $\|\dot{\varepsilon}\|_F$ . Using nonlinear uncertainty propagation, we find SNR to be

$$\text{SNR}(p) = \frac{\mu_{\dot{\varepsilon}_{nn}}(p)^2 + \mu_{\dot{\varepsilon}_{ee}}(p)^2 + 2\mu_{\dot{\varepsilon}_{en}}(p)^2}{(C_{\dot{\varepsilon}_{nn}}(p,p)\mu_{\dot{\varepsilon}_{nn}}(p)^2 + C_{\dot{\varepsilon}_{ee}}(p,p)\mu_{\dot{\varepsilon}_{ee}}(p)^2 + 4C_{\dot{\varepsilon}_{en}}(p,p)\mu_{\dot{\varepsilon}_{en}}(p)^2)^{\frac{1}{2}}}, \quad (5.15)$$

where the subscripts “n” and “e” denote north and east, respectively. For simplicity, we have ignored covariances between the transient strain rate components in eq. (5.15), even though they are non-zero.

## 5.4 Outlier detection

In our formulation for estimating transient strain rates, we have assumed that noise in the data vector is normally distributed. This is not an appropriate assumption for GNSS data, which often have more outliers than would be predicted for normally distributed noise. It follows that proposed methods for analyzing GNSS data should be robust against outliers (e.g., Blewitt *et al.*, 2016). In order to make our estimates of transient strain more robust, we automatically identify and remove outliers in the GNSS data as a pre-processing step.

Our method for detecting outliers is based on the data editing algorithm described in Gibbs (2011). We calculate the residuals between the observations and a best fitting model. Data with residuals that are anomalously large are then identified as outliers. We treat  $\mathbf{d}_*$  as a sample of  $\mathbf{d}$  and assume that there is no correlated noise (i.e.,  $\eta(p) = 0$ ). The best fitting model for  $\mathbf{d}_*$  is considered to be the expected value of the random vector  $u(\mathbf{P}) + \mathbf{G}\mathbf{a}$  after conditioning it with non-outlier observations. We still consider  $u$  to have a separable covariance function as in eq. (5.2), and the choice for  $X$  and  $T$  does not need to be the same as that used in Section 5.3. Since outliers are determined based on how well a spatially and temporally dependent model fits the data, we are able to identify anomalous observations which may not be immediately apparent from inspecting individual time series.

To begin the algorithm, we let  $\Omega$  be the index set of non-outliers in  $\mathbf{d}_*$  and initiate it with all  $n$  indices. This algorithm is iterative, and for each iteration we calculate the residual

vector

$$\mathbf{r} = \frac{\mathbf{d}_* - \mathbb{E} \left[ (u(\mathbf{P}) + \mathbf{G}\mathbf{a}) | \tilde{\mathbf{d}}_* \right]}{\sigma} \quad (5.16)$$

$$= \frac{1}{\sigma} \left( \mathbf{d}_* - \begin{bmatrix} C_u(\tilde{\mathbf{P}}, \tilde{\mathbf{P}}) & \mathbf{G} \end{bmatrix} \begin{bmatrix} C_u(\tilde{\mathbf{P}}, \tilde{\mathbf{P}}) + \text{diag}(\tilde{\sigma}^2) & \tilde{\mathbf{G}} \\ \tilde{\mathbf{G}}^T & \mathbf{0} \end{bmatrix}^{-1} \begin{bmatrix} \tilde{\mathbf{d}}_* \\ \mathbf{0} \end{bmatrix} \right), \quad (5.17)$$

where the tilde indicates that only elements corresponding to indices in  $\Omega$  are retained (e.g.,  $\tilde{\mathbf{P}} = \{P_i\}_{i \in \Omega}$ ). We then update  $\Omega$  to be

$$\Omega = \{i : |r_i| < \lambda \cdot \text{RMS}\}, \quad r_i \in \mathbf{r}, \quad (5.18)$$

where RMS is the root-mean-square of  $\tilde{\mathbf{r}}$  and  $\lambda$  is an outlier tolerance. We use  $\lambda = 4$  in this study, which in our experience accurately identifies outliers without unnecessarily decimating the data. Iterations continue until the new  $\Omega$  is equal to the previous  $\Omega$ .

It should be noted that this algorithm does not identify jumps in GNSS time series, which are another common issue. Some, but not all, jumps can be automatically removed by looking up the dates of equipment changes and earthquakes. However, it is still necessary to manually find and remove jumps of unknown origin. That being said, this outlier detection algorithm significantly reduces the effort needed to manually clean GNSS data.

## 5.5 Application to Cascadia slow slip events

We use our method to estimate transient strain rates in Cascadia, and we are specifically interested in identifying strain resulting from SSEs (e.g., *Dragert et al.*, 2001). In Cascadia, SSEs can be detected by monitoring for associated seismic tremor (*Rogers and Dragert*, 2003), which is actively being done by the Pacific Northwest Seismic Network (*Wech*, 2010). We can thus compare the tremor records to the transient strain rates estimated with GPR to verify that we are indeed identifying strain from SSEs.

We use the daily displacement solutions generated by the Geodesy Advancing Geosciences and EarthScope (GAGE) facility for continuous GNSS stations (*Herring et al.*, 2016). This data is publicly available and can be found at [www.unavco.org](http://www.unavco.org). We limit the dataset to the stations and time ranges which are pertinent to the seven most recent SSEs in the Puget Sound region. The earliest SSE considered in this study began in August 2010, and the most recent SSE began in February 2017. We use these most recent SSEs because the station coverage is sufficiently dense for us to use maximum likelihood methods to constrain prior models. The positions of GNSS stations used to estimate transient strain rates are

shown in Figure 5.1.

### 5.5.1 Noise model

Before we determine the transient strain rates, we must establish a prior for the transient displacements,  $u$ , and the noise,  $\eta$ . In this section we discuss our choice for the noise covariance function  $C_\eta$ . There have been numerous studies on temporally correlated noise in GNSS data (e.g., *Zhang et al.*, 1997; *Mao et al.*, 1999; *Williams et al.*, 2004; *Langbein*, 2008). In these studies, temporally correlated noise was described with some combination of Brownian motion, a first-order Gauss-Markov (FOGM) process, and/or flicker noise. There is some physical justification for using Brownian motion as a noise model because it accurately describes the power spectrum of motion resulting from instability in geodetic monuments (e.g., *Wyatt*, 1982, 1989). Here we describe the time dependence of  $\eta$  as a FOGM process and consider  $\eta$  to be spatially uncorrelated. A FOGM process is a solution to the stochastic differential equation

$$\dot{\eta}(t) + \alpha\eta(t) = \beta w(t), \quad (5.19)$$

where  $w(t)$  is white noise with unit variance. The FOGM process degenerates to the commonly used Brownian motion noise model under the condition that  $\alpha = 0$  and  $\eta(0) = 0$ . Our noise model that satisfies eq. (5.19) is a Gaussian process with zero mean and the covariance function

$$C_\eta((\vec{x}, t), (\vec{x}', t')) = \frac{\beta^2}{2\alpha} \exp(-\alpha|t - t'|) \delta(\|\vec{x} - \vec{x}'\|_2). \quad (5.20)$$

We constrain the hyperparameters for  $\eta$ ,  $\alpha$  and  $\beta$ , with a set of 38 continuous GNSS stations in Cascadia that are east of 121°W. These stations are sufficiently far from the subduction zone that they are unlikely to contain transient signal associated with SSEs. We clean the data for these stations by removing jumps at times of equipment changes, and we remove outliers that have been detected with the algorithm described in Section 5.4. We then find  $\alpha$  and  $\beta$  for each station time series with the Restricted Maximum Likelihood (REML) method (e.g., *Harville*, 1974; *Cressie*, 1993; *Hines and Hetland*, 2017a). The REML method finds the hyperparameters, which we collectively refer to as  $\theta$ , that maximize the likelihood function

$$\mathcal{L}(\theta) = \left( \frac{|\mathbf{G}^T \mathbf{G}|}{(2\pi)^{n-6m} |\boldsymbol{\Sigma}(\theta)| |\mathbf{G}^T \boldsymbol{\Sigma}(\theta)^{-1} \mathbf{G}|} \right)^{\frac{1}{2}} e^{-\frac{1}{2} \mathbf{d}_*^T \mathbf{K}(\theta) \mathbf{d}_*}, \quad (5.21)$$

where

$$\mathbf{K}(\theta) = \boldsymbol{\Sigma}(\theta)^{-1} - \boldsymbol{\Sigma}(\theta)^{-1} \mathbf{G} (\mathbf{G}^T \boldsymbol{\Sigma}(\theta)^{-1} \mathbf{G})^{-1} \mathbf{G}^T \boldsymbol{\Sigma}(\theta)^{-1}. \quad (5.22)$$

*Harville* (1974) showed that choosing the hyperparameters which maximize eq. (5.21) is

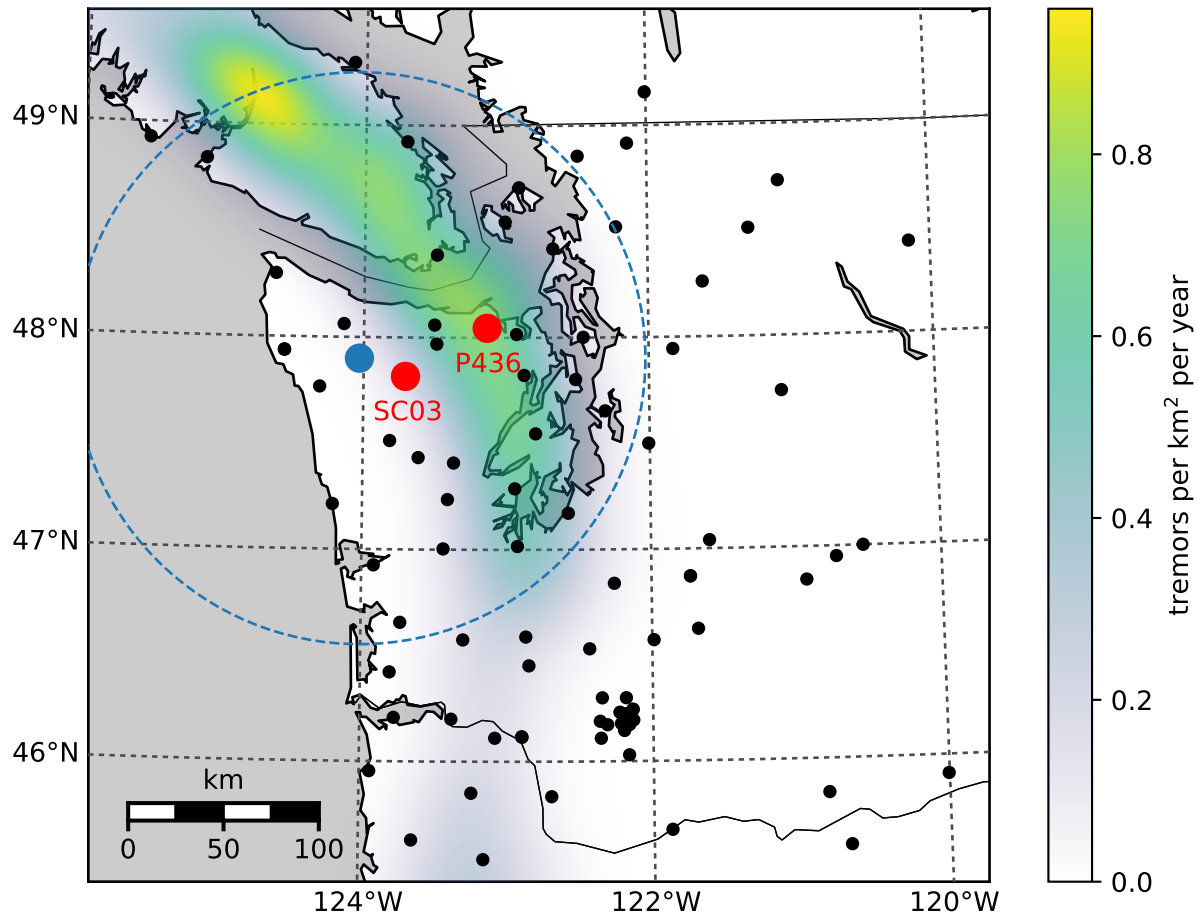


Figure 5.1: Positions of continuous GNSS stations used to estimate transient strain rates. The colored regions indicate the distribution of seismic tremor as determined by *Wech (2010)*. The red dots show the positions of GNSS stations mentioned in this paper. The blue dot indicates the location of the transient strain rates shown in Figure 5.7 and the signal-to-noise ratio shown in Figure 5.8. The blue dashed circle demarcates the spatial extent of the tremors shown in Figure 5.8.

equivalent to choosing the hyperparameters which maximize the probability of drawing  $\mathbf{d}_*$  from  $\mathbf{d}$ . We use the REML method over the maximum likelihood method (e.g., *Langbein and Johnson*, 1997) because the REML method accounts for the improper prior that we assigned to  $\mathbf{a}$  (*Hines and Hetland*, 2017a). We independently estimate  $\theta$  for each station, and so  $\mathbf{d}_*$  consists of displacements for an individual station. We are assuming  $u(p) = 0$  when estimating the noise hyperparameters for this section. The distribution of inferred  $\alpha$  and  $\beta$  are shown in Figure 5.2. The amplitude of FOGM noise,  $\beta$ , for the easting and northing components is notably low and are clustered around  $0.5 \text{ mm/yr}^{0.5}$ . The corresponding estimates of  $\alpha$  tend to cluster around  $0 \text{ yr}^{-1}$ , suggesting that noise can be described with Brownian motion. We also estimate hyperparameters for the vertical component of displacements, under the hope that vertical deformation gradients could reveal some geophysical signal. The amplitude of FOGM noise for the vertical component is relatively large with a median value of  $13.5 \text{ mm/yr}^{0.5}$ . The inferred values for  $\alpha$  are also higher for the vertical component with a median value of  $8.21 \text{ yr}^{-1}$ . In Figure 5.3, we use the median values of  $\alpha$  and  $\beta$  to generate two random samples of FOGM noise for each component. The samples span five years and over these five years the easting and northing samples drift by about 1 mm. In the context of detecting SSEs, which produce several mm's of surface displacement on the time-scale of weeks, the estimated FOGM noise for the easting and northing component is negligible. In contrast, the estimated FOGM noise for the vertical component is larger than the signal we would expect from SSEs. We suspect that the higher amplitude for the FOGM noise in the vertical component is accommodating for deficiencies in our rather simple seasonal model. Based on this analysis, we henceforth ignore temporally correlated noise in the easting and northing component because of its low amplitude. We also do not use vertical displacements because of the presumably low signal-to-noise ratio.

Another significant source of noise in GNSS data is common mode error (e.g., *Wdowinski et al.*, 1997; *Dong et al.*, 2006), which is noise that is highly spatially correlated. When not accounted for, common mode error manifests as spatially uniform undulations in estimated transient displacements. However, estimated transient strain rates are insensitive to common mode error. We therefore do not include common mode error in our noise model. We then make the simplifying assumption that  $\eta(p) = 0$  for the easting and northing component of GNSS data.

### 5.5.2 Prior model

We next establish our prior model for transient displacements. Specifically, we discuss our choice for the covariance functions  $X(\vec{x}, \vec{x}')$  and  $T(t, t')$ . For  $X$ , we use the squared expo-

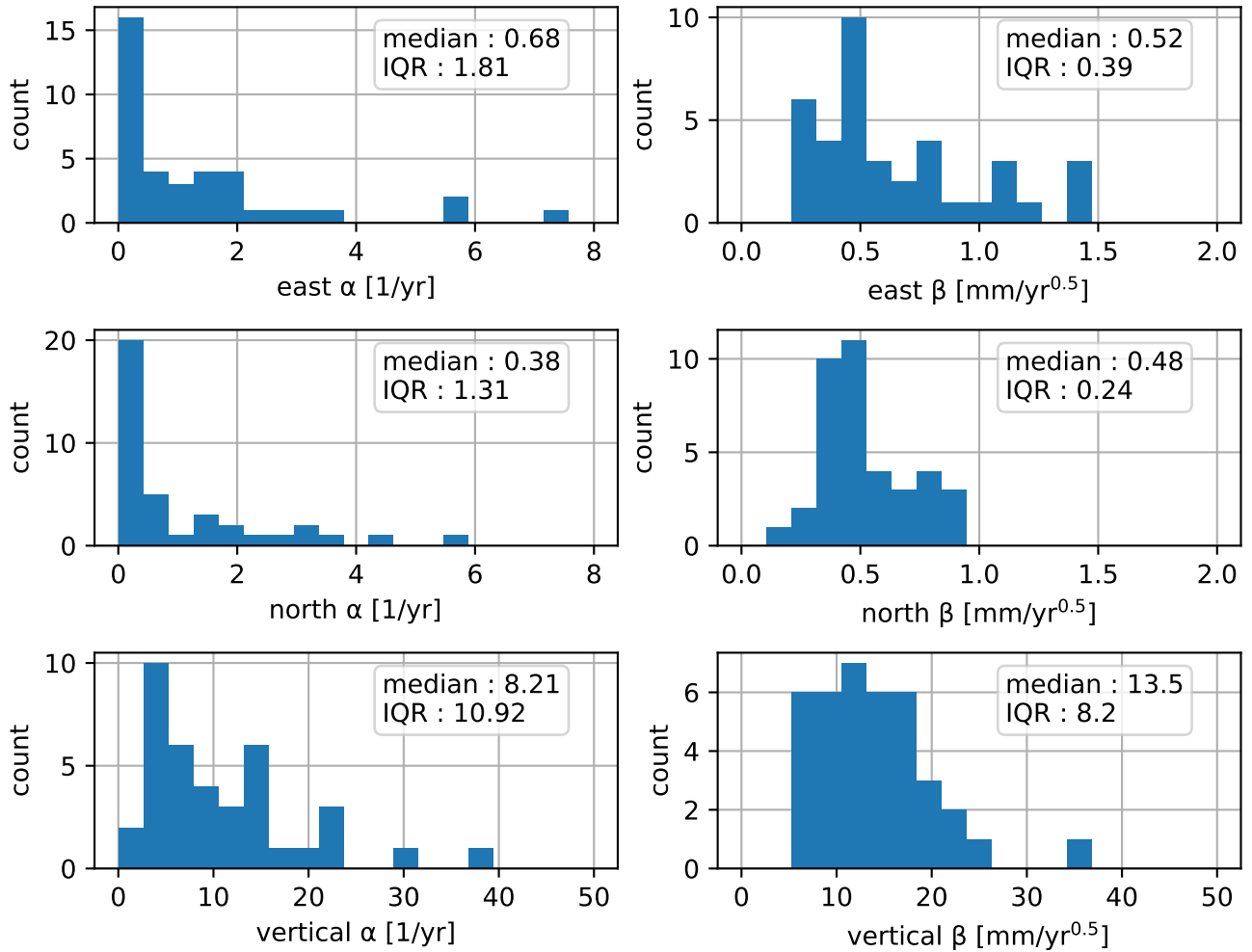


Figure 5.2: Distribution of estimated FOGM hyperparameters (eq. 5.20). Hyperparameters are estimated with the REML method for 38 stations in Cascadia that are east of  $121^\circ\text{W}$ . “IQR” is the interquartile range.

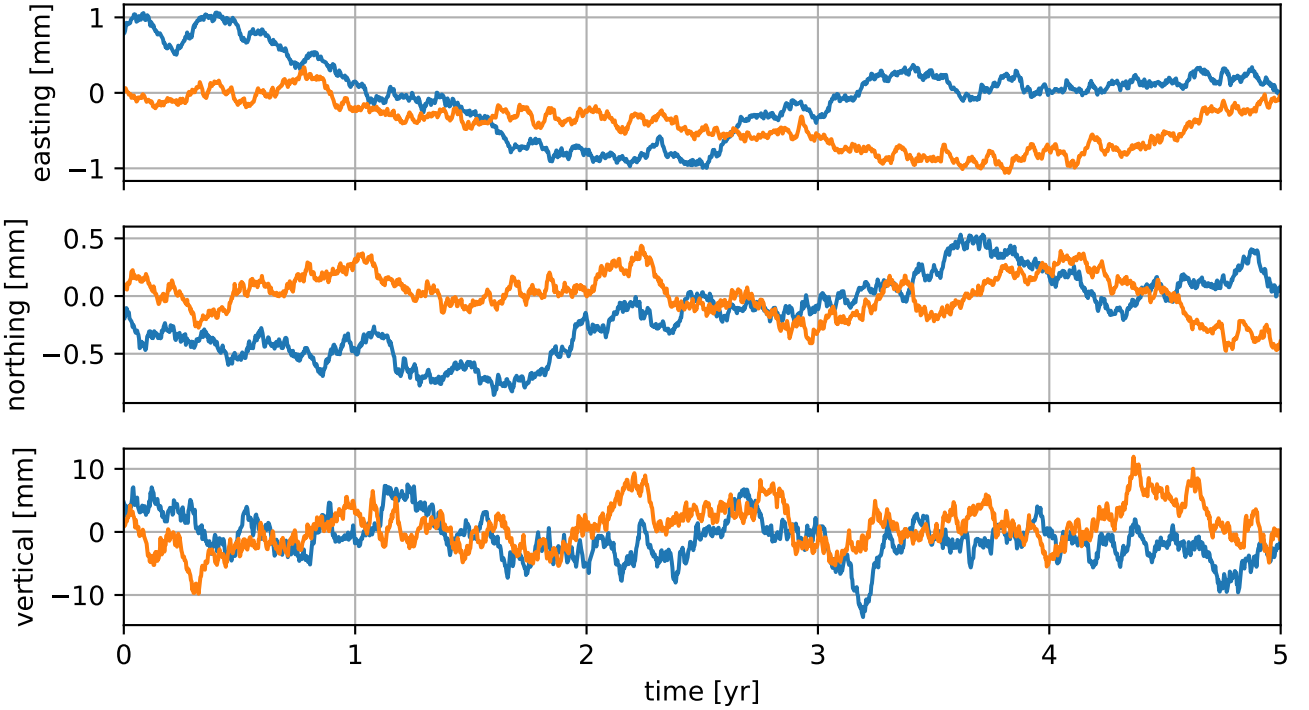


Figure 5.3: Two FOGM noise samples for each component. The FOGM hyperparameters have been set to the median values from Figure 5.2.

ponential (SE) covariance function,

$$X(\vec{x}, \vec{x}') = \exp\left(\frac{-||\vec{x} - \vec{x}'||_2^2}{2\ell^2}\right). \quad (5.23)$$

The SE covariance function is commonly used in kriging (e.g., *Cressie*, 1993) and Gaussian process regression (e.g., *Rasmussen and Williams*, 2006). The SE is a positive definite covariance function for any number of spatial dimensions. A Gaussian process with an SE covariance function is isotropic and has realizations that are infinitely differentiable. In terms of geodetic applications, *Kato et al.* (1998) and *El-Fiky and Kato* (1998) demonstrated that the SE accurately describes the covariance of secular GNSS derived velocities in Japan.

We consider three potential models for the temporal covariance of  $u$ . First, we consider the one-dimensional SE covariance function,

$$T(t, t') = \phi^2 \exp\left(\frac{-|t - t'|^2}{2\tau^2}\right). \quad (5.24)$$

Note that  $T$  includes the hyperparameter  $\phi$ , which serves to scale the covariance function  $C_u$ . Second, we consider integrated Brownian motion (IBM). IBM has zero mean and its

covariance function can be found by integrating the covariance function for Brownian motion as

$$T(t, t') = \int_0^t \int_0^{t'} \phi^2 \min(s, s') ds' ds \quad (5.25)$$

$$= \frac{\phi^2}{2} \min(t, t')^2 \left( \max(t, t') - \frac{1}{3} \min(t, t') \right), \quad t, t' \geq 0. \quad (5.26)$$

IBM has been used in the context of Kalman filtering as a non-parametric model for the time dependence of geophysical signals (e.g., *Segall and Mathews*, 1997; *McGuire and Segall*, 2003; *Ohtani et al.*, 2010; *Hines and Hetland*, 2016). It should be emphasized  $t = 0$  is a reference time at which the Gaussian process is exactly zero. For some geophysical signals, it is appropriate to have this reference time. For example, if we are trying to identify postseismic deformation then  $t$  should be zero at the time of the earthquake. However, if we are interesting in detecting transient events, where there is no known start time, then IBM may not be an appropriate prior, and an isotropic Gaussian process should be preferred. In the following analysis, we make the quite arbitrary choice that  $t$  is zero on the first epoch of  $\mathbf{d}_*$ . Using an earlier reference time does not change the results discussed in this section. Our third option for  $T$  is the Wendland class of covariance functions (*Wendland*, 2005). Wendland covariance functions have compact support and hence their corresponding covariance matrices are sparse. In our analysis, we exploit this sparsity with the CHOLMOD software package (*Chen et al.*, 2008). Wendland functions are positive definite in  $\mathbb{R}^d$ , and they describes an isotropic Gaussian process with realizations that can be differentiated  $k$  times. The form of the covariance function depends on the choice of  $d$  and  $k$ . We use  $d = 1$  since we are describing the temporal covariance of  $u$ . We use  $k = 2$ , giving samples of  $u$  continuous velocities and accelerations. The corresponding Wendland covariance function is

$$T(t, t') = \phi^2 \left( 1 - \frac{|t - t'|}{\tau} \right)_+^5 \left( \frac{8|t - t'|^2}{\tau^2} + \frac{5|t - t'|}{\tau} + 1 \right), \quad (5.27)$$

where

$$(t)_+ = \begin{cases} t, & t > 0 \\ 0, & \text{otherwise.} \end{cases} \quad (5.28)$$

We next determine appropriate hyperparameters for  $X$  and each of the three candidate covariance functions for  $T$ . First, we clean the GNSS datasets by removing offsets at times of equipment changes and removing outliers with the method describe in Section 5.4. For the outlier detection algorithm, our prior model,  $u$ , is chosen to have a length-scale and time-scale which is able to approximately describe SSE displacements. We use the SE covariance

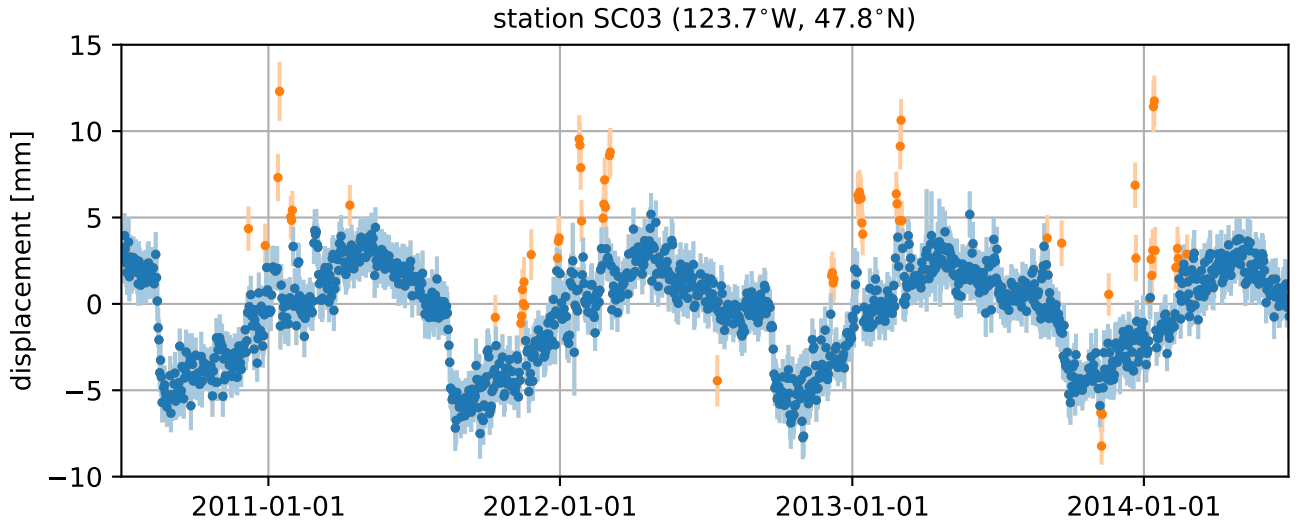


Figure 5.4: Detrended easting component of displacements at station SC03, which is located on Mount Olympus in Washington. The orange markers indicate outliers that were automatically detected using the algorithm from Section 5.4. The error bars show one standard deviation uncertainties. Note that outliers tend to be observed in the winter, suggesting that they were caused by snow or ice.

function for  $X$  with length-scale  $\ell = 100$  km, and we use the Wendland covariance function for  $T$ , due to its computational efficiency, with time-scale  $\tau = 0.1$  yr and  $\phi = 1$  mm. The outlier detection algorithm is particularly effective at removing outliers for stations at high elevation (Figure 5.4), which can be adversely affected by ice or snow during the winter (Lisowski *et al.*, 2008). After cleaning the dataset, we divide it into seven subsets which are four months long and each centered on the time of a SSE. The times of the seven SSEs are determined with tremor records from Wech (2010). We use the REML method to find the optimal hyperparameters for  $T$  and  $X$  for each subset of data. We choose to make each data subsets four months long because it is long enough to encompass a SSE in Cascadia, while it is short enough to still be computationally tractable. However, four months is too short to resolve the sinusoids in  $\mathbf{d}$ , and they are omitted from  $\mathbf{d}$  in this REML analysis for Cascadia SSEs. The estimated hyperparameters for  $u$  are summarized in Table 1. Based on the interquartile ranges, the estimated hyperparameters for the SE and Wendland covariance functions do not vary significantly between SSEs. This suggests that the median of estimated hyperparameters should be an appropriate prior model for all Cascadia SSEs. For the IBM model, there are several anomalously large values for  $\ell$  and  $\phi$ , which results in large interquartile ranges.

Next we identify which covariance function for  $T$  best describes the SSEs. One approach is to compare the REML likelihoods for each covariance function, similar to the analysis in Langbein (2004). In Table 1, we summarize how the log REML likelihoods for the Wend-

Table 5.1: Optimal hyperparameters for the prior on transient displacements determined with the REML method. The temporal covariance function is indicated by the “ $T$ ” column. The SE, IBM, and Wendland covariance functions are defined in eqs. (5.24), (5.25), and (5.27), respectively. The spatial covariance function,  $X$ , is the squared exponential (eq. 5.23) in all cases. The hyperparameters are estimated for each of the seven SSEs considered in this study, and the tabulated values indicate the median and interquartile ranges of estimates. The “diff log(REML)” column compares the log REML likelihood to the log REML likelihood when using the SE covariance function for  $T$ . Negative values indicate that observations are more consistent with the SE covariance function.

$T$	direction	$\ell$	$\phi$	$\tau$	diff. log(REML)
SE	east	$92 \pm 25$ km	$0.62 \pm 0.11$ mm	$0.026 \pm 0.011$ yr	-
SE	north	$91 \pm 53$ km	$0.43 \pm 0.05$ mm	$0.030 \pm 0.017$ yr	-
Wendland	east	$95 \pm 30$ km	$0.66 \pm 0.15$ mm	$0.093 \pm 0.044$ yr	$0.78 \pm 0.87$
Wendland	north	$92 \pm 57$ km	$0.46 \pm 0.10$ mm	$0.116 \pm 0.057$ yr	$0.08 \pm 0.58$
IBM	east	$110 \pm 130$ km	$290 \pm 420$ mm/yr <sup>1.5</sup>	-	$-16.4 \pm 7.8$
IBM	north	$150 \pm 560$ km	$110 \pm 250$ mm/yr <sup>1.5</sup>	-	$-10.1 \pm 2.3$

land and IBM covariance functions compare to the SE covariance function. Based on the differences in log REML likelihoods, the data is substantially more likely to come from a Gaussian process with a SE or Wendland covariance function than an IBM covariance function. The REML likelihoods do not definitively indicate whether the SE or Wendland covariance function is preferable.

To further explore which covariance function for  $T$  best describes SSEs, we compare the observations to the predicted displacements for each covariance function. We consider the data prediction vector to be  $\hat{\mathbf{d}} = (u(\mathbf{P}) + \mathbf{G}\mathbf{a})|\mathbf{d}_*$ . Following a similar procedure as in Section 5.3, it can be shown that  $\hat{\mathbf{d}}$  is normally distributed with mean

$$\mu_{\hat{d}} = \begin{bmatrix} C_u(\mathbf{P}, \mathbf{P}) & \mathbf{G} \end{bmatrix} \begin{bmatrix} \Sigma & \mathbf{G} \\ \mathbf{G}^T & \mathbf{0} \end{bmatrix}^{-1} \begin{bmatrix} \mathbf{d}_* \\ \mathbf{0} \end{bmatrix} \quad (5.29)$$

and covariance

$$\mathbf{C}_{\hat{\mathbf{d}}} = C_u(\mathbf{P}, \mathbf{P}) - \begin{bmatrix} C_u(\mathbf{P}, \mathbf{P}) & \mathbf{G} \end{bmatrix} \begin{bmatrix} \Sigma & \mathbf{G} \\ \mathbf{G}^T & \mathbf{0} \end{bmatrix}^{-1} \begin{bmatrix} C_u(\mathbf{P}, \mathbf{P}) \\ \mathbf{G}^T \end{bmatrix}. \quad (5.30)$$

We compute  $\hat{\mathbf{d}}$  using SE, Wendland, and IBM covariance functions for  $T$  and the median hyperparameters from Table 1. Figure 5.5 compares the easting component of  $\mathbf{d}_*$  to  $\hat{\mathbf{d}}$  for the winter 2015-2016 SSE at station P436, which is among the stations that record the strongest signal. The data prediction vector reasonable fits the displacements throughout the SSE, regardless of the choice of  $T$ . The prediction for the IBM covariance function contains slightly more high frequency, and perhaps spurious, features. The predictions for the Wendland and

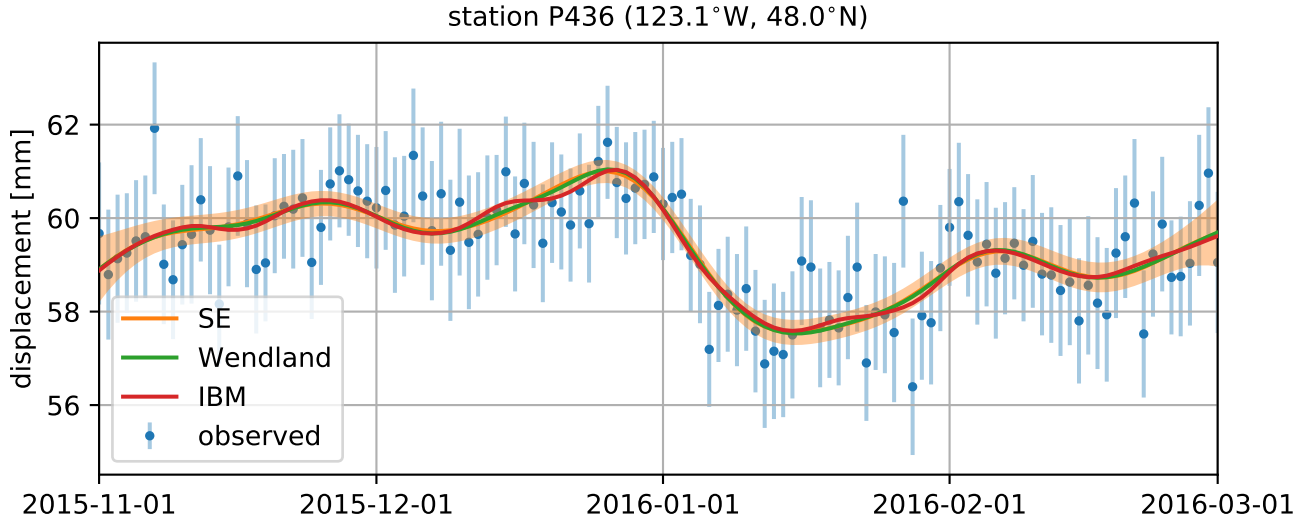


Figure 5.5: Observed easting component of displacements at station P436 and predicted displacements when using different covariance functions for  $T$ . The one standard deviation uncertainties are shown for the observations and the predicted displacements when using the SE covariance function. For clarity, uncertainties are not shown for the IBM and Wendland covariance functions, but they are nearly equivalent to the uncertainties for the SE covariance function.

SE covariance functions are nearly indistinguishable. Overall, the predicted displacements are not strongly sensitive to the choice of temporal covariance function. In our estimates of transient strain discussed in the next section, we ultimately settle on the Wendland covariance function for  $T$  and use the median values from Table 1 for the hyperparameters. We choose the Wendland covariance function over the SE covariance function because of its computational advantages.

### 5.5.3 Transient strain rates

Having established a noise model and a prior for transient displacements, we use the cleaned GNSS dataset to calculate transient strain rates in the Puget Sound region. We calculate transient strain rates for each day from January 1, 2010 to May 15, 2017. The strain rates are estimates at a grid of points spanning the study area. In Figure 5.6 we show the transient strain rates on January 1, 2016, which coincides with the height of an SSE. We have included an animation showing the map view of strain rates through time as supplementary material. The strain rates shown in Figure 5.6 are generally similar to the strain rates during the other six SSEs considered in this study. The SSEs cause trench perpendicular compression in the Olympic Peninsula and extension east of Puget Sound. The strain transitions from compressional to extensional strain around the southern tip of Vancouver Island, which coincides with the location of where thrust slip tends to be inferred for SSEs in the Puget

Sound region (e.g., *Dragert et al.*, 2001; *Wech et al.*, 2009; *Schmidt and Gao*, 2010). Thus, this pattern of strain is to be expected. During the period in between SSEs, secular strain rates indicate trench perpendicular compression throughout this study region (*Murray and Lisowski*, 2000; *McCaffrey et al.*, 2007, 2013). When comparing inferred strain rates from SSEs to the secular strain rates, we see that SSEs are concentrating tectonically accumulated strain energy towards the trench, and presumably pushing the subduction zone closer to failure.

In Figure 5.7 we show the time dependence of estimated transient strain rates at a position on the Olympic Peninsula, where transient strain rates from SSEs are largest. To verify that the estimated transient strain rates are accurately identifying geophysical signal, we compare the signal-to-noise ratio from eq. (5.15) to the frequency of seismic tremor (Figure 5.8). A signal-to-noise ratio greater than  $\sim 3$  can be interpreted as a detected geophysical signal. For each detected event there is a corresponding peak in seismic tremor. We are also able to clearly identify transient strain associated with a more subtle SSE in August 2014. In between peaks in seismic tremor, the signal-to-noise ratio is consistently between 0 and 2, suggesting that all the transient strain detected at this location is associated with SSEs.

The results we have presented thus far indicate that we are identifying the strain that we should expect to see. There are, however, subtle features in our estimated transient strain rates which we were not expecting. For example, there is a brief period of east-west extension on the Olympic Peninsula several days prior to some of the SSEs. This feature can be seen before the summer 2012 and winter 2015-2016 SSEs in Figure 5.7 as well as in the supplementary animation. While this deformation is noteworthy, a discussion on the mechanisms causing it is outside the scope of this study.

## 5.6 Discussion

Our results demonstrate that GPR is an effective tool for estimating transient strain from GNSS data, which can then be used to detect geophysical processes. One may argue that geophysical signal can also be detected by merely inspecting the GNSS displacement time series. Indeed, the SSEs identified in Figure 5.8 do produce visible displacements in the GNSS data. However, the GNSS data also contains outliers and non-tectonic deformation that is localized to individual stations. In contrast, our estimates of transient strain only identify features that are sufficiently spatially and temporally coherent, based on our chosen prior model. Furthermore, our estimates of transient strain are insensitive to common mode noise, which is highly spatially correlated noise resulting from factors such as reference frame error. Common mode noise can obscure geophysical signal in the GNSS data, but it gets

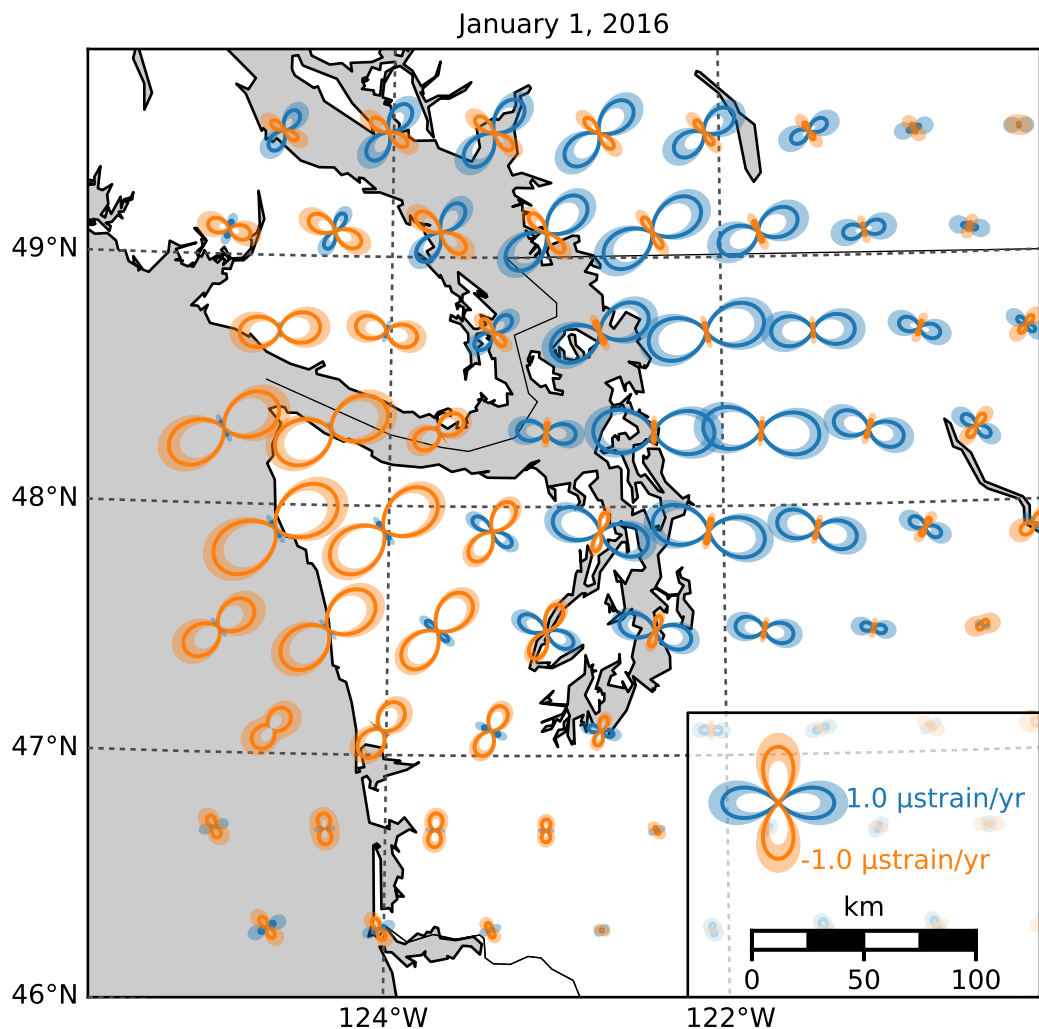


Figure 5.6: Estimated transient strain rates during the Winter 2015-2016 SSE. Strain glyphs show the normal strain rate along each azimuth, where orange indicates compression and blue indicates extension. The shaded regions indicate one standard deviation uncertainties in the normal strain rates.

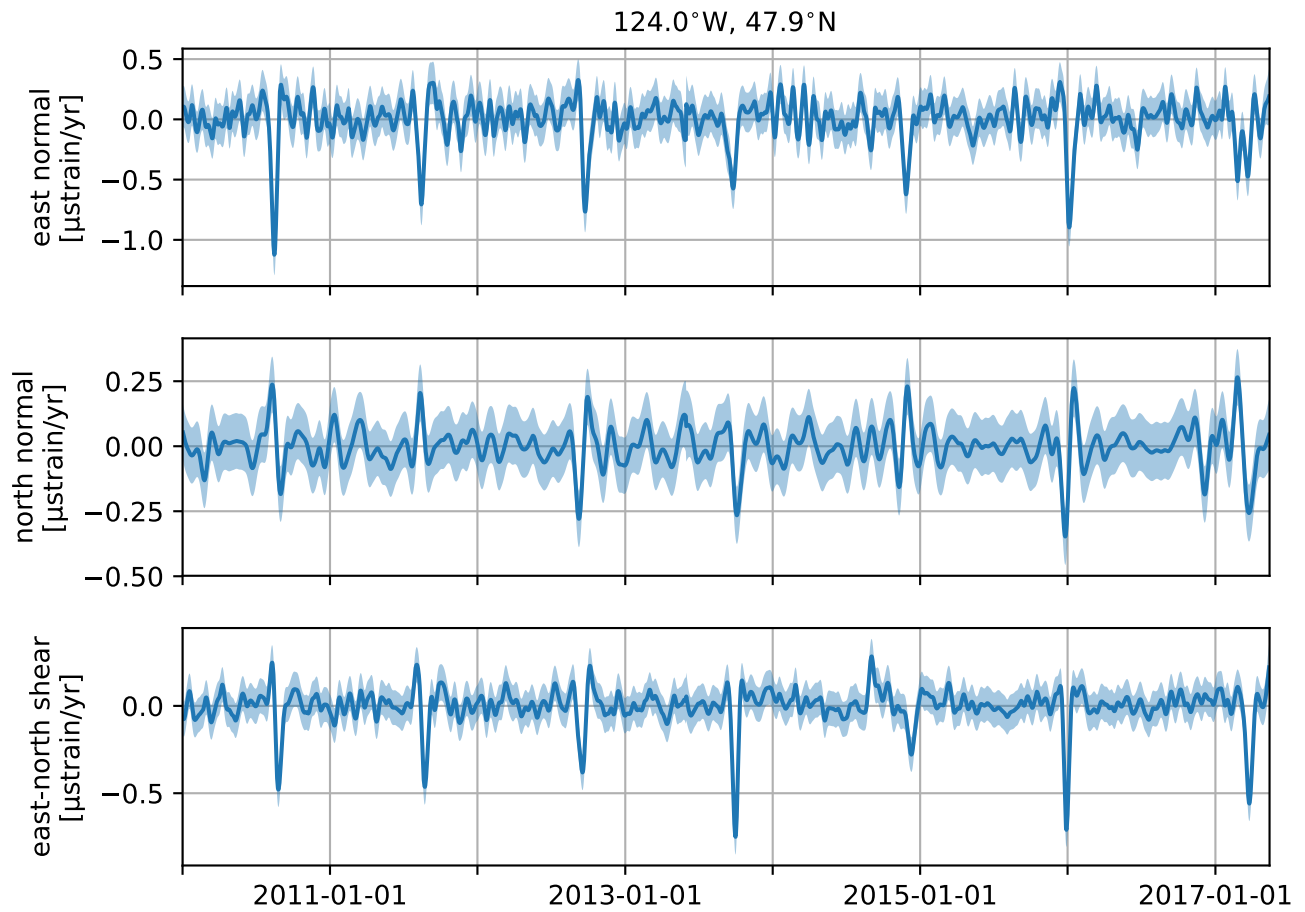


Figure 5.7: Three components of the transient horizontal strain rate tensor estimated at the position shown in Figure 5.1. The shaded regions indicate one standard deviation uncertainty.

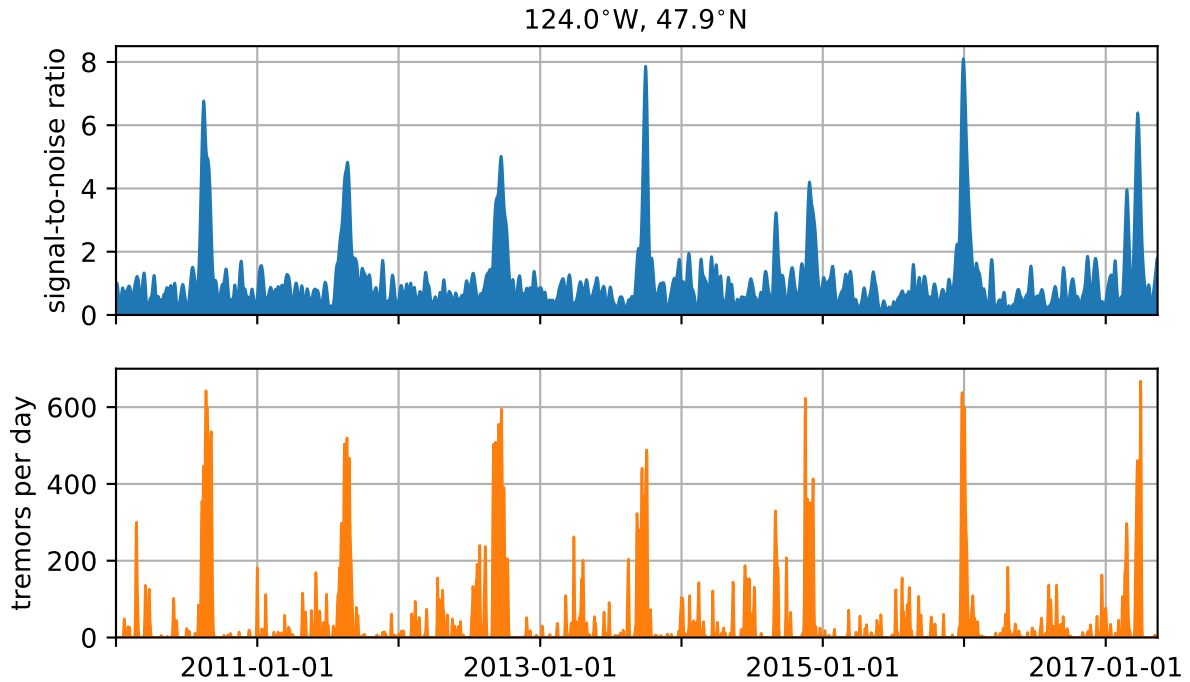


Figure 5.8: (top) Signal-to-noise ratio (eq. 5.15) at the position shown in Figure 5.1. (bottom) Frequency of tremors in the region shown in Figure 5.1.

canceled out when computing the transient strain. Lastly, our estimates of transient strain rates are a spatial and temporal derivative of displacements, and thus any geophysical signal in the transient strain rates tends to be more pronounced than in the GNSS data. For these reasons, we argue that transient strain rates estimated with the method described in Section 5.3 can illuminate geophysical signal that may not be discernible from the noise in the GNSS displacement data.

In addition to detecting geophysical processes, the GNSS derived transient strain rates can be used to better understand the data from borehole strain meters (BSMs). The Plate Boundary Observatory maintains about forty BSMs in the Pacific Northwest, and it has been demonstrated that BSMs are able to record transient geophysical events such as SSEs (e.g., *Dragert and Wang, 2011*). However, there are complications that prevent BSM data from being used quantitatively in geophysical studies. One difficulty is that BSM data should be calibrated with a well known strain source, such as diurnal and semidiurnal tides (*Hart et al., 1996; Roeloffs, 2010; Hodgkinson et al., 2013*). Unfortunately, the tidal forces at BSMs which record SSEs are strongly influenced by local bodies of water such as the Straight of Juan de Fuca, making it difficult to form a theoretical prediction of tidal strains (*Roeloffs, 2010*). Another complication is that noise in BSM data is not well understood. The noise

consists, in part, of a long-term decay resulting from the instrument equilibrating with the surrounding rock (*Gladwin et al.*, 1987). Typically, this noise is dealt with in an ad-hoc manner by fitting and removing exponentials and low-order polynomials. We envision that the GNSS derived strain rates from this paper can be used as a reference strain for calibrating BSM data and quantify its noise.

There is potential for a more thorough analysis of the spatio-temporal noise in GNSS data,  $\eta$ , than what was performed in Section 5.5.1. We did not explore the spatial covariance of  $\eta$ , which would describe common mode noise. We are able to ignore common mode error in this study; however, for other geophysical studies based on GNSS data, such as fault slip inversions, it may be necessary to incorporate a spatially covarying noise model (e.g., *Miyazaki et al.*, 2003). We can also improve upon the seasonal model used in this study, which consists of four spatially uncorrelated sinusoids for each station. We did not explore the spatial covariance of seasonal deformation or the temporal roughness (i.e., the number of sinusoids needed to describe the observations). The periodic Gaussian process (*Mackay*, 1998) is an alternative model for seasonal deformation and is well suited for exploring the roughness of seasonal deformation. The periodic Gaussian process has zero mean and the covariance function

$$T(t, t') = \phi^2 \exp\left(\frac{-\sin(\pi|t - t'|)^2}{2\tau^2}\right). \quad (5.31)$$

Realizations have annual periodicity and the roughness is controlled by  $\tau$ . Decreasing  $\tau$  has the same effect as including higher frequency sinusoids in the seasonal model. The optimal value for  $\tau$  can be found with the REML method as described in Section 5.5.1.

The transient strain rates estimated in this study are constrained by about seven years of daily displacement observations from 94 GNSS stations. It can be computationally intensive to evaluate eqs. (5.10) and (5.11) for a dataset with this size. We significantly reduce the amount of memory needed to estimate transient strain rates by describing the temporal covariance of displacements with a compact Wendland covariance function. Using a compact covariance function for our prior turns eqs. (5.10) and (5.11) into sparse systems of equations, which we then solve with CHOLMOD. CHOLMOD is designed for solving sparse, positive definite systems of equations. The matrix being inverted in eqs. (5.10) and (5.11) is not positive definite; however, we can use another partitioned matrix inversion identity from *Press et al.* (2007) to partition it into positive definite submatrices to be inverted. Even when using a compact covariance function, it may still be necessary to reduce the computational burden by dividing the data into subsets and evaluating transient strain rates for each subset.

## 5.7 Conclusion

In this paper we propose using Gaussian process regression (GPR) to estimate transient strain rates from GNSS data. Most other methods for estimating strain rates assume a parametric representation of deformation, which can bias the results if the parameterization is not chosen carefully. Here we assume a stochastic, rather than parametric, prior model for displacements. Our prior model describes how much we expect transient displacements to covary spatially and temporally. If we know nothing about the underlying signal that we are trying to recover, then the prior model can be chosen objectively with maximum likelihood methods. Because GPR is a Bayesian method, the uncertainties on our estimated transient strain rates are well quantified, allowing one to discern geophysical signal from noise. We demonstrate that GPR is an effective tool for detecting geophysical phenomena, such as slow slip events, in our application to GNSS data from Cascadia. One limitation with GPR is that it is not robust against outliers. To overcome this limitation, we have introduced an effective pre-processing method for identifying and removing outliers from GNSS datasets. Another complication with GPR is that it usually involves inverting a dense matrix where the number of rows and columns is equal to the number of observations. This is prohibitive when using several years of daily GNSS observations from a network of several hundred stations. We significantly reduce the computational burden of GPR by using compact Wendland covariance function to describe our prior model. While this paper just focuses on estimating transient strain rates, we believe that GPR is a powerful tool that can be applied to a wide range of geophysical problems.

## 5.8 Acknowledgements

This material is based upon work supported by the National Science Foundation under grant EAR 1245263. The EarthScope Plate Boundary Observatory data is provided by UNAVCO through the GAGE Facility with support from the National Science Foundation (NSF) and National Aeronautics and Space Administration (NASA) under NSF Cooperative Agreement EAR-1261833. An implementation of the method described in this paper is named Python-based Geodetic Network Strain software (PyGeoNS). PyGeoNS is distributed under the MIT License and can be found at [www.github.com/treverhines/PyGeoNS](http://www.github.com/treverhines/PyGeoNS).

## CHAPTER 6

### Validating Plate Boundary Observatory borehole strainmeter data with GNSS derived strain

#### 6.1 Introduction

The Plate Boundary Observatory (PBO) contains 82 borehole strain meters (BSMs), most of which are installed along the western United States. BSMs are able to detect geophysical processes such as coseismic and postseismic deformation (e.g., *Langbein et al.*, 2006; *Langbein*, 2015), slow slip events (SSEs) (e.g., *Dragert and Wang*, 2011), and seismic wave propagation (*Barbour and Crowell*, 2017). BSMs are intended for measuring deformation over timescales of minutes to months. At longer timescales, BSM data is contaminated by factors such as borehole relaxation (*Gladwin et al.*, 1987). SSEs and postseismic deformation occur on timescales that near the upper limit of what BSMs can be expected to resolve. Another complication with BSM data is that the strain measured at the borehole may deviate from the regional strain due to local topographic or geologic features (*Berger and Beaumont*, 1976). Due to these sources of noise, it can be difficult to use BSM data quantitatively in, for example, geophysical inverse problems. In this study, we assess the ability of BSMs to measure strain resulting from SSEs on the Cascadia subduction zone. This is done by comparing BSM data to strain derived from GNSS data.

#### 6.2 BSM Data

There are about forty PBO BSMs in the Pacific Northwest, and only five of them, B003, B004, B005, B007, and B018, record noticeable deformation from SSEs. We limit our attention to these five stations in this study. The remaining stations either contain too much noise on the timescale of SSEs or are too far away from the SSEs to observe any strain. Each of the PBO BSMs are Gladwin four-component tensor strainmeters, which are about 2 m long, 8.7 cm in diameter, and are installed at about 100 to 200 m depth. Each BSM contains four extensometers, or gauges. Only three gauges are necessary to completely determine the

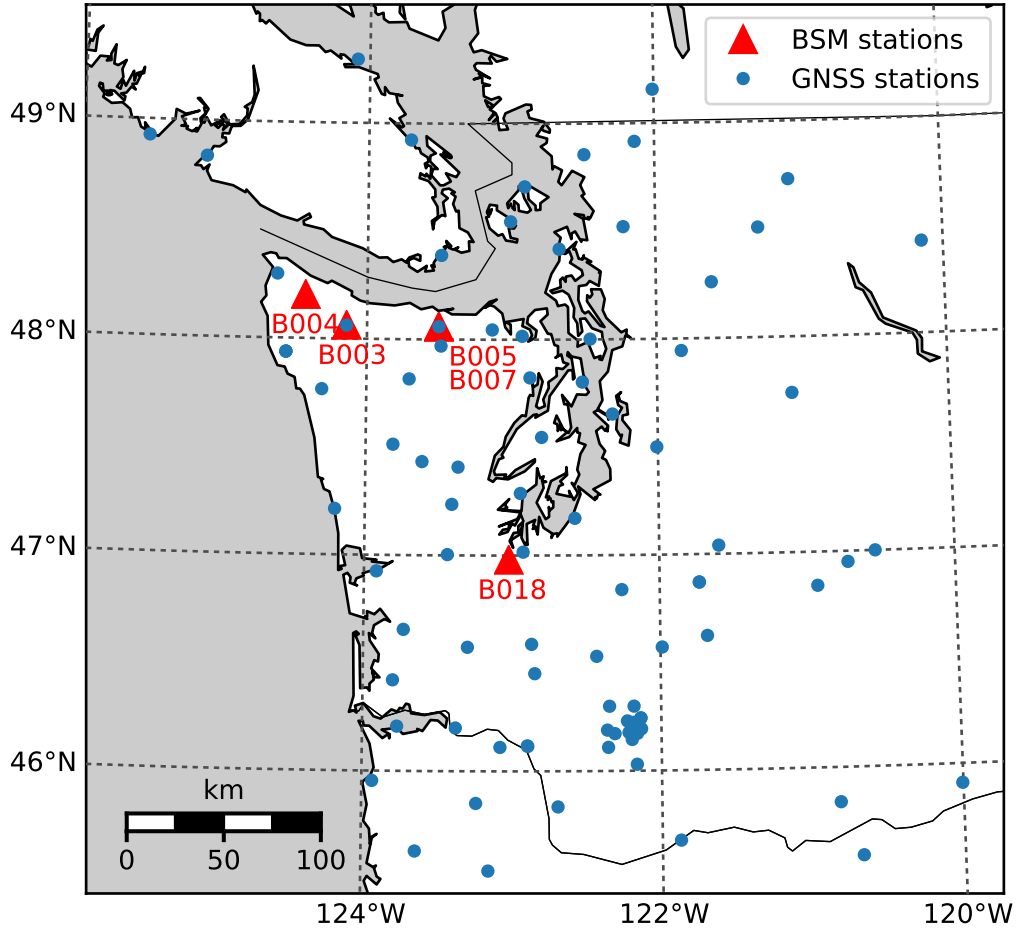


Figure 6.1: Location of BSM and GNSS stations used in this study.

horizontal strain tensor, and the fourth gauge is included for redundancy. Gauges 1, 2, and 3 are oriented  $60^\circ$ ,  $120^\circ$ , and  $150^\circ$  counterclockwise from gauge 0.

We use the level 2 gauge data provided by UNAVCO at [www.unavco.org](http://www.unavco.org), which has undergone several post-processing steps. In the level 2 gauge data a borehole curing trend is estimated and removed by fitting two exponential terms and a linear trend to the data. The level 2 data is corrected for tidal strains by estimating and removing sinusoids with known tidal frequencies. There is also a correction for barometric pressure because the normal stress imposed on the surface by barometric pressure results in horizontal strains recorded by the BSM. The barometric pressure correction is the observed barometric pressure at each site multiplied by a best fitting scaling factor. Lastly, offsets have been removed in the level 2 data product.

We denote the extension measured at gauge  $i$  as  $e_i$ , and the horizontal strain tensor components as  $\varepsilon_{xx}$ ,  $\varepsilon_{yy}$ , and  $\varepsilon_{xy}$ , where  $x$  and  $y$  indicate the east and north direction, respectively. The extensions measured at BSMs are traditionally converted to areal strain,  $\varepsilon_a = \varepsilon_{xx} + \varepsilon_{yy}$ ,

differential strain,  $\varepsilon_d = \varepsilon_{xx} - \varepsilon_{yy}$ , and engineering shear strain,  $\varepsilon_s = 2\varepsilon_{xy}$ . We follow this convention and use  $\varepsilon_a$ ,  $\varepsilon_d$ , and  $\varepsilon_s$  for comparing BSM data to GNSS derived strains. Using  $\theta_0$  to denote the orientation of gauge 0, in degrees north of east, these strain components can be expressed in terms of the gauge measurements through the equation

$$\begin{bmatrix} \varepsilon_a \\ \varepsilon_d \\ \varepsilon_s \end{bmatrix} = 2\mathbf{K}^{-1} \begin{bmatrix} 1 & \cos(2\theta_0) & \sin(2\theta_0) \\ 1 & \cos(2(\theta_0 + 60)) & \sin(2(\theta_0 + 60)) \\ 1 & \cos(2(\theta_0 + 120)) & \sin(2(\theta_0 + 120)) \\ 1 & \cos(2(\theta_0 + 150)) & \sin(2(\theta_0 + 150)) \end{bmatrix}^+ \begin{bmatrix} e_0 \\ e_1 \\ e_2 \\ e_3 \end{bmatrix}, \quad (6.1)$$

where “+” indicates the Moore-Penrose pseudoinverse and  $\mathbf{K}$  is a coupling matrix describing how the instrument strains relate to the crustal strains (*Hart et al.*, 1996). The components  $\varepsilon_a$ ,  $\varepsilon_d$ , and  $\varepsilon_s$  represent crustal strains, and  $e_i$  are instrument strains. We assume that BSMs are installed in homogeneous, isotropic rock, allowing us to write the coupling matrix as

$$\mathbf{K} = \begin{bmatrix} c & 0 & 0 \\ 0 & d & 0 \\ 0 & 0 & d \end{bmatrix}, \quad (6.2)$$

where  $c$ , and  $d$  are response factors that depend on the elastic properties of the instrument, the grout, and surrounding rock (*Gladwin and Hart*, 1985). Based on the analysis of *Gladwin and Hart* (1985), we use  $c = 1.5$  and  $d = 3.0$ . UNAVCO, the organization responsible for maintaining the PBO BSMs and disseminating their data, use these same response factors for their final data products.

Local topographic or geologic features can cause  $\mathbf{K}$  to have non-zero off diagonal elements. If possible, the components of  $\mathbf{K}$  should be determined in-situ by calibrating the BSM data with a well known strain source, such as diurnal and semi-diurnal tides (*Hart et al.*, 1996; *Roeloffs*, 2010; *Hodgkinson et al.*, 2013). *Hart et al.* (1996) calibrated a BSM at Pinyon Flat, using the tidal strains recorded at a collocated laser strain meter. This calibration method is, of course, not possible for most PBO BSMs. *Roeloffs* (2010) and *Hodgkinson et al.* (2013) calibrated PBO BSMs using theoretical predictions of tidal strains (e.g., *Agnew*, 1997). This approach is still not adequate for BSMs near large local bodies of water, which can make it difficult to form an accurate theoretical estimate of tidal strains. As determined by *Roeloffs* (2010), the five BSM stations considered in this paper are too close to the Straight of Juan de Fuca to be accurately calibrated with tidal strains. Since in-situ calibration is not possible, we note that our choice for  $\mathbf{K}$  is likely to be a significant source of error in BSM data. Another potential source of error is the assumed orientation for  $\theta_0$ . This orientation is determined by

a compass on the instrument, and it is possible that magnetic minerals in the surrounding rock can give the compass an incorrect reading.

### 6.3 GNSS derived strain

We compare the BSM strain components to transient strains estimated from GNSS data. Here we consider transient strains to be any deviation from the secular strain rate. We use daily GNSS displacement solutions for 94 continuous GNSS stations in the Pacific Northwest (Figure 6.1). This data has also been made available through UNAVCO. We convert the GNSS data to transient strains using Gaussian process regression (GPR) as described in *Hines and Hetland* (2017b). With GPR, we select a prior spatio-temporal covariance model for the geophysical signal that we want to recover. Following *Hines and Hetland* (2017b), we assume that our prior for displacements is a Gaussian process with zero mean, and covariance function described by

$$C_u((t, x), (t', x')) = \phi^2 T(t, t') X(x, x'), \quad (6.3)$$

where  $T$  is the Wendland covariance function

$$T(t, t') = \left(1 - \frac{|t - t'|}{\tau}\right)_+^5 \left(\frac{8|t - t'|^2}{\tau^2} + \frac{5|t - t'|}{\tau} + 1\right), \quad (6.4)$$

and  $X$  is the squared exponential covariance function

$$X(\vec{x}, \vec{x}') = \exp\left(\frac{-||\vec{x} - \vec{x}'||_2^2}{2\ell^2}\right). \quad (6.5)$$

The hyperparameters  $\phi$ ,  $\tau$ , and  $\ell$  control the amplitude, characteristic time-scale, and characteristic length-scale of the prior, respectively. *Hines and Hetland* (2017b) found that the optimal hyperparameters for describing displacements from SSEs are roughly  $\phi = 0.5$  mm,  $\tau = 0.1$  yr, and  $\ell = 100$  km. These parameters were chosen objectively using maximum likelihood methods; however based on our experience, this prior may not be sufficiently flexible to describe all the observed data. Consequently, we explore using lower values for  $\tau$  and  $\ell$  and a higher value for  $\phi$ . For each tested set of hyperparameters, we condition the prior with the observed GNSS data and visually compare the posterior displacements to the observations. We settle on the values  $\phi = 1.0$  mm,  $\tau = 0.05$  yr, and  $\ell = 80$  km. With this final set of hyperparameters, we condition the prior with the GNSS data and then spatially differentiate the posterior displacements to obtain transient strain.

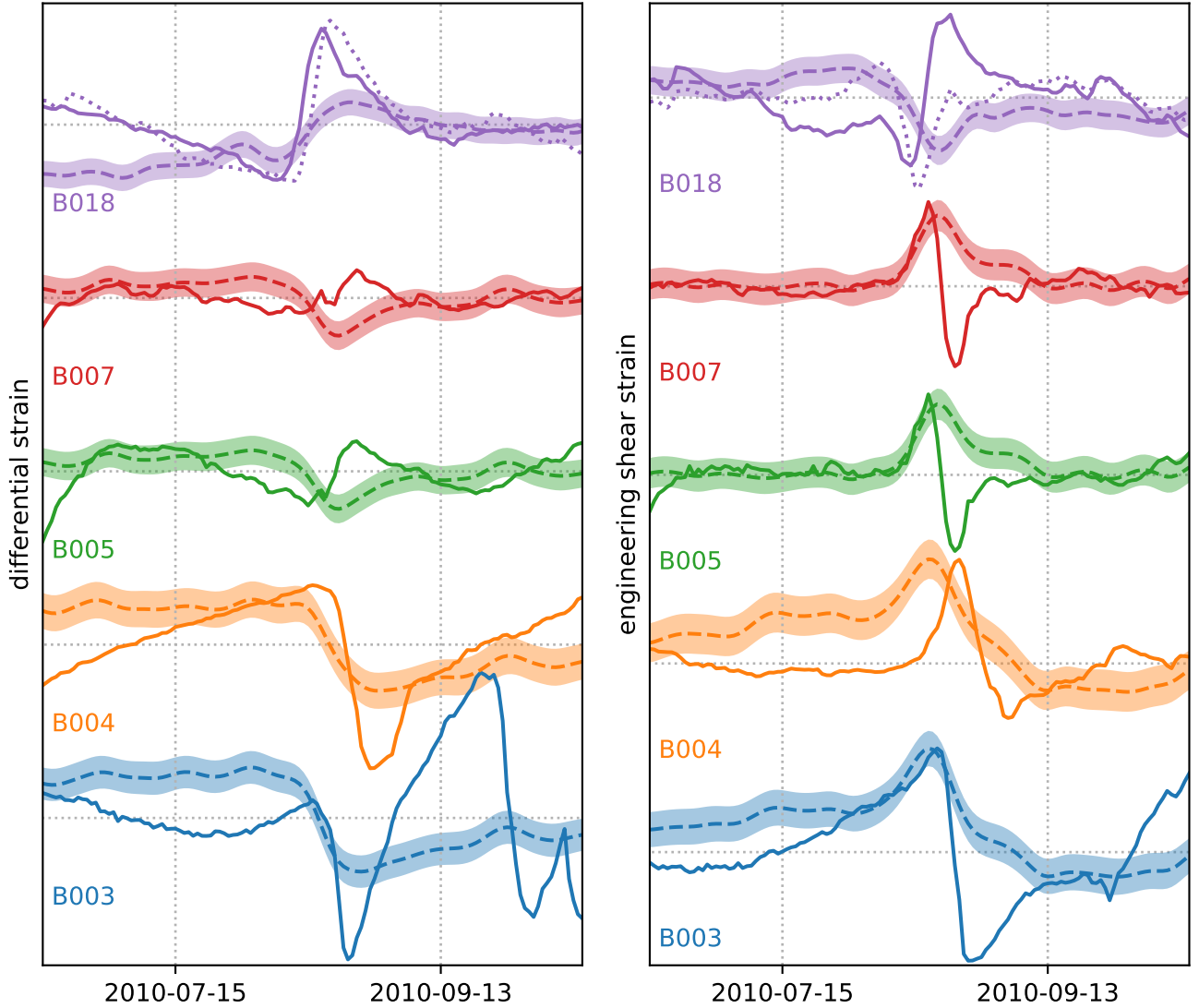


Figure 6.2: differential (left) and engineering shear (right) strains during the summer 2010 SSE observed at BSMs (solid) and derived from GNSS data (dashed). The horizontal dotted lines are spaced by 0.1 micro-strain. The shaded region around the GNSS derived strains show the one standard deviation confidence interval. The dotted line for station B018 shows the BSM data using the optimal instrument orientation. The shown BSM data has been detrended by estimating and removing a second-order polynomial from each timeseries.

## 6.4 Results

We compare the BSM data to GNSS derived strains for eight SSEs in the Puget Sound region. The earliest SSE considered occurred in spring 2009 and the latest SSE occurred in winter 2017. The two datasets are in best agreement for the summer 2010 SSE, which is shown in Figure 6.2. The data for the remaining SSEs are included at the end of this manuscript in Figures 6.7 through 6.13. We only show the differential and engineering shear strains because there is no clear signal in the areal strain for either the GNSS derived strains or the BSM data. *Roeloffs* (2010) also expressed doubt in the areal strains measured at stations B003, B004, B007, and B018 because the areal strains derived from different combinations of gauges at these stations are not self consistent. *Roeloffs* (2010) also noted an inconsistency in the differential strains at B003.

Station B004 records differential and engineering shear strains that are most consistent with the GNSS derived strains. However, the initiation of SSE strains recorded at B004 tend to lag several days behind the GNSS derived strains. The strain rates recorded at B004 also tend to be greater than the GNSS derived strains. One possible explanation for this discrepancy is that the GNSS station spacing is too wide to resolve a relatively sharp pulse of strain from the SSE as it traverses along the subduction zone.

The engineering shear strain, but not the differential strain, recorded at B003 contain a clear signal from each SSE that is consistent with the GNSS derived strains. Similar to B004, the recorded strain rates exceed those predicted by the GNSS data. There are many spurious features in the differential strains recorded at B003, which makes it difficult determine whether or not that component contains signal from SSEs.

Stations B005 and B007, which are located within a few hundred meters of each other, both show clear SSE signals in their engineering shear strains. However, the temporal pattern of strain recorded at these stations are not consistent with the GNSS derived strains. For the summer 2010 and summer 2011 SSEs, the GNSS derived strains predict a single positive pulse of engineering shear strain at these locations, but both B005 and B007 record an initially positive pulse that then becomes negative. We cannot explain this discrepancy with mis-oriented instruments because both B005 and B007 would need to have nearly identical orientation errors. If the negative pulse of engineering shear strain were a regional ( $\gtrsim 50$  km scale) feature, then it would have been recognized in the GNSS data. We then suspect that the discrepancy can be explained with topographic or geologic features that may distort the local strain field. While, we are not saying that the engineering shear strains at B005 and B007 are erroneous, it is clear that they are inconsistent with the regional scale strains. The differential strains at station B005 and B007 do not show any clear SSE signal, even though

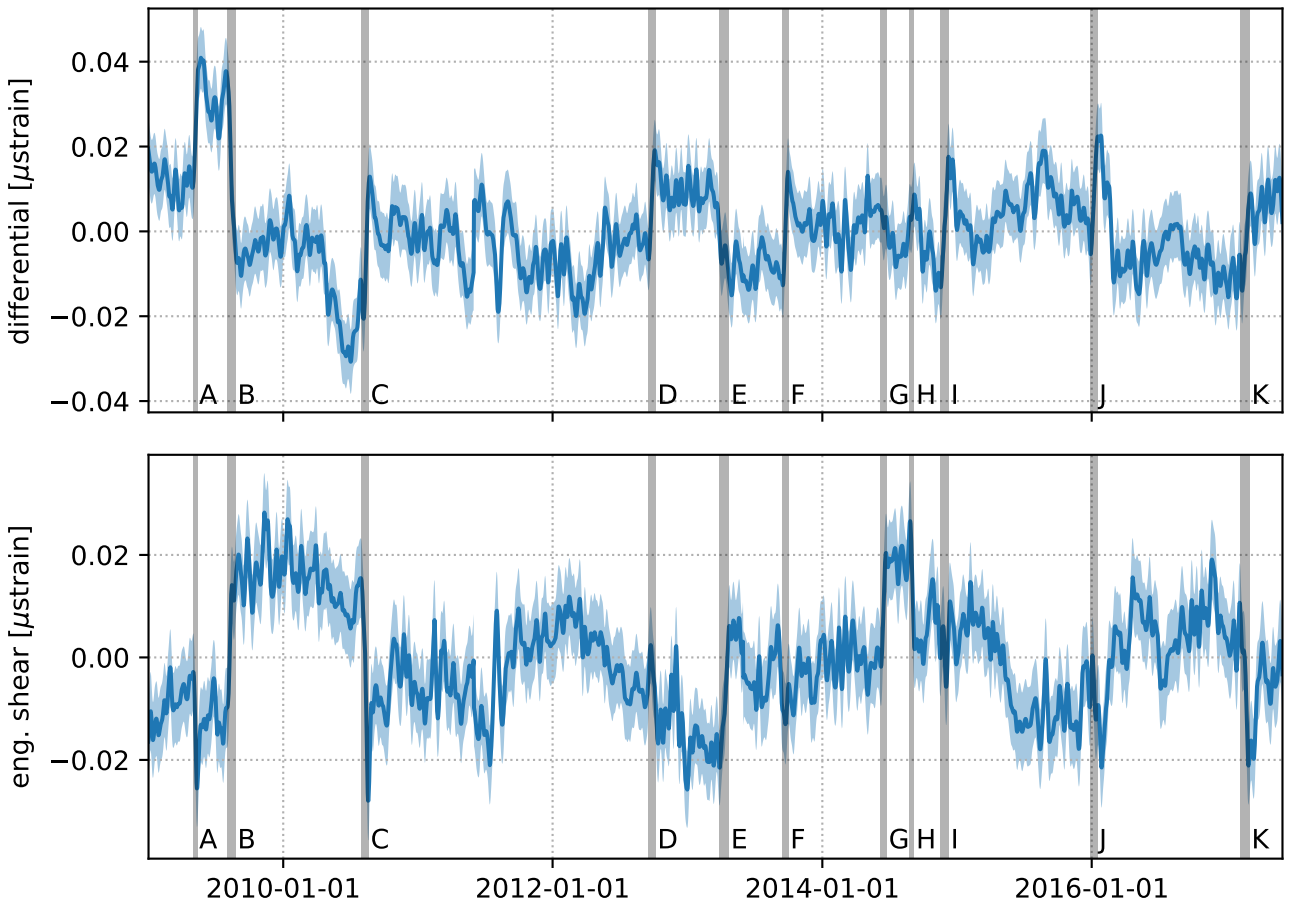


Figure 6.3: GNSS derived differential and engineering shear strains for station B018. The shaded blue regions indicate the one standard deviation confidence interval. The shaded gray regions indicate times of strain drops, which are the result of SSEs.

a signal is observed in the GNSS derived strains. This too could be due to distortion of the strain field from local features.

The differential and engineering shear strains recorded at station B018 have notably less noise than most BSMs. Nonetheless, the engineering shear strains at B018 are not consistent with the GNSS derived strains. For example, BSM data shows a strain increase from the summer 2010 SSE, and the GNSS derived strains predict a strain decrease with about equal magnitude. We consider the possibility that this discrepancy is due to an error in the instrument orientation, and we identify a new, optimal orientation for station B018. We want to find the value for  $\theta_0$  that causes the strain drops (or increases) recorded at B018 to best match the strain drops derived from GNSS data. We identify 11 strain drops in the GNSS derived strains, which are due to SSEs in the Puget Sound region and in Oregon (Figure 6.3). We define strain drops as the total strain change over the hand-selected intervals

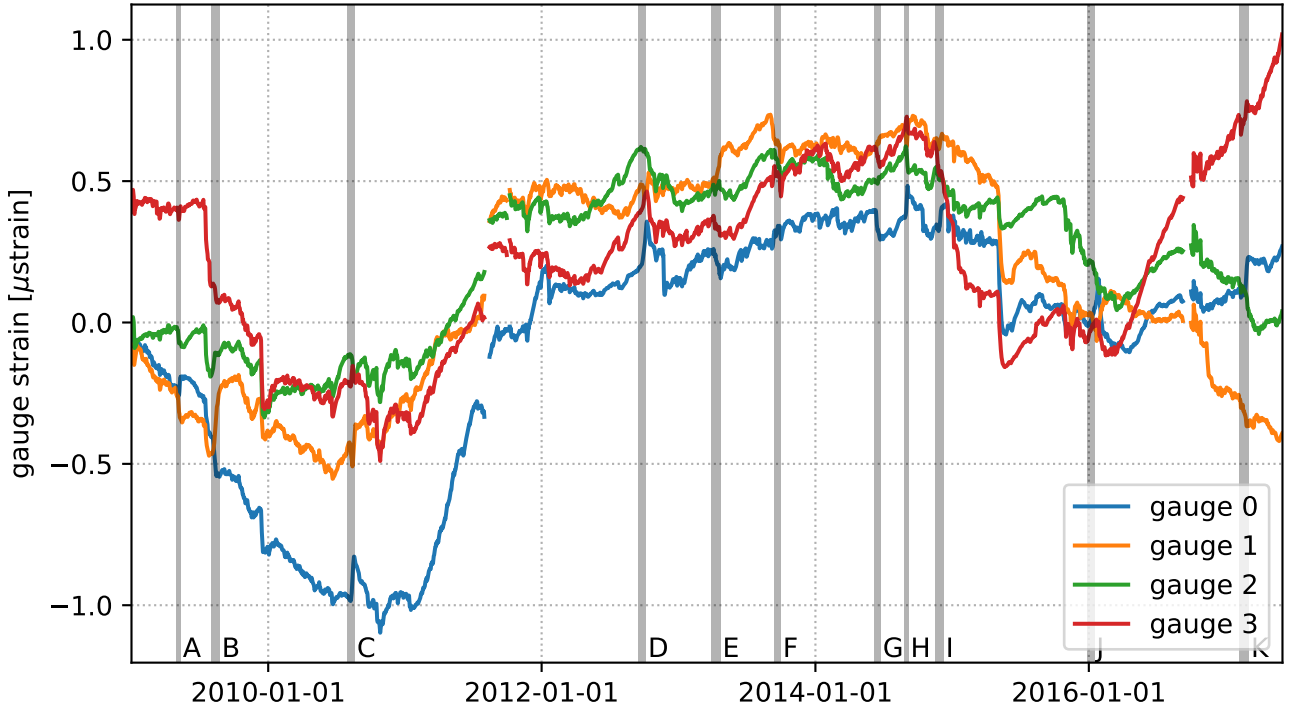


Figure 6.4: Gauge readings at station B018. The gray shaded regions indicate times of strain drops from Figure 6.3.

shown in Figure 6.3. The strain drops for each event are shown in Figure 6.5. For each tested  $\theta_0$ , we use eq. (6.1) to convert the strain drops recorded at each gauge (Figure 6.4) to the differential and engineering shear strain drops. We then use the L2 norm of the residuals, the difference between the BSM strain drops and the GNSS derived strain drops, as the misfit metric. We find an optimal value of  $\theta_0$  to be 293° east of north, which can be compared to the recorded value of 267° (Figure 6.6). With the new orientation, the engineering shear strain recorded at B018 decreases during the summer 2010 SSE, which is now consistent with the GNSS data (Figure 6.2). The differential strains at B018 are roughly consistent with the GNSS derived strains, regardless of whether the recorded  $\theta_0$  or optimal  $\theta_0$  is used.

## 6.5 Conclusion

We have compared BSM data to GNSS derived strains for eight of the past SSEs in the Puget Sound region. The summer 2010 SSE produced the clearest signal in both the BSM data and GNSS derived strain, and yet it is still difficult to reconcile the two datasets. Of the five BSM stations that record strain from SSEs, only one of them, B004, records differential and engineering shear strains that are consistently in agreement with the GNSS derived strains.

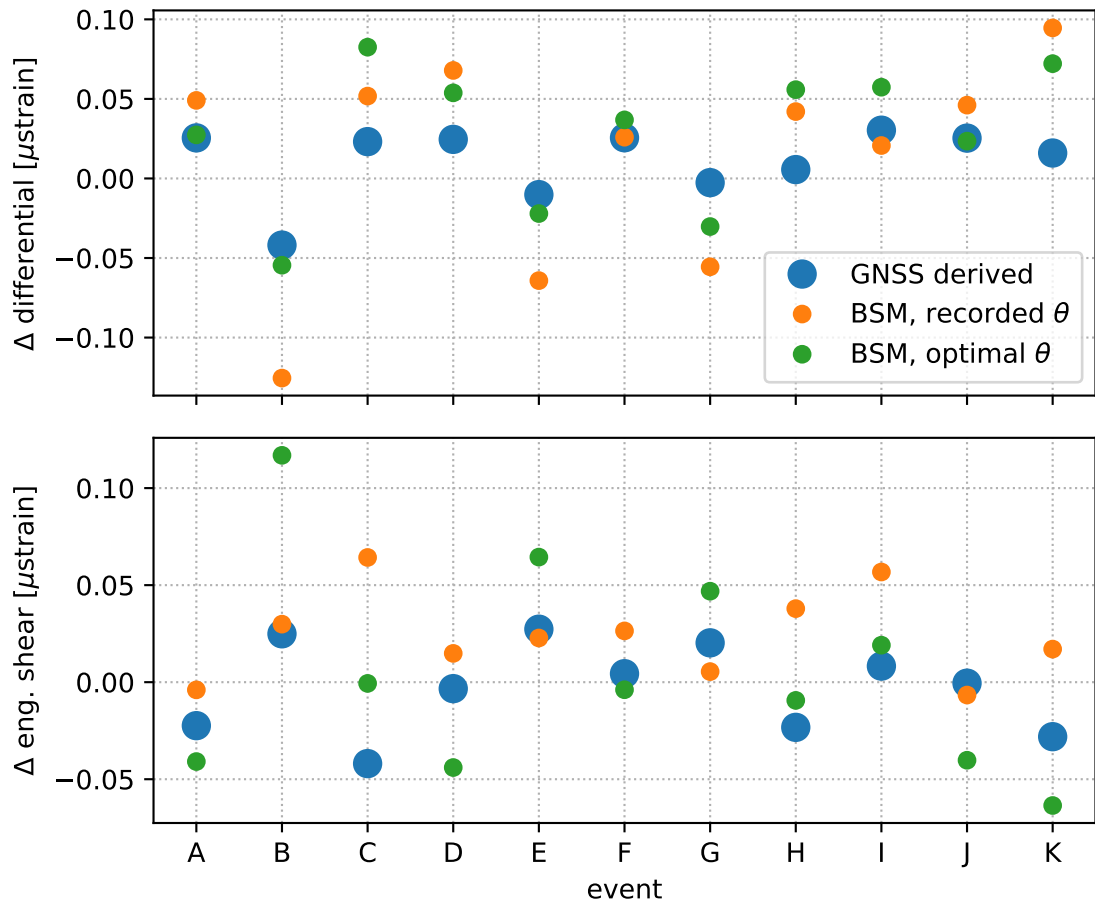


Figure 6.5: GNSS derived strain drops at station B018 during the 11 events identified in Figure 6.3 (blue dots), BSM strain drops using the recorded orientation for B018 (orange dots), and BSM strain drops using the optimal orientation for B018 (green dots).

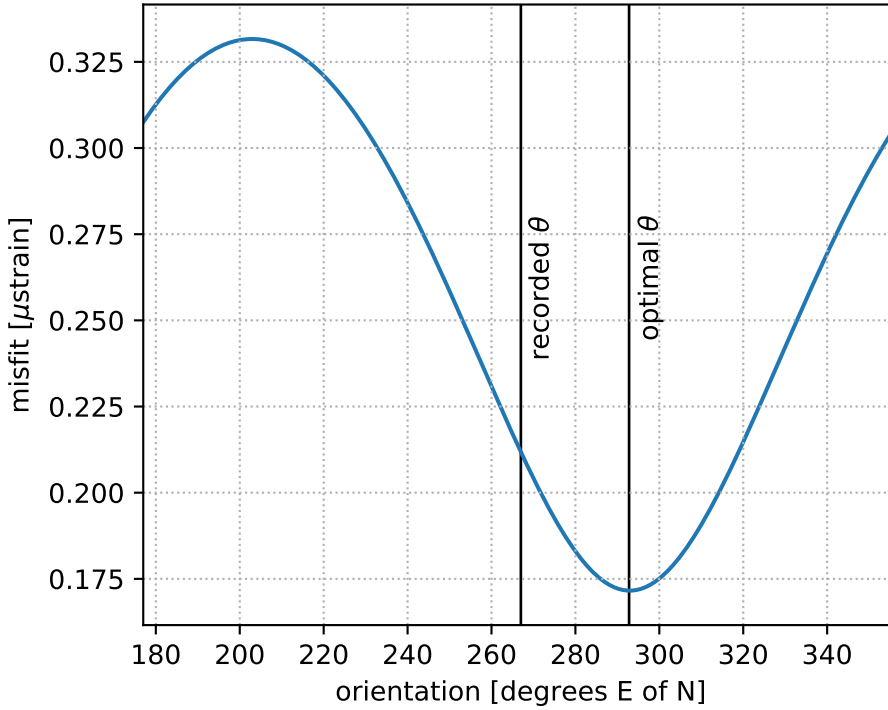


Figure 6.6: Misfit as a function of instrument orientation for station B018.

For station B003, only the engineering shear strains are consistent with the GNSS data. Both the differential and engineering shear strains recorded at B018 can be made to agree with the GNSS data when assuming a new instrument orientation. For station B005 and B007 it may be necessary to use a coupling matrix other than the isotropic one considered in this study. We are unaware of a reliable calibration method for these stations, since tidal calibration is not possible. In general, we urge caution when attempting to use BSM data to describe regional strains.

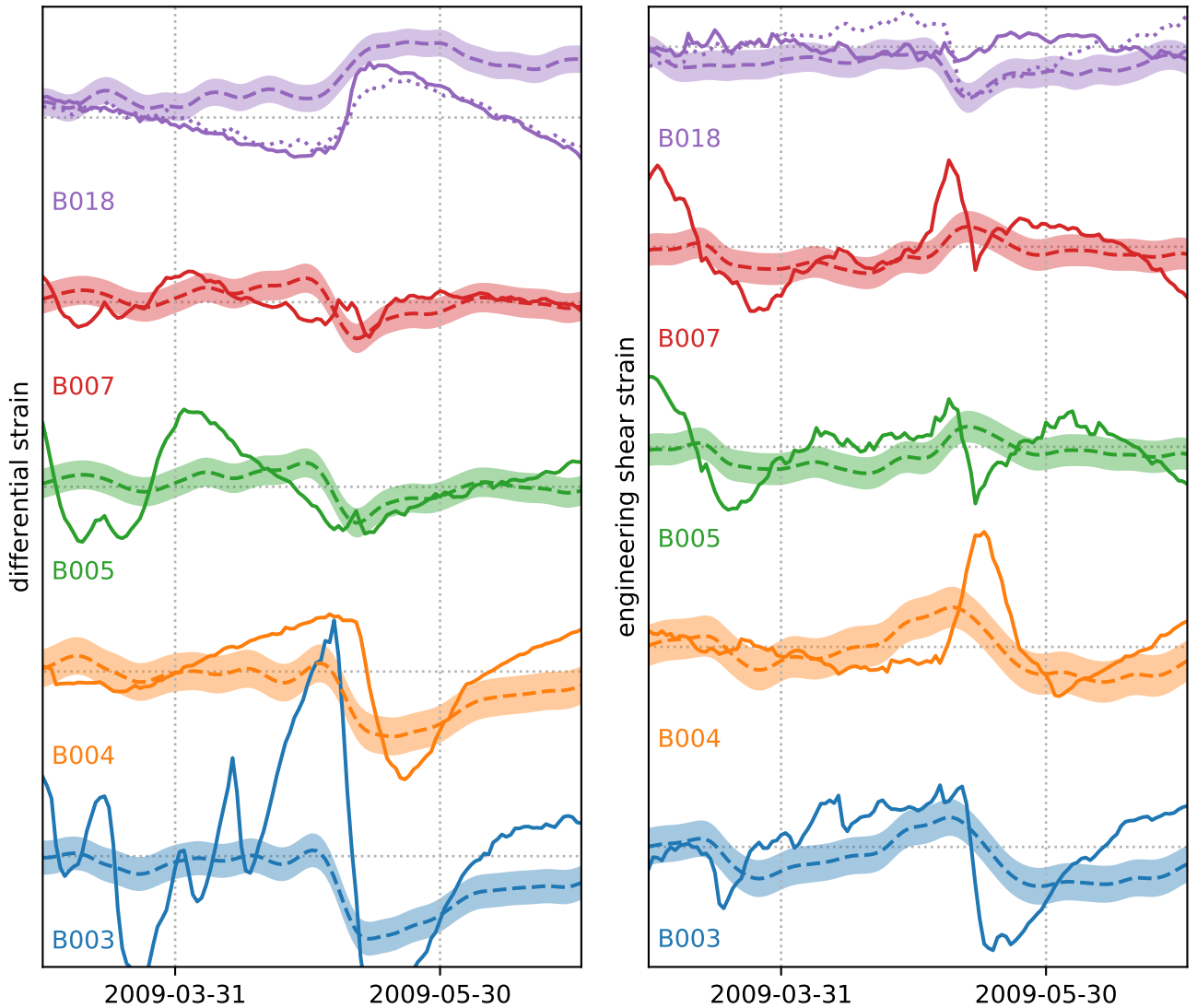


Figure 6.7: Same as Figure 6.2, but for the spring 2009 SSE.

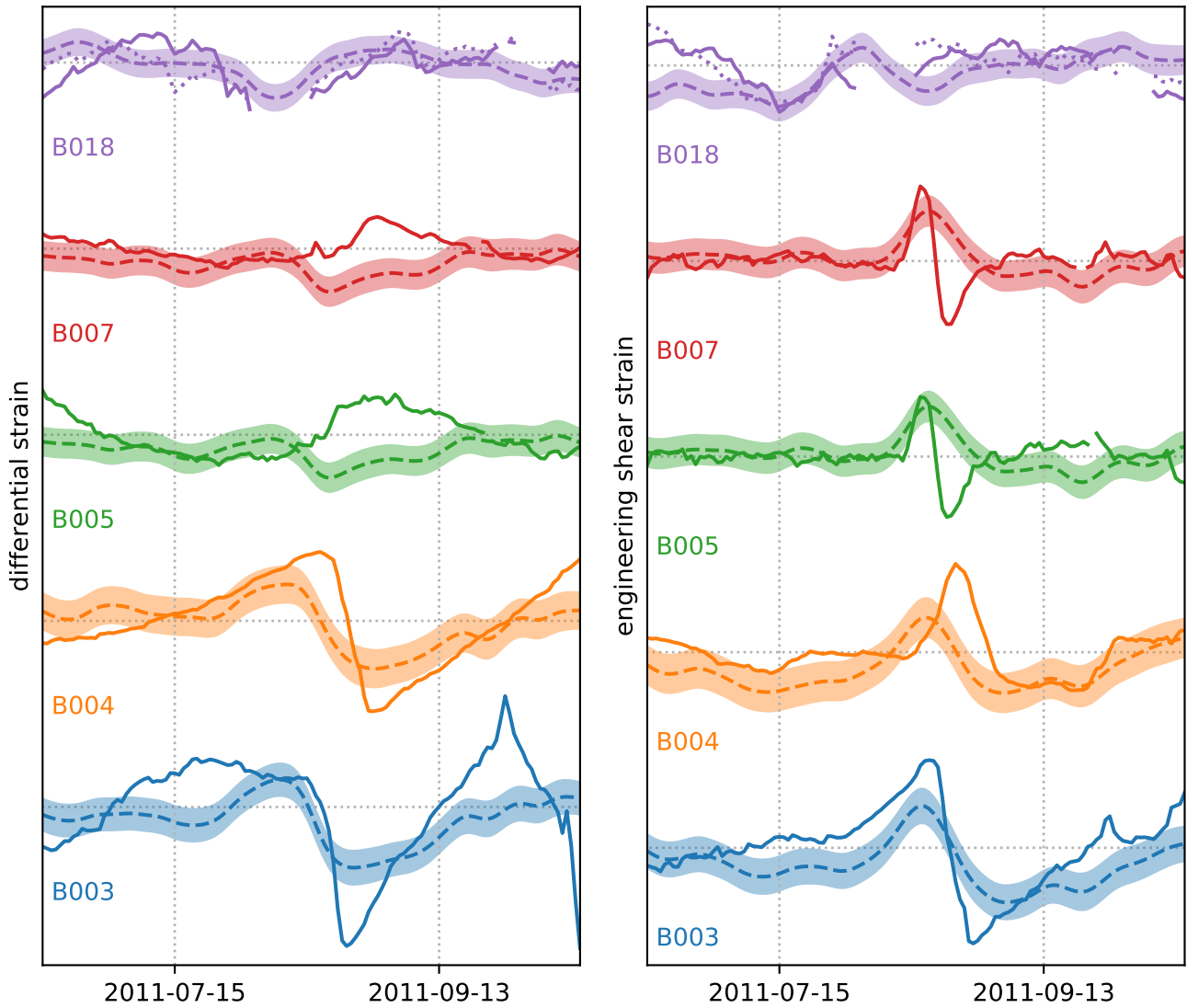


Figure 6.8: Same as Figure 6.2, but for the summer 2011 SSE.

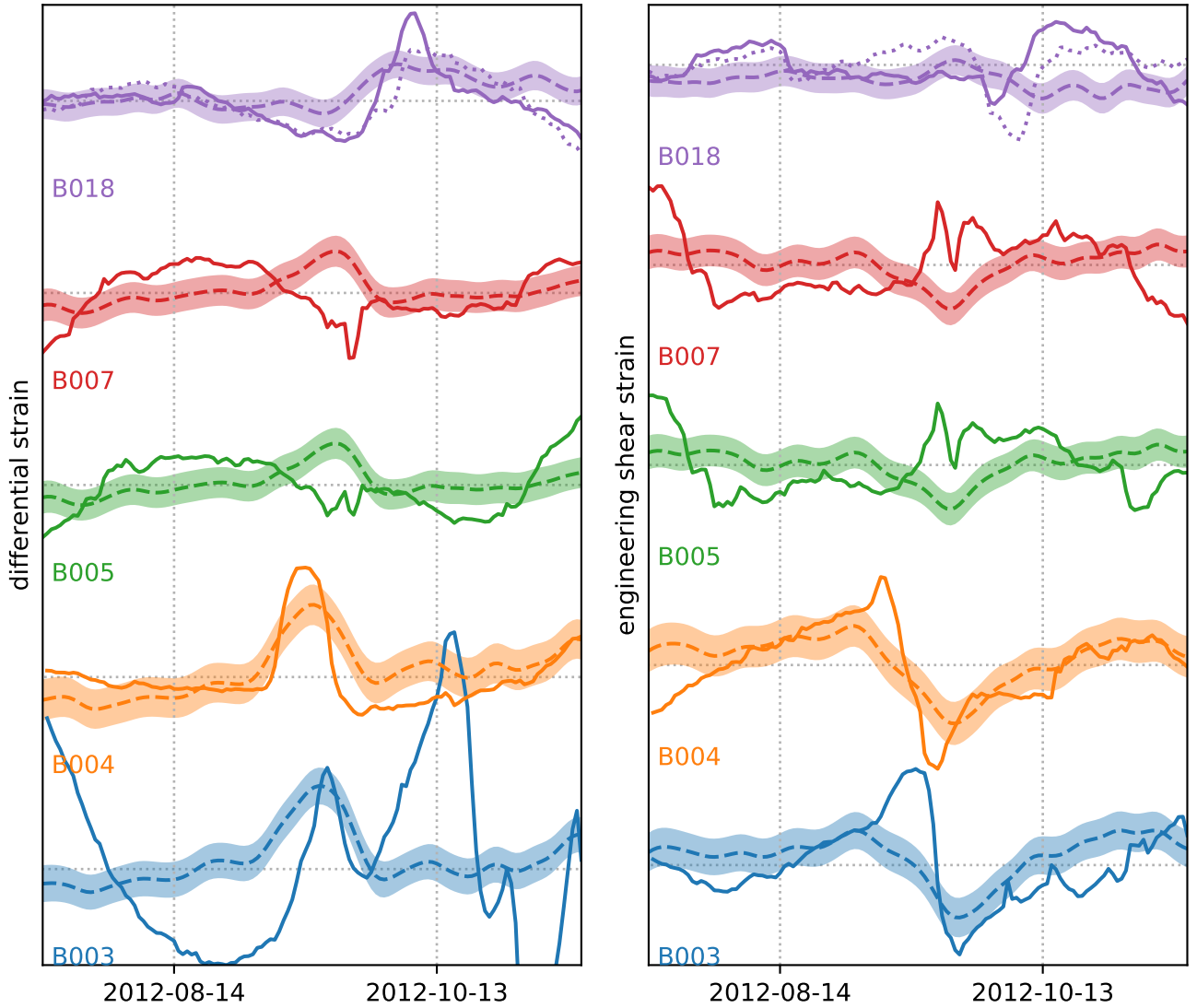


Figure 6.9: Same as Figure 6.2, but for the summer 2012 SSE.

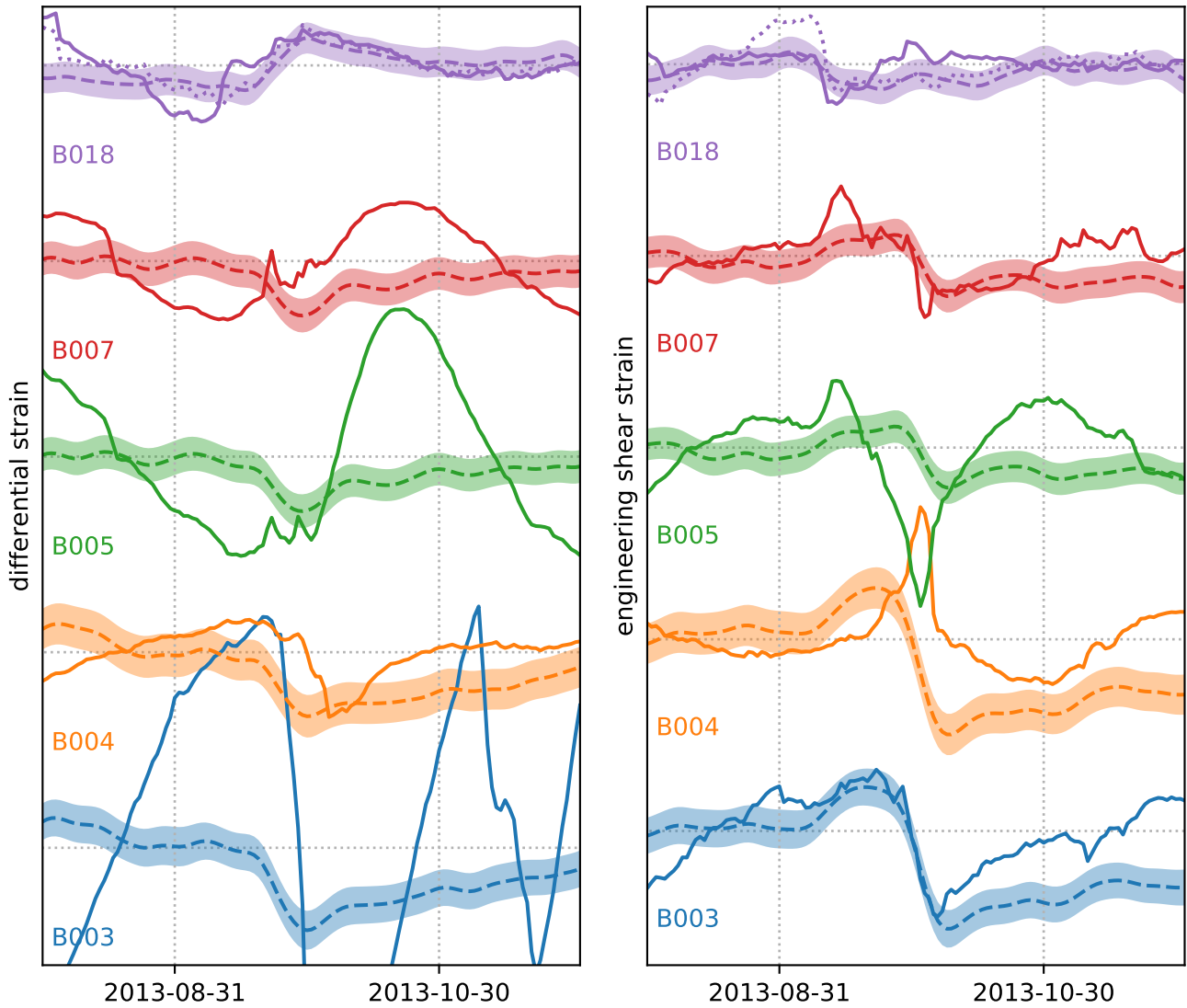


Figure 6.10: Same as Figure 6.2, but for the fall 2013 SSE.

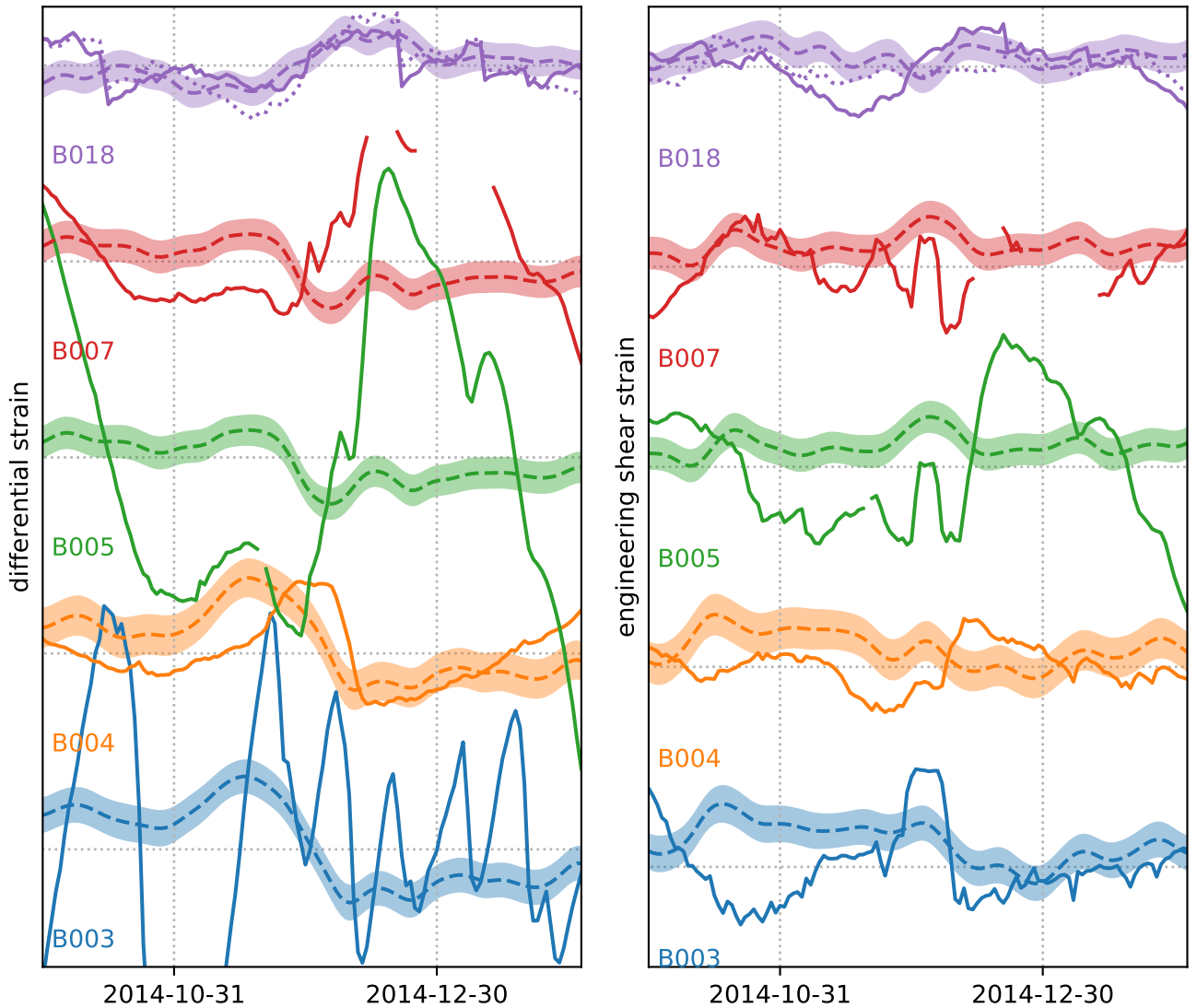


Figure 6.11: Same as Figure 6.2, but for the fall 2014 SSE.

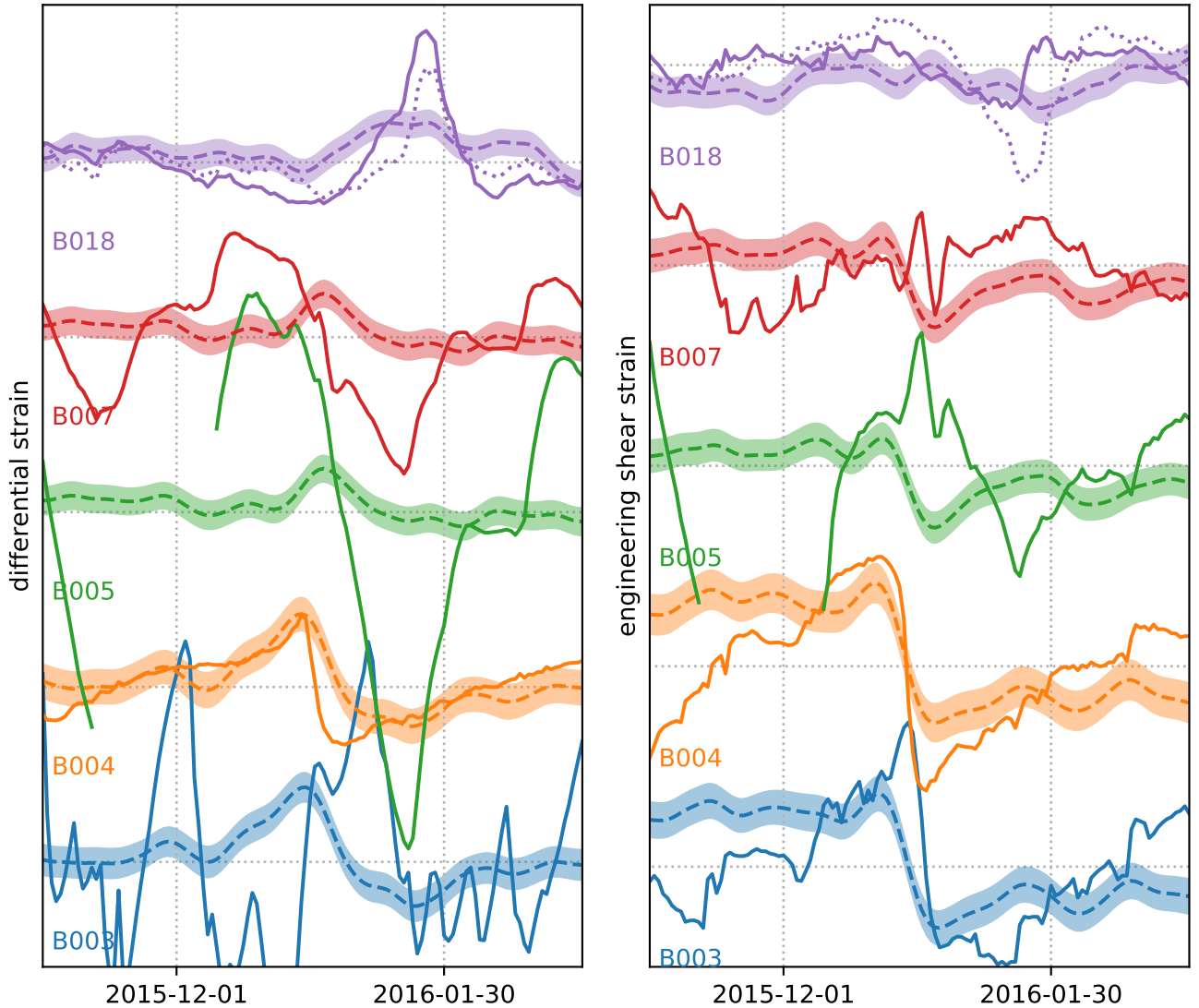


Figure 6.12: Same as Figure 6.2, but for the winter 2015-2016 SSE.

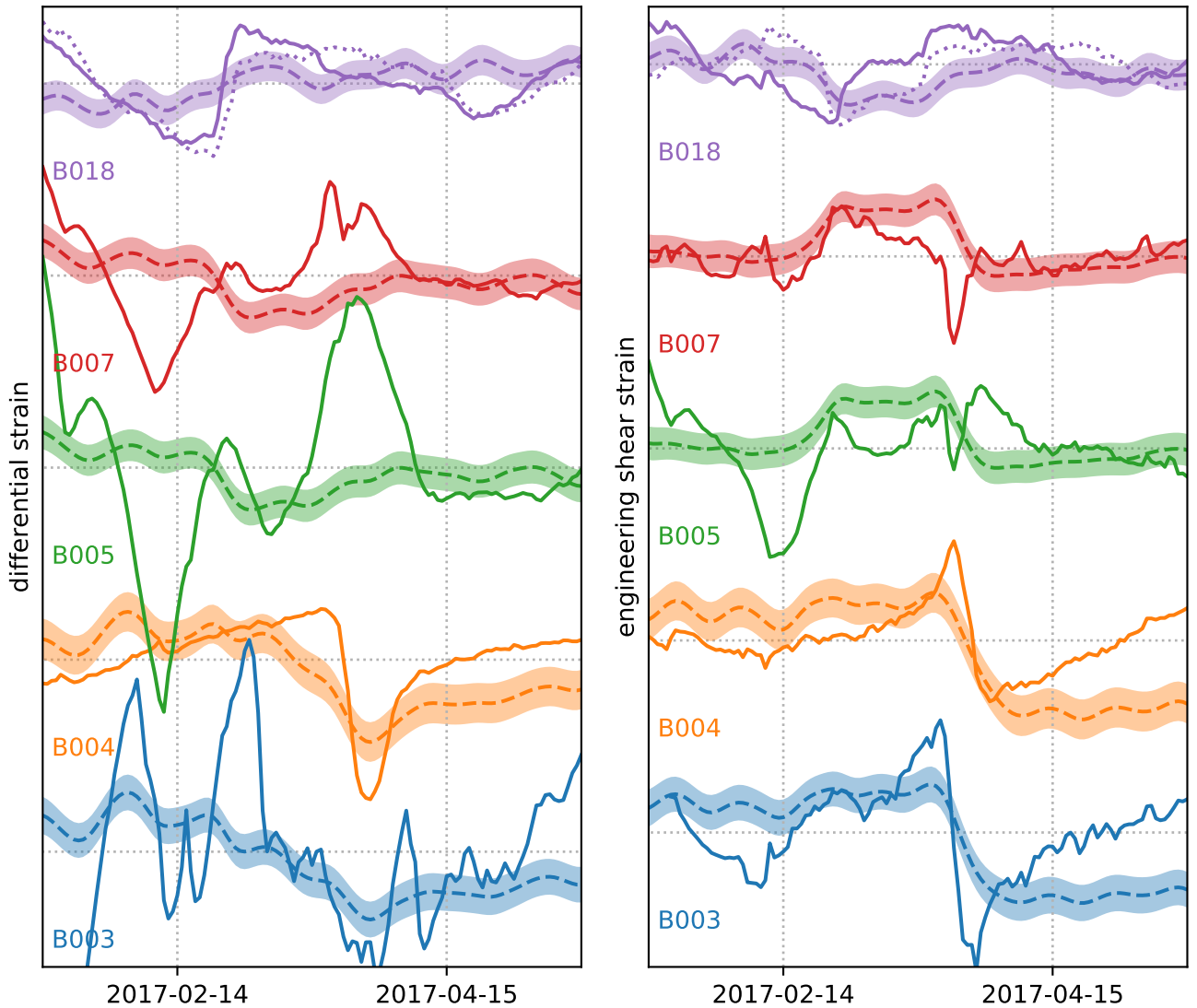


Figure 6.13: Same as Figure 6.2, but for the winter 2017 SSE.

## REFERENCES

- Aagaard, B. T., M. G. Knepley, and C. A. Williams (2013), A domain decomposition approach to implementing fault slip in finite-element models of quasi-static and dynamic crustal deformation, *Journal of Geophysical Research: Solid Earth*, 118, 3059–3079, doi: 10.1002/jgrb.50217.
- Agnew, D. C. (1992), The time-domain behavior of power-law noises, *Geophysical Research Letters*, 19(4), 333–336.
- Agnew, D. C. (1997), NLOADF: A program for computing ocean-tide loading, *Journal of Geophysical Research*, 102, 5109–5110.
- Amiri-Simkooei, A. R., C. C. J. M. Tiberius, and P. J. G. Teunissen (2007), Assessment of noise in GPS coordinate time series: Methodology and results, *Journal of Geophysical Research: Solid Earth*, 112(7), 1–19, doi:10.1029/2006JB004913.
- Argus, D. F., M. B. Heflin, G. Peltzer, F. Crampé, and F. H. Webb (2005), Interseismic strain accumulation and anthropogenic motion in metropolitan Los Angeles, *Journal of Geophysical Research B: Solid Earth*, 110(B04401), 1–26, doi:10.1029/2003JB002934.
- Aster, R. C., B. Borchers, and C. H. Thurber (2011), *Parameter Estimation and Inverse Problems*, vol. 90, 360 pp.
- Barbot, S., and Y. Fialko (2010), A unified continuum representation of post-seismic relaxation mechanisms: Semi-analytic models of afterslip, poroelastic rebound and viscoelastic flow, *Geophysical Journal International*, 182(3), 1124–1140, doi:10.1111/j.1365-246X.2010.04678.x.
- Barbot, S., Y. Fialko, and Y. Bock (2009), Postseismic deformation due to the Mw 6.0 2004 Parkfield earthquake: Stress-driven creep on a fault with spatially variable rate-and-state friction parameters, *Journal of Geophysical Research: Solid Earth*, 114, 1–26, doi:10.1029/2008JB005748.

- Barbour, A. J., and B. W. Crowell (2017), Dynamic Strains for Earthquake Source Characterization, *Seismological Research Letters*, 88(2A), 354–370, doi:10.1785/0220160155.
- Bawden, G. W., W. Thatcher, R. S. Stein, K. W. Hudnut, and G. Peltzer (2001), Tectonic contraction across Los Angeles after removal of groundwater pumping effects., *Nature*, 412, 812–815, doi:10.1038/35090558.
- Beavan, J., and J. Haines (2001), Contemporary horizontal velocity and strain rate fields of the Pacific-Australian plate boundary zone through New Zealand, *Journal of Geophysical Research*, 106(B1), 741–770.
- Berger, J., and C. Beaumont (1976), An analysis of tidal strain observations from the United States of America II. The inhomogeneous tide, *Bulletin of the Seismological Society of America*, 66(6), 1821–1846.
- Bills, B. G., and G. M. May (1987), Lake Bonneville: Constraints on Lithospheric Thickness and Upper Mantle Viscosity From Isostatic Warping of Bonneville, Provo, and Gilbert Stage Shorelines, *Journal of Geophysical Research-Solid Earth and Planets*, 92(B11), 11,493–11,508, doi:10.1029/JB092iB11p11493.
- Blewitt, G., C. Kreemer, W. C. Hammond, and J. Gazeaux (2016), MIDAS robust trend estimator for accurate GPS station velocities without step detection, *Journal of Geophysical Research : Solid Earth*, 121, 2054–2068, doi:10.1002/2015JB012552.Received.
- Bürgmann, R., and G. Dresen (2008), Rheology of the Lower Crust and Upper Mantle: Evidence from Rock Mechanics, Geodesy, and Field Observations, *Annual Review of Earth and Planetary Sciences*, 36, 531–567, doi:10.1146/annurev.earth.36.031207.124326.
- Bürgmann, R., M. E. Ayhan, E. J. Fielding, T. J. Wright, S. McClusky, B. Aktug, C. Demir, O. Lenk, and A. Türkezer (2002), Deformation during the 12 November 1999 Düzce, Turkey, earthquake, from GPS and InSAR data, *Bulletin of the Seismological Society of America*, 92(February), 161–171, doi:10.1785/0120000834.
- Çakir, Z., S. Ergintav, H. Özener, U. Dogan, A. M. Akoglu, M. Meghraoui, and R. Reilinger (2012), Onset of aseismic creep on major strike-slip faults, *Geology*, 40(12), 1115–1118, doi:10.1130/G33522.1.
- Cavalié, O., M. P. Doin, C. Lasserre, and P. Briole (2007), Ground motion measurement in the Lake Mead area, Nevada, by differential synthetic aperture radar interferometry time series analysis: Probing the lithosphere rheological structure, *Journal of Geophysical Research: Solid Earth*, 112(B03403), 1–18, doi:10.1029/2006JB004344.

Cetin, E., Z. Cakir, M. Meghraoui, S. Ergintav, and A. M. Akoglu (2014), Extent and distribution of aseismic slip on the Ismetpasa segment of the North Anatolian Fault (Turkey) from Persistent Scatterer InSAR, *Geochemistry, Geophysics, Geosystems*, 15, doi:10.1002/2014GC005307. Received.

Chen, Y., T. a. Davis, and W. W. Hager (2008), Algorithm 887 : CHOLMOD , Supernodal Sparse Cholesky Factorization and Update/downdate, *ACM Transactions on Mathematical Software*, 35(3), 1–12, doi:10.1145/1391989.1391995.

Chinnery, M. A., and D. B. Jovanovich (1972), Effect of earth layering on earthquake displacement fields, *Bulletin of the Seismological Society of America*, 62(6), 1629–1639.

Chopra, P. N. (1997), High-temperature transient creep in olivine rocks, *Tectonophysics*, 279, 93–111, doi:10.1016/S0040-1951(97)00134-0.

Cressie, N. (1993), *Statistics for Spatial Data*, rev. ed., John Wiley & Sons, New York, doi:10.1111/j.1365-3121.1992.tb00605.x.

Crittenden, M. (1967), Viscosity and Finite Strength of the Mantle as Determined from Water and Ice Loads, *Geophysical Journal of the Royal Astronomical Society*, pp. 261–279, doi:10.1111/j.1365-246X.1967.tb06243.x.

Davis, J. L., B. P. Wernicke, and M. E. Tamisiea (2012), On seasonal signals in geodetic time series, *Journal of Geophysical Research: Solid Earth*, 117(B01403), 1–10, doi:10.1029/2011JB008690.

Desbrun, M., M. Meyer, P. Schröder, and A. H. Barr (1999), Implicit fairing of irregular meshes using diffusion and curvature flow, *Proceedings of the 26th annual conference on Computer graphics and interactive techniques - SIGGRAPH '99*, 33, 317–324, doi:10.1145/311535.311576.

Dmitrieva, K., P. Segall, and C. DeMets (2015), Network-based estimation of time-dependent noise in GPS position time series, *Journal of Geodesy*, 89(6), 591–606, doi:10.1007/s00190-015-0801-9.

Dong, D., P. Fang, Y. Bock, M. K. Cheng, and S. Miyazaki (2002), Anatomy of apparent seasonal variations from GPS-derived site position time series, *J. Geophys. Res.*, 107(B4), 2075, doi:10.1029/2001JB000573.

- Dong, D., P. Fang, Y. Bock, F. Webb, L. Prawirodirdjo, S. Kedar, and P. Jamason (2006), Spatiotemporal filtering using principal component analysis and Karhunen-Loeve expansion approaches for regional GPS network analysis, *Journal of Geophysical Research: Solid Earth*, 111(3), 1–16, doi:10.1029/2005JB003806.
- Dragert, G., K. Wang, and T. S. James (2001), A silent slip event on the deeper Cascadia subduction interface., *Science*, 292, 1525–1528, doi:10.1126/science.1060152.
- Dragert, H., and K. Wang (2011), Temporal evolution of an episodic tremor and slip event along the northern Cascadia margin, *Journal of Geophysical Research: Solid Earth*, 116(12), 1–12, doi:10.1029/2011JB008609.
- El-Fiky, G. S., and T. Kato (1998), Continuous distribution of the horizontal strain in the Tohoku district, Japan, predicted by least-squares collocation, *Journal of Geodynamics*, 27(2), 213–236, doi:10.1016/S0264-3707(98)00006-4.
- Ergintav, S., S. McClusky, E. Hearn, R. Reilinger, R. Cakmak, T. Herring, H. Ozener, O. Lenk, and E. Tari (2009), Seven years of postseismic deformation following the 1999, M = 7.4 and M = 7.2, Izmit-Düzce, Turkey earthquake sequence, *Journal of Geophysical Research: Solid Earth*, 114, doi:10.1029/2008JB006021.
- Feigl, K. L., and W. Thatcher (2006), Geodetic observations of post-seismic transients in the context of the earthquake deformation cycle, *Comptes Rendus - Geoscience*, 338, 1012–1028, doi:10.1016/j.crte.2006.06.006.
- Feigl, K. L., R. W. King, and T. H. Jordan (1990), Geodetic measurement of tectonic deformation in the Santa Maria Fold and Thrust Belt, California, *Journal of Geophysical Research: Solid Earth*, 95(B3), 2679–2699, doi:10.1029/JB095iB03p02679.
- Field, E. H., et al. (2014), Uniform California Earthquake Rupture Forecast, version 3 (UCERF3) -The time-independent model, *Bulletin of the Seismological Society of America*, 104(3), 1122–1180, doi:10.1785/0120130164.
- Fletcher, J. M., et al. (2014), Assembly of a large earthquake from a complex fault system: Surface rupture kinematics of the 4 April 2010 El Mayor-Cucapah (Mexico) Mw 7.2 earthquake, *Geosphere*, 10(4), 797–827, doi:10.1130/GES00933.1.
- Flügge, W. (1975), *Viscoelasticity*, Springer-Verlag Berlin Heidelberg, doi:10.1007/978-3-662-02276-4.

- Freed, A. M. (2007), Afterslip (and only afterslip) following the 2004 Parkfield, California, earthquake, *Geophysical Research Letters*, 34, 1–5, doi:10.1029/2006GL029155.
- Freed, a. M., and J. Lin (2001), Delayed triggering of the 1999 Hector Mine earthquake by viscoelastic stress transfer., *Nature*, doi:10.1038/35075548.
- Freed, A. M., R. Bürgmann, E. Calais, and J. Freymueller (2006a), Stress-dependent power-law flow in the upper mantle following the 2002 Denali, Alaska, earthquake, *Earth and Planetary Science Letters*, 252, 481–489, doi:10.1016/j.epsl.2006.10.011.
- Freed, A. M., R. Bürgmann, E. Calais, J. Freymueller, and S. Hreinsdóttir (2006b), Implications of deformation following the 2002 Denali, Alaska, earthquake for postseismic relaxation processes and lithospheric rheology, *Journal of Geophysical Research: Solid Earth*, 111(B01401), 1–23, doi:10.1029/2005JB003894.
- Freed, A. M., R. Bürgmann, and T. Herring (2007), Far-reaching transient motions after Mojave earthquakes require broad mantle flow beneath a strong crust, *Geophysical Research Letters*, 34(L19302), 1–5, doi:10.1029/2007GL030959.
- Fukahata, Y., and M. Matsu'ura (2006), Quasi-static internal deformation due to a dislocation source in a multilayered elastic/viscoelastic half-space and an equivalence theorem, *Geophysical Journal International*, 166(1), 418–434, doi:10.1111/j.1365-246X.2006.02921.x.
- Gibbs, B. P. (2011), *Advanced Kalman Filtering, Least-Squares and Modeling: A Practical Handbook*, John Wiley & Sons, Hoboken, NJ, doi:10.1002/9780470890042.
- Gladwin, M. T., and R. Hart (1985), Design parameters for borehole strain instrumentation, *Pure and Applied Geophysics*, 123(1), 59–80, doi:10.1007/BF00877049.
- Gladwin, M. T., R. L. Gwyther, R. Hart, M. Francis, and M. J. S. Johnston (1987), Borehole tensor strain measurements in California, *Journal of Geophysical Research: Solid Earth*, 92(B8), 7981–7988, doi:10.1029/JB092iB08p07981.
- Gonzalez-Ortega, A., Y. Fialko, D. Sandwell, F. A. Nava-pichardo, J. Fletcher, J. Gonzalez-garcia, B. Lipovsky, M. Floyd, and G. Funning (2014), El Mayor-Cucapah (Mw7.2) earthquake: early near-field postseismic deformation from InSar and GPS observations, *Journal of Geophysical Research*, 119, 1482–1497, doi:10.1002/2013JB010193.
- Harris, R. a., and P. Segall (1987), Detection of a locked zone at depth on the Parkfield, California, segment of the San Andreas Fault, *Journal of Geophysical Research*, 92, 7945, doi:10.1029/JB092iB08p07945.

- Hart, R. H. G., M. T. Gladwin, R. L. Gwyther, D. C. Agnew, and F. K. Wyatt (1996), Tidal calibration of borehole strain meters: Removing the effects of small-scale inhomogeneity, *Journal of Geophysical Research*, 101(96).
- Harville, D. A. (1974), Bayesian Inference for Variance Components Using Only Error Contrasts, *Biometrika*, 61(2), 383–385.
- Hauksson, E., J. Stock, K. Hutton, W. Yang, J. A. Vidal-Villegas, and H. Kanamori (2011), The 2010 Mw 7.2 El mayor-cucapah earthquake sequence, Baja California, Mexico and Southernmost California, USA: Active seismotectonics along the Mexican pacific margin, *Pure and Applied Geophysics*, 168, 1255–1277, doi:10.1007/s00024-010-0209-7.
- Hearn, E. H. (2003), What can GPS data tell us about the dynamics of post-seismic deformation ?, *Geophysical Journal International*, 155, 753–777.
- Hearn, E. H., R. Bürgmann, and R. E. Reilinger (2002), Dynamics of zmit earthquake postseismic deformation and loading of the Düzce earthquake hypocenter, *Bulletin of the Seismological Society of America*, 92(1), 172–193, doi:10.1785/0120000832.
- Hearn, E. H., S. McClusky, S. Ergintav, and R. E. Reilinger (2009), Izmit earthquake post-seismic deformation and dynamics of the North Anatolian Fault Zone, *Journal of Geophysical Research: Solid Earth*, 114(B08405), 1–21, doi:10.1029/2008JB006026.
- Herring, T. A., et al. (2016), Plate Boundary Observatory and related networks: GPS data analysis methods and geodetic product, *Reviews of Geophysics*, pp. 1–50, doi: 10.1002/2016RG000529.Received.
- Hetland, E. A. (2003), Postseismic relaxation across the Central Nevada Seismic Belt, *Journal of Geophysical Research*, 108(B8), 1–13, doi:10.1029/2002JB002257.
- Hetland, E. A., and B. H. Hager (2005), Postseismic and interseismic displacements near a strike-slip fault: A two-dimensional theory for general linear viscoelastic rheologies, *Journal of Geophysical Research: Solid Earth*, 110, 1–21, doi:10.1029/2005JB003689.
- Hetland, E. A., and G. Zhang (2014), Effect of shear zones on post-seismic deformation with application to the 1997 Mw 7.6 manyi earthquake, *Geophysical Journal International*, 206(2), 1–11, doi:10.1093/gji/ggu127.
- Hill, E. M., J. L. Davis, P. Elósegui, B. P. Wernicke, E. Malikowski, and N. A. Niemi (2009), Characterization of site-specific GPS errors using a short-baseline network of braced monuments at Yucca Mountain, southern Nevada, *Journal of Geophysical Research: Solid Earth*, 114(11), 1–13, doi:10.1029/2008JB006027.

Hines, T. T., and E. A. Hetland (2013), Bias in estimates of lithosphere viscosity from interseismic deformation, *Geophysical Research Letters*, 40(16), 4260–4265, doi: 10.1002/grl.50839.

Hines, T. T., and E. A. Hetland (2015), Rapid and simultaneous estimation of fault slip and heterogeneous lithospheric viscosity from post-seismic deformation, *Geophysical Journal International*, 204(1), 569–582, doi:10.1093/gji/ggv477.

Hines, T. T., and E. A. Hetland (2016), Rheologic constraints on the upper mantle from five years of postseismic deformation following the El Mayor-Cucapah earthquake, *Journal of Geophysical Research: Solid Earth*, 121, doi:10.1002/2016JB013114.

Hines, T. T., and E. A. Hetland (2017a), Unbiased characterization of noise in geodetic data, *submitted to Journal of Geodesy*.

Hines, T. T., and E. A. Hetland (2017b), Revealing transient strain in geodetic data with Gaussian process regression, *submitted to Geophysical Journal International*, pp. 1–25.

Hodgkinson, K., D. Agnew, and E. Roeloffs (2013), Working With Strainmeter Data, *Eos, Transactions American Geophysical Union*, 94(9), 91–91, doi:10.1002/2013EO090011.

Holt, W. E., and G. Shcherbenko (2013), Toward a Continuous Monitoring of the Horizontal Displacement Gradient Tensor Field in Southern California Using cGPS Observations from Plate Boundary Observatory (PBO), *Seismological Research Letters*, 84(3), 455–467, doi: 10.1785/0220130004.

Hsu, Y.-J., M. Simons, J.-P. Avouac, J. Galetzka, K. Sieh, M. Chlieh, D. Natawidjaja, L. Prawirodirdjo, and Y. Bock (2006), Frictional Afterslip Following the 2005 Nias-Simeulue Earthquake, Sumatra, *Science*, 312(June), 1921–1926.

Jacobs, A., D. Sandwell, Y. Fialko, and L. Sichoix (2002), The 1999 (Mw7.1) Hector Mine, California, Earthquake: Near-Field Postseismic Deformation from ERS Interferometry, *Bulletin of the Seismological Society of America*, 92(4), 1433–1442.

Johnson, K. M., and P. Segall (2004), Viscoelastic earthquake cycle models with deep stress-driven creep along the San Andreas fault system, *Journal of Geophysical Research B: Solid Earth*, 109(B10403), 1–19, doi:10.1029/2004JB003096.

Johnson, K. M., G. E. Hilley, and R. Bürgmann (2007), Influence of lithosphere viscosity structure on estimates of fault slip rate in the Mojave region of the San Andreas fault system, *Journal of Geophysical Research: Solid Earth*, 112, 1–15, doi:10.1029/2006JB004842.

Johnson, K. M., R. Bürgmann, and J. T. Freymueller (2009), Coupled afterslip and viscoelastic flow following the 2002 Denali Fault, Alaska earthquake, *Geophysical Journal International*, 176(3), 670–682, doi:10.1111/j.1365-246X.2008.04029.x.

Jónsson, S., P. Segall, R. Pedersen, and G. Bjornsson (2003), Post-earthquake ground movements correlated to pore-pressure transients, *Nature*, 424, 179–183, doi:10.1038/nature01758.1.

Kato, T., G. S. El-Fiky, E. N. Oware, and S. Miyazaki (1998), Crustal strains in the Japanese islands as deduced from dense GPS array, *Geophysical Research Letters*, 25(18), 3445–3448, doi:10.1029/98GL02693.

Kaufmann, G., and F. Amelung (2000), Reservoir-induced deformation and continental rheology in vicinity of Lake Mead, Nevada, *Journal of Geophysical Research*, 105(B7), 16,341, doi:10.1029/2000JB900079.

Kenner, S. J., and P. Segall (2003), Lower crustal structure in northern California: Implications from strain rate variations following the 1906 San Francisco earthquake, *Journal of Geophysical Research*, 108(B1), doi:10.1029/2001JB000189.

King, M. A., and S. D. P. Williams (2009), Apparent stability of GPS monumentation from short-baseline time series, *Journal of Geophysical Research: Solid Earth*, 114(10), 1–21, doi:10.1029/2009JB006319.

Kirby, S. H., and A. K. Kronenberg (1987), Rheology of the Lithosphere ' Selected Topics, *Reviews of Geophysics*, 25, 12191,244.

Kohlstedt, D. L., B. Evans, and S. J. Mackwell (1995), Strength of the lithosphere: Constraints imposed by laboratory experiments, *Journal of Geophysical Research*, 100(B9), 17,587–17,602, doi:10.1016/S0016-0032(16)90156-X.

Kroll, K. A., E. S. Cochran, K. B. Richards-Dinger, and D. F. Sumy (2013), Aftershocks of the 2010 Mw 7.2 El Mayor-Cucapah earthquake reveal complex faulting in the Yuha Desert, California, *Journal of Geophysical Research: Solid Earth*, 118(October), 6146–6164, doi:10.1002/2013JB010529.

Langbein, J. (2004), Noise in two-color electronic distance meter measurements revisited, *Journal of Geophysical Research: Solid Earth*, 109(4), 1–16, doi:10.1029/2003JB002819.

Langbein, J. (2008), Noise in GPS displacement measurements from Southern California and Southern Nevada, *Journal of Geophysical Research: Solid Earth*, 113(5), 1–12, doi:10.1029/2007JB005247.

- Langbein, J. (2012), Estimating rate uncertainty with maximum likelihood: Differences between power-law and flicker-random-walk models, *Journal of Geodesy*, 86(9), 775–783, doi:10.1007/s00190-012-0556-5.
- Langbein, J. (2015), Borehole strainmeter measurements spanning the 2014 Mw6.0 South Napa Earthquake, California: The effect from instrument calibration, *Journal of Geophysical Research B: Solid Earth*, 120(10), 7190–7202, doi:10.1002/2015JB012278.
- Langbein, J., and H. Johnson (1997), Correlated errors in geodetic time series: Implications for time-dependent deformation, *Journal of Geophysical Research*, 102(B1), 591–603, doi:10.1029/96JB02945.
- Langbein, J., J. R. Murray, and H. A. Snyder (2006), Coseismic and initial postseismic deformation from the 2004 Parkfield, California, earthquake, observed by global positioning system, electronic distance meter, creepmeters, and borehole strainmeters, *Bulletin of the Seismological Society of America*, 96(4 B), 304–320, doi:10.1785/0120050823.
- Lawson, C. L., and R. J. Hanson (1995), Solving least squares problems, *SIAM classics in applied mathematics*, 15, 337, doi:10.2307/2005340.
- Lekic, V., S. W. French, and K. M. Fischer (2011), Lithospheric Thinning Beneath Rifted Regions of Southern California, *Science*, 334, 783–787.
- Lisowski, M., D. Dzurisin, R. P. Denlinger, and E. Y. Iwatsubo (2008), Analysis of GPS-Measured Deformation Associated with the 2004–2006 Dome-Building Eruption of Mount St. Helens, Washington, *Tech. Rep. September 1984*.
- Liu, H.-P., D. L. Anderson, and H. Kanamori (1976), Velocity dispersion due to anelasticity; implications for seismology and mantle composition, *Geophysical Journal of the Royal Astronomical Society*, 47, 41–58, doi:10.1111/j.1365-246X.1976.tb01261.x.
- Lohman, R. B., and J. R. Murray (2013), The SCEC Geodetic Transient-Detection Validation Exercise, *Seismological Research Letters*, 84(3), 419–425, doi:10.1785/0220130041.
- Lundgren, P., E. A. Hetland, Z. Liu, and E. J. Fielding (2009), Southern San Andreas-San Jacinto fault system slip rates estimated from earthquake cycle models constrained by GPS and interferometric synthetic aperture radar observations, *Journal of Geophysical Research: Solid Earth*, 114(2), 1–18, doi:10.1029/2008JB005996.
- Lyzenga, G. A., W. R. Panero, and A. Donnellan (2000), Deformation, *Journal of Geophysical Research*, 105(B2), 3151–3157.

- Mackay, D. J. C. (1998), Introduction to Gaussian processes, *Neural Networks and Machine Learning*, 168(1996), 133–165, doi:10.1007/s10067-003-0742-1.
- Mao, A., G. A. Harrison, and H. Dixon (1999), Noise in GPS coordinate time series, *Journal of Geophysical Research*, 104(B2), 2797–2816.
- Marone, C. J., C. H. Scholz, and R. Bilham (1991), On the mechanics of earthquake afterslip, *Journal of Geophysical Research*, 96(B5), 8441–8452.
- McCaffrey, R., A. I. Qamar, R. W. King, R. Wells, G. Khazaradze, C. A. Williams, C. W. Stevens, J. J. Vollick, and P. C. Zwick (2007), Fault locking, block rotation and crustal deformation in the Pacific Northwest, *Geophysical Journal International*, 169(3), 1315–1340, doi:10.1111/j.1365-246X.2007.03371.x.
- McCaffrey, R., R. W. King, S. J. Payne, and M. Lancaster (2013), Active tectonics of northwestern U.S. inferred from GPS-derived surface velocities, *Journal of Geophysical Research: Solid Earth*, 118, 709–723, doi:10.1029/2012JB009473.
- McGuire, J. J., and P. Segall (2003), Imaging of aseismic fault slip transients recorded by dense geodetic networks, *Geophysical Journal International*, 155, 778–788, doi:10.1111/j.1365-246X.2003.02022.x.
- Meade, B. J. (2007), Algorithms for the calculation of exact displacements, strains, and stresses for triangular dislocation elements in a uniform elastic half space, *Computers and Geosciences*, 33(8), 1064–1075, doi:10.1016/j.cageo.2006.12.003.
- Meade, B. J., and B. H. Hager (2005), Block models of crustal motion in southern California constrained by GPS measurements, *Journal of Geophysical Research: Solid Earth*, 110, 1–19, doi:10.1029/2004JB003209.
- Meade, B. J., Y. Klinger, and E. A. Hetland (2013), Inference of multiple earthquake-cycle relaxation timescales from irregular geodetic sampling of interseismic deformation, *Bulletin of the Seismological Society of America*, 103(5), 2824–2835, doi:10.1785/0120130006.
- Miyazaki, S., J. J. McGuire, and P. Segall (2003), A transient subduction zone slip episode in southwest Japan observed by the nationwide GPS array, *Journal of Geophysical Research*, 108(B2), 1–15, doi:10.1029/2001JB000456.
- Montési, L. G. J., and G. Hirth (2003), Grain size evolution and the rheology of ductile shear zones: From laboratory experiments to postseismic creep, *Earth and Planetary Science Letters*, 211, 97–110, doi:10.1016/S0012-821X(03)00196-1.

Moritz, H. (1978), Least-Squares Collocation, *Reviews of Geophysics*, 16(3), 421–430, doi: 10.1029/RG016i003p00421.

Murray, J. R., and P. Segall (2005), Spatiotemporal evolution of a transient slip event on the San Andreas fault near Parkfield, California, *Journal of Geophysical Research : Solid Earth*, 110(B09407), 1–12, doi:10.1029/2005JB003651.

Murray, J. R., and J. Svart (2017), Global Positioning System Data Collection, Processing, and Analysis Conducted by the U.S. Geological Survey Earthquake Hazards Program, *Seismological Research Letters*, 88(3), 1 – 10, doi:10.1785/0220160204.

Murray, M. H., and M. Lisowski (2000), Strain accumulation along the Cascadia subduction zone in western Washington, *Geophysical Research Letters*, 27(22), 3631–3634.

Nur, A., and G. Mavko (1974), Postseismic viscoelastic rebound, *Science*, 183(4121), 204–206, doi:10.1038/098448b0.

O'Connell, R. J. (1971), Rheology of the Mantle, *EOS, Transactions, American Geophysical Union*, 52, 140–142.

Ohtani, R., J. J. McGuire, and P. Segall (2010), Network strain filter: A new tool for monitoring and detecting transient deformation signals in GPS arrays, *Journal of Geophysical Research: Solid Earth*, 115(12), 1–17, doi:10.1029/2010JB007442.

Okada, Y. (1992), Internal deformation due to shear and tensile faults in a half space, *Bulletin of the Seismological Society of America*, 82(2), 1018–1040.

Oskin, M. E., et al. (2012), Near-field deformation from the El Mayor-Cucapah earthquake revealed by differential LIDAR, *Science*, 335(6069), 702–705, doi:10.1126/science.1213778.

Papoulis, A. (1991), *Probability, Random Variables, and Stochastic Processes*, 3 ed., McGraw-Hill, New York.

Patterson, H. D., and R. Thompson (1971), Recovery of Inter-Block Information when Block Sizes are Unequal, *Biometrika*, 58(3), 545–554.

Peltzer, G., P. Rosen, F. Rogez, and K. Hudnut (1998), Poroelastic rebound along the Landers 1992 earthquake surface rupture, *Journal of Geophysical Research*, 103(B12), 30,131, doi:10.1029/98JB02302.

Perfettini, H., J. P. Avouac, and J. C. Ruegg (2005), Geodetic displacements and aftershocks following the 2001  $Mw = 8.4$  Peru earthquake: Implications for the mechanics of the earthquake cycle along subduction zones, *Journal of Geophysical Research B: Solid Earth*, 110(9), 1–19, doi:10.1029/2004JB003522.

Pollitz, F., C. Wicks, and W. Thatcher (2001), Mantle Flow Beneath a Continental Strike-Slip Fault : Postseismic Deformation After the 1999 Hector Mine Earthquake, *Science*, 293, 1814–1818, doi:10.1126/science.1061361.

Pollitz, F. F. (1997), Gravitational viscoelastic postseismic relaxation on a layered spherical Earth, *Journal of Geophysical Research*, 102, 17,921, doi:10.1029/97JB01277.

Pollitz, F. F. (2003), Transient rheology of the uppermost mantle beneath the Mojave Desert, California, *Earth and Planetary Science Letters*, 215, 89–104, doi:10.1016/S0012-821X(03)00432-1.

Pollitz, F. F. (2005), Transient rheology of the upper mantle beneath central Alaska inferred from the crustal velocity field following the 2002 Denali earthquake, *Journal of Geophysical Research B: Solid Earth*, 110, 1–16, doi:10.1029/2005JB003672.

Pollitz, F. F. (2015), Postearthquake relaxation evidence for laterally variable viscoelastic structure and water content in the Southern California mantle, *Journal of Geophysical Research: Solid Earth*, 120, 2672–2696, doi:10.1002/2014JB011603.

Pollitz, F. F., and W. Thatcher (2010), On the resolution of shallow mantle viscosity structure using postearthquake relaxation data: Application to the 1999 Hector Mine, California, earthquake, *Journal of Geophysical Research: Solid Earth*, 115(10), 1–20, doi:10.1029/2010JB007405.

Pollitz, F. F., G. Peltzer, and R. Bürgmann (2000), Mobility of continental mantle: Evidence from postseismic geodetic observations following the 1992 Landers earthquake, *Journal of Geophysical Research*, 105(B4), 8035–8054, doi:10.1029/1999JB900380.

Pollitz, F. F., R. Bürgmann, and W. Thatcher (2012), Illumination of rheological mantle heterogeneity by the M7.2 2010 El Mayor-Cucapah earthquake, *Geochemistry, Geophysics, Geosystems*, 13(6), 1–17, doi:10.1029/2012GC004139.

Press, W. H., B. P. Flannery, S. A. Teukolsky, and W. T. Vetterling (2007), *Numerical Recipes: The Art of Scientific Computing*, 3 ed., Cambridge University Press, Cambridge, doi:10.1137/1031025.

Rasmussen, C. E., and C. K. I. Williams (2006), *Gaussian processes for machine learning*, The MIT Press.

Rauch, H. E., F. Tung, and C. T. Striebel (1965), Maximum likelihood estimates of linear dynamic systems, *AIAA Journal*, 3(8), 1445–1450.

Riva, R. E. M., and R. Govers (2009), Relating viscosities from postseismic relaxation to a realistic viscosity structure for the lithosphere, *Geophysical Journal International*, 176, 614–624, doi:10.1111/j.1365-246X.2008.04004.x.

Roeloffs, E. (2010), Tidal calibration of Plate Boundary Observatory borehole strainmeters: Roles of vertical and shear coupling, *Journal of Geophysical Research: Solid Earth*, 115(6), 1–25, doi:10.1029/2009JB006407.

Roeloffs, E. A. (2006), Evidence for Aseismic Deformation Rate Changes Prior To Earthquakes, *Annual Review of Earth and Planetary Sciences*, 34(1), 591–627, doi:10.1146/annurev.earth.34.031405.124947.

Rogers, G., and H. Dragert (2003), Episodic tremor and slip on the Cascadia subduction zone: the chatter of silent slip., *Science*, 300, 1942–1943, doi:10.1126/science.1084783.

Rollins, C., S. Barbot, and J.-P. Avouac (2015), Postseismic Deformation Following the 2010 M7.2 El Mayor-Cucapah Earthquake: Observations, Kinematic Inversions, and Dynamic Models, *Pure and Applied Geophysics*, 172(5), 1305–1358, doi:10.1007/s00024-014-1005-6.

Rybicki, K. (1971), The elastic residual field of a very long strike-slip fault in the presence of a discontinuity, *Bulletin of the Seismological Society of America*, 61(1), 79–92.

Ryder, I., B. Parsons, T. J. Wright, and G. J. Funning (2007), Post-seismic motion following the 1997 Manyi (Tibet) earthquake: InSAR observations and modelling, *Geophysical Journal International*, 169, 1009–1027, doi:10.1111/j.1365-246X.2006.03312.x.

Sandwell, D. T., and P. Wessel (2016), Interpolation of 2-D vector data using constraints from elasticity, *Geophysical Research Letters*, pp. 1–7, doi:10.1002/2016GL070340.Received.

Savage, J. C. (1990), Equivalent strike-slip earthquake cycles in half-space and lithosphere–asthenosphere earth models, *Journal of Geophysical Research*, 95(B4), 4873–4879, doi:10.1029/JB095iB04p04873.

Savage, J. C., and R. O. Burford (1973), Geodetic determination of relative plate motion in central California, *Journal of Geophysical Research*, 78(5), 832–845.

Savage, J. C., and W. H. Prescott (1978), Asthenosphere readjustment and the earthquake cycle, *Journal of Geophysical Research*, 83(8), 3369, doi:10.1029/JB083iB07p03369.

Savage, J. C., and J. L. Svare (1997), Postseismic deformation associated with the 1992 Mw=7.3 Landers earthquake, southern California, *Journal of Geophysical Research*, 102(B4), 7565–7577.

Savage, J. C., and J. L. Svare (2009), Postseismic relaxation following the 1992 M 7.3 Landers and 1999 M 7.1 Hector Mine earthquakes , southern California, *Journal of Geophysical Research*, 114(B01401), doi:10.1029/2008JB005938.

Savage, J. C., J. L. Svare, and S. B. Yu (2005a), Postseismic relaxation and transient creep, *Journal of Geophysical Research: Solid Earth*, 110(11), 1–14, doi:10.1029/2005JB003687.

Savage, J. C., J. L. Svare, and S. B. Yu (2005b), Postseismic relaxation and transient creep, *Journal of Geophysical Research: Solid Earth*, 110(B11402), 1–14, doi:10.1029/2005JB003687.

Schmidt, D. A., and H. Gao (2010), Source parameters and time-dependent slip distributions of slow slip events on the Cascadia subduction zone from 1998 to 2008, *Journal of Geophysical Research: Solid Earth*, 115(4), 1–13, doi:10.1029/2008JB006045.

Segall, P. (2010), *Earthquake and volcano deformation*, Princeton University Press, Princeton, NJ.

Segall, P., and M. Mathews (1997), Time dependent inversion of geodetic data, *Journal of Geophysical Research*, 102(B10), 22,391–22,409.

Shen, Z., M. Wang, Y. Zeng, and F. Wang (2015), Optimal Interpolation of Spatially Discretized Geodetic Data, *Bulletin of the Seismological Society of America*, 105(4), 2117–2127, doi:10.1785/0120140247.

Shen, Z. K., D. D. Jackson, B. X. Ge, and X. G. Bob (1996), Crustal deformation across and beyond the Los Angeles basin from geodetic measurements, *Journal of Geophysical Research*, 101(B12), 27,927–27,957, doi:10.1029/96JB02544.

Spinler, J. C., R. A. Bennett, C. Walls, L. Shawn, and J. J. G. Garcia (2015), Assessing long-term postseismic deformation following the M7.2 4 April 2010, El Mayor-Cucapah earthquake with implications for lithospheric rheology in the Salton Trough, *Journal of Geophysical Research: Solid Earth*, 120, 3664–3679, doi:10.1002/2014JB011613.Received.

Tape, C., P. Musé, M. Simons, D. Dong, and F. Webb (2009), Multiscale estimation of GPS velocity fields, *Geophysical Journal International*, 179(2), 945–971, doi:10.1111/j.1365-246X.2009.04337.x.

Thatcher, W., and F. F. Pollitz (2008), Temporal evolution of continental lithospheric strength in actively deforming regions, *GSA Today*, 18(4), 4–11, doi:10.1130/GSAT01804-5A.1.

Vauchez, a., and a. Tommasi (2003), Wrench faults down to the asthenosphere: geological and geophysical evidence and thermomechanical effects, *Geological Society, London, Special Publications*, 210, 15–34, doi:10.1144/GSL.SP.2003.210.01.02.

Wdowinski, S., J. Zhang, P. Fang, and J. Genrich (1997), Southern California Permanent GPS Geodetic Array: Spatial filtering of daily positions for estimating coseismic and postseismic displacements induced by the 1992 Landers earthquake, *102*(97), 57–70.

Wech, A. G. (2010), Interactive Tremor Monitoring, *Seismological Research Letters*, 81(4), 664 – 669, doi:10.1785/gssrl.

Wech, A. G., K. C. Creager, and T. I. Melbourne (2009), Seismic and geodetic constraints on Cascadia slow slip, *Journal of Geophysical Research: Solid Earth*, 114(10), 1–9, doi: 10.1029/2008JB006090.

Wei, M., D. Sandwell, Y. Fialko, and R. Bilham (2011a), Slip on faults in the Imperial Valley triggered by the 4 April 2010 Mw 7.2 El Mayor-Cucapah earthquake revealed by InSAR, *Geophysical Research Letters*, 38(L01308), doi:10.1029/2010GL045235.

Wei, M., Y. Liu, Y. Kaneko, J. J. McGuire, and R. Bilham (2015), Dynamic triggering of creep events in the Salton Trough, Southern California by regional M5.4 earthquakes constrained by geodetic observations and numerical simulations, *Earth and Planetary Science Letters*, 427, 1–10, doi:10.1016/j.epsl.2015.06.044.

Wei, S., et al. (2011b), Superficial simplicity of the 2010 El MayorCucapah earthquake of Baja California in Mexico, *Nature Geoscience*, 4, 615–618, doi:10.1038/ngeo1213.

Wendland, H. (2005), *Scattered data approximation*, 348 pp., doi:10.2277/0521843359.

Williams, S. D. P., Y. Bock, P. Fang, P. Jamason, R. M. Nikolaidis, L. Prawirodirdjo, M. Miller, and D. J. Johnson (2004), Error analysis of continuous GPS position time series, *Journal of Geophysical Research: Solid Earth*, 109(B3), doi:10.1029/2003JB002741.

- Wyatt, F. (1982), Displacement of Surface Monuments: Horizontal Motion, *Journal of Geophysical Research*, 87(B2), 979–989.
- Wyatt, F. K. (1989), Displacement of surface monuments: Vertical motion, *Journal of Geophysical Research*, 94(B2), 1655–1664.
- Yamasaki, T., and G. a. Houseman (2012a), The signature of depth-dependent viscosity structure in post-seismic deformation, *Geophysical Journal International*, 190, 769–784, doi:10.1111/j.1365-246X.2012.05534.x.
- Yamasaki, T., and G. a. Houseman (2012b), The crustal viscosity gradient measured from post-seismic deformation: A case study of the 1997 Manyi (Tibet) earthquake, *Earth and Planetary Science Letters*, 351-352, 105–114, doi:10.1016/j.epsl.2012.07.030.
- Yang, M., and M. N. Toksöz (1981), Time-dependent deformation and stress relaxation after strike-slip earthquakes, *J. Geophys. Res.*, 86(80), 2889–2901.
- Yuen, D. A., and W. R. Peltier (1982), Normal modes of the viscoelastic earth, *Geophysical Journal of the Royal Astronomical Society*, 69, 495–526, doi:10.1111/j.1365-246X.1982.tb04962.x.
- Zhang, J., Y. Bock, H. Johnson, P. Fang, S. Williams, J. Genrich, S. Wdowinski, and J. Behr (1997), Southern California Permanent GPS Geodetic Array: Error analysis of daily position estimates and site velocities, *Journal of Geophysical Research*, 102(B8), 18,035–18,055.